

Separation of Nitrogen from Natural Gas: Conventional and Emerging Technologies

Zhikao Li

Master of Science in Chemical and Biological Engineering



This thesis is presented for the degree of Doctor of Philosophy

of The University of Western Australia

School of Mechanical and Chemical Engineering

Fluid Science and Resources Division

2018

THESIS DECLARATION

I, Zhikao Li, certify that:

This thesis has been substantially accomplished during enrolment in the degree.

This thesis does not contain material which has been submitted for the award of any other degree or diploma in my name, in any university or other tertiary institution.

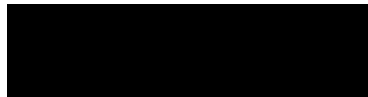
No part of this work will, in the future, be used in a submission in my name, for any other degree or diploma in any university or other tertiary institution without the prior approval of The University of Western Australia and where applicable, any partner institution responsible for the joint-award of this degree.

This thesis does not contain any material previously published or written by another person, except where due reference has been made in the text and, where relevant, in the Declaration that follows.

The work(s) are not in any way a violation or infringement of any copyright, trademark, patent, or other rights whatsoever of any person.

This thesis contains published work and work prepared for publication, some of which has been co-authored.

Signature:

A solid black rectangular box used to redact the signature of the author.

Date: April 05, 2018

ABSTRACT

Natural gas (NG) is considered to be one of the most environmentally-friendly energy sources for the coming century due to its lower rate of carbon emissions to the environment compared to coal and petroleum. The growth in global demand for NG and the depletion of conventional resources have boosted the development of sub-quality natural gas reserves that contain high levels of impurities, such as nitrogen gas (N_2) (>4%). The removal of N_2 from natural gas remains one of the most challenging tasks in the natural gas upgrading process. Currently, cryogenic distillation technology is the principal technology for separating N_2 from methane (CH_4) on a large scale (> 20 MMscfd). However, this technology is very energy-intensive. Alternative technologies to remove N_2 from NG in a more economical and environmentally-friendly way are required.

In this thesis, an extensive review is conducted to study the mechanisms and prospective processes by which N_2 and CH_4 could be separated. The physical and chemical differences of N_2 and CH_4 are the foundation of any such separation and are used to critically analyze the state of the art of conventional separation approaches as well as several emerging separation approaches. New experimental approaches, namely N_2 separation from CH_4 by differences in adsorption kinetics, N_2 capture by transition metal complexes (TMC) solutions, and N_2 capture by lithium metal, were developed and conducted.

Adsorption based processes are one of the well-established technologies to separate gas mixtures. Adsorption equilibria and kinetics are two sets of properties crucial to the design and simulation of adsorption-based gas separation processes. The adsorption equilibria and kinetics of N_2 and CH_4 on four commercial adsorbents were experimentally studied in this work. The adsorption measurements were carried out using a commercial volumetric apparatus, which was operated in its rate of adsorption mode. Calibration experiments were conducted using helium to correct for the impact of gas expansion on the observed uptake dynamics. Correcting the rate of adsorption data for N_2 and CH_4 using the non-isothermal Fickian diffusion (FD) model was also found to be essential. The measured sorption kinetics had no dependence on the gas pressure but their temperature dependence was consistent with an Arrhenius-type relation. The effective sorption rates extracted using the FD model were able to resolve inconsistencies in the literature for similar measurements.

A continuous recirculating absorption process operating at ambient temperature would have clear advantages over cryogenic distillation processes. The key to the development of such an absorption process is to find a N_2 -selective solvent. Although this can be extremely challenging as N_2 is very stable and inert at ambient conditions, N_2 can function as a weak ligand and be bound to certain TMCs. An aqueous solution consisting of a "task-specific" TMC which can selectively and reversibly bond N_2 is

reported. The absorption equilibrium capacities of N_2 in this TMC aqueous solution were measured using a custom-built volumetric apparatus at temperatures of 293.15, 303.15 and 313.15 K and pressures ranging from 0 to 4000 kPa. The results show that the ruthenium-based (Ru-based) TMC aqueous solution could selectively bond N_2 over CH_4 with a specific capacity of up to 0.5 mole N_2 per mole of Ru^{II} , which is half of the stoichiometric amount. The reversibility of N_2 bonding in this TMC solution was also verified by desorption tests. The calculated N_2 absorption energy (20-70 kJ/mol) was moderate, indicating a viable regeneration energy requirement.

Finally, the ability of lithium metal (Li) to capture N_2 from natural gas was investigated experimentally. The Li and N_2 reaction was characterized in this work by SEM, TGA-DSC and synchrotron XRD measurements. In addition, the separation performance was examined using a custom-built flow-through apparatus. Compared to conventional adsorbents, Li metal showed significant advantages for separating N_2 from CH_4 : (1) the theoretical loading capacity of N_2 on Li is 24 mmol N_2/g , which is an order of magnitude higher than the best reported N_2 selective adsorbents[1]; and (2) Li does not react with CH_4 at room temperature, which indicates that Li could have a near infinite selectivity for N_2 over CH_4 . Two approaches to recycle Li from Li_3N are discussed: (1) lithium recycling by thermal decomposition of Li_3N ; (2) lithium recycling by a closed chemical loop.

In conclusion, while the kinetic separation of N_2 from CH_4 on various adsorbents only delivered a moderate performance, the other two more innovative approaches have both clear advantages and significant challenges that need to overcome. Based on the performance of the separation of N_2 from CH_4 using Ru-based TMC solution, an attractive and promising alternative approach is proposed. Although the limited availability of Ru^{II} and the low concentration of this Ru-based TMC in aqueous solution will likely impede its industrial-scale application, this study serves as a proof-of-concept for the future development of economically viable nitrogen bonding TMCs. Lastly, while the tremendous potential of Li to selectively capture N_2 are demonstrated in this thesis, the in situ thermal regeneration of Li was proved to be impractical. An alternative batch mode regeneration process involving a chemical loop was then proposed, which was estimated to be technically and economically more feasible.

TABLE OF CONTENTS

Contents

THESIS DECLARATION	2
ABSTRACT	3
TABLE OF CONTENTS.....	5
LIST OF TABLES	8
LIST OF FIGURES.....	10
ACKNOWLEDGEMENTS	14
AUTHORSHIP DECLARATION: CO-AUTHORED PUBLICATIONS	15
Chapter 1: Introduction.....	1
1.1 <i>The Need for Energy and Natural Gas</i>	<i>1</i>
1.2 <i>The Need to Separate Nitrogen from Natural Gas</i>	<i>2</i>
1.3 <i>The Challenges of Separating Nitrogen and Methane.....</i>	<i>3</i>
1.3.1 Physical Properties.....	3
1.3.2 Chemical Properties.....	5
1.3.3 Separation Processes and Mechanisms.....	6
1.4 <i>Thesis Objectives and Outline</i>	<i>7</i>
Chapter 2: Background and Overview	9
2.1 <i>Separation of Nitrogen from Natural gas by Conventional Technologies</i>	<i>10</i>
2.1.1 Cryogenic Distillation	10
2.1.2 Membranes.....	11
2.1.3 Adsorption	17
2.1.4 Absorption	21
2.2 <i>Separation of Nitrogen by Emerging Technologies.....</i>	<i>24</i>
2.2.1 Biological Nitrogen Fixation (BNF)	24
2.2.2 Transition Metal Complex (TMC) Based Processes.....	30
2.2.3 Haber - Bosch Process.....	37
2.2.4 Electrochemical Nitrogen Fixation.....	37
2.2.5 Lithium Based Process	41

2.3	<i>Conclusions</i>	43
Chapter 3: Adsorption Equilibria and Kinetics of CH₄ and N₂ on Commercial Zeolites and Carbons47		
3.1	<i>Forward</i>	47
3.2	<i>Abstract</i>	47
3.3	<i>Introduction</i>	47
3.4	<i>Experimental Section</i>	50
3.4.1	Method and Materials	50
3.4.2	Calibration with Helium	52
3.5	<i>Models for Adsorption Kinetics</i>	53
3.6	<i>Results and Discussion</i>	56
3.6.1	Adsorption Equilibria	56
3.6.2	Kinetic Measurement Calibration	62
3.6.3	Sorption Rate Determination from Dynamic Uptake with Kinetic Models.....	64
3.6.4	Kinetic Adsorption Results	65
3.7	<i>Conclusions</i>	72
3.8	<i>Acknowledgements</i>	73
Chapter 4: Separation of Nitrogen from Methane Using A Transitional Metal Complex (TMC) Solution ..74		
4.1	<i>Forward</i>	74
4.2	<i>Summary of the Screened TMC Solutions</i>	74
4.3	<i>Abstract</i>	77
4.4	<i>Introduction</i>	78
4.5	<i>Materials and Apparatus</i>	80
4.5.1	Materials Preparation	80
4.5.2	Apparatus.....	82
4.6	<i>Analysis and Uncertainty</i>	83
4.7	<i>Results and Discussion</i>	86
4.7.1	Validation Measurements	86
4.7.2	Nitrogen Absorption in K[Ru ^{II} (EDTA)] Aqueous Solution	88
4.8	<i>Conclusion</i>	97
Chapter 5: Separation of Nitrogen from Natural Gas by Lithium Metal99		

5.1	<i>Introduction</i>	99
5.2	<i>Experimental Section</i>	101
5.2.1	Materials and Preparation of Samples	101
5.2.2	Sample Characterisation	103
5.2.3	The Reaction of Lithium with Dry Nitrogen	103
5.2.4	Binary Gas Mixture Breakthrough	104
5.3	<i>The Results of the Reaction of Lithium with Nitrogen</i>	108
5.3.1	Synchrotron XRD	108
5.3.2	Thermogravimetric Measurements of Uptake	111
5.3.3	ASAP2020 Measurements of Uptake	112
5.3.4	SEM-EDS Characterisation	113
5.3.5	Discussion	116
5.4	<i>Separation of Nitrogen from A Binary Gas Mixture of Nitrogen and Methane Lithium</i>	118
5.5	<i>Regeneration of Lithium from Lithium Nitride</i>	119
5.5.1	Regeneration of Lithium by Thermal Decomposition of Lithium Nitride	119
5.5.2	Regeneration of Lithium by A Chemical Loop	128
5.6	<i>Conclusion</i>	129
Chapter 6:	Conclusion and Future Work	131
6.1	<i>Conclusion</i>	131
6.2	<i>Recommendations and Future Work</i>	134
Appendix A:	Uptake of N₂ on Zeolite 4A	136
Appendix B:	TMC Synthesis Method	136
Appendix B.1.	<i>K[Ru^{II}(EDTA)]</i>	136
Appendix B.2.	<i>Fe(H)₂(P(OEt)₃)₄</i>	142
Reference	146

LIST OF TABLES

Table 1.1 Key physical properties of nitrogen and methane [15, 16] (Adapted from ref. 15 and 16) ...	4
Table 1.2 Property differences and separation mechanism matrix for N ₂ and CH ₄	7
Table 2.1 Conventional and emerging technologies for the separation of nitrogen from natural gas covered in this chapter	10
Table 2.2 Overview of types of membranes and their applications	12
Table 2.3 Summary of separation properties of polymer membranes[53]	13
Table 2.4 Comparison of N ₂ /CH ₄ separations through inorganic membranes[66] (Table adapted from ref. 25).....	16
Table 2.5 The loading capacities of nitrogen on Fe-Mo cofactor and nitrogenase and the required amount of Fe-Mo cofactor and nitrogenase to absorb the nitrogen in 1 m ³ of natural gas (nitrogen concentration = 10%).....	27
Table 2.6 The annual fixation amount of nitrogen by biological nitrogen fixation (BNF) in 2005 (unit Tg)[121].....	28
Table 2.7 Worldwide natural gas production in 2014 (billion m ³)[125]	28
Table 2.8 Successful examples of sorbents based on TMC for different applications of binary gas mixture separation. Such TMC adsorbents are named as π -complexation.....	34
Table 2.9 The estimated areas of electrolytic membrane and their capital cost to handle different natural gas flow rates with different ammonia production rates	41
Table 2.10 Review of conventional and emerging technologies of nitrogen separation from natural gas covered in this chapter	45
Table 3.1 Physical properties of the adsorbents.....	51
Table 3.2 Pure methane and nitrogen single component adsorption capacities, Q_e , along with their standard uncertainties, $u(Q_e)$, on the four adsorbents tested in this study. $u(Q_e)$ was calculated using Eqn. 14 with standard uncertainties for sample mass: 0.0001 g, pressure: 0.15 % of reading, temperature: 0.02 K, and volume: 0.074 mL.....	57
Table 3.3. Effective sorption rate and associated parameters for the non-isothermal FD model in eqs (6)-(12) for CH ₄ and N ₂ on activated carbon Norit RB3. Values are not reported for conditions where 90% of the uptake occurred within 1 s.	68
Table 3.4 Effective sorption rate of CH ₄ and N ₂ on zeolite 13X obtained from the non-isothermal FD model Values are not reported for conditions where 90% of the uptake occurred within 1 s.....	69
Table 3.5 Effective sorption rate of CH ₄ and N ₂ on carbon molecular sieve MSC-3K 172 obtained from the non-isothermal FD model.....	70
Table 3.6 Effective sorption rate of CH ₄ and N ₂ on Zeolite 4A obtained from the non-isothermal FD model	71
Table 4.1 Summary of the performance of the TMC solutions that have been studied in this project	76
Table 4.2 The uncertainties of the components associated with the static solubility apparatus	85

Table 4.3 Loading capacities of nitrogen in water with the associated uncertainties and their deviations from MF. MF: multiflash.	88
Table 4.4 The capacities and the specific capacities of nitrogen in $K[Ru^{II}(EDTA)]$ aqueous solution and pure water at 20 °C, 30 °C and 40 °C.	93
Table 4.5 The absorption enthalpies of the nitrogen on Ru^{II} . [29, 32]	95
Table 4.6 The absorption/desorption of nitrogen on Ru^{II} with an uncertainty of 0.01 mol N_2 /mol Ru^{II} . At a pressure range from 0 to 3000 kPa and at temperatures of 30 °C and 60 °C.	97
Table 5.1 The geometrical diameters and the density of the original lithium sample and the produced lithium nitride. (The geometrical diameters were measured by a caliper with an uncertainty of 0.01 mm).....	118
Table 5.2 Thermochemistry data of studied materials[293, 294]	121

LIST OF FIGURES

Figure 1.1. (a) Primary energy consumption by fuel; (b) Share of primary energy[5].....	1
Figure 2.1 The solubilities of methane and nitrogen in liquid ammonia. Due to the lack of solubilities data at the same temperature, the solubilities of nitrogen (●) were shown at 38 °C and the solubilities of methane (■) were shown at 40 °C. The extracted Henry's selectivity of nitrogen over methane is around 0.25.....	23
Figure 2.2 Schematic of FeMo nitrogenase. (A) MoFe protein complex with the Fe protein homodimer shown in tan, the MoFe protein α subunit in green, and the β subunit in cyan. (B) Space-filling and stick models for the 4Fe-4S cluster (F), P-cluster (P), and FeMo-co (M). [109].....	26
Figure 2.3 Cellular respiration: (a) Aerobic Respiration; (b) Anaerobic Respiration. ATP stands for adenosine triphosphate, ADP stands for adenosine diphosphate and P_i stands for phosphate. One glucose molecule can produce 38 ATP through aerobic respiration or 2 ATP through anaerobic respiration.....	29
Figure 2.4 End-on bonding mode (Michael and Samuel, 2000). The shading means the two π orbitals (on nitrogen or on metal) are in an orthogonal position.....	31
Figure 2.5 Schematic illustration of electrochemical conversion of nitrogen to ammonia using a natural gas stream as the source of nitrogen. A natural gas stream mainly containing nitrogen and methane is sent to the nitrogen chamber where nitrogen is converted to ammonia. The effluent stream from the nitrogen chamber mainly contains the produced ammonia and the remaining methane. Due to the large difference in their physical properties, the binary gas mixture of ammonia and methane can be separated relatively easier compared to the binary gas mixture of nitrogen and methane.	38
Figure 3.1 Variations in effective sorption rate (D/r^2) reported in the literature for N_2 and CH_4 on activated carbon (AC) [94, 200, 203, 206], zeolite 13X [207-209], carbon molecular sieve (CMS) [199, 202, 210] and zeolite 4A [211-213].....	49
Figure 3.2 Examples of rate of adsorption measurements for CH_4 on Norit RB3 (fast) and zeolite 4A (slow) for three consecutive pressure steps at 303 K. The solid curves correspond to ROA measurements, while the dashed curve indicates the pressure evolution that occurred prior to the attainment of equilibrium.....	52
Figure 3.3. Schematic of the volumetric adsorption system: red solid line represents the apparatus' reference volume, used to calculate the amount of gas dosed into the sample volume below V_{12} . The four pressure transducers could also be isolated (valves not shown) from the manifold whenever the pressure exceeded their full scale.	53
Figure 3.4 Measured adsorption capacity of pure methane (solid symbols) and pure nitrogen (hollow symbols) on four adsorbents at a) 303 K, and, b) 273 K for pressures up to 120 kPa.....	57
Figure 3.5 Pressure readings in methane rate of adsorption measurements on Norit RB3 at around 80 kPa at 273 K together with corresponding helium calibration pressure readings.	63
Figure 3.6 Experimental and theoretical (black solid lines representing FD model for both CH_4 and N_2 , and blue dash line representing LDF model for CH_4) uptake curves of CH_4 and N_2 on a) Norit RB3, b) Zeolite 13X, c) carbon molecular sieve MSC-3K 172, and d) zeolite 4A pellet at 273 K with pressure around 100 kPa	65

Figure 3.7 Effective diffusion time constant for CH ₄ and N ₂ on Norit RB3, zeolite 13X, zeolite 4A and carbon molecular sieve MSC-3K 172 obtained by non-isothermal Fickian diffusion model at 303 K (solid) and 273 K (hollow) at various pressures: a) effective sorption rate constant for CH ₄ , b) effective sorption rate constant for N ₂	66
Figure 3.8 Temperature dependence of effective sorption rate	72
Figure 4.1 Summary of the performance of the TMC solutions studied in this project. Red: the capacity of nitrogen in pure solvents (pure water or pure TEG); Blue: the increased capacities of nitrogen in TMC solutions	77
Figure 4.2 Schematic of the air-bath static gas solubility apparatus. V: valve; AC: Accumulation cell; SC: solubility cell. An ISCO pump is used to inject the gas component into the AC to a specific pressure. An air oven (shown as the blue rectangle) is used to control and maintain the experimental temperatures. Four high pressure needle valves are used to connect the two cells and the associated line, which are extended to outside of the oven. A valve (V _e) is used to depressurize the system and a vacuum pump is used to evacuate the system.....	83
Figure 4.3 Isotherms of nitrogen loading in water at 30 °C. Absorption (●) and desorption (○) data were measured based on a cumulative method. The prediction data (dash line) were obtained from CPA-Infochem model implemented within MultiFlash (MF).[270]	86
Figure 4.4 Deviations of absorption from CPA-Infochem model which is implemented within MultiFlash. The pressure range is from 0 kPa to 3000 kPa and the testing temperature is 30 °C.	87
Figure 4.5 Schematic of nitrogen binding to [Ru(EDTA)] ⁻ . The shaded balloon stands for the vacant site of [Ru(EDTA)] ⁻ which accepts nitrogen at high pressure; while at low pressure, nitrogen escapes from [Ru(EDTA)] ⁻ and makes this nitrogen-binding process reversible.....	89
Figure 4.6 The loading capacities of nitrogen in pure water and K[Ru ^{II} (EDTA)] aqueous solutions at the pressure range of 0 to 3000 kPa and at the temperatures of 20, 30 and 40 °C. The capacities of nitrogen in pure water are shown with hollowed markers; the capacities of nitrogen in K[Ru ^{II} (EDTA)] aqueous solutions are shown with solid markers.	90
Figure 4.7 Comparison of the specific capacities of nitrogen on Ru ^{II} solution in this work and in the literature for a pressure range from 0 kPa to 3000 kPa. Three temperatures (20, 30 and 40 °C) were studied in this work; while only two temperatures (20 and 40 °C) were reported by Friesen, et al., (1993). The results in this work are shown with the solid markers; the results reported in literatures were shown with hollow markers.....	91
Figure 4.8 The comparison of the capacity of nitrogen in K[Ru ^{II} (EDTA)] aqueous solution and the capacities of N ₂ and CH ₄ in pure water at the pressure range from 0 to 3000 kPa and at the temperature of 30 °C.	92
Figure 4.9 The absorption enthalpies of the nitrogen on Ru ^{II} Calculated with Equation 4.3. The solid circle stands for the absorption enthalpy of nitrogen on Ru ^{II} calculated from the absorption capacities measured in this work at three temperatures (20, 30 and 40 °C); the hollow circle stands for the absorption enthalpy of nitrogen on Ru ^{II} calculated from the absorption capacities reported in literature at two temperatures (20 and 41 °C).[29, 32].....	94
Figure 4.10 The absorption (■) and desorption (□_30 °C and Δ_60 °C) of nitrogen in K[Ru ^{II} (EDTA)] aqueous solution at a pressure range from 0 to 3000 kPa and temperatures of 30 and 60 °C	96

Figure 5.1 Schematic of the activation of lithium samples by water moisture. The two flasks were located in an Ar-filled glove box. An isolation valve was used to stop moisture flowing after the lithium samples were activated. The left flask was filled with DI water (light blue color); the right flask was filled with as received lithium samples (light grey color). 103

Figure 5.2 Schematic (a) and picture (b) of the gas mixture breakthrough apparatus. The system was filled with helium before the binary gas mixture test and the helium flow rate was controlled by MFC-1. The binary gas mixture of nitrogen and methane was made by setting the flow rates with MFC-2 and MFC-3. The lithium-containing column and its associated lines were located in an air bath with a controllable temperature range from 30 to 400 °C. An air cooler was used to cool down the effluent gas stream to room temperature. An MFM was used to measure the effluent flow rate. The water sensor and the drier were used to avoid moisture entering the UGA. 105

Figure 5.3 In situ synchrotron XRD patterns of phase transformation from lithium to the lithium nitride in the atmosphere of nitrogen at 90 °C. (a) In situ synchrotron XRD patterns obtained from the static cell; (b) In situ synchrotron XRD patterns obtained from the flow-through cell with a nitrogen flowrate of 50 mL/min. The scanning angle (2 theta) is plotted as the x-axis; while the time of measurement is plotted as the y-axis. Characteristic peaks of lithium are located at 19, 27.3, and 33.5, while the characteristic peaks of lithium nitride are located at 12.3, 15.1, 25.3, 26.1, 29.0 and 36.0. Additionally, the main peak characteristic of LiOH is located at 17.3. 110

Figure 5.4 The uptakes of nitrogen and methane as a function of time on both non-activated and pre-activated lithium samples at 60°C and 138 kPa..... 111

Figure 5.5 Heat flow of the reactions of different lithium samples with nitrogen at the experimental temperature of 60 °C and pressure of 138 kPa. The integrated enthalpy for the reaction of pre-activated lithium with nitrogen is 55 kJ/mol (Li); the integrated enthalpy of the reaction of non-activated lithium with nitrogen is 0 kJ/mol (Li). 112

Figure 5.6 The uptakes of nitrogen and methane on non-activated and pre-activated lithium samples at 60°C and at a pressure range of 0 to 100 kPa..... 113

Figure 5.7 SEM and EDS of (a) as received lithium sample and (b) air-exposed lithium sample. The circled area confirms the SEM pictures are taken at the same position of the lithium metal. The oxygen content on the surface of lithium increased from 85.9 wt% to 94.5 wt% after exposure to air for 5 minutes. 114

Figure 5.8 Surface morphologies of (a) pre-activated lithium and (b) produced lithium nitride. The circled area on the surface of lithium nitride are cracks on lithium nitride, which provide the channels for the diffusion of nitrogen molecules. 115

Figure 5.9 Simplified schematic of the reaction routes of lithium with dry nitrogen. Route A has been proposed in the literature; [185, 186] Routes B and C are based on the tests conducted with the TGA and ASAP2020 in this work 117

Figure 5.10 Breakthrough curve of nitrogen (10 mol %) and methane (90 mol %) feed mixture passing through a lithium loaded column with, the total flow rate of 20 sccm and lithium sample mass of 0.80 g..... 119

Figure 5.11 Predicted Gibbs energy for the thermal decomposition of lithium nitride as a function of temperature. The calculation suggests that only when the temperature is above 1250 °C, will the thermal decomposition of lithium nitride become spontaneous..... 122

Figure 5.12 The thermal decomposition temperature of lithium nitride as a function of the partial pressure of nitrogen estimated by thermodynamic calculation, together with previously reported computed[192] and experimental data[288, 289] 124

Figure 5.13 Comparison of the saturated vapor pressure of lithium and the lithium partial pressure of lithium decomposed from lithium nitride as a function of temperature 124

Figure 5.14 Thermal decomposition tests of lithium nitride on the thermogravimetric analyzer (TGA) with the ceramic crucible. The blue line corresponds to the weight change of the lithium nitride sample, shown on the left vertical axis. The red line corresponds to the temperature profile, shown on the right vertical axis. (a) Experiment 1 with a temperature target of 500 °C at a ramp rate of temperature of 30 °C/min; the partial pressure of nitrogen is estimated to be smaller than 0.55 Pa. (b) Experiment 2 with an initial temperature target of 500 °C at a ramp rate of 30 °C/min, and a second temperature target of 800 °C at the same ramp rate; the partial pressure of nitrogen is estimated to be smaller than 0.55 Pa. 126

Figure 5.15 Thermal decomposition of lithium nitride on the thermogravimetric analyzer (TGA) with the platinum crucible. The green line corresponds to the weight change of the lithium nitride sample, shown on the left vertical axis. The blue line corresponds to the temperature profile, shown on the right vertical axis. The target temperature was 800 °C at a ramp rate of 5 °C/min; the partial pressure of nitrogen was estimated to be smaller than 0.55 Pa..... 127

Figure 5.16 Platinum crucible after the thermal decomposition of lithium nitride experiment at 800 °C. The bottom of the platinum crucible was “melted” by the produced lithium vapor, which was due to the formation of Li-Pt alloy. 128

Figure 5.17 Lithium recycle loop for the capture of nitrogen and production of NH₃ 128

ACKNOWLEDGEMENTS

First, I would like to thank my primary supervisor, Professor Eric May, for giving me the opportunity to pursue science in this research group. Your guidance and support have helped me to develop essential skills to go through this journey, and your dedication and vision in research is truly an inspiration to me. I really appreciate all the efforts and time you have put into this work.

I would like to thank Dr. Gongkui (James) Xiao, Dr. Gang (Kevin) Li and Dr. Brendan Graham for guiding me for the past four years. Thank you for all the insightful discussions and all the skills I have learned from you. Without your support, I would not have been able to finish this study and none of the work completed in this thesis would have been possible. I would like to thank our technicians Mr Craig Grimm and Mr David Amm, and all our group members. You are always there whenever I look for help.

I would also like to thank all my friends. Thank you for all the happy and sad moments that we have had together in this city. Thank you for supporting me and tolerating me during hardships and when my spirit was low. The journey of completing a Ph.D is not easy, but I am lucky enough to have you guys here as companions through this adventure.

Finally, I would like to thank my family. Thank you for your understanding, your patience, your encouragement, and your love during these pivotal four years.

This research was funded by Chevron Cooperation and supported by scholarship for international research fees (SIRF), university international stipend (UIS) and UIS scholarship.

The synchrotron XRD studied was supported by the Australian Synchrotron. The author gratefully acknowledges Dr. Qinfen Gu for his help and insightful discussion.

The author gratefully acknowledges the use of a simultaneous thermogravimetric analyzer and differential scanning calorimeter (Model: SDT Q600) from Professor Dongke Zhang and a thermogravimetric analyzer Q50 (TGA Q50) from Professor Hong Yang.

The author gratefully acknowledges the use of a scanning electron microscope & energy-dispersive X-ray spectroscopy (SEM-EDS) from the Centre for Microscopy, Characterisation and Analysis at University of Western Australia.

AUTHORSHIP DECLARATION: CO-AUTHORED PUBLICATIONS

This thesis contains work that has been published and prepared for publication.

Details of the work:

Adsorption equilibria and kinetics of CH₄ and N₂ on commercial zeolites and carbons

Location in thesis:

Chapter 3

Student contribution to work:

Zhikao Li contributed to the project by being involved in the designing and carrying out of experiments and data analysis.

Co-author signatures and dates: Gongkui Xiao, Thomas L Saleman

Date: April 03, 2018

Details of the work:

Separation of Nitrogen from Methane Using A Transitional Metal Complex (TMC) Solution

Location in thesis:

Chapter 4

Student contribution to work:

Zhikao Li contributed to the study by synthesizing the chemicals, designing and conducting experiments and data analysis, interpreting the results, and writing the manuscript

Co-author signatures and dates:

April 03, 2018

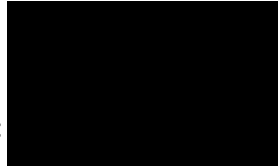
Student signature:



Date: April 05, 2018

I, Eric May, certify that the student statements regarding their contribution to each of the works listed above are correct

Coordinating supervisor signature:



Date: April 05, 2018

Chapter 1: Introduction

1.1 The Need for Energy and Natural Gas

As the world's population and productivity increase, the global economy is expected to almost double by 2035.[2] Matched with improvements in efficiency, world energy consumption is predicted to rise by 28% between 2015 and 2040.[3] Most of the new consumption will come from non-OECD countries, such as China and India. Within these countries, energy consumption is expected to rise by 41% between 2015 and 2040 due to strong economic growth, increased access to energy markets, and the demand from a quickly growing population.[3] The largest share of this energy consumption will continue to come from the industrial sector, such as mining, agriculture, manufacturing, and construction.[3, 4]

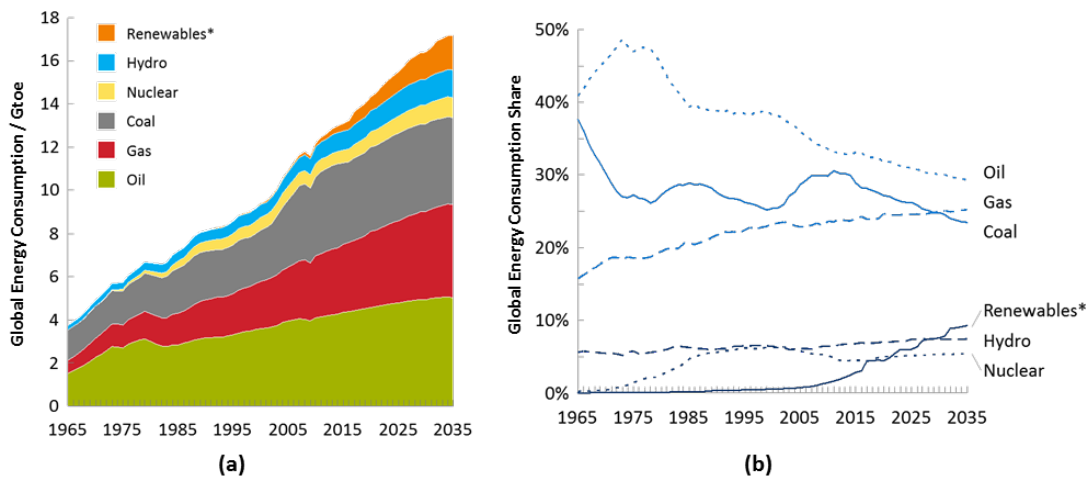


Figure 1.1. (a) Primary energy consumption by fuel; (b) Share of primary energy[5]

Historically, the industrial sector has relied heavily on fossil fuels, mostly oil and coal as an energy source, but the fuel mix has been gradually changing. Figure 1.1 shows that coal is increasingly being replaced by natural gas, renewables, hydro and nuclear power. This trend of weakening demand for coal can be observed in many sectors, such as electricity generation. [5]

Renewable energy, such as wind, solar, geothermal, biomass, and biofuels, is the fast-growing source of energy at a rate of 7.1% annually. However, this would still put its share at around 10% of primary energy supply by 2035.[4] Fossil fuels, such as oil, gas, and coal remain as dominant sources of energy powering the world economy.

While the growth of coal is projected to decline to 0.2% annually, and the growth of oil is projected at 0.7% annually and expected to slow gradually, natural gas will become the world's fastest-growing fossil fuel, increasing by 1.4 – 1.6% annually.[3, 4] The use of natural gas is predicted to rise by 45% by 2040, led by demand from mostly industrial and electric power sectors, which would account for a quarter of global energy demand in 2040.[6]

The appeal of using natural gas for new power plants is not only because of the lower capital costs, favourable heat rates, and relatively low fuel cost,[3, 6] but also because of the combustion of natural gas emitting significantly less carbon dioxide and negligible amounts of CO, NO_x, SO_x and particulates compared to the combustion of oil or coal.[7] As such, while the renewables sector continues to ramp up, utilizing natural gas would help to achieve the transition to clean energy as mandated by many environmental regulations set up by governments and their environmental agencies.[8]

Natural gas trade occurs mostly through pipelines; however, most of the current and future demand for energy consumption will come from non-OECD countries. As these countries are not necessarily natural gas producers, it becomes increasingly important to be able to transport natural gas to more distant destinations. Almost 90% of long distance gas trade will occur through the transport of liquefied natural gas (LNG) to 2040.[6] By cooling the natural gas to -161°C to reach its liquid state, the volume occupied by liquid methane is reduced by more than 600 times, allowing the practical storage and transport of LNG.[1]

In Australia, natural gas has become increasingly important both domestically and for export. Within Australia, the share of natural gas as primary energy is expected to increase from 26% in 2013 to 34% in 2050, making it the second largest source of energy after oil.[9] Australia also continues to export its gas via LNG production, mostly to Japan and South Korea, and in the process, it is about to overtake Qatar as the world's top LNG exporter.[10]

1.2 The Need to Separate Nitrogen from Natural Gas

Nitrogen is an almost inevitable component in natural gas, and its amount in the mixture varies with different sources of natural gas reservoirs. Due to its inert nature, nitrogen is challenging to be removed, and it is usually not separated as long as its content remains below the sales specification: about 3% for pipeline gas or about 1 % for LNG.[1] High nitrogen content natural gas can be blended with low nitrogen content natural gas to meet such specifications, but this requires a low nitrogen content gas reservoir to be available nearby.[7] However, with the depletion of low nitrogen content natural gas and the increasing world demand for LNG, the production of LNG from high nitrogen content gas reservoirs, which historically have been considered as sub-quality gas reservoirs, becomes

economically feasible and necessary.[11, 12] Although detailed data about the quality of natural gas reserves are limited on the market, it was reported in 1998 that in general, 24 trillion cubic feet of natural gas in the US contains > 4 mol % nitrogen gas, and which were considered as sub-quality gas reservoirs.[7] At that time, this represented around 16% of the proved reserves of natural gas in the world. Furthermore, while the recently developed technologies of enhanced gas recovery (EGR) and nitrogen fracturing have improved the production of natural gas significantly, they have at the same time aggravated the nitrogen contamination in the natural gas[13]. Thus, there is a significant motivation to develop economical separation technologies to remove nitrogen from natural gas.

For the production of LNG, nitrogen has to be removed from the natural gas mixture for three reasons. Firstly, it is an inert gas which does not contribute any heating value. Secondly, the liquefaction of natural gas is an extremely energy intensive process and the presence of excess nitrogen results in more energy consumption and larger sizes of the low-temperature equipment and vessels. The higher the nitrogen concentration, the higher the additional operational and capital costs have to be. Lastly, a high content nitrogen presence in LNG tanks (>1%) can cause safety hazards. Since LNG is a multi-component liquid, a high content of nitrogen, which is more volatile than methane in LNG tank, increases the risk of rollover which is a potentially fatal safety hazard. Studies have shown that if the nitrogen content in LNG is less than 1%, such rollover risks can be eliminated.[14]

Both pipeline gas and LNG production would benefit from the development of a process that can remove nitrogen from natural gas economically. To be adopted, such process should also have a relatively small capital and operating cost. Ideally, the nitrogen separation technology should be scalable so that it can be applied to both small plants as well as in large-scale facilities.

1.3 The Challenges of Separating Nitrogen and Methane

1.3.1 Physical Properties

To separate a binary gas mixture, the two components must have one or more relatively large differences in their properties: the greater the difference in these properties, the more efficient the separation process based on these properties will be. Unfortunately, nitrogen and methane have very similar physical properties, as shown in Table 1.1.[1]

Table 1.1 Key physical properties of nitrogen and methane [15, 16] (Adapted from ref. 15 and 16)

Molecule	T_b (K)	σ (Å)	α (Å ³)	μ (D)	Θ (D*Å)
N ₂	77.3	3.64	1.710	0.000	1.54
CH ₄	111.7	3.80	2.448	0.000	0.02

T_b : Normal boiling point;

σ : Kinetic diameter

α : Polarisability

μ : Dipole moment

Θ : Quadrupole moment

The difference in nitrogen and methane's normal boiling points is relatively large, and thus an effective distillation process can be developed to efficiently separate this mixture. The major issue with this approach, however, is that the required cryogenic conditions are extremely energy-intensive to achieve. To make this process economical, a large flow rate of the natural gas is typically required. Nevertheless, cryogenic distillation is currently the dominant technology to separate nitrogen from methane.

Both nitrogen and methane do not have an overall dipole moment and thus they are non-polar molecules. Their solubilities in common polar solvents, such as water, are low. Methane has a relatively larger solubility in organic solvents than nitrogen does, such as in lean oil mixtures (discussed further in section 2.4.2). No solvent has been reported to have larger physical solubilities for nitrogen than methane; the only reported pure solvent that has relatively large nitrogen solubility (it is still methane-selective) is liquid ammonia (discussed further in section 2.4.3). Based on solubility differences, a continuous circulating absorption process can be designed.

Polarizability, dipole moment and quadrupole moment are parameters contributing to the interacting potential between gas species and a solid surface. Separation processes that exploit these three parameters include adsorption and membrane technologies. Polarisability contributes to both van der Waals (non-electrostatic interaction) and electrostatic interactions. Dipole moments contribute to electrostatic interaction but the dipole moments for both of nitrogen and methane are zero.

Quadrupole moments contribute to electrostatic interactions when a gradient in the electric field is present (i.e. near a solid surface). Methane has larger polarisability and nitrogen has a larger quadrupole moment, thus the overall interaction difference between nitrogen and methane is usually relatively small.

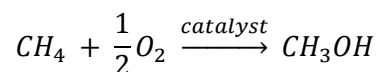
A molecule's kinetic diameter provides a measure of the likelihood of a collision with another molecule or a solid pore wall. Gas mixtures can therefore be separated based on differences in their kinetic diameters by the so-called molecular sieve effect. However, nitrogen and methane have similar kinetic diameters, which makes molecular sieving extraordinarily difficult. Molecular sieves with micropores between 3.68 Å and 3.8 Å are required to separate such a gas mixture.[15] The detailed mechanism will be discussed in section 2.2.4.

1.3.2 Chemical Properties

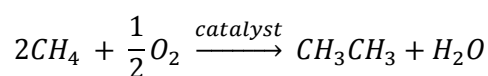
Nitrogen and methane do have significant differences in their chemical properties. Methane can be converted to other chemicals by various approaches in which nitrogen is essential inert; while nitrogen can be fixed under different conditions when methane remains inactive. The typical chemical properties of methane and nitrogen are summarized here. However, considering the amount of methane in natural gas that needs to be converted, it is likely that chemically converting nitrogen will be more feasible.

Methane conversion to other chemicals that are more valuable than methane:

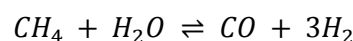
- (1) Methane conversion to methanol[17, 18]



- (2) Oxidative coupling of methane[19, 20]

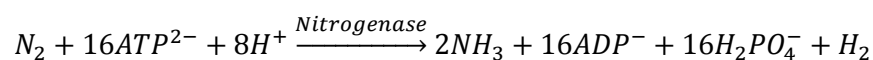


- (3) Methane steam reforming[21, 22]



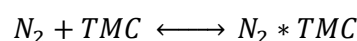
Nitrogen fixation reactions:

- (1) Biological nitrogen fixation by nitrogenase[23-26]



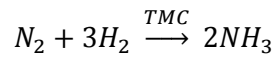
- (2) Nitrogen fixation by transition metal complex (TMC)

- (A) Reversible nitrogen bonding on TMC[27-32]

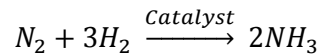


TMC bonds nitrogen at high pressure and low temperature and release nitrogen at low pressure and high temperature.

(B) Nitrogen reduction by TMC which function as a catalyst[33, 34]

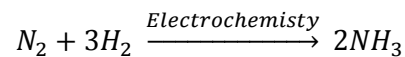


(3) Nitrogen fixation by Haber-Bosch process[35, 36]

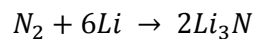


The most common catalyst is an iron-based catalyst. This process requires high pressure and high temperature.

(4) Electrochemical Nitrogen fixation[37-40]



(5) Nitrogen fixation by lithium metal[41-46]



1.3.3 Separation Processes and Mechanisms

Typically, there are four types of process that have been developed and been employed for nitrogen and methane separation: distillation, adsorption, absorption and membrane. These mainly utilize the differences in nitrogen and methane's physical properties. The chemical conversion of methane or nitrogen to other chemicals have not been systematically studied and represents the basis of a fifth separation process. However, the chemical conversion of nitrogen or methane to other chemicals could require a novel process design somewhat different to the existing four processes. Table 1-2 shows a matrix showing the gas component's property which serves as the mechanism upon which the associated separation processes is based.

Table 1.2 Property differences and separation mechanism matrix for N₂ and CH₄

		Distillation	Membrane	Adsorption	Absorption	Conversion
Physical property	Volatility	√				
	Kinetic diameter		√	√		
	Polarizability		√	√	√	
	Quadrupole moment			√		
	Solubility		√		√	
Chemical property	N ₂ as a weak ligand		√	√	√	
	N ₂ conversion					√
	CH ₄ conversion					√

1.4 Thesis Objectives and Outline

This thesis seeks to explore both conventional and emerging technologies with the potential to overcome the challenges of separating gaseous mixtures of nitrogen and methanes. In Chapter 2, a detailed review and analysis of technologies for separating nitrogen from natural gas will be presented. The review will cover both conventional technologies as well as emerging technologies, and will outline the advantages and challenges of each technology. The work of this thesis begins in Chapter 3, where a new measurement approach is demonstrated to provide consistent results for adsorption kinetics on various adsorbents as is needed for conventional separation technologies based on physical adsorption. Mass transfer coefficient data are reported for several adsorbents that can be used for nitrogen – methane separations. In Chapter 4 and Chapter 5, two emerging technologies for the separation of nitrogen from natural gas are explored. First the use of transition metal complexes (TMC) to selectively absorb the nitrogen into a liquid solution is investigated in Chapter 4. Then, in Chapter 5, the use of lithium to to remove nitrogen from the natural gas mixture

is explored experimentally. Finally, the summary of results from the studies as well as outlook and recommendations for future work are provided in Chapter 6.

Chapter 2: Background and Overview

As the global demand for energy grows, the need for natural gas as an energy source becomes even more necessary. Currently, one of the forefront challenges in the field of natural gas is to remove nitrogen (N_2), which is an inert gas with no heating value, so that the transport and storage of liquefied natural gas (LNG) can be done more efficiently.

In this chapter, technologies that have potentials in separating nitrogen from natural gas will be presented and critically analyzed. Below are some general criteria on which the technologies will be assessed on.

1. **Energy efficient**

As the natural gas feed is coming at high pressure, it would be advantageous the resulting methane (CH_4) feed could be kept at high pressure as it gets processed further into liquefied natural gas. To do so, the technology needs to be nitrogen selective, as if it was methane selective, additional energy would be required to depressurize and pressurize the methane gas, which will result in additional steps and higher operational costs.

2. **Scalable**

Since current natural gas processing plants process volumes to the order of several billions of cubic feet per day, the flow rate at which the natural gas feed is coming in can vary. It is important for the viable technology to be robust and able to be scaled up easily to handle larger volume.

3. **Meets safety standard**

The ideal technology must also meet safety requirement and operate at moderate temperature and pressure, so that it would be easily adaptable to current industrial processing plants.

To answer these criteria, assessment of various technologies, both conventional and emerging will be performed. The list of all technologies covered in this chapter is given in Table 2.1. Conventional technologies have mainly relied on the physical properties of nitrogen and methane. The conventional technologies include cryogenic distillation, membrane, adsorption and absorption processes. In addition, emerging technologies with the potential to be developed to separate nitrogen from natural gas will also be reviewed. These emerging technologies mainly rely on the distinct chemical properties of the nitrogen, and include biological nitrogen capture, transition metal complex (TMC) nitrogen capture, Haber-Bosch process and electrochemical nitrogen capture, which are all inspired by the

nitrogen fixation from atmosphere studies. Additionally, a novel technology to separate nitrogen by lithium metal will also be introduced.

Table 2.1 Conventional and emerging technologies for the separation of nitrogen from natural gas covered in this chapter

Conventional technology	Emerging technology
<ul style="list-style-type: none"> ○ Cryogenic distillation ○ Membranes ○ Adsorption ○ Absorption 	<ul style="list-style-type: none"> ○ Biological nitrogen fixation ○ Transitional metal complex (TMC) <ul style="list-style-type: none"> ● Mixed matrix membranes ● Adsorption ● Absorption ○ Haber Bosch process ○ Electrochemical nitrogen fixation ○ Lithium

Following the introduction of each technology, the benefits and challenges will be discussed. Ultimately, according to the defined criteria, three technologies will be selected to be investigated further in the remainder of this thesis.

2.1 Separation of Nitrogen from Natural gas by Conventional Technologies

Conventional methods used to separate nitrogen from natural gas include cryogenic distillation, membrane, adsorption and absorption processes. These methods are all based on the difference of physical properties between nitrogen and methane. Although these methods have a number of limitations, they are well established in the industry and still have some distinct merits that will be discussed further in each of the subsection.

2.1.1 Cryogenic Distillation

Distillation is one of the most well-established separation technologies, with the driving force being the difference in physical properties of the molecules, namely its volatility. The volatility difference between nitrogen (normal boiling point = -195.8 °C) and methane (normal boiling point = -161.5 °C) is large enough to drive an effective distillation separation process. The process has been reported to achieve high purity gases – up to 98% methane recovery with less than 1% nitrogen content in the resulting methane feed, and less than 1% of methane in the nitrogen vent stream. However, the distillation process would need to be operated under cryogenic conditions which require (1) pre-

treatment of the feed gas to remove moisture and carbon dioxide (CO₂); (2) high capital cost of the cryogenic equipment; (3) additional operational costs to liquefy nitrogen in the natural gas mixture. The cryogenic requirement has also made it difficult to meet the criteria for the ideal nitrogen separation technology, which include energy efficiency and safety.

Currently, nitrogen rejection units (NRU) are already available at the end of liquefaction process for LNG productions to operate under cryogenic conditions, but considerable capital and operational costs are still needed to handle the unnecessary large volume of nitrogen component. The current focus of the cryogenic distillation is process optimization of the heat exchanger network, which can recover the “cold” to a certain extent. However, at the same time, such process optimization will add complexity in the process design and raise operational issues, especially when nitrogen content varies as the reservoir is being depleted.[47, 48] Subjected to the high capital and operational costs, cryogenic distillation process is only economical in LNG production with a flow rate higher than 15 MMSCFD.[16]

2.1.2 Membranes

2.1.2.1 Membranes in General

Membranes serve as semi-permeable barriers to separate a feed gas stream into an enriched permeate stream and an enriched retentate stream. The driving force of this separation technique is the difference in the partial pressures between the feed side and the permeate side. The commercialization of the first H₂ separation membrane – Prism[®] in 1980 has boosted the development of this technology and motivated the scientists to expand its application to different areas.[49] This technology has several intrinsic advantages: (1) no phase change– nitrogen can be removed under moderate temperature and no cryogenic conditions are required; (2) simple process flow scheme, compact footprint and high adaptability especially for offshore application; (3) relatively low capital costs, user-friendly and easy operation with inexpensive running costs.[1, 50, 51]

There are three types of membranes based on the composition of the material, all of which have been studied to separate the gas mixture of nitrogen and methane: (1) Organic polymer membrane; (2) Inorganic molecular sieve membrane; (3) Mixed matrix membrane. Organic polymer membrane and mixed matrix membrane can be either nitrogen selective or methane selective, while inorganic molecular sieve membrane is mainly nitrogen selective due to the molecular sieve effect. Table 2.2 summarizes the types of membranes types and main applications.

Table 2.2 Overview of types of membranes and their applications

	Polymer membrane		Inorganic molecular sieve membrane	Mixed matrix membrane
	Rubbery polymer membrane	Glassy polymer membrane		
CH ₄ selective	√			√
N ₂ selective		√	√	√

2.1.2.2 Polymer Membrane

Within the category of organic polymer membranes, they can be further classified by their transition temperature into two types: rubbery polymer and glassy polymer. When the process at which the polymer membrane is used is above the glass transition temperature of the polymer, the polymer chains become flexible, and it is called a rubbery polymer membrane. Due to the flexibility of the polymer chains, rubbery polymer membranes show weak ability to distinguish the molecular size around 3.8Å and gives similar diffusion coefficients to either nitrogen or methane. The diffusion selectivity of nitrogen over methane on rubbery polymer membrane ranges from 1.5-2.2.

When the operating temperature is below the glass transition temperature of the polymer, the membrane, the polymer chain becomes relatively rigid, and it is called glassy polymer membrane. The rigid structure in glassy polymer membrane enables improved differentiation on the size of nitrogen and methane and thus gives relatively higher diffusion selectivity, typically ranging from 3-6. For sorption selectivity, there are no big differences between rubbery polymer membrane and glassy polymer membrane. Typically, the nitrogen over methane sorption selectivity ranges between 0.2-0.5, as shown in Table 2.3. It can be seen from Table 2.3 that the permselectivity (CH₄/N₂) for CH₄ selective rubber membrane is usually under 4;[50] while simulation studies show that the required permselectivity for one stage CH₄ selective membrane process is 6.[52]

Table 2.3 Summary of separation properties of polymer membranes[53]

	Rubbery polymer	Glassy polymer	Membrane material
K_{N_2}/K_{CH_4}	0.2-0.5	0.2-0.5	
D_{N_2}/D_{CH_4}	1.5-2.0	3-6	
Highest α_{N_2/CH_4} reported		2.3[54]	Polyimide (6FDA-BAHF)*
Highest α_{CH_4/N_2} reported	4.2[55]		Polyamide–polyether block copolymer (Pebax® 2533)

- There is an editing error in reference 11. The highest α_{N_2/CH_4} should be achieved on Polyimide (6FDA-BAHF)

Multi-stage process design can help to achieve sale gas specification based on the performance of existing membranes. So far, the NitroSep™ membrane process developed by MTR, Inc is the sole example of industrial methane selective membrane technology.[56, 57] This process employs either single stage or two-stage membrane units under low-temperature conditions to reject nitrogen for flowrate ranging from 0.005 to 30 MMscfd. Field demonstrations showed that natural gas streams with a nitrogen concentration lower than 12% could achieve 93% CH₄ recovery. However, when the nitrogen concentration is higher than 30%, this system becomes economically unfeasible.[53, 56-59] Also, the methane selective membrane approach suffers a drawback in energy efficiency as the wellhead pressure must be sacrificed. Since the methane stream loses its high pressure after passing through the membrane, additional energy and costs are required to recompress the enriched methane stream to a sale gas pressure.

To address this issue, a nitrogen selective membrane process which can remove the nitrogen from methane and at the same time maintain the high head pressure of methane would be preferred. In the 1970s, Kim and Koros et al. reported glass polymer membranes owning a “reverse selectivity”, meaning that nitrogen would permeate such membranes faster than methane does.[60] The membrane has a relatively rigid structure due to the limited mobility of glassy polymer segments and

is able to distinguish the molecular size more effectively, making the diffusion-selective effect predominant over the sorption effect. [53]

There are three limitations of the glassy polymer membrane: (1) The trade-off between nitrogen permeability and the selectivity; as in high permeability is usually achieved by sacrificing the selectivity.[61, 62] (2) Plasticization of the membrane; as over usage under high pressure and flow rate of methane and other impurities in the natural gas stream, such as carbon dioxide and heavy hydrocarbons, the polymeric membrane would plasticize and swell, raising issues resulting in a decrease of diffusion selectivity. Lastly, simulation studies have shown that a $\alpha_{N_2/CH_4} > 17$ is required to treat a 10% N₂ and 90% CH₄ binary mixture with a single stage membrane process to meet pipeline specification (<3% N₂).^[52] The required high nitrogen over methane selectivity is due to the relatively low nitrogen partial pressure compared to that of methane in the feed stream. However, the best performing glass polymer membranes with acceptable permeabilities reported so far are only able to provide a $\alpha_{N_2/CH_4} \approx 2.3$,^[54] which is still too small to be economically feasible.

2.1.2.3 Inorganic Membrane

In contrast to organic polymer membranes, inorganic membranes have more rigid and controllable porous structures. Inorganic membranes, such as zeolite, metal-organic framework (MOF) and carbon molecular sieve membranes can be artificially designed to have micropores that can distinguish nitrogen from methane more effectively. The molecular sieve effect in such materials dominates the diffusion separation performance. The equation for diffusion selectivity, $\frac{D_{N_2}}{D_{CH_4}}$, is shown in Equation 2.1.[12, 63-65]

$$\frac{D_{N_2}}{D_{CH_4}} = \left[\frac{\lambda_{N_2}^2}{\lambda_{CH_4}^2} \right] * \left[\exp\left(\frac{\Delta S_{D(N_2-CH_4)}}{R}\right) \right] * \left[\exp\left(-\frac{\Delta H_{D(N_2-CH_4)}}{RT}\right) \right] \quad \text{Equation 2.1}$$

λ_i Jump length of component *i*, which is the distance between two adjacent micropores

$\Delta S_{D(N_2-CH_4)}$ The difference in diffusion transition state entropy of nitrogen and methane

$\Delta H_{D(N_2-CH_4)}$ The difference in diffusion transition state enthalpy of nitrogen and methane

R Gas constant

T Absolute temperature

The diffusion selectivity defined in Equation 2.5 can further divide into three terms: the jump length selectivity, the enthalpic selectivity, and the entropic selectivity.

$$\left[\frac{\lambda_{N_2}^2}{\lambda_{CH_4}^2} \right] \quad \text{Jump length selectivity}$$
$$\left[\exp\left(\frac{\Delta S_{D(N_2-CH_4)}}{R}\right) \right] \quad \text{Entropic selectivity}$$
$$\left[-\frac{\Delta H_{D(N_2-CH_4)}}{RT} \right] \quad \text{Enthalpic selectivity}$$

Within the inorganic membrane matrix, diffusion will occur when long-range segmental motions open a gap of sufficient size into which the penetrant can jump. However, the jump length for nitrogen and methane are almost the same, which results in the jump length selectivity, $\left[\frac{\lambda_{N_2}^2}{\lambda_{CH_4}^2} \right]$, to be close to unity. The diffusion entropy is a function of the shape and size of the gas species. Due to the slimmer shape of nitrogen compared to methane, the entropic selectivity, $\left[\exp\left(\frac{\Delta S_{D(N_2-CH_4)}}{R}\right) \right]$, would be the main contributor to a high diffusion selectivity if the pore gate can be controlled precisely.[65] Finally, the diffusion enthalpy is the sum of the repulsion enthalpy from the pore gate of the membrane pores and the desorption enthalpy from the membrane pores. Usually, the diffusion enthalpy selectivity, $\left[-\frac{\Delta H_{D(N_2-CH_4)}}{RT} \right]$, is nitrogen favorable and the sorption enthalpy selectivity varies depending on the nature of the inorganic materials.

In sum, the inorganic membranes give much better nitrogen and methane separation performance for both permeance and selectivity, compared to the polymer membranes. The performance of these inorganic membranes is summarised in Table 2.4.

Table 2.4 Comparison of N₂/CH₄ separations through inorganic membranes[66] (Table adapted from ref. 25)

Material	A	N ₂ permeance (GPU)	Thickness (μm)
Carbon molecular sieve	7.7	~0.1	70 ± 15
SSZ-13	13	66	7.8
SAPO-34	5–7	300	2.0–3.0
SAPO-34	8	500	6.2
SAPO-34 prepared	6.5–7.4	880–1300	3.0–4.2

Although the separation performance has been improved, there is a major drawback of inorganic membranes that hinders them from meeting all three criteria of energy efficiency, scalability, and safety. Since the inorganic membranes have fragile mechanical properties, it is extremely challenging to engineer large-scale defect-free inorganic membranes, therefore, it would be difficult to scale up. Continued work in the field of membrane science are underway to address this issue, namely by developing the carbon molecular sieve (CMS) membranes which are prepared from polymer membrane precursors through pyrolysis, and thus, would be relatively easier to process[12, 65], however, much progress is still required to realize this technology to be fully scalable and commercially viable.

2.1.2.4 Mixed Matrix Membrane

Integration of inorganic molecular sieves into a polymer matrix is a strategy to utilize both the advantages of these two membranes. The resulting composite membrane is called a mixed matrix membrane, which would have the improved separation performance as well as the strong and flexible mechanical properties. However, the implementation of this idea has been very challenging to do in practice due to the poor compatibility between these two materials. As a result, the overall selectivity can only be enhanced slightly compared to the mother polymer matrix, still far from the required values (For one stage membrane process, the simulation shows a selectivity of $\alpha_{N_2/CH_4}=17$ is required.[52]).

In sum, although the membrane technology offers a promising alternative in separation technique, as well as being scalable, safe, and energy efficient (if the membrane is nitrogen selective), much

advancement in the field of material science, both for the selections of filler and matrix, as well as the mixing and casting technique to obtain membranes with satisfactory morphology, are required before the separation performance of these membranes is able to compete against other mature conventional technologies, such as the cryogenic distillation, in being viable to be used as the main technology to remove the nitrogen content from natural gas.

2.1.3 Adsorption

Adsorption based separation processes are well-established in the industry for a variety of applications in separating gas mixtures, namely as leading technology used in the purification of air [67], production of hydrogen gas [68-70], and the capture of carbon dioxide from flue gases[1, 71-74]. In the past several decades, adsorption-based processes for separating nitrogen and methane have also attracted significant attention in the natural gas processing industry [1, 75], mainly because of the potentially huge savings in energy costs and capital investment when compared to other mature technology, such as cryogenic distillation.

However, although modern adsorption-based technologies have been used in large industrial scale, it is still limited to only handle relatively small volume in separating nitrogen from natural gas. For instance, the processing capacity of the cutting edge adsorption-based technologies is only around 15 MMscfd of natural gas feed, while a commercial cyclic pressure swing adsorption processes are already producing high purity hydrogen gas from a 200 MMscfd feed of steam methane reformers.[76] The reason behind the two significantly different volumes in the throughputs of gases is the composition of feed gases. For the purification of hydrogen, the feed stream was mainly composed of hydrogen with a small amount of carbon dioxide, nitrogen, and methane, which could be adsorbed by the adsorbents, allowing the non-adsorbing hydrogen gas to simply flow through the adsorption bed. Hence, this requires a relatively small inventory of adsorbents. However, for the removal of nitrogen from natural gas, the feed stream is mainly composed of methane balanced with nitrogen. Since commonly, methane is more selectively adsorbed gas, this results in a prohibitively large inventory of adsorbents, which in turn leads to larger than normal adsorbers. The two key conceptual strategies that may help develop adsorption-based processes for nitrogen removal from natural gas at LNG scales or gas fields with very high contaminant concentrations are (1) modifications to pressure swing adsorption (PSA) process configurations, and (2) improved performance, cost and reliability of adsorbents.

In this chapter, the focus of the review will be on the application of adsorption-based processes for nitrogen removal from natural gas, which covers the fundamental principles of adsorption processes,

the state of the art of adsorbents for nitrogen and methane separation, and current adsorption based technologies for nitrogen removal from natural gas.

2.1.3.1 Adsorption in General

For a separation of any given mixture, the first step in designing an adsorption-based process to achieve the required separation performance is the selection of adsorbents. Specifically, the adsorbents selected must have optimal adsorption equilibria and kinetics for the desired components to be adsorbed on the adsorbents. To optimize the adsorption equilibria, high adsorption capacity and selectivity, ease of regeneration, and fast adsorption and desorption kinetics must all be obtained. Achieving an optimal adsorption equilibria could be a challenging task, as there might be a trade-off between adsorption equilibrium equilibria and kinetics; for instance, some adsorbents might have higher equilibrium adsorption capacities for the component, but prohibitively slow adsorption kinetics in real applications.

The selectivity of the adsorbents for the components could be defined as either the equilibrium selectivity (ratio of adsorption amount at equilibrium) or the kinetic selectivity (ratio of adsorption rates). For nitrogen and methane separation, most current adsorbents have higher methane over nitrogen equilibrium selectivity, and only a selected few have a higher kinetic selectivity of nitrogen over methane.

2.1.3.2 Adsorbent Selectivity

The equilibrium selectivity of an adsorbent, α_{ij} , for two components in a gas mixture (i is the more adsorbed component and j the less adsorbed component) is defined in Equation 2.2 [77]:

$$\alpha_{ij} = \left(\frac{x_i}{x_j}\right)\left(\frac{y_j}{y_i}\right) \quad \text{Equation 2.2}$$

where, y and x are the mole fractions of a component in the vapor and adsorbed phase, respectively. Separations based on differences in sorption rates may still be possible even if $\alpha_{ij} \leq 1$. To quantify this, it is convenient to define a kinetic selectivity factor, β_{ij} , which incorporates the effects of each component's sorption mass transfer coefficient, shown in Equation 2.3.

$$\beta_{ij} = \alpha_{ij} \sqrt{\frac{k_i}{k_j}} \quad \text{Equation 2.3}$$

As discussed by Ruthven[78], the kinetic selectivity depends on both the diffusivity ratio (assuming $k_i \propto D_{c,i}$) and the equilibrium selectivity. Thus, evaluating β_{ij} is an important part of screening potential adsorbents for a given gas separation application.

2.1.3.3 Adsorbents

In addition to the equilibrium capacity, selectivity, and kinetics of the adsorbents, the selection of adsorbents for a given process objective is also subjected to the impact of other factors such as the cost and availability of the material. Zeolites and carbon-based adsorbents have successfully been used in natural gas processing for the separation of nitrogen from methane. Most zeolites and carbon adsorbents are known to be methane selective based on thermodynamic equilibrium, and the equilibrium selectivity of methane over nitrogen can be 3 to 4 for these materials. Certain zeolites and carbon adsorbents also exhibit much larger adsorption kinetic rates for nitrogen than methane, which could be explored in the design of adsorption processes using kinetic separations. In this section, these two classes of adsorbents will be discussed in further detail.

The adsorption capacities of methane and nitrogen have been reported for many different types of zeolites including mordenite[79], ZSM-5 [80, 81], β -zeolite [82, 83], chabazite [84], silicate [85, 86], and 13X [87]. The molecular structures of these zeolite frameworks are well known and characterized, such as a 12-ring window of the 13X framework, which when balanced by a sodium cation, results in a cage opening of 7.8 Å [88]. Zeolites such as 4A, clinoptilolites and the adsorbent ETS-4 (a titanosilicate material) have smaller pore openings that are near the kinetic diameters of methane (3.758 Å) and nitrogen (3.64-3.8 Å) which can result in an appreciable kinetic selectivity for the smaller nitrogen molecule, although these materials are often methane equilibrium-selective. [89-91]

A new zeolite subclass that has recently been reported is the ionic liquid zeolite, which combines the high capacity and fast kinetics of zeolites with the high selectivity of ionic liquids to produce an adsorbent that exceeded the separation performance of either of the base materials.[92] This adsorbent was synthesized within our laboratory by ion exchange of sodium Y-type zeolite with a solution containing tetra- methyl-ammonium (TMA) cations. The resulting TMA-Y adsorbent was found to have increased methane and decreased nitrogen adsorption compared to the base Na-Y adsorbent, significantly increasing its methane selectivity. Preliminary measurements with pure fluids indicated this material had a methane-nitrogen selectivity around 5.

Activated carbons are produced from carbonaceous materials such as coal, charcoal, wood, coconut husks, or nut shells which are pyrolyzed in the absence of oxygen or any halogen to convert the material to carbon before they are activated with an oxidizing agent[93]. The base material and the

conditions under which they are created control the particular properties of the final adsorbent material. Advanced synthesis techniques can manufacture carbon adsorbents that have the exceptionally high surface area, as achieved for example by the Maxwell activated carbon [94]. This adsorbent has a measured surface area of $2250 \text{ m}^2 \cdot \text{g}^{-1}$, a total pore volume of $1.15 \text{ cm}^3 \cdot \text{g}^{-1}$ and fast kinetics for methane (2.9 s^{-1}) and nitrogen (8.3 s^{-1}); ideal properties for the nitrogen-methane separation, although it only has an average methane selectivity (~ 2.8). While many activated carbon adsorbents have a large adsorption capacity and fast kinetics of both methane and nitrogen, they tend to have a selectivity less than three which makes it difficult to design an effective separation process [95]. Molecular sieving carbons (MSC), also known as carbon molecular sieve (CMS), are activated carbons that are mainly composed of microspores less than 20 \AA in width. These small pores are often of a similar scale to the adsorbing molecules, which causes a significantly large number of collisions between the molecule and the pore mouths. The relative size and surface interactions of the molecules can result in a significantly different rate of diffusion into the pores for similar molecules [93]. Previous investigations of a carbon molecular sieve produced by Japan EnviroChemicals (formerly Takeda) have found that the sorption rate of methane is hundreds of times smaller than that of nitrogen. [96, 97] Measurements of the pore size of MSC 3K-161 have shown that the largest contribution to the total pore volume was from pores in the range $(3.7\text{-}4) \text{ \AA}$ [98] which is near the kinetic diameters of methane (3.758 \AA) and nitrogen ($3.64\text{-}3.8 \text{ \AA}$). These materials will absorb a larger quantity of methane than nitrogen if left for long enough; however, the difference in kinetics can be exploited so that the material absorbs more nitrogen within a certain period.

2.1.3.4 Adsorption Processes

Adsorption processes can be classified into temperature swing adsorption (TSA) and pressure swing adsorption (PSA) according to the methods employed to regenerate the adsorbents. TSA is widely used in natural gas processing for gas dehydration with adsorbents being zeolite molecular sieve and silica gel. In TSA gas dehydration units, one TSA cycle (including the heating and cooling the bed) can take several hours (or even days). This TSA process is feasible for dehydration because the water content in the gas streams is much smaller than that of other components and that the adsorbents have a large capacity and high selectivity for water compared to other natural gas components. However, TSA is not a feasible solution to the separation of nitrogen and methane in the context of natural gas processing because of the high concentrations of nitrogen and methane in the gas streams and the much smaller capacities of adsorbents for nitrogen and methane than that for water. PSA is the potential adsorption process for nitrogen and methane separation.

In the PSA method, adsorption occurs at elevated pressure and desorption occurs at a pressure lower than the adsorption pressure, making use of the difference in adsorption amount between these two pressures. Using the PSA method, adsorbent beds can be depressurized and re-pressurized rapidly, allowing cycle times of several minutes or even several seconds to be utilized. Accordingly, the amount of adsorbent required for PSA processes can be much smaller than for an equivalent TSA processes. There have been only a few industrial PSA processes for nitrogen and methane separation, and a list of these commercial nitrogen-methane separation processes can be found in a review by Rufford et.al[1]. Most of these commercial processes use methane equilibrium selective adsorbents except for one that uses nitrogen kinetic-selective adsorbent[99], carbon molecular sieve.

In summary, the adsorption based process, in particular PSA, offers the capability to separate nitrogen from the natural gas feed that could also address the three criteria listed earlier in the chapter by being energy efficient, scalable, and industrially safe. Despite the existing current challenges of selecting the right kind of adsorbents materials for this application, the technology is largely promising and worth to be explored further.

2.1.4 Absorption

2.1.4.1 Absorption in General

Absorption is another mature, well-developed, and widely applied separation process, which utilizes a liquid solution to separate a gas mixture in an absorption tower. In the tower, the lean liquid solution flows down from the top and makes contact with the gas mixture that is bubbled from the bottom of the tower. Gas components with higher solubility in the liquid are absorbed, while the remaining purified gas components are collected at the top of the tower. The enriched liquid solution is pumped to another regeneration tower called a stripper to be regenerated by temperature swing, pressure swing, or the combination of these two. The absorbed gas component is then liberated and collected. The most well-known example of an absorption process in the natural gas processing plant is the use of amine solution to strip carbon dioxide gas. An aqueous solution of amines have high carbon dioxide capacity and can effectively remove carbon dioxide from the natural gas feed. Currently, the amine absorption process remains the leading technology of carbon dioxide removal from natural gas.

To implement a gas-liquid absorption process for the separation of nitrogen from natural gas akin to the carbon dioxide adsorption process, the desired liquid solution should have a higher capacity of one component of the feed gas mixtures (either the N_2 or CH_4) than the other. Moreover, there are three main cost factors: (1) the required liquid circulation rate, which is determined by the amount of impurity that must be rejected from the feed gas stream and the impurity loading capacity in the

sorbent (2) the energy required to regenerate the sorbent; (3) and the recompression energy needed to compress the CH₄ stream to a sale pressure.[1]The nitrogen rejection using liquid absorption-based technology is not widely employed in the natural gas plants mainly due to the difficulty of finding a proper liquid solution that can either absorb methane or nitrogen effectively and can meet the above three cost factors. Nevertheless, there are two kinds of absorption process for nitrogen rejection that have been reported so far: a lean oil CH₄-selective absorption process and a liquid ammonia N₂-selective absorption process.

2.1.4.2 Lean oil CH₄-Selective Absorption Process

The lean-oil CH₄-selective absorption process is a physical absorption process where the loading capacities of CH₄ and N₂ in the solvent follow Henry's law. The Henry constant of methane is much larger in organic solvents than that of nitrogen, therefore the majority of methane goes to lean oil leaving nitrogen as the vent gas. The separation performance of this process improves at high pressure and low temperature. Accordingly, the lean-oil can be regenerated under low pressure or high temperature in a stripper tower. Advanced Extraction Technologies, Inc. (AET) has designed and constructed a lean-oil based absorption process with a capacity of 2-30 MMscfd.[100] This process requires chilling the feed gas to -30°C to maximize the methane loading capacity. The CH₄ recovery can reach up to 90% with the enriched CH₄ streams contains less than 4% N₂. The enriched N₂ stream which is maintained at feed pressure and low temperature can be recycled to chill the feed gas and/or be recycled for Enhanced Oil Recovery operations if the stream can be economically pumped to a wellhead. The CH₄ enriched stream liberated from the stripper is at low pressure, and thus, energy is required to recompress the stream to sale gas pressure. As CH₄ is the majority in the feed gas, a considerable lean-oil solvent circulation rate is necessary to achieve high CH₄ recovery.

The costs of these two factors, high recompression energy and large solvent circulation rate, are prohibitive when it comes employing this CH₄ absorption process for LNG production. Since this technology does not meet the energy efficiency requirement defined as one of the three criteria earlier in this chapter, it will not be discussed further in this chapter.

2.1.4.3 Liquid ammonia N₂-Selective Absorption Process

In natural gas streams, N₂ is the minority component (<50%), and thus a process selectively removing N₂ is preferred. In such process, a relatively small amount of solvent is required and the associated equipment size is reduced compared to the methane selective absorption process. Furthermore, the purified CH₄ stream remains at the high feed gas pressure, and thus, no further recompression is needed.

Studies were conducted between the 1930s to 1950s focusing on using liquid ammonia to separate N_2 from natural gas.[101, 102] In the absorption tower, the ammonia was pressurized to around 50 bar at the temperature range from 21 to 43 °C (ammonia stays in liquid form at this condition) to promote the N_2 loading capacity.[102] The methane stream collected from the top of the absorption. The N_2 enriched ammonia stream left the absorption tower bottom and was chilled to between -100°C to -30°C by a series of cooler and chiller system. At the same time, this stream was depressurized to 20-25 psi and then goes into a stripper. As ammonia is relatively volatile and toxic, for safety and operation cost consideration, it requires an ammonia recovery section after the stripper and before N_2 stream is released. The methane and nitrogen solubilities in liquid ammonia are shown in Figure 2.1. Because of the lack of solubility data at the same temperature, the solubility data can only be shown at similar temperatures – the solubility of methane is shown at 40 °C and solubility of nitrogen is shown at 38 °C. The extracted Henry's selectivity of nitrogen over methane is around 0.25 at the temperature range of 38-40 °C.[103, 104]

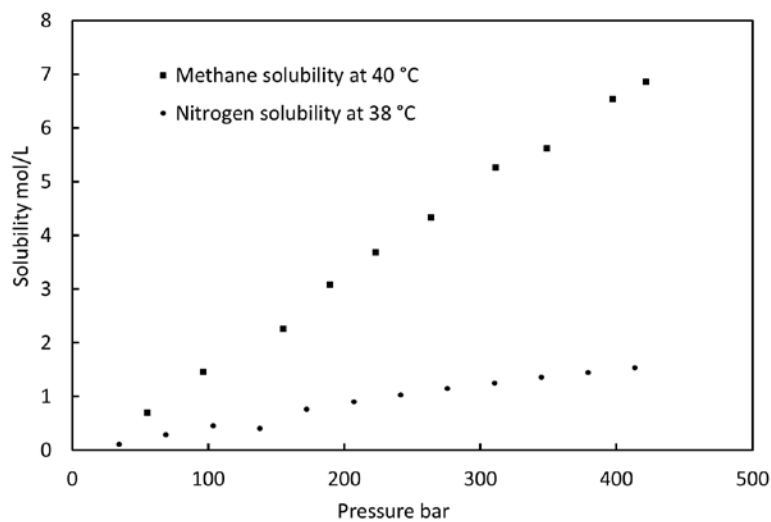


Figure 2.1 The solubilities of methane and nitrogen in liquid ammonia. Due to the lack of solubilities data at the same temperature, the solubilities of nitrogen (●) were shown at 38 °C and the solubilities of methane (■) were shown at 40 °C. The extracted Henry's selectivity of nitrogen over methane is around 0.25.

There are three main drawbacks to this process: (1) it involves hazardous operation issues, especially in handling liquid ammonia at high pressure and low temperature in the cooler and chiller systems; (2) the high cost of the refrigeration cycle for the cooler and chiller systems and the extra ammonia recovery sections make this process not economically feasible; and (3) the small selectivity of nitrogen

over methane sacrifices the methane recovery and additional steps are required to deal with the nitrogen stream, which contains significant amount of methane.

As described earlier in this chapter, the ideal technology for nitrogen removal from natural gas feed must meet the criteria of energy efficiency, scalability, and safety. The three drawbacks described above have made the ammonia absorption process unsuitable choice, given the energy inefficiency and high costs as well as the safety hazards. Nowadays, no reports indicate that natural gas plants are employing this process.

2.2 Separation of Nitrogen by Emerging Technologies

All of the conventional technologies are based on the physical property differences of nitrogen and methane. However, since the differences are not great, it has been challenging to separate them efficiently by such conventional technologies. In the following section, some emerging technologies that mainly utilize chemical property differences will be examined.

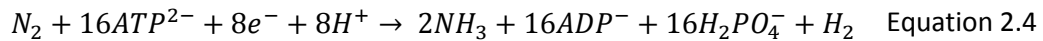
2.2.1 Biological Nitrogen Fixation (BNF)

It has long been known that molecular nitrogen in the air can be captured and converted to fertilizer by certain microorganisms. This biological nitrogen fixation (BNF) is one of the most important natural processes in the world. BNF can occur under atmospheric temperature and pressure due to the high catalytic ability of nitrogenase – the bio-catalyst for BNF. To date, studies have characterized three distinct kinds of nitrogenase enzymes which contain different metal cofactors: molybdenum-iron complex, vanadium–iron complex, or sole iron-complex constituting their active sites.[105]

Among these enzymes, the molybdenum-iron complex (FeMo) based nitrogenase is the predominant form, constituting an electron delivery Fe protein and a catalytic FeMo protein, shown in Figure 2.2.[25, 26, 106] The overall stoichiometry equation of nitrogen reduction by nitrogenase is shown in Equation 2.4. For each electron delivery, the Fe protein consumes two adenosine triphosphate (ATP) to attach to the FeMo protein and then transfer one electron. ATP is a compound consisting of an adenosine molecule bonded with three phosphate groups. The breakage of one phosphate group (P_i) from ATP forming adenosine diphosphate (ADP) releases 34 kJ/mol of energy for many metabolic processes, shown in Equation 2.5.[107] ATP is present in all forms of life and functions as the "molecular unit of currency" of intracellular energy transfer.[108] Overall, 8 electrons and 16 ATP are obligatory to reduce one nitrogen molecule.[109] Regarding kinetics, the overall nitrogen fixation rate cannot be significantly increased, with the disconnection of the Fe protein from FeMo protein after

electron delivery thought to be the rate-limiting step in the whole BNF process, which has a relatively fixed turn-over rate.[110]

Analogous to the biological CO₂ fixation,[111, 112] the intensively studied BNF[24, 109] provides an alternative, green way to capture N₂ from natural gas under moderate conditions. There has been no reported study of the possibility of using this BNF to separate nitrogen from methane yet. However, following critical analysis of the feasibility of this approach is conducted.



Although it has been intensively studied over the past decades, the mechanism of nitrogenase catalytic reduction of nitrogen remains a mystery due to its abstruse nature and the difficulty of trapping the reaction intermediates.[23-25, 109, 113-115]. For the sake of brevity, in this section, the detailed catalytic mechanism will not be examined; rather the three “macro-aspects” of this BNF will be analyzed: (1) Capacity, (2) Kinetics: fixing rate, (3) Energy input.

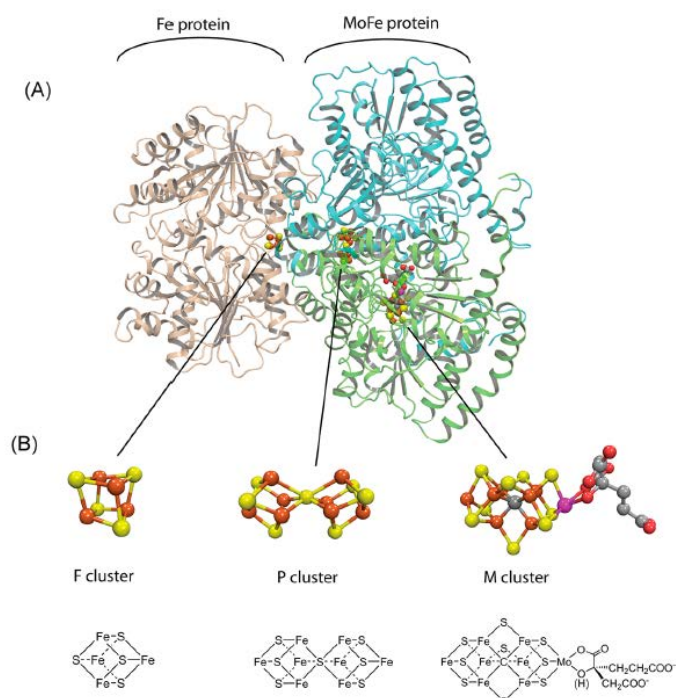


Figure 2.2 Schematic of FeMo nitrogenase. (A) MoFe protein complex with the Fe protein homodimer shown in tan, the MoFe protein α subunit in green, and the β subunit in cyan. (B) Space-filling and stick models for the 4Fe-4S cluster (F), P-cluster (P), and FeMo-co (M). [109]

2.2.1.1 Nitrogenase Capacity

Capacity is one of the key parameters that determine whether the BNF process could be practical for nitrogen capture from natural gas. It describes how much nitrogen can be captured per unit nitrogenase. In this report, the nitrogenase composed of Fe-Mo cofactor is taken as an example. Theoretically, one Fe-Mo cofactor can only bond one N_2 molecule, and one nitrogenase only contains one Fe-Mo cofactor. Without immersing into the details of the mechanisms, the overall capacity of N_2 on Fe-Mo cofactor and nitrogenase has been calculated, shown in Table 2.5. The molecular weight of Fe-Mo cofactor and nitrogenase are calculated or estimated from the literature.[116-120] These absolute values could vary with different Fe-Mo cofactors or nitrogenase, but they would be of the same order.

Table 2.5 The loading capacities of nitrogen on Fe-Mo cofactor and nitrogenase and the required amount of Fe-Mo cofactor and nitrogenase to absorb the nitrogen in 1 m³ of natural gas (nitrogen concentration = 10%)

	Fe-Mo cofactor	Nitrogenase
MW	1395 g/mol	344, 000 g/mol
Capacity	0.7168 mol/kg	0.0029 mol/kg
Amount required to treat 1 m ³ of Natural Gas (10% N ₂ , 1bar, 273.15K)	6.7 kg	1600 kg

It is evident from Table 2.5 that the nitrogen capacity on nitrogenase is extremely small: 0.0029 mol/kg. This small capacity is mainly due to the huge molecular weight of the nitrogenase, which contains not only Fe-Mo cofactor but also associated proteins. The nitrogen capacity of Fe-Mo cofactor and nitrogenase are too small compared to the reported adsorbents and too small to make this process industrially practical.

2.2.1.2 The Natural Gas Production by BNF with Current BNF Kinetics

Another important parameter to consider is the kinetics, which indicates how fast a process would occur. This parameter is just as crucial as the equilibrium capacity in determining whether a method would be suitable to be adopted in the industry. By understanding the kinetics of BNF, the maximum amount of natural gas that can be processed by global BNF annually can be theoretically estimated. Table 2.6 shows the annually global BNF in 2005,[121] which is around 180 Tg, including 60 Tg anthropogenic sources and 220 Tg natural sources. Two assumptions are made here to estimate the natural gas production by global BNF: (1) the content of nitrogen in the raw natural gas stream is 10%; (2) the efficiency of natural gas production by BNF is 1%.

Table 2.6 The annual fixation amount of nitrogen by biological nitrogen fixation (BNF) in 2005 (unit Tg)[121]

		BNF Amount(Tg)	Ref.
Anthropogenic sources		60 (50-70)	[122]
Natural Sources	terrestrial	58 (50-100)	[123]
	marine	160 (140-177)	[121, 124]
Total BNF		280	

Table 2.7 Worldwide natural gas production in 2014 (billion m³)[125]

Rank	Country	2016 production	2016 share of total
1	US	749.2	21.10%
2	Russia	579.4	16.30%
3	Iran	202.4	5.70%
4	Qatar	181.2	5.10%
5	Canada	152.0	4.30%
6	China	138.4	3.90%
7	Norway	116.6	3.30%
8	Saudi Arabia	109.4	3.10%
9	Algeria	91.3	2.60%
10	Australia	91.2	2.60%
Natural gas production by global BNF		20.4	0.58%

Based on these assumptions, the annual natural gas production by global BNF based on current BNF kinetics is estimated to be 20.4 billion m³, which only counts 0.58 % of the annual production of natural gas in 2016, as shown in Table 2.7. It is evident that the global availability of BNF is yet to be of scale that could handle natural gas production.

2.2.1.3 Energy Consumption

Another concern with BNF is its high energy consumption. Although nitrogenase can reduce nitrogen to ammonia under moderate conditions, it consumes 16 moles of ATP, or 488 kJ energy, to reduce each mole of nitrogen to ammonia.[25, 109] Such high energy consumption is due to the inert triple covalent bond of nitrogen.[126, 127] In addition, the energy form in the reduction process of nitrogen is ATP, which is mainly biosynthesized from cellular respiration and cannot be artificially provided by commonly used industrial energy forms, such as heat, electricity or mechanical energy.

One of the most common sources of ATP is glucose. The schematic process of oxidizing glucose by aerobic respiration and anaerobic respiration to produce ATP is shown in Figure 2.3. In total, 38 ATP and 2 ATP molecules can be produced from one glucose molecule decomposition by aerobic respiration and anaerobic respiration respectively. The high energy consumption of BNF (488 kJ/mol N₂) and the highly specific form of energy (ATP) required make the approach of BNF impractical to fix nitrogen from natural gas.

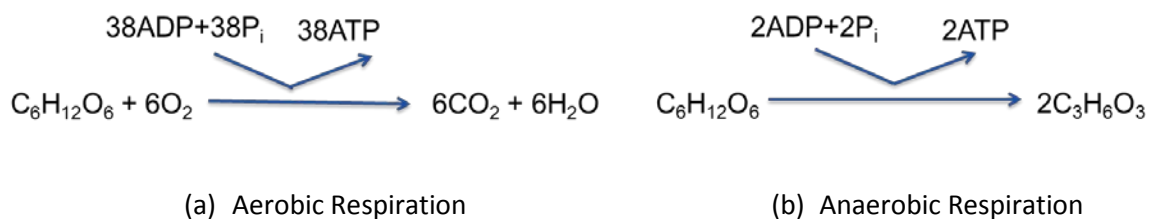


Figure 2.3 Cellular respiration: (a) Aerobic Respiration; (b) Anaerobic Respiration. ATP stands for adenosine triphosphate, ADP stands for adenosine diphosphate and P_i stands for phosphate. One glucose molecule can produce 38 ATP through aerobic respiration or 2 ATP through anaerobic respiration.

To summarize, although the BNF process is an elegant approach inspired by nature, it is determined through critical analysis that this would not be practical for the application of nitrogen removal from natural gas. The main drawbacks of this technology are its small capacity to be scaled up, its limited availability, its high energy consumption and the required specific energy form. As described earlier in this chapter, the ideal technology for nitrogen removal from natural gas feed must meet the criteria of energy efficiency, scalability, and safety. The three challenges described above have made the BNF process unsuitable choice, and therefore will not be explored further throughout of this work. However, the approach by which it works remains an inspiring motivation to scientists, and will be discussed in the following subsections 2.2.2 – 2.2.4.

2.2.2 Transition Metal Complex (TMC) Based Processes

2.2.2.1 TMC-N₂ Coordinating Chemistry

The previous section has introduced FeMo cofactor as the active site for the binding of nitrogen in BNF process, and its challenges to be directly adapted as a technology for nitrogen removal. However, given this knowledge, researchers have been attempting to replicate the function of FeMo cofactor as the active site using smaller molecules known as transition metal complexes (TMC) for decades, with the main goal of fixing nitrogen under moderate conditions.

In general, a TMC is a bulky molecule composed of a transition metal ion center and associated various supporting ligands. A transition metal is an element that has an incomplete sub-shell in its valence electronic configuration. Ligands are neutral or anionic non-metallic species which can bond to the metal center by sharing electron density with it. The properties of TMCs strongly depend on the properties of the metal center and the supporting ligands. To be more specific, the nitrogen bonding ability of the TMC depends on the electronegativity, the oxidative level, the geometry of the metal center, and the electron affinity and the steric hindrance effect of the ligands. In principle, careful tuning the combination of metal center and the associated ligands can lead to achieve the aim of developing a TMC that can reversibly bind nitrogen under moderate conditions.

The nitrogen molecule has two lone electron pairs which are available to initiate a dative single σ bond with the metal center of TMC. In the dative single σ bond, nitrogen molecule contributes more electron density than the TMC does. Although this σ bond is too weak to fix a nitrogen molecule to the TMC, it is robust enough to draw nitrogen close enough to TMC metal center to initiate a back π bond by letting the nitrogen molecule attract more electron density from the high energy π orbital of the metal center to its low energy π^* orbital. The imbalance in the electron sharing through a σ bond and a back π bond between nitrogen and TMC could serve as the mechanism of nitrogen bonding to TMCs.

The extent of electron density transfer from the TMC metal center to the nitrogen through the back π bond depends on the energy level of the d orbital of the metal center and the geometry of the metal center. In general, the higher energy d orbital has, the more electron density would be transferred from the metal center to the nitrogen molecule. As the d -orbital energy decreases from left to right for the transition metals in the periodic table, the TMCs further to the right tend to have weaker interaction with nitrogen ligands compared to the TMCs formed from the left transition metals.[128] Also, for the same transition metal, the lower oxidation state of the metal center is, the higher the d -orbital energy would be. Usually, a low oxidation state of the metal center leads to a strong back π

bonding.[113, 129-132] In addition, the geometry of the metal center of TMCs also plays an important role in determining the distribution of electron density in the complexes. Certain geometric shapes, for example, trigonal-planar and tetrahedral geometries, tend to have stronger π back bonding.[133] The supporting ligands are essential in determining the strength of the nitrogen-TMC bonds. Compared to Cp-type supporting ligands which draw electron density from the metal center, π -donor supporting ligands, such as aryloxy and amido ligands,[134, 135] can donate electron density to the metal center and thus increase the energy level of its d -orbital, which eventually leads to a strong π back bond between the nitrogen molecule and the TMC. Transition metals with low d orbital energies can bind nitrogen molecule only when arming with active π -donor supporting ligands. [136-138] However, such strong π -donor supporting ligands are usually very active and sometimes become unstable under moderate conditions. For example, the phosphine ligands are strong π -donor ligands and can facilitate Fe center to bond nitrogen, but they are hypergolic when exposing to air.[27, 139] Intensive screening studies are required to explore TMCs that can bind nitrogen at moderate conditions and at the same time remain stable under operating conditions in natural gas processing plants.

Nitrogen can bind to TMC in different modes and in total four N_2 -TMC bonding modes have been proposed,[131] and the most common and relevant mode for the application of nitrogen and methane separation is a mode called mononuclear end-on, as shown in Figure 2.4. It involves a σ -donation from the lone electron pairs of nitrogen molecule to the empty d_{z^2} or $d_{x^2-y^2}$ orbitals of the metal center and a back- π -donation from the filled d_{xz} , d_{yz} , or d_{xy} orbitals of metal center to the vacant π^* orbitals of nitrogen molecule.[131]

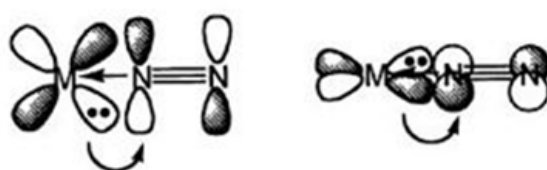


Figure 2.4 End-on bonding mode (Michael and Samuel, 2000). The shading means the two π orbitals (on nitrogen or on metal) are in an orthogonal position.

2.2.2.2 TMC- CH_4 Coordinating Chemistry

Unlike the nitrogen molecule, the methane molecule exhibits a tetrahedral configuration with all electrons bound to the C and H atom via single (σ) bonds. Therefore, it does not have any additional lone pairs of electrons to form σ bond with the TMC or an empty π^* orbital to accept electrons from the TMC to form a π back-bond. As a result, binding methane to TMC is a far less energetically favored

process.[131] This difference between nitrogen and methane is one key parameter that can be exploited to develop a separation process that selectively removes nitrogen from methane.

2.2.2.3 TMC-based Membranes Process

The first approach in leveraging TMC for nitrogen removal from natural gas is TMC-based membranes. As mentioned in section 2.1.2, it is challenging to find membrane materials with higher physical sorption of N_2 due to the poor condensability of N_2 compared to CH_4 . One possibly feasible way to improve the sorption selectivity of nitrogen over methane (K_{N_2/CH_4}) is to integrate the nitrogen binding TMCs into polymer matrix and develop a mixed matrix membrane. Xue & Koros et al. conducted an initial study of this strategy.[64] Although no nitrogen sorption improvement was observed in this initial study, this finding has opened a new avenue to improve K_{N_2/CH_4} . To further advance this approach, a rigorous screening study of such TMC-polymer-solvent combination is still required.

One of such example is the Cr-MIL (Cr = chromium; MIL = Matériaux de l'Institut Lavoisier) composite membranes. After pre-treating at elevated temperature, Cr-MIL-100 and Cr-MIL-101 showed improved nitrogen capacities due to the nitrogen binding on the unsaturated Cr sites.[140, 141] In addition, Cr-MIL-101 (non-pre-treated under high temperature) has been shown to have better compatibility with certain polymers and has been successfully integrated into a polysulfone membrane. The resulted mixed matrix membrane gave improved gas separation performance.[142] The mixed matrix membranes composed pre-treated nitrogen binding Cr-MIL-101 and polysulfone or other mother-polymers serves as one of the potential candidates that can be explored further.

In sum, the TMC-polymer mixed matrix membrane strategy remains a promising approach to remove N_2 from natural gas. As introduced in the conventional technologies section, membrane technology would be able to address the criteria requirement of being energy efficient, scalable, and safe. However, the research is still in very early stage and requires deep expertise in material science to be able to address the poor compatibility issue and improve separation performance significantly.

2.2.2.4 TMC-based Adsorption Process

As discussed before, nitrogen and methane are difficult to be distinguished efficiently only by their physical sorption interactions with adsorbents. Their van der Waals and electrostatic interactions with the adsorbates are similar, and usually slightly methane-favorable. The nitrogen's coordinating interaction with unsaturated transition metal sites on adsorbents can serve as an additional interaction that contributes to a higher nitrogen selectivity, shown in Equation 2.10.

$$S = \frac{\phi_{N_2}}{\phi_{CH_4}}$$

Equation 2.6

$$= \frac{\phi_{N_2, \text{van der Waals potential}} + \phi_{N_2, \text{electrostatic potential}} + \phi_{N_2, \text{coordination potential}}}{\phi_{CH_4, \text{van der Waals potential}} + \phi_{CH_4, \text{electrostatic potential}}}$$

where ϕ stands for the interaction between the adsorbate and the adsorbent.

The coordinating interaction between adsorbate and adsorbents have been well studied for other applications in the past and is well known as π -complexation sorbents.[93] There are four potential methods to integrate transition metal/ions and porous adsorbents: (1) Monolayer or near-monolayer salts dispersed on porous substrates; (2) Ion-exchanged zeolites; (3) Ion-exchanged resins; and (4) Solid form solution. The first three methods have been intensively discussed by Yang et al., focusing on the application of this TMC coordination chemistry to separate/purify gas species containing π bonds, such as CO, NO, ethylene and aromatics.[93] These successful examples are summarised in Table 2.8 below.

Table 2.8 Successful examples of sorbents based on TMC for different applications of binary gas mixture separation. Such TMC adsorbents are named as π -complexation.

Adsorbate	TMC	Substrate	Reference
		Al ₂ O ₃	[143]
CO from syngas	CuCl monolayer	Carbon or Coked Al ₂ O ₃	[144]
		NaY zeolite	[145]
	Ag ⁺ exchanged resin	Exchanged resins	[146, 147]
Olefin/paraffin	CuCl monolayer	r-Al ₂ O ₃	[146, 147]
		pillared clays	[148]
	AgNO ₃ monolayer	SiO ₂	[149, 150]
Aromatics/Apliphatics	PdCl ₂ monolayer	SiO ₂	[151]
benzene/cyclohexane	AgY zeolite	Y zeolite	[152, 153]
	AgY zeolite	Y zeolite	[154]
Dienes/Olefins	CuY Zeolite	Y zeolite	[155]

Nitrogen as a weak binding ligand is not as well-studied as other gaseous ligands mentioned in Table 2.8. Nevertheless, it has been shown that under moderate temperature and low pressure, nitrogen can bind to transition metal ion-exchanged zeolites, such as Ni-exchanged MFI zeolite,[156] Cu⁺ exchanged MFI zeolite[156-160] and Cu⁺ exchanged ZSM zeolite.[161, 162] On Cu⁺ exchanged MFI zeolite, the adsorbed nitrogen to Cu⁺ ratio can reach as high as 0.8 at 15 kPa.[160] The adsorption enthalpy of nitrogen on Cu⁺ exchanged MFI zeolite is between from 30 to 60 kJ/mol which indicates that only moderate regeneration energy would be required.[157] Even though this would have met the criteria of being energy efficient, the performance is still far too low to be economically feasible for industrial application. The overall adsorption capacities reported are lower than 1 mmol/g up to 100 kPa, and thus no continued study has been conducted for the nitrogen and methane separation on these materials yet.

Another type of adsorbent is metal-organic frameworks (MOFs). In 2014, Kyuho Lee and his co-workers conducted quantum mechanical computations, aiming to predict a particular metal-organic

framework that can selectively bind nitrogen without tremendous experimental screening.[163] Their results show that a MOF structure with unsaturated-coordinated V(II) sites can selectively bind nitrogen through a coordinating bond between the nitrogen and the V(ii)'s d orbital. However, the experimental synthesis of this particular V-MOF proves to be unattainable so far. In 2017, MOFs based on chromium rather than vanadium, Cr-MIL-100 and Cr-MIL-101, were synthesized with unsaturated Cr sites that can reversibly bind nitrogen under moderate conditions.[164] A significant higher overall affinity to nitrogen than to methane had been observed on this type of MOF through the pressure range of 0 kPa up to 500 kPa, which is mainly due to the strong coordinating interaction between nitrogen and the unsaturated Cr sites. However, when the pressure is higher than 500 kPa, the methane adsorption capacities exceed the ones of nitrogen. There are two reasons for this: (1) the ratio of nitrogen to the task-specific unsaturated Cr sites can only be up to one and high pressures would not contribute to binding more nitrogen on these sites once they are saturated; (2) the physical interactions start to play a dominant role at high pressure, which usually favor methane adsorption. Since these materials become methane selective at high pressure, it is not scalable. Thus, it does not meet our defined criteria for nitrogen removal from natural gas, and therefore will not be pursued further in this thesis.

2.2.2.5 TMC-based Absorption Process

A nitrogen selective absorption process has attractive advantages compared to a methane selective absorption process, which has been stimulating scientists to explore liquid solutions that can chemically and selectively absorb N₂ since the 1990s. Two research institutes studied such TMC solutions in the 1990s.[29, 32, 165, 166] Stanford Research Institute International (SRI) is one of the two companies leading this research.[165, 166] They have summarized the preferred properties of potential TMC solutions as follow:

1. Reversibility – can bind nitrogen at high pressure/low temperature and desorb nitrogen at low pressure/high temperature
2. High nitrogen capacity – high nitrogen loading at feed gas conditions can reduce the TMC solution flow rate and thus reduce the operation cost
3. High selectivity – such TMC should not react with methane; methane solubility in the solvent should be as small as possible to maximize high methane recovery.

4. Fast kinetics – reaction kinetics of TMC-nitrogen binding is preferentially faster than the gas transportation kinetics in the TMC solution to minimize the absorption tower diameter and height, and thus reduce capital cost.
5. Thermal and pressure stability – the TMC should maintain its activity under operation conditions.
6. Tolerance – the TMC should retain its activity in the presence of natural gas impurities, such as carbon dioxide, hydrogen sulfide, and oxygen.

The best TMC system identified by SRI is (bis)tricyclohexylphosphine molybdenum tricarbonyl in toluene solution. This TMC system can selectively bind nitrogen forming a precipitate from the solution and then can be regenerated by heating and/or vacuuming. However, severe issues with regeneration of this TMC was encountered in the demonstrated batch process: firstly, the precipitate size is uncontrollable which leads to absorbents lost by bypassing the filtration step or tube blockage by large precipitates; secondly, this TMC degrades at an unexpectedly fast rate. Furthermore, the aromatic solvent – toluene is not desirable due to the high solubility of methane in it, which leads to a low nitrogen selectivity over methane. Nevertheless, their economic analysis based on this molybdenum compound, assuming the regeneration issue could be fixed, indicates that such a nitrogen absorption process could be competitive with the current cryogenic process when TMC lifetime could be extended to 5 years.

Bend Research Inc. (BRI) is the other organization that systematically studied TMC solution based absorption process.[29, 32] They reported two kinds of TMC systems: Ru-EDTA system and iron(ii)-phosphine system. The Ru-based TMC has a capacity of 0.6mol N₂ per mol Ru²⁺ at around 20 bar and 21 °C and shows reversibility under low pressure and high temperature. However, this TMC system cannot be scaled up due to the limited Ruthenium production – approximately 12 tons per year which makes this TMC material too expensive to be feasible.[167] The best iron(ii)-phosphine TMC water solution has a nitrogen capacity of 0.5 mol N₂ per mol Fe²⁺ at 20 °C and 10 bar, with a nitrogen selectivity over methane reaching 6. Also, these TMCs systems show stability to maintain their nitrogen capacity up to 100 cycles at the presence of CO₂, H₂S. in addition, the solvent for this TMC system is water which is claimed to be the best solvent. The desorption process can be achieved through a pressure swing or a combination of a pressure swing process and a temperature swing.

So far, there have been no reports showing the commercialized application of these TMC-based chemical absorption process for removing nitrogen from natural gas. Three main reasons may be responsible for this. Firstly, the types of TMCs reported are too expensive to be scaled up. Ruthenium

only has a limited production; the phosphine ligands in Iron-based TMCs are challenging to synthesize. Secondly, iron-phosphine TMCs involve pyrophoric ligands which may cause serious safety hazards in the natural gas processing plants. Thirdly, before the recent boost of large-scale LNG production, there was not strong enough driving force to develop efficient nitrogen rejection technologies under moderate conditions.

However, with the development of LNG production, natural gas plants are more eager for economic nitrogen rejection processes, which could provide a strong enough driving force for a more rigorous screening of TMCs. Since the technology is largely promising and has the potential to meet the criteria described earlier in this chapter, it will be studied in further details in Chapter 4 of this thesis.

2.2.3 Haber - Bosch Process

Every year, the industrial Haber-Bosch processes produce more than 150 million tons of ammonia from nitrogen and hydrogen.[105] The well-established process, as well as the potential to produce ammonia to be sold, could be considered to be adapted for the process of nitrogen removal from natural gas.

Nowadays, the most common catalysts for this reaction are iron-based catalysts which require extreme reaction conditions, with a temperature higher than 400 °C, and pressure between 200 and 300 bar. Even the most advanced plants, performing the Kellogg Advanced Ammonia Process (KAAP) based on an iron-ruthenium mixed catalyst, need a total pressure around 90 bar.[105] For example, assuming that the N₂ concentration in natural gas stream is 10%, the natural gas stream needs to be at least 225 bar and 400 °C for the KAAP process, which is much harsher than the current natural gas processing conditions (50 to 70 bar and at ambient temperature).[1] Furthermore, the Haber Bosch process is extremely energy intensive and consumes 1% of the global power production.[168] Therefore, the possibility of converting the nitrogen in the natural gas stream directly to ammonia by mimicking the Haber-Bosch process is not feasible so far due to the high N₂ partial pressure and high temperature required.

In conclusion, although this process could be scaled up if it were able to be adapted to remove nitrogen from natural gas, it would have not been able to meet the criteria of energy efficiency and safety. Therefore, it will not be pursued further in this thesis.

2.2.4 Electrochemical Nitrogen Fixation

The electrochemical route is another possible alternative technology, similar to TMC catalysis, to produce ammonia. This technology has been claimed to save more than 20% of the energy

consumption compared to the Haber - Bosch process,[37, 169] and thus shows the potential to be modified to capture nitrogen from natural gas. In this section, its feasibility for processing large natural gas streams is considered.

Electrochemical reduction of nitrogen to ammonia happens on equipment called electrolytic cells which are composed of two electrodes on each side and electrolytes in the middle. A schematic illustration of the electrochemical conversion of nitrogen to ammonia utilizing a natural gas stream as the source of nitrogen has been proposed and is shown in Figure 2.5. A natural gas stream is sent to the cathode chamber to provide nitrogen and another hydrogen stream is sent to the anode chamber. By applying an external voltage, the hydrogen molecule loses electrons and become protons that transfer through the electrolyte to the cathode chamber. In the cathode chamber, protons, electrons and nitrogen react on the cathode and produce ammonia. The product of ammonia can be easily separated from methane due to the significant difference in their volatilities.

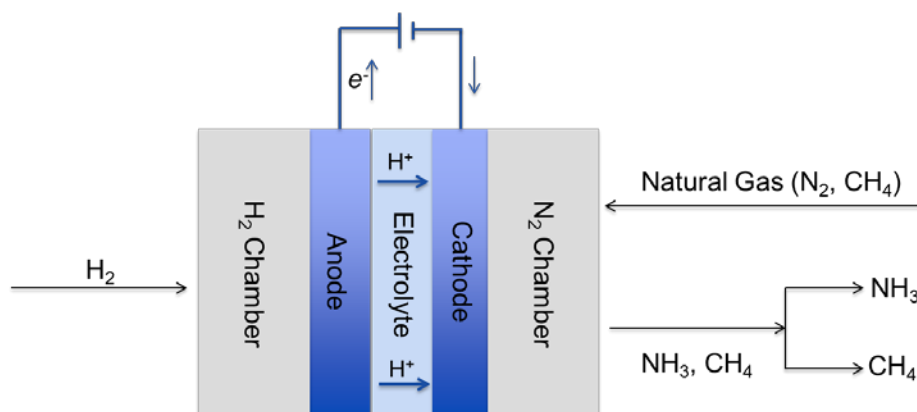


Figure 2.5 Schematic illustration of electrochemical conversion of nitrogen to ammonia using a natural gas stream as the source of nitrogen. A natural gas stream mainly containing nitrogen and methane is sent to the nitrogen chamber where nitrogen is converted to ammonia. The effluent stream from the nitrogen chamber mainly contains the produced ammonia and the remaining methane. Due to the large difference in their physical properties, the binary gas mixture of ammonia and methane can be separated relatively easier compared to the binary gas mixture of nitrogen and methane.

The electrochemical reduction of nitrogen to ammonia is still in its infantile phase, and so far there is no reported study of using this method to capture nitrogen from natural gas. In order to estimate its feasibility for the application of nitrogen capture from natural gas, the parameter called ammonia

production rate would be examined in this section, which indicates how fast nitrogen can be captured from natural gas and then converted to ammonia. Similar to the analysis of BNF, a fast enough ammonia production rate is essential to process large natural gas streams with a reasonable scale of the electrolytic cells.

The highest ammonia production rate so far is achieved by electrolytic cells using polymer proton exchange membrane (PEM) as the electrolyte.[170] Because of their high proton conductivity at low temperature and the well-established knowledge and techniques of cell construction and assembly in the area of the fuel cell, PEM based electrochemical cells show the greatest potential for the electrochemical reduction of nitrogen from natural gas streams. Kordali et al. are among the first scientists who study ammonia synthesis under atmospheric pressure and below 100 °C and the ammonia production rate they observed is $2.12 \times 10^{-11} \text{ mol cm}^{-2} \text{ s}^{-1}$ at 90°C with a low current efficiency of 0.24%.100°C.[171] [172] Xu et al. reported the highest ammonia production rate of $1.13 \times 10^{-8} \text{ mol cm}^{-2} \text{ s}^{-1}$ with a current efficiency of 90% at 80°C, which was achieved by using Nafion® membrane 102 as the electrolyte, $\text{SmFe}_{0.7}\text{Cu}_{0.1}\text{Ni}_{0.2}\text{O}_{3-\delta}$ as the cathode and Ni-samarium doped ceria ($\text{Ce}_{0.8}\text{Sm}_{0.2}\text{O}_{2-\delta}$) (Ni-SDC) as the anode.[170, 172] Following this work, although other combinations of anode, cathode and electrolyte have been investigated, [170] [173] $1.13 \times 10^{-8} \text{ mol cm}^{-2} \text{ s}^{-1}$ remains the highest ammonia production rate. Because the PEM in this ammonia production electrolytic cell is similar to that in the well-studied fuel cell, the ammonia production rate thus has the potential to rise to the range of $4.3 - 8.7 \times 10^{-7} \text{ mol cm}^{-2} \text{ s}^{-1}$ when the current densities could achieve $0.25 - 0.5 \text{ A cm}^{-2}$ with a 50% current efficiency.[37]

The highest reported ammonia production rate and the highest potential ammonia production rate will be used to estimate the feasibility of using electrolytic cells to capture nitrogen from methane. Given a natural gas flow rate which is assumed to contain 10% nitrogen, the required area of the PEM can be estimated from the ammonia production rate. Table 2.9 summarises the required areas of electrolytic cell based on the above two ammonia production rates to process different natural gas flow rates. The price of PEM, Nafion® membrane 102, varies but locates within the range of 1000 – 3000 USD/m² on the current market (USD: United States Dollar). The capital cost of the PEM only is shown in Table 2.9. It is apparent from Table 2.9 that electrochemical route technically has the potential to capture N₂ from natural gas and then convert it to ammonia, but the capital cost of the PEM only is already far too high to make it economically feasible.

Despite the promising theoretical performance, this technology is still in its early stage and the actual current ammonia production rate is still far from the theoretical one. Furthermore, the required area of PEM is too large to be processed and the scale-up of the anode and cathode catalysts also pose

processing difficulties. More importantly, the capital cost for PEM only is already far too high to be scalable, no mention the capital cost of the anode and cathode which can only be produced on a laboratory scale. This electrochemical approach is still immature for industrial application of nitrogen separation from natural gas, and therefore will not be pursued in this thesis.

Table 2.9 The estimated areas of electrolytic membrane and their capital cost to handle different natural gas flow rates with different ammonia production rates

Ammonia Production Rate	Natural Gas Flow rate (10 mol % Nitrogen)	Area of Nafion® membrane ^③	Capital cost of Nafion® membrane
mol/s/cm ²	MMscfd	10 ³ m ²	million USD
1.13E-08 ^①	1	24.5	24.49
	15	367	367.29
	75	1840	1836.45
8.70E-07 ^②	1	0.318	0.32
	15	4.77	4.77
	75	23.9	23.85

① The highest ammonia production rate reported so far.

② The ammonia production rate that could be potentially achieved at the current of 0.25 – 0.5 A cm⁻² with a 50% current efficiency, similar to that has been accomplished in fuel cells.

③ Nafion® membrane is a proton conductivity membrane and functions the electrolyte

2.2.5 Lithium Based Process

Lithium reactions with different gas species, including nitrogen, have been studied for decades. The primary reason for this is the safety hazards caused by lithium spills in fusion reactors[174, 175], in which lithium functions as a tritium breeder blanket and as a coolant.[176, 177] Recently, lithium has also been proposed as carriers in energy circuits based on renewable energy.[178-180] Lithium reacts with CO₂ and N₂, the flue gas from power plants to generate electricity, and the resulting Li₃N and Li₂CO₃ would go through a series of treatments to become LiCl and eventually be electrolyzed back to lithium metal by seasonal renewable energy (wind energy, solar energy). All the studies mentioned above are focusing on the reactions of lithium with nitrogen at high temperatures and some of them involves lithium combustion in nitrogen atmosphere usually at temperatures above 1000 °C.[46] Such

harsh conditions would pose serious safety hazards to the natural gas processing plants, and thus these high-temperature reactions are not suitable to be utilized to separate nitrogen from methane.

The reaction of lithium with nitrogen at low temperatures, especially at temperatures lower than the melting point of lithium (180.6 °C), are relatively less documented and the mechanism remains a mystery. In the presence of moisture, lithium can react with nitrogen smoothly under moderate conditions.[41, 46, 181-183] However, when water is absent, it becomes complicated. Some studies show that, at the absence of water moisture, lithium remains stable in dry nitrogen and even dry air for days under room temperature;[41, 184] while, others claim that the lithium can react with dry nitrogen readily under moderate temperatures.[42, 185, 186] Here, dry nitrogen usually means nitrogen that contains less than 10 ppm water moisture, but usually the nitrogen are pretreated with the various method and the water contents should be smaller than 2 ppm.[182] Interestingly to notice the lithium metal that can not react with dry nitrogen under moderate temperatures are usually have a storage history, either in hydrocarbon solvents[41], or in Ar atmosphere. In contrast, the lithium that can react with dry nitrogen is in-situ freshly made, either by recrystallization from molten lithium,[42] vapor lithium,[185] or by electrodeposition.[186] Or, the lithium metal has fresh cut edges where the reaction always started.[183] After the reaction of lithium with nitrogen is initiated, it becomes self-sustained and gives a sigmoid growth curve with time.[42, 183, 185]

One of the applications of the reaction of lithium with nitrogen at moderate temperatures is a lithium battery. Some researchers claimed that a passivation layer of lithium nitride on the surface of the lithium anode could prevent the dendritic growth, and thus improve the performance of lithium metal battery significantly.[186] While, other researchers reported that under room temperature the charge-discharge cycles in the lithium-ion battery could facilitate the reaction of lithium and nitrogen, which could serve as a novel method for the preparation of lithium nitride. Traditionally, the preparation of lithium nitride usually involves high temperatures where lithium metal stays in liquid form, and thus poses safety hazards during operation.[187-189]

In the 1990s, the use of lithium metal started to show up in the area of gas separation, patented to separate trace amounts of nitrogen impurities from crude argon.[190, 191] The crude argon passes through a nitrogen removal unit which contains lithium supported on high surface area materials or staying in a molten state. The preferred operating temperature ranges from 100°C to 200°C (low temperatures for high surface area materials supporting lithium and high temperatures for molten lithium). Due to lithium's high reactivity under such conditions, nitrogen can be removed and converted to lithium nitride effectively.

A similar process to the purification process of argon can be designed to remove nitrogen from natural gas using the reaction of lithium with nitrogen under moderate conditions. This nitrogen separation process by lithium metal can be operated in a batch mode which is akin to a pressure or temperature swing adsorption process. A significant advantage of using lithium to separate nitrogen is that the theoretical loading capacity of nitrogen on lithium has the potential reach 24mmol/g, which is an encouragingly high capacity compared to those of traditional adsorbents, which are smaller than 1mmol/g at 100 kPa.[190] Moreover, because lithium does not react with methane, the selectivity of nitrogen over methane on lithium would be significantly high which would lead to a full recovery of methane in such a nitrogen separation process. The two challenges of such process are (1) making the reaction of lithium with nitrogen happen under moderate conditions; (2) regeneration of lithium metal from produced lithium nitride which might need many harsh conditions.[43, 192]

No studies of utilizing lithium to remove nitrogen from natural gas have been reported so far, yet given the right operating condition, lithium-based technology to remove nitrogen from natural gas could be potential to meet the criteria of being energy efficient, scalable, and safe. Additionally, lithium has more than an order magnitude higher capacity of nitrogen loading compared to traditional adsorbents. As such, an intensive study of using lithium to capture nitrogen from methane will be discussed in Chapter 5.

2.3 Conclusions

In this chapter, a review of conventional and emerging technologies to remove nitrogen from natural gas has been given. Additionally, a set of criteria to examine these technologies have also been presented, namely being energy efficient, scalable, and safe according to industrial standards. A review of conventional and emerging technologies of nitrogen separation from natural gas covered in this chapter has been summarized in Table 2.10.

Through the critical analysis laid out in this chapter, three technologies are selected to be studied in more depth within this thesis: (1) Adsorption, the most promising amongst the other conventional technologies. The adsorption method is largely mature, however have much potential for optimization within the particular application of nitrogen removal from natural gas, (2) TMC based Absorption, an emerging technology which is inspired by BNF and able to deliver good performance even at higher flowrate of natural gas feed, but would have been better and much more attractive for industrial application if the right TMC and solvent pair could be determined, and (3) Lithium metal based separation, an emerging technology from the 1990s that worth further reevaluation due to its prominent benefit of having a large nitrogen loading capacity and the pressing and growing global

demand of LNG. These three technologies to remove nitrogen from natural gas are intensively studied in Chapter 3, 4 and 5.

Table 2.10 Review of conventional and emerging technologies of nitrogen separation from natural gas covered in this chapter

Conventional Technologies							
	Cryogenic distillation	Membranes			Adsorption	Absorption	
		Polymer	Inorganic	Mixed Matrix		CH ₄ selective	N ₂ selective
Advantages	Mature technology	Easy to scale up	Superior performance	Promising concept	Cheap material, mature technology (based on kinetics)	Mature technology	Energy efficient, since CH ₄ is kept at high pressure
Challenges	Energy-intensive, costly	Performance is inferior (low permeance and selectivity)	Difficult to scale up	Still early stage, requires highly technical intensive screening	Need to find better match for porous materials	Lose high pressure therefore energy intensive, inferior performance	Dangerous, inferior performance
Emerging Technologies							
		Transitional metal complex (TMC)			Haber Bosch		Lithium

	Biological nitrogen fixation	Mixed Matrix Membranes	Adsorption	Absorption		Electrochemical nitrogen fixation	
Advantages	Concept from nature	Promising concept	Performance at low pressure is good	N ₂ selective, promising, still good performance at high pressure, easy to scale up	Inspired by mature technology	Well known concept, continuous process	High N ₂ loading capacity
Challenges	Low capacity, low availability of bacteria	Early stage, technically very challenging	At high pressure, reverse selectivity	Need to find the right materials (both TMC and solvent)	Conditions are too harsh, not feasible	Need good performing cathode, anode, electrolyte, currently still early stage	Expensive, hard to regenerate

Chapter 3: Adsorption Equilibria and Kinetics of CH₄ and N₂ on Commercial Zeolites and Carbons

3.1 Forward

This chapter forms the basis of a journal paper published on *Adsorption* (January 2017, Volume 23, Issue 1, pp 131–147) and so has been written in that format.

3.2 Abstract

Adsorption equilibria and kinetics are two sets of properties crucial to the design and simulation of adsorption based gas separation processes. The adsorption equilibria and kinetics of N₂ and CH₄ on commercial activated carbon Norit RB3, zeolite 13X, zeolite 4A and molecular sieving carbon MSC-3K 172 were studied experimentally at temperatures of (273 and 303) K in the pressure range of (5 to 120) kPa. These measurements were in part motivated by the lack of consistent adsorption kinetic data available in the literature for these systems, which forces the use of empirical estimates with large uncertainties in process designs. The adsorption measurements were carried out on a commercial volumetric apparatus. To obtain reliable kinetic data, the apparatus was operated in its rate of adsorption mode with calibration experiments conducted using helium to correct for the impact of gas expansion on the observed uptake dynamics. Analysis of the corrected rate of adsorption data for N₂ and CH₄ using the non-isothermal Fickian diffusion (FD) model was also found to be essential; the FD model was able to describe the dynamic uptake observed to better than 1 % in all cases, while the more commonly applied isothermal Linear Driving Force model was found to have a relative root mean square deviation of around 10 %. The measured sorption kinetics had no dependence on gas pressure but their temperature dependence was consistent with an Arrhenius-type relation. The effective sorption rates extracted using the FD model were able to resolve inconsistencies in the literature for similar measurements.

3.3 Introduction

Adsorption based processes are well-established technologies for the separation of gas mixtures in, for example, the air separation industry [67], the hydrogen production industry [68-70], and the capture of carbon dioxide from flue gases [1, 71-74]. In the past several decades, adsorption based processes for separating nitrogen and methane have attracted significant attention in areas such as

natural gas production [1, 75], landfill gas upgrading [193, 194], coalbed methane enrichment [195], and coal mine methane/ventilation air methane purification [196].

In the design of an adsorption process for nitrogen and methane separation, estimates of the lengths of the saturation and mass transfer zones are crucial to specify the height of the adsorption bed. Equilibria data for nitrogen and methane mixtures, which are often available either from literature reports or direct measurements, are the foremost information required for such estimates. Information about the effective sorption kinetics is also essential to properly estimate the length of the mass transfer zone in the bed because, for many adsorption based applications, the mass transfer from gas phase to solid phase is limited by sorption kinetics. This mass transfer limitation arises from the fact that the diffusion of gases into the porous interior of the adsorbent is restricted and that the intrinsic adsorption rate is usually much faster than the diffusion rate [197]. The kinetics are especially important when the adsorbents do not possess high equilibrium selectivity for the mixture components because for such scenarios the mass transfer fronts for different adsorbates could be very close to each other. Adsorption kinetics are even more vital to the design of pressure swing adsorption (PSA) separations for nitrogen and methane mixtures that exploit differences in their sorption rates, and are crucial parameters in the development of accurate and reliable simulations of industrial PSA processes intended to separate N_2 and CH_4 . However, kinetic parameters must often be estimated empirically for such applications since the relevant data in the literature are limited and inconsistent, even for commercial adsorbents. This is partly because of the difficulty associated with accurate measurements of adsorption kinetics [198].

In principle, adsorption kinetics can be measured experimentally using a variety of techniques, for example, by monitoring the time-dependence of volumetric or gravimetric sorption capacity [199, 200], by the combined pressure-swing and volume-swing frequency response technique [201, 202], using a dynamic column breakthrough apparatus [203], and via zero length column (ZLC) experiments [204, 205]. However, the results of kinetic measurements made by different groups and/or with different techniques tend to have large deviations. A survey of literature (Figure 3.1) revealed that the reported effective sorption rates for N_2 and CH_4 on commercial adsorbents similar to those measured in this work have large variations, ranging in some cases over two orders of magnitude.

after it was confirmed that any heat and mass transfer limitations due to sample size were negligible. The kinetics were obtained from rate of adsorption measurements made using the volumetric method at two temperatures of 273 K and 303 K with gas pressures up to 120 kPa. Two important steps were applied to the analysis of the dynamic uptake data to extract reliable values of the effective sorption rate (D/r^2) for methane and nitrogen on each adsorbent: calibration of the effects at short time scales due to gas expansion using helium, and regression of a non-isothermal kinetic model to the measured data. The impact of adsorption heat on the apparent kinetics was evaluated by comparing the results of isothermal and non-isothermal kinetic models. The effect of temperature on the adsorption kinetics was also studied and compared to an Arrhenius-type correlation.

3.4 Experimental Section

3.4.1 Method and Materials

The Norit RB3 extrude pellet used in this work is the same activated charcoal studied by Rufford et al. [203], supplied by IMCD Australia Ltd. Zeolite 13X APG extrude pellet was supplied by Shanghai MLC Molecular Sieve Co., Ltd. The Linde zeolite 4A extrude pellet was purchased from Sigma-Aldrich (Castle Hill, NSW, Australia). The granular molecular sieving carbon MSC-3K 172 was obtained from Japan EnviroChemicals, Ltd. (Osaka, Japan). The properties of these adsorbents relevant to the rate of adsorption measurements are summarised in Table 3.1; other properties for these materials can be found in elsewhere [203, 219, 220]. The sample mass to be used in these experiments was determined by first conducting ROA measurements for N_2 on zeolite 4A at 283 K. Two sample masses of 0.7704 g and 0.3694 g were tested for the measurements and the uptake data for these two masses are presented in the supporting information (SI Figure 1). It is clear from the figure that the signal-to-noise for each of these two masses is much larger than for the other results presented in this work. One reason for these noisy data is the low overall N_2 adsorption that occurs for that amount of sample at 283 K, which is comparable to the measurement's uncertainty. Thus, for measurements at 303 K, one would expect the signals to be even noisier than those measured at 283 K if the same amount of adsorbent were used, since the adsorption capacity at 303 K is lower than that at 283 K. We then used 1 gram of zeolite 4A for the N_2 ROA measurement at 303 K and it was found this was an appropriate sample size for ROA measurements. Accordingly, we used about 1 gram of zeolite 4A for all our measurements and used a similar mass for all other adsorbents for the sake of comparison on an equivalent basis. All gases used for analysis were of high purity supplied by Coregas Australia, with the following specified molar purities: CH_4 : 99.995 %; N_2 : 99.999 % and He: 99.995%.

Table 3.1 Physical properties of the adsorbents

	Norit RB3	Zeolite 13X	Zeolite 4A	MSC-3K 172
Sample mass (g)	1.0077	0.8092	1.0328	1.0511
Particle Diameter* (mm)	3.2	1.4	2.0	1.0
Particle length* (mm)	4.0	4.0	3.6	2.0
Pore volume (cm ³ /g)	0.21	0.33	0.28	0.22
Pellet density* (g/cm ³)	0.85	1.12	1.09	0.90

*Assuming cylindrical, averaged over measurements of 20 particles

Equilibrium adsorption capacity in terms of pellet mass and adsorption rates of CH₄ and N₂ on four adsorbents were measured at two temperatures (273 and 303) K using a volumetric adsorption measurement system, the Micromeritics ASAP 2020, in Rate of Adsorption (ROA) mode. Prior to these measurements, each of the adsorbents was degassed under vacuum (1 Pa) in a sample tube for 12 hours at the recommended temperatures for the given adsorbents: 473 K for Norit RB3 and MSC-3K 172, 623 K for zeolite 13X and zeolite 4A [72, 203, 220, 221]. After degassing, the sample tube was backfilled with helium and transferred to the analysis port for measurement of the adsorption amount and rate of pure gases. The measurements were then carried out from low pressure (5 kPa) to high pressure (120 kPa) incrementally to ensure that upon a step pressure change the driving force of adsorption was sufficiently small to be considered linear as assumed by the Fickian diffusion model [218, 222]. In the ROA mode of the ASAP2020, the pressure in the sample tube was automatically monitored and recorded by the data acquisition software on the instrument once a certain amount of gas was dosed. The pressure change in the sample tube was then converted to molar amount of gas adsorbed per unit mass of the adsorbent using the reference equation of state for the respective pure gases [223, 224]. In this work, the pressure change in the sample tube was recorded every 0.4 s immediately following the introduction of a gas dose (0.223 mmol gas per gram of adsorbent). The 0.4 s data acquisition period, which limits the fastest sorption rate that can be measured with the apparatus, is the smallest meaningful time interval that can be studied with the instrument even though the operating software allows a 0.1 s interval to be specified, because the data acquisition system on the ASAP 2020 executes a 400 ms averaging of the analogue pressure transducer signals. For all the rate of adsorption measurements, 1000 pressure data points (the maximum number allowable by the data acquisition software) were recorded following the introduction of the gas dose. Representative uptake curves of three consecutive equilibrium pressure points for “slow” and “fast” cases are shown in Figure 3.2. For systems with slow adsorption, the rate of adsorption over a pressure

step was monitored for only the first 400 seconds ($0.4 \text{ s} \times 1000$) and then the uptake rate on the adsorbent was no longer recorded while the system was allowed to proceed towards equilibrium. Once the equilibrium criterion (a pressure change of less than 0.01 % in a time interval of 30 s) was satisfied, the measurement of the next pressure point was automatically initiated. For systems with faster adsorption where equilibrium could be obtained within 400 seconds, all of the uptake data of gas on the adsorbent were recorded.

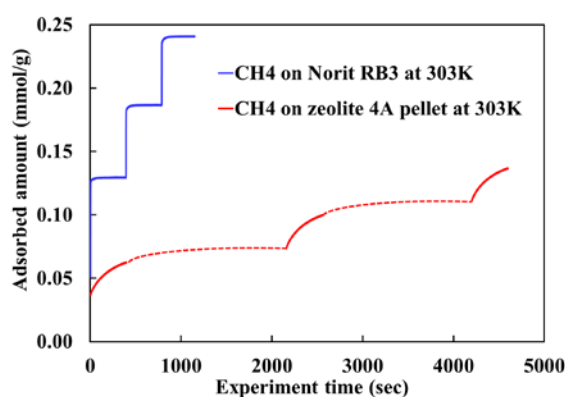


Figure 3.2 Examples of rate of adsorption measurements for CH₄ on Norit RB3 (fast) and zeolite 4A (slow) for three consecutive pressure steps at 303 K. The solid curves correspond to ROA measurements, while the dashed curve indicates the pressure evolution that occurred prior to the attainment of equilibrium.

3.4.2 Calibration with Helium

To properly analyse the data acquired during the rate of adsorption measurements, blank experiments with helium were carried out for each of the adsorbents with exactly the same run files as for CH₄ and N₂ at the same temperatures. This enabled measurement of the pressure in the sample tube following the opening of the dose valve due to the gas expansion and in the absence of any adsorption (assuming the adsorption of helium on the adsorbents was negligible [225]). The blank experiments were particularly important for two reasons: first, the very first pressure data point recorded for each rate of adsorption measurement by the ASAP 2020 data acquisition system actually corresponded to the pressure in the reference volume (solid red line in Figure 3.3) before Valve 12 (Figure 3.3) was opened to introduce gas into the sample tube and was not representative of the actual pressure in the sample tube. Second, for most measurements of gas adsorption kinetics based on the volumetric technique it is important to account for the time required for gas flow and expand into the sample tube. Determining the correct initial pressure in the sample tube is critical because it sensitively affects a

key parameter (α^*) in the non-isothermal dynamic model to which the dynamic pressure data are regressed, as discussed further in Section 3.

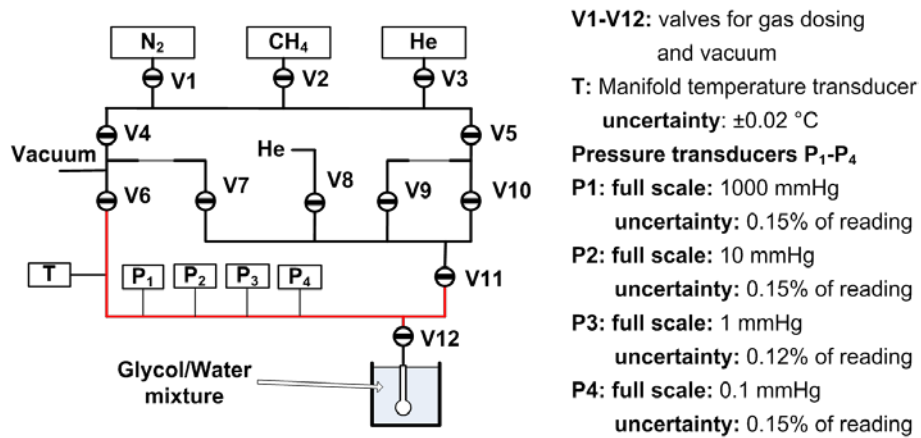


Figure 3.3. Schematic of the volumetric adsorption system: red solid line represents the apparatus' reference volume, used to calculate the amount of gas dosed into the sample volume below V12. The four pressure transducers could also be isolated (valves not shown) from the manifold whenever the pressure exceeded their full scale.

3.5 Models for Adsorption Kinetics

The linear driving force (LDF) and Fickian diffusion (FD) equations are two kinetic models commonly used to extract adsorption kinetics information from experimentally measured rate of adsorption data [200, 207, 226, 227]. Commonly, the LDF model is used instead of the FD model to represent adsorption kinetics within adsorption process simulations even though LDF predictions often show larger deviations from experimentally measured kinetic data than those made with FD models. This results from the fact that in adsorption process simulations, the LDF model allows elimination of the integration step at the particle level which is required for the FD model and, thus, use of the LDF model significantly reduces computational time [226]. However, the widespread availability of high performance computers nowadays may enable the use of more accurate FD models to simulate cyclic adsorption processes even though they are more computationally intensive.

The linear driving force model was initially developed by Glueckauf and Coates [228] for interpreting the incomplete equilibrium of the front boundary in adsorption chromatography under isothermal conditions, and it has since been adopted for describing adsorption kinetics as summarised by Sircar [226]. The general form of the LDF model for a single adsorbate is given by:

$$\frac{dm_t}{dt} = k[m_\infty - m_t] \quad \text{Eqn. 1}$$

Here m_t is the molar adsorbed amount of adsorbate on the adsorbent particle at time t , and m_∞ is the equilibrium adsorbed amount of adsorbate at the gas phase pressure P and the adsorbent temperature T . The k is the effective LDF mass transfer coefficient for the equilibrium adsorbed amount of m_∞ . The analytical solution of the LDF model [226] is used for the regression of data obtained via constant volume-variable pressure experiments when the adsorption process can be assumed an isothermal process:

$$\frac{m_t - m_0}{m_\infty - m_0} = 1 - \exp[-(1 + \alpha^*)kt] \quad \text{Eqn. 2}$$

$$\frac{\alpha^*}{1 + \alpha^*} = \frac{P^{0+} - P^\infty}{P^{0+} - P^{0-}} \quad \text{Eqn. 3}$$

Here m_0 is the equilibrium adsorbed amount on the adsorbent at the start of a pressure step, α^* is dimensionless and related to the ratio of the amount gas adsorbed during the pressure step to the amount of gas introduced to the system at time zero of the pressure step as indicated in Eqn. 3, P^{0+} is the gas phase pressure immediately after opening the dosing valve, P^∞ is the final equilibrium pressure for a pressure step, P^{0-} is the gas phase pressure before opening the dosing valve. The mass transfer coefficient k can be correlated with the sorption rate D/r^2 using the commonly recommended relation $k = 15D/r^2$ for adsorption process design [229].

The Fickian diffusion (FD) model describes the mass transfer between the gas and adsorbed phases using Fick's law of diffusion in terms of the sorption rate (D/r^2) for a gas on given adsorbents. For a constant volume system, and under the assumptions (1) that the gas diffusivity is independent of the amount of adsorbed phase, and (2) the uptake is isothermal, the analytical solution to the dynamic mass balance equation is given as follows [218]:

$$\frac{m_t}{m_\infty} = 1 - \sum_{n=1}^{\infty} \frac{6(1 + \alpha^*) \exp(-q_n^2 \frac{D}{r^2} t)}{9\alpha^*(1 + \alpha^*) + q_n^2} \quad \text{Eqn. 4}$$

where

$$q_n = (1 + q_n^2 / 3\alpha^*) / \cot q_n \quad \text{Eqn. 5}$$

Here q_n is the root of transcendental equation (Eqn. 5). Eqn. 4 is strictly limited to the analysis of isothermal uptake data for cases where the heat resulting from the adsorption can be considered as being instantaneously dissipated to the environment. To account for situations where the heat released by adsorption cannot be dissipated fast enough to achieve an isothermal condition, the non-isothermal kinetic model developed by Kocirik et. al. [218] can be used. This model was obtained for non-isothermal, constant-volume but variable-pressure conditions, by deriving an analytical solution to the simultaneous mass and heat transport equations. The main assumptions for this model are that the adsorption rate was controlled by intracrystalline gas diffusion and heat (arising from heat of adsorption) transfer from the adsorbent surface to the surrounding environment. The analytical solution is as follows:

$$\frac{m_t}{m_\infty} = 1 - \sum_{n=1}^{\infty} \frac{9(1 + \alpha^*) \left[\frac{Y_n}{-q_n^2} \right]^2 \exp\left(-q_n^2 \frac{D}{r^2} t\right)}{\frac{1}{\beta_n^*} + \frac{3}{2} \frac{\beta}{\beta_n^*} \left[q_n \cot q_n \left(\frac{Y_n}{q_n^2} \right) + 1 \right] + \frac{3}{2} \frac{\alpha^* B_n}{q_n^4 \beta_n^*}} \quad \text{Eqn. 6}$$

Here q_n is given by the roots of the following equation:

$$\left(-q_n^2 + \alpha\right) + 3\beta Y_n - \frac{3\alpha^*}{q_n^2} \left(-q_n^2 + \alpha\right) Y_n = 0 \quad \text{Eqn. 7}$$

with:

$$Y_n = q_n \cot q_n - 1 \quad \text{Eqn. 8}$$

and with the additional parameters defined as follows:

$$\alpha = \frac{ha}{\rho_s c_s} \frac{D}{r^2} \quad \text{Eqn. 9}$$

$$\beta = \frac{\Delta H}{c_s} \left(\frac{\partial q^*}{\partial T} \right)_{c_g(0), T_0} \quad \text{Eqn. 10}$$

$$\frac{1}{\beta_n^*} = \frac{1}{\beta} \left(1 - \frac{3\alpha^* Y_n}{q_n^2} \right) \quad \text{Eqn. 11}$$

$$B_n = Y_n [(q_n^2 - \alpha) q_n \cot q_n - 2\alpha] + q_n^2 (q_n^2 - \alpha) \quad \text{Eqn. 12}$$

Here h is the overall heat transfer coefficient between the external surface of the adsorbent and its surroundings, a is the external surface area per unit volume of the adsorbent, ρ_s is the adsorbent density, c_s is the heat capacity of the adsorbent at constant pressure, and ΔH is heat of adsorption.

Both the isothermal LDF model (Eqn. 2) and non-isothermal FD model (Eqn. 6) were regressed to the experimental uptake curves by adjusting the parameter D/r^2 in the LDF model and by adjusting the parameters α , β and D/r^2 in the non-isothermal FD to minimise the root mean squared deviation (RMSD) between the dynamic uptake data and the model according to Eqn.13.

$$RMSD = \sqrt{\frac{\sum_{i=1}^N [(1-m_t/m_\infty)_{exp} - (1-m_t/m_\infty)_{model}]^2}{N}}$$

Eqn. 13

where N is the number of experimental data points. Since $(1 - m_t/m_\infty)$ is normalised and dimensionless, the RMSD should have a value between 0 (indicating a perfect fit) and 1 (indicating a very bad fit).

3.6 Results and Discussion

3.6.1 Adsorption Equilibria

Figure 3.4 shows the measured pure component adsorption isotherms for CH₄ and N₂ on the four adsorbents, and Table 3.2 lists the data measured for these isotherms, together with their combined standard uncertainties which were calculated according to uncertainty propagation formula shown in Eqn. 14 [230]. Assuming that the input quantities are not correlated, the combined standard uncertainty in the adsorption capacity for the present measurements can be calculated as

$$u(Q_e) = \sqrt{\left[\left(\frac{\partial Q_e}{\partial m}\right) u(m)\right]^2 + \left[\left(\frac{\partial Q_e}{\partial P}\right) u(P)\right]^2 + \left[\left(\frac{\partial Q_e}{\partial T}\right) u(T)\right]^2 + \left[\left(\frac{\partial Q_e}{\partial V}\right) u(V)\right]^2}$$

Eqn. 14

where $u(x)$ denotes the standard uncertainty of a quantity x and V is sample tube volume. The uncertainty in the sample mass was estimated from the balance resolution, the uncertainty of the pressure was taken to be 0.15 % of the equilibrium reading, and the uncertainty of the temperature was set by the stability of the liquid bath. The uncertainty in the volume was estimated from the standard deviation in the free gas volume (≈ 20 mL) determined automatically by the apparatus corresponding to each equilibrium pressure measurement. Numerical values of these component uncertainties are listed in Table 3.2.

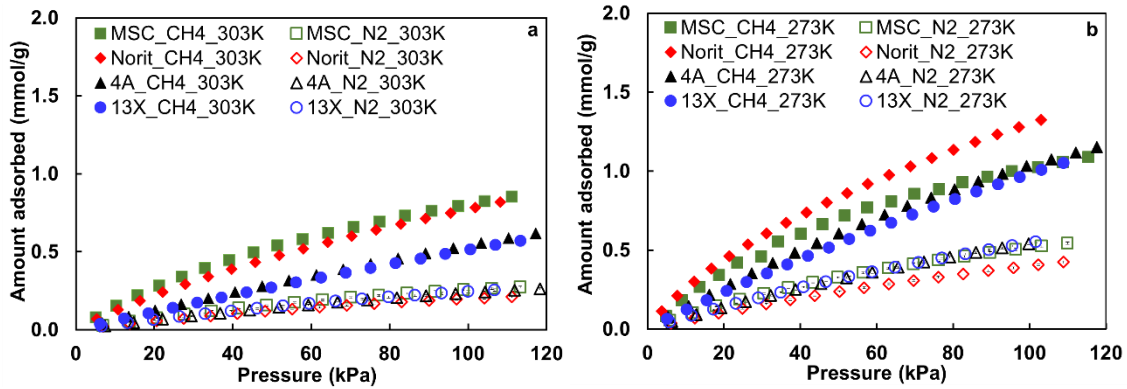


Figure 3.4 Measured adsorption capacity of pure methane (solid symbols) and pure nitrogen (hollow symbols) on four adsorbents at a) 303 K, and, b) 273 K for pressures up to 120 kPa

Table 3.2 Pure methane and nitrogen single component adsorption capacities, Q_e , along with their standard uncertainties, $u(Q_e)$, on the four adsorbents tested in this study. $u(Q_e)$ was calculated using Eqn. 14 with standard uncertainties for sample mass: 0.0001 g, pressure: 0.15 % of reading, temperature: 0.02 K, and volume: 0.074 mL

Temperature (K)	Pressure (kPa)	Q_e (mmol/g)	$u(Q_e)$ (mmol/g)	Temperature (K)	Pressure (kPa)	Q_e (mmol/g)	$u(Q_e)$ (mmol/g)
Zeolite 4A							
Methane				Nitrogen			
273.15	5.40	0.0735	0.0019	273.15	5.42	0.0418	0.0019
273.15	10.57	0.1393	0.0027	273.15	11.43	0.0830	0.0027
273.15	15.79	0.2037	0.0033	273.15	17.49	0.1230	0.0033
273.15	21.00	0.2679	0.0038	273.15	23.55	0.1615	0.0038
273.15	26.26	0.3299	0.0042	273.15	29.63	0.1985	0.0042
273.15	31.54	0.3911	0.0046	273.15	35.72	0.2346	0.0046
273.15	36.88	0.4506	0.0050	273.15	41.82	0.2694	0.0050
273.15	42.35	0.5106	0.0053	273.15	48.10	0.3038	0.0053
273.15	47.91	0.5680	0.0056	273.15	54.41	0.3371	0.0056
273.15	53.52	0.6231	0.0059	273.15	60.71	0.3690	0.0059
273.15	59.15	0.6774	0.0062	273.15	67.05	0.4000	0.0062
273.15	64.73	0.7307	0.0065	273.15	73.41	0.4296	0.0065
273.15	70.48	0.7817	0.0068	273.15	79.82	0.4588	0.0068
273.15	76.33	0.8314	0.0070	273.15	86.20	0.4861	0.0070

273.15	82.13	0.8802	0.0073	273.15	92.61	0.5124	0.0073
273.15	87.98	0.9246	0.0075	273.15	99.03	0.5375	0.0075
273.15	93.95	0.9680	0.0078	273.15	105.49	0.5619	0.0078
273.15	99.87	1.0131	0.0080	273.15	111.96	0.5853	0.0080
273.15	105.88	1.0547	0.0082				
273.15	111.97	1.0940	0.0084				
303.15	5.54	0.0362	0.0016	303.15	5.16	0.0186	0.0016
303.15	11.82	0.0737	0.0022	303.15	12.05	0.0394	0.0022
303.15	18.13	0.1108	0.0027	303.15	18.92	0.0593	0.0027
303.15	24.52	0.1475	0.0031	303.15	25.77	0.0783	0.0031
303.15	30.85	0.1837	0.0035	303.15	32.61	0.0966	0.0035
303.15	37.28	0.2195	0.0038	303.15	39.45	0.1142	0.0038
303.15	43.68	0.2546	0.0042	303.15	46.31	0.1306	0.0042
303.15	50.19	0.2895	0.0044	303.15	53.28	0.1466	0.0044
303.15	56.73	0.3238	0.0047	303.15	60.28	0.1620	0.0047
303.15	63.30	0.3572	0.0050	303.15	67.31	0.1764	0.0050
303.15	69.82	0.3902	0.0052	303.15	74.26	0.1899	0.0052
303.15	76.33	0.4223	0.0054	303.15	81.27	0.2026	0.0054
303.15	82.93	0.4543	0.0057	303.15	88.29	0.2147	0.0057
303.15	89.54	0.4856	0.0059	303.15	95.36	0.2259	0.0059
303.15	96.12	0.5158	0.0061	303.15	102.37	0.2363	0.0061
303.15	102.72	0.5455	0.0063	303.15	109.39	0.2458	0.0063
303.15	109.36	0.5750	0.0065				
Zeolite 13X APG							
Methane				Nitrogen			
273.15	5.38	0.0684	0.0016	273.15	4.76	0.0393	0.0016
273.15	9.85	0.1206	0.0022	273.15	9.67	0.0747	0.0022
273.15	14.34	0.1717	0.0027	273.15	14.60	0.1090	0.0027
273.15	18.90	0.2227	0.0031	273.15	19.54	0.1421	0.0031
273.15	23.39	0.2723	0.0035	273.15	24.50	0.1740	0.0035
273.15	27.95	0.3217	0.0038	273.15	29.46	0.2052	0.0038
273.15	32.53	0.3707	0.0041	273.15	34.43	0.2351	0.0041
273.15	37.12	0.4186	0.0044	273.15	39.43	0.2646	0.0044
273.15	41.70	0.4656	0.0047	273.15	44.53	0.2932	0.0047

273.15	46.39	0.5124	0.0049	273.15	49.64	0.3210	0.0049
273.15	51.07	0.5592	0.0052	273.15	54.75	0.3481	0.0052
273.15	55.81	0.6047	0.0054	273.15	59.89	0.3742	0.0054
273.15	60.55	0.6501	0.0056	273.15	65.05	0.3994	0.0056
273.15	65.28	0.6946	0.0058	273.15	70.21	0.4239	0.0058
273.15	70.06	0.7383	0.0060	273.15	75.39	0.4475	0.0060
273.15	74.85	0.7816	0.0062	273.15	80.55	0.4703	0.0062
273.15	79.64	0.8241	0.0064	273.15	85.75	0.4925	0.0064
273.15	84.47	0.8657	0.0066	273.15	90.98	0.5137	0.0066
273.15	89.28	0.9061	0.0068	273.15	96.21	0.5344	0.0068
273.15	94.11	0.9466	0.0070	273.15	101.42	0.5546	0.0070
273.15	98.97	0.9864	0.0071	273.15	106.67	0.5738	0.0071
273.15	103.84	1.0255	0.0073	273.15	111.93	0.5922	0.0073
273.15	108.68	1.0636	0.0075				
273.15	113.57	1.1010	0.0076				
303.15	4.93	0.0317	0.0019	303.15	5.24	0.0200	0.0019
303.15	10.14	0.0611	0.0027	303.15	10.77	0.0378	0.0027
303.15	15.35	0.0899	0.0033	303.15	16.29	0.0549	0.0033
303.15	20.57	0.1187	0.0038	303.15	21.82	0.0715	0.0038
303.15	25.76	0.1468	0.0043	303.15	27.33	0.0873	0.0043
303.15	30.98	0.1746	0.0047	303.15	32.93	0.1025	0.0047
303.15	36.35	0.2029	0.0051	303.15	38.48	0.1171	0.0051
303.15	41.70	0.2308	0.0054	303.15	44.00	0.1310	0.0054
303.15	47.06	0.2584	0.0058	303.15	49.62	0.1444	0.0058
303.15	52.39	0.2857	0.0061	303.15	55.22	0.1572	0.0061
303.15	57.78	0.3127	0.0064	303.15	60.85	0.1695	0.0064
303.15	63.18	0.3395	0.0066	303.15	66.46	0.1811	0.0066
303.15	68.58	0.3660	0.0069	303.15	72.08	0.1920	0.0069
303.15	73.90	0.3921	0.0072	303.15	77.73	0.2022	0.0072
303.15	79.17	0.4175	0.0074	303.15	83.37	0.2121	0.0074
303.15	84.55	0.4429	0.0077	303.15	89.03	0.2211	0.0077
303.15	89.96	0.4683	0.0079	303.15	94.69	0.2296	0.0079
303.15	95.33	0.4933	0.0081	303.15	100.33	0.2373	0.0081
303.15	100.72	0.5179	0.0084	303.15	106.00	0.2447	0.0084

303.15	106.02	0.5419	0.0086	303.15	111.66	0.2514	0.0086
303.15	111.42	0.5661	0.0088				
MSC-3K 172							
Methane				Nitrogen			
273.15	4.86	0.0820	0.0018	273.15	5.87	0.0544	0.0018
273.15	9.03	0.1823	0.0026	273.15	11.87	0.1019	0.0026
273.15	13.69	0.2665	0.0032	273.15	17.99	0.1458	0.0032
273.15	18.70	0.3407	0.0036	273.15	24.21	0.1866	0.0036
273.15	23.55	0.4197	0.0041	273.15	30.51	0.2250	0.0041
273.15	29.78	0.4583	0.0045	273.15	36.87	0.2609	0.0045
273.15	34.18	0.5552	0.0048	273.15	43.35	0.2948	0.0048
273.15	40.21	0.6030	0.0052	273.15	49.84	0.3271	0.0052
273.15	45.80	0.6645	0.0055	273.15	56.45	0.3571	0.0055
273.15	51.67	0.7174	0.0058	273.15	63.02	0.3857	0.0058
273.15	57.54	0.7699	0.0060	273.15	69.60	0.4115	0.0060
273.15	63.82	0.8085	0.0063	273.15	76.26	0.4363	0.0063
273.15	69.82	0.8554	0.0066	273.15	82.94	0.4602	0.0066
273.15	76.36	0.8863	0.0068	273.15	89.66	0.4833	0.0068
273.15	82.52	0.9304	0.0071	273.15	96.39	0.5046	0.0071
273.15	88.99	0.9640	0.0073	273.15	103.16	0.5247	0.0073
273.15	95.42	0.9997	0.0075	273.15	109.94	0.5432	0.0075
273.15	102.20	1.0252	0.0077				
273.15	108.76	1.0576	0.0079				
273.15	115.39	1.0875	0.0081				
303.15	5.15	0.0782	0.0016	303.15	6.90	0.0276	0.0016
303.15	10.33	0.1530	0.0023	303.15	13.79	0.0527	0.0023
303.15	15.73	0.2204	0.0028	303.15	20.71	0.0762	0.0028
303.15	21.26	0.2836	0.0033	303.15	27.65	0.0985	0.0033
303.15	27.00	0.3402	0.0037	303.15	34.61	0.1193	0.0037
303.15	32.96	0.3966	0.0040	303.15	41.57	0.1391	0.0040
303.15	39.06	0.4472	0.0043	303.15	48.66	0.1575	0.0043
303.15	45.26	0.4943	0.0046	303.15	55.76	0.1750	0.0046
303.15	51.40	0.5398	0.0049	303.15	62.89	0.1911	0.0049
303.15	57.83	0.5807	0.0052	303.15	70.10	0.2066	0.0052

303.15	64.34	0.6208	0.0054	303.15	77.25	0.2203	0.0054
303.15	70.89	0.6587	0.0057	303.15	84.43	0.2332	0.0057
303.15	77.41	0.6942	0.0059	303.15	91.63	0.2449	0.0059
303.15	83.99	0.7306	0.0061	303.15	98.85	0.2558	0.0061
303.15	90.73	0.7620	0.0064	303.15	106.05	0.2655	0.0064
303.15	97.52	0.7928	0.0066	303.15	113.29	0.2744	0.0066
303.15	104.31	0.8237	0.0068				
303.15	111.16	0.8522	0.0070				
Norit RB3							
Methane				Nitrogen			
273.15	3.69	0.1129	0.0017	273.15	6.16	0.0368	0.0017
273.15	7.82	0.2106	0.0024	273.15	12.37	0.0697	0.0024
273.15	12.18	0.3000	0.0029	273.15	18.58	0.1009	0.0029
273.15	16.72	0.3836	0.0034	273.15	24.81	0.1306	0.0034
273.15	21.41	0.4615	0.0038	273.15	31.08	0.1590	0.0038
273.15	26.23	0.5353	0.0041	273.15	37.37	0.1860	0.0041
273.15	31.18	0.6053	0.0045	273.15	43.78	0.2125	0.0045
273.15	36.32	0.6734	0.0048	273.15	50.25	0.2379	0.0048
273.15	41.57	0.7391	0.0051	273.15	56.69	0.2623	0.0051
273.15	46.87	0.8018	0.0053	273.15	63.17	0.2856	0.0053
273.15	52.26	0.8615	0.0056	273.15	69.66	0.3079	0.0056
273.15	57.69	0.9198	0.0058	273.15	76.11	0.3292	0.0058
273.15	63.22	0.9762	0.0061	273.15	82.66	0.3500	0.0061
273.15	68.85	1.0310	0.0063	273.15	89.19	0.3699	0.0063
273.15	74.43	1.0833	0.0065	273.15	95.74	0.3888	0.0065
273.15	80.08	1.1343	0.0067	273.15	102.32	0.4070	0.0067
273.15	85.77	1.1844	0.0069	273.15	108.90	0.4241	0.0069
273.15	91.51	1.2328	0.0071	273.15	115.50	0.4409	0.0071
273.15	97.21	1.2795	0.0073				
273.15	103.02	1.3255	0.0075				
273.15	108.87	1.3705	0.0077				
273.15	114.76	1.4146	0.0079				
303.15	5.28	0.0689	0.0016	303.15	6.89	0.0212	0.0016
303.15	10.73	0.1294	0.0022	303.15	13.74	0.0398	0.0022

303.15	16.37	0.1867	0.0027	303.15	20.62	0.0572	0.0027
303.15	22.10	0.2410	0.0032	303.15	27.47	0.0737	0.0032
303.15	27.89	0.2920	0.0035	303.15	34.32	0.0894	0.0035
303.15	33.72	0.3408	0.0039	303.15	41.18	0.1043	0.0039
303.15	39.71	0.3882	0.0042	303.15	48.24	0.1186	0.0042
303.15	45.74	0.4338	0.0045	303.15	55.11	0.1319	0.0045
303.15	51.83	0.4777	0.0048	303.15	62.13	0.1446	0.0048
303.15	57.98	0.5202	0.0050	303.15	69.05	0.1564	0.0050
303.15	64.18	0.5615	0.0053	303.15	76.06	0.1674	0.0053
303.15	70.31	0.6008	0.0055	303.15	83.07	0.1778	0.0055
303.15	76.56	0.6396	0.0057	303.15	90.07	0.1870	0.0057
303.15	82.87	0.6774	0.0059	303.15	97.06	0.1956	0.0059
303.15	89.17	0.7142	0.0061	303.15	104.11	0.2036	0.0061
303.15	95.49	0.7497	0.0063	303.15	111.14	0.2108	0.0063
303.15	101.86	0.7846	0.0065				
303.15	108.23	0.8185	0.0067				
303.15	114.64	0.8517	0.0069				

Figure 3.4 clearly shows that all of these adsorbents have higher CH₄ capacities than N₂ capacities at the same temperature and pressure. At 303 K, MSC-3K 172 and Norit RB3 exhibited a similar adsorption capacity for methane, which is about 40% higher than the corresponding methane capacities observed for zeolite 4A and zeolite 13X at around 100 kPa. The nitrogen adsorption capacity for MSC-3K 172, Norit RB3, zeolite 4A and zeolite 13X were essentially identical at 303 K. At 273 K, both MSC-3K 172 and Norit RB3 displayed slightly higher (~20%) capacities for methane than those for the other adsorbents at pressures up to 40 kPa. The nitrogen adsorption capacity for MSC-3K 172, zeolite 4A and zeolite 13X were essentially identical at 273 K, and about 30% higher than that for Norit RB3.

3.6.2 Kinetic Measurement Calibration

To accurately measure sorption kinetics using a volumetric system, the time delay in recorded data caused by the effects of the valve and the sensors' response needs to be accounted for when processing the uptake data. In the work of Hu et al. [217], for example, the initial 5 seconds of pressure data were discarded by the authors presumably because, as we found, the dynamics of the early transient is not captured correctly by existing models. The objective of this work is to explicitly account for those very early dynamics through the use of a helium blank run at the corresponding pressures

where measurements with CH₄ and N₂ (which both adsorb but also experience similar transient dynamics) were acquired. Helium was used to calibrate the effects of gas expansion upon dosing for all the kinetic measurements conducted in this work to enable correction of the initial condition (time origin and pressure) for the subsequent analysis of the dynamic uptake. Figure 3.5 shows an example of why the helium calibration was necessary to obtain accurate sorption kinetics from the raw pressure readings acquired with the apparatus, through the comparison of ROA data obtained for helium and methane on Norit RB3 at 80 kPa and 273 K. At 273 K, the methane pressure dropped quickly from 86.74 kPa at $t = 0$ to 80.63 kPa at $t = 0.8$ s, with the final equilibrium pressure being 80.08 kPa. These raw pressure data superficially indicate that 92 % of the sorption capacity at 273 K was reached within 0.8 seconds of gas dosage, which could be interpreted erroneously as extremely fast sorption kinetics if these raw data were used. However, comparison of these raw pressure data for methane with those obtained during the corresponding helium calibration experiment shows that those initial rapid pressure changes were more likely caused by gas expansion rather than adsorption given that the experiment with helium also exhibited a similar rapid pressure drop within the first 0.8 seconds, with a negligible pressure decrease thereafter. Clearly then, the pressure drop occurring in the first 0.8 seconds is dominated by gas expansion, and the condition from which the initial time and pressure datum should be taken for the analysis of sorption kinetics is $t = 0.8$ s and $p \approx 80.63$ kPa. To capture a more precise estimate of the initial pressure, which accounts for any possible methane adsorption that did occur during the first 0.8 s, the pressure ratio obtained for helium between $t = 0.8$ s and $t = 0$ s can be applied to the methane pressure recorded at $t = 0$ s. Across all the experiments conducted, the time scale of the gas expansion effect as measured with helium ranged from 0.8 to 5.6 s, and it was found to be important to perform helium calibration runs for each adsorbent.

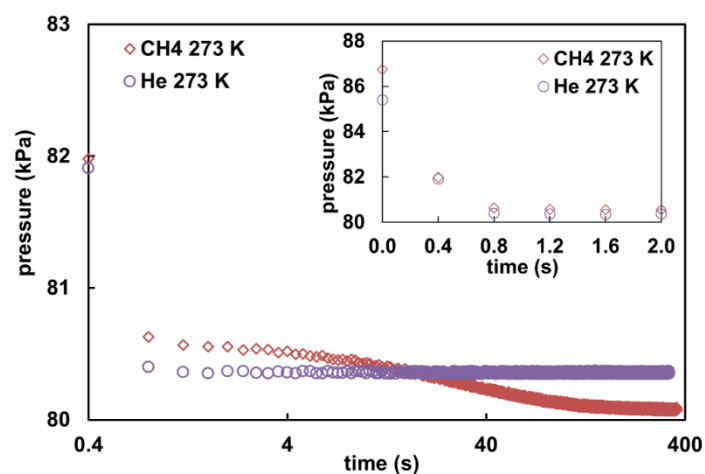


Figure 3.5 Pressure readings in methane rate of adsorption measurements on Norit RB3 at around 80 kPa at 273 K together with corresponding helium calibration pressure readings.

3.6.3 Sorption Rate Determination from Dynamic Uptake with Kinetic Models

The objective of this paper is to demonstrate a new robust method of extracting effective reliable sorption kinetic data for materials that may be used in industrial adsorption process design. Accordingly, we do not discuss extensively the mechanisms governing the observed uptake rates, in part because it is well known that the controlling mechanism for nitrogen and methane diffusion in Norit RB3 and zeolite 13X is macropore diffusion [203, 207, 217] and that for zeolite 4A and molecular sieve carbon is micropore diffusion [199, 211].

Figure 3.6 shows pairs of representative CH₄ and N₂ uptake data obtained at 273 K and about 100 kPa for Norit RB3, zeolite 13X, MSC 3K-172 and zeolite 4A. For both gases, the non-isothermal Fickian diffusion models resulting from the regression to the CH₄ and N₂ uptake data are presented along with the experimental data. Additionally, the results of the isothermal LDF model regression to the CH₄ data are shown.

The LDF model is the most widely-used correlation for representing gas adsorption kinetics in adsorption process simulations. Therefore, fits of this model to the gas uptake data were tested for each of the adsorbents. However, the LDF fit had particularly large deviations from the experimental data for Norit RB3 (RMSD = 12.26 %) and zeolite 13X (RMSD = 7.44 %) measured in this study. The LDF model tends to predict an overall faster approach to equilibrium for these large pore sized adsorbents but a slower adsorption rate at the initial stage of the adsorption. The deviations of the LDF model from the experimental data can be explained by the fact that in the experiments, the approach to adsorption equilibrium was initially accelerated by faster gas diffusion due to the temperature rise associated with heat-transfer limitations, before the reduction in the adsorbent's equilibrium capacity adversely affected the sorption driving force [222]. The isothermal LDF model cannot capture such heat related effects, and instead assumes that the rate of adsorption depends solely on the initial driving force for adsorption. The deviations of the LDF model from the experimental data for MSC-3K 172 (RMSD = 1.27 %) and zeolite 4A (RMSD = 2.6 %) are smaller compared to those for the other two adsorbents, which can be attributed to the small micropores within MSC-3K 172 and zeolite 4A, which slow gas diffusion therein. This enables the heat of adsorption to be dissipated to the environment relatively rapidly in comparison with the time scale for sorption, thereby maintaining the system at near constant temperature.

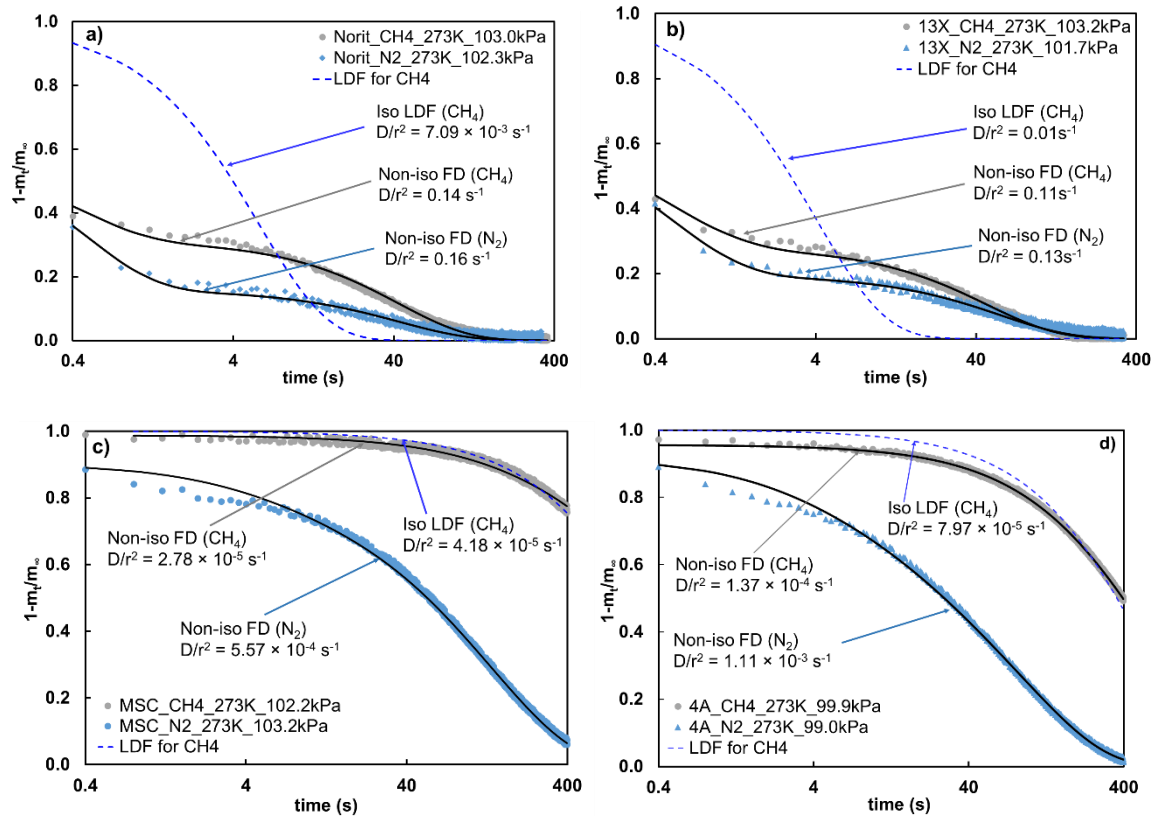


Figure 3.6 Experimental and theoretical (black solid lines representing FD model for both CH₄ and N₂, and blue dash line representing LDF model for CH₄) uptake curves of CH₄ and N₂ on a) Norit RB3, b) Zeolite 13X, c) carbon molecular sieve MSC-3K 172, and d) zeolite 4A pellet at 273 K with pressure around 100 kPa

When the non-isothermal FD model was used to regress the experimental uptake data, the respective RMSDs were much smaller than that for LDF model: 0.91 % for Norit RB3, 0.82 % for zeolite 13X, 0.95 % for MSC-3K 172 and 0.96 % for zeolite 4A. The effective sorption rates obtained with the LDF model were 10 to 20 times smaller than those obtained with the FD model for Norit RB3 and zeolite 13X, and differed by about a factor of two for MSC-3K 172 and zeolite 4A. Clearly, the non-isothermal FD model provided a much better description of the experimental uptake curves on all four adsorbents than the LDF model and for this reason we exclusively used the FD model in all subsequent analysis.

3.6.4 Kinetic Adsorption Results

Figure 3.7 shows the effective sorption rate of CH₄ and N₂ on Norit RB3, zeolite 13X, zeolite 4A and MSC-3K 172 as a function of pressure at 303 K and 273 K. The effective sorption rates for CH₄ are of the same order of magnitude for adsorbents Norit RB3 and zeolite 13X, which are approximately 10³ times faster than that of CH₄ in zeolite 4A and 10⁴ times faster than that of CH₄ in MSC-3K 172. The effective sorption rates for N₂ are also of the same order of magnitude for adsorbents Norit RB3 and

zeolite 13X, which are approximately 10^2 times faster than that of N_2 in zeolite 4A and 10^3 times faster than that of N_2 in MSC-3K 172. The effective sorption rate showed only a weak dependence on pressure, which is consistent with the assumption of the FD model that the sorption rates are independent of loading of adsorbed phase on the adsorbents [218] in the range of pressures studied in this work.

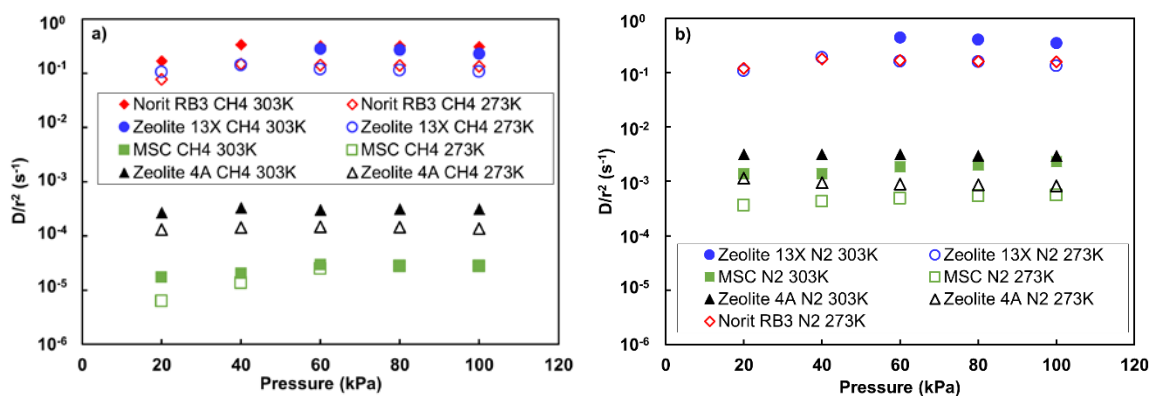


Figure 3.7 Effective diffusion time constant for CH_4 and N_2 on Norit RB3, zeolite 13X, zeolite 4A and carbon molecular sieve MSC-3K 172 obtained by non-isothermal Fickian diffusion model at 303 K (solid) and 273 K (hollow) at various pressures: a) effective sorption rate constant for CH_4 , b) effective sorption rate constant for N_2

Values of the effective sorption rate for Norit RB3 are listed in Table 3.3, ranging from $(0.13 \text{ to } 0.15) \text{ s}^{-1}$ for CH_4 and being no smaller than 0.16 s^{-1} for N_2 at 273 K. At 303 K they ranged from $(0.31 \text{ to } 0.35) \text{ s}^{-1}$ for CH_4 but the rate of N_2 adsorption was too fast (more than 90 % of adsorption capacity over the pressure step was achieved within 1 second) to obtain meaningful values given the limited temporal resolution of the apparatus. To the best of our knowledge, there has been only one work reporting the kinetics of CH_4 and N_2 on activated carbon Norit RB3 by Rufford et al. [203]. They used an isothermal linear driving force model to extract mass transfer coefficients for CH_4 and N_2 from breakthrough experiments conducted in a fixed bed column. However, even the largest effective sorption rate derived from their reported mass transfer coefficients are about 100 times smaller than our results. We suspect that the apparent sorption rates extracted from the measurements of Rufford et al. [21] were significantly afflicted by heat transfer limitations in the fixed bed, and we have since updated our approach to such DCB sorption rate measurements [231, 232]. Meanwhile, our results are similar to that of a work by Malek and Farooq [206] for CH_4 on an activated carbon. Their measurements were performed at temperatures from (299 to 338) K and pressures in the range of (199 to 651) kPa with dynamic breakthrough experiments using dilute CH_4 mixtures. The effective

sorption rate reported by them for these conditions ranged from (0.41 to 0.66) s^{-1} . In addition, our measurements are consistent with effective sorption rates obtained from N_2+CH_4 breakthrough experiments conducted on a Maxsorb activated carbon at 300 K and 1 atm by Sheikh et. al. [94] (0.197 s^{-1} for CH_4 and 0.55 s^{-1} for N_2). More recently, Ju et al. [200] reported the kinetics of pure CH_4 and N_2 on cylindrical activated carbon granules with effective sorption rate of (0.06 to 0.08) s^{-1} for CH_4 in the pressure range of (25 to 78) kPa and (0.06 to 0.08) s^{-1} for N_2 in the pressure range of (20 to 90) kPa at 308 K. These values for methane are about 30 to 50 times smaller than our results at 303 K. However, we note that the dynamic uptake data shown graphically in reference [200] for CH_4 on activated carbon are reasonably consistent with our dynamic uptake data. Figure 3 of reference [200] suggests that 90 % of the uptake occurred in about 20 seconds, which is even faster than our observations of 80 % uptake within 20 seconds for CH_4 on activated carbon. As indicated above, systematically low estimates of the effective sorption rate can occur if the LDF model is used to analyse data with appreciable heating effects. However, Ju et al. [200] stated they used the non-isothermal FD model to regress their data. Bulow [233] has suggested alternative reasons for the apparently low sorption rates reported by Ju et al. [200], such as neglecting to deduct the overall response time of the apparatus or the delay caused by forcing the gas to pass through a 0.5 micron ceramic frit on top of the adsorbent.

Table 3.3. Effective sorption rate and associated parameters for the non-isothermal FD model in eqs (6)-(12) for CH₄ and N₂ on activated carbon Norit RB3. Values are not reported for conditions where 90% of the uptake occurred within 1 s.

Norit RB3									
Methane					Nitrogen				
273.15 K					273.15 K				
P (kPa)	$ha/\rho_s c_s$ (s ⁻¹)	β	D/r ² (s ⁻¹)	u(D/r ²) (s ⁻¹)	P (kPa)	$ha/\rho_s c_s$ (s ⁻¹)	β	D/r ² (s ⁻¹)	u(D/r ²) (s ⁻¹)
21.41	0.033	0.249	0.14	0.02	24.81	-	-	-	-
41.57	0.033	0.345	0.15	0.02	43.78	-	-	-	-
63.22	0.032	0.541	0.14	0.01	63.178	-	-	-	-
80.08	0.033	0.653	0.14	0.01	82.66	0.034	0.257	0.16	0.04
103.02	0.034	0.736	0.13	0.01	102.32	0.034	0.253	0.16	0.03
303.15 K					303.15 K				
22.10	0.032	0.155	0.34	0.04	20.62	-	-	-	-
39.71	0.034	0.203	0.34	0.04	41.18	-	-	-	-
64.18	0.034	0.334	0.32	0.05	62.13	-	-	-	-
82.87	0.035	0.384	0.32	0.05	83.07	-	-	-	-
101.86	0.032	0.358	0.31	0.05	104.11	-	-	-	-

The effective sorption rates measured for CH₄ and N₂ on zeolite 13X are listed in Table 3.4, and range from (0.11 to 0.29) s⁻¹ and (0.13 to 0.43) s⁻¹, respectively. These are broadly consistent with kinetic results reported in the literature. Delgado et al. used pulse experiments to measure the effective sorption rate for CH₄ at 289 K and 324 K on a zeolite 13X with results ranging from (0.18 and 0.33) s⁻¹ [209]. Dantas et al. [208] obtained N₂ mass transfer coefficients on a zeolite 13X using binary gas breakthrough experiments at 1 bar of pressure at various temperatures, and at about 303K, the effective sorption rate reported for N₂ was 0.18 s⁻¹. However, Park et al. [207] recently reported the kinetics of pure CH₄ and N₂ on spherical pelletised UOP zeolite 13X with effective time of 0.05-0.07 s⁻¹ for CH₄ and 0.01-0.08 s⁻¹ for N₂ in the pressure range of 10-80 kPa and temperature range of (293 to 323) K. These values are about 3~20 times smaller than our results, which might be explained by the fact that Park et al. [207] used the same apparatus and method as Ju et al. [200].

Table 3.4 Effective sorption rate of CH₄ and N₂ on zeolite 13X obtained from the non-isothermal FD model Values are not reported for conditions where 90% of the uptake occurred within 1 s.

Zeolite 13X									
Methane					Nitrogen				
273.15 K					273.15 K				
P (kPa)	$ha/\rho_s c_s$ (s ⁻¹)	β	D/r ² (s ⁻¹)	u(D/r ²) (s ⁻¹)	P (kPa)	$ha/\rho_s c_s$ (s ⁻¹)	β	D/r ² (s ⁻¹)	u(D/r ²) (s ⁻¹)
18.9	0.027	0.258	0.11	0.03	19.5	–	–	–	–
42.1	0.029	0.404	0.14	0.02	39.4	0.029	0.271	0.19	0.05
60.6	0.027	0.484	0.12	0.02	59.9	0.028	0.334	0.16	0.03
79.6	0.026	0.468	0.11	0.01	80.6	0.027	0.380	0.16	0.03
103.2	0.029	0.583	0.11	0.01	101.7	0.028	0.338	0.13	0.02
303.15 K					303.15 K				
20.6	–	–	–	–	21.8	–	–	–	–
41.7	–	–	–	–	38.5	–	–	–	–
63.2	0.026	0.169	0.29	0.09	60.9	0.030	0.178	0.43	0.08
79.2	0.025	0.167	0.27	0.07	83.4	0.029	0.149	0.40	0.07
100.7	0.027	0.217	0.23	0.05	100.3	0.028	0.138	0.34	0.05

The values of effective sorption rate for MSC-3K 172 are listed in Table 3.5, and at pressures from (20 to 120) kPa range from $(0.95 \text{ to } 27.8) \times 10^{-5} \text{ s}^{-1}$ for CH₄ and $(3.61 \text{ to } 5.57) \times 10^{-4} \text{ s}^{-1}$ for N₂ at 273 K, and from $(1.72 \text{ to } 2.95) \times 10^{-5} \text{ s}^{-1}$ for CH₄ and $(0.88 \text{ to } 1.35) \times 10^{-3} \text{ s}^{-1}$ for N₂ at 303 K. Our results are consistent with the data of Bae and Lee [210] for CH₄ and N₂ on a CMS-T3A carbon molecular sieve. Their measurements were performed at 303 K with pressures in the range of 0-1500 kPa with a volumetric-type apparatus. The effective sorption rate reported by them for these conditions ranged from $(0.05 \text{ to } 8) \times 10^{-5} \text{ s}^{-1}$ for CH₄ and $(2 \text{ to } 30) \times 10^{-4} \text{ s}^{-1}$ for N₂. More recently, Yang et. al. [199] reported the kinetics of pure CH₄ and N₂ on carbon molecular sieve CMS-131510 with pellet diameters of (0.11 to 0.13) cm using a magnetic suspension microbalance. The effective time constants reported were $(4.25 \text{ to } 6.71) \times 10^{-6} \text{ s}^{-1}$ for CH₄ at 343 K and $(1.44 \text{ to } 2.56) \times 10^{-4} \text{ s}^{-1}$ for N₂ at 303 K in the pressure range of (0 to 100) kPa. In addition, Hossain [202] measured the effective sorption rate for N₂ using volume

swing frequency response method at temperatures between (293 and 332) K on MSC-3K 172 with values ranging from $(4.9 \text{ to } 13.0) \times 10^{-4} \text{ s}^{-1}$, which fall in the range of our results for N_2 .

Table 3.5 Effective sorption rate of CH_4 and N_2 on carbon molecular sieve MSC-3K 172 obtained from the non-isothermal FD model

MSC-3K 172									
Methane					Nitrogen				
273.15 K					273.15 K				
P (kPa)	$ha/\rho_s c_s$ (s^{-1})	β	D/r^2 $\times 10^5 (\text{s}^{-1})$	$u(D/r^2)$ $\times 10^5 (\text{s}^{-1})$	P (kPa)	$ha/\rho_s c_s$ (s^{-1})	β	D/r^2 $\times 10^4 (\text{s}^{-1})$	$u(D/r^2)$ $\times 10^4 (\text{s}^{-1})$
23.55	0.010	79.915	0.95	0.36	24.21	0.012	0.67	3.61	0.01
40.21	0.014	69.746	1.94	0.38	43.35	0.011	0.88	4.25	0.02
63.82	0.012	32.067	2.49	0.39	63.02	0.010	0.66	4.85	0.02
82.52	0.012	39.470	2.76	0.75	82.94	0.010	0.54	5.41	0.02
102.20	0.012	12.481	2.78	0.39	101.7	0.012	0.21	5.57	0.02
303.15 K					303.15 K				
21.26	0.011	40.567	1.72	0.32	20.71	0.102	0.02	8.81	0.08
39.06	0.013	39.197	2.04	0.54	41.57	0.011	0.03	10.30	0.09
64.34	0.013	24.557	2.95	0.42	62.89	0.010	0.03	11.89	0.37
83.99	0.010	10.558	3.28	0.32	84.43	0.011	0.02	12.69	0.34
104.31	0.011	12.781	4.24	0.72	106.05	0.012	0.00	13.51	0.73

The effective sorption rates measured for CH_4 and N_2 on zeolite 4A are listed in Table 3.6, and at pressures from (20 to 120) kPa range from $(1.30 \text{ to } 1.48) \times 10^{-4} \text{ s}^{-1}$ for CH_4 and $(1.11 \text{ to } 1.15) \times 10^{-3} \text{ s}^{-1}$ for N_2 at 273 K, and from $(2.68 \text{ to } 3.12) \times 10^{-4} \text{ s}^{-1}$ for CH_4 and $(2.96 \text{ to } 3.16) \times 10^{-3} \text{ s}^{-1}$ for N_2 at 303 K. The values obtained in this work are similar to kinetic results reported for zeolite 4A in the work by Haq and Ruthven [213]. They used the chromatographic method to study the diffusion of N_2 and CH_4 on zeolite 4A at various temperatures and obtained sorption rates of $(2.95 \text{ to } 11.5) \times 10^{-3} \text{ s}^{-1}$ for N_2 at temperatures from (298 to 363) K and $(6.06 \text{ to } 59.2) \times 10^{-4} \text{ s}^{-1}$ for CH_4 at temperatures from (323 to 473) K. Mohr et al. [212] measured pure and binary gas adsorption kinetics of CH_4 and N_2 on zeolite 4A by the isotope exchange technique, and stated that the experiments were carried out isothermally.

They used the isothermal Fickian diffusion model to extract the “self-diffusivities” of CH₄ and N₂ which are effectively the sorption kinetics as we used in this work. They measured the diffusion of pure N₂ and pure CH₄ at three temperatures and obtained sorption rates of $3.0 \times 10^{-3} \text{ s}^{-1}$ for N₂ and $2.5 \times 10^{-4} \text{ s}^{-1}$ for CH₄ at 273 K. They also measured binary N₂/CH₄ diffusion at the same temperature and obtained values of $(2.34 \text{ to } 2.61) \times 10^{-4} \text{ s}^{-1}$ for CH₄ and $(2.86 \text{ to } 3.52) \times 10^{-3} \text{ s}^{-1}$ for N₂. These measured sorption rates are reasonably consistent with our results considering the adsorbents were from different manufacturers. No obvious pressure dependence in the effective sorption rate was observed by Mohr et al. [212] for either CH₄ or N₂.

Table 3.6 Effective sorption rate of CH₄ and N₂ on Zeolite 4A obtained from the non-isothermal FD model

Zeolite 4A									
Methane					Nitrogen				
273.15 K					273.15 K				
P (kPa)	$ha/\rho_s c_s$ (s ⁻¹)	β	$D/r^2 \times 10^4$ (s ⁻¹)	$u(D/r^2) \times 10^4$ (s ⁻¹)	P (kPa)	$ha/\rho_s c_s$ (s ⁻¹)	β	$D/r^2 \times 10^3$ (s ⁻¹)	$u(D/r^2) \times 10^3$ (s ⁻¹)
21.00	0.027	27.77	1.30	0.03	17.49	0.024	0.769	1.15	0.08
42.35	0.024	19.36	1.34	0.01	41.82	0.023	0.604	1.15	0.06
59.15	0.028	19.39	1.48	0.01	60.71	0.025	0.567	1.12	0.05
82.13	0.027	16.14	1.46	0.01	79.82	0.024	0.951	1.14	0.04
99.87	0.028	11.07	1.37	0.01	99.03	0.028	0.456	1.11	0.04
303.15 K					303.15 K				
18.13	0.024	5.692	2.68	0.02	18.92	0.025	0.233	3.16	0.38
43.68	0.024	5.009	3.29	0.02	39.45	0.024	0.298	3.14	0.50
63.30	0.029	5.520	3.01	0.02	60.28	0.026	0.304	3.12	0.47
82.93	0.029	5.221	3.11	0.02	81.27	0.026	0.338	2.98	0.45
102.72	0.028	4.244	3.12	0.03	102.37	0.028	0.385	2.96	0.50

The temperature dependence of the effective sorption rate for the four adsorbents is shown in Figure 3.8 with higher sorption rates observed at higher temperatures. The sorption rate of CH₄ for all the adsorbents showed a strong temperature dependence, as did the sorption rate of N₂ for the three

adsorbents measured at both temperatures (zeolite 13X, zeolite 4A and MSC-3K 172). The activation energies of CH₄ and N₂ diffusion were estimated using an Arrhenius type equation [211], and were found to be (10 – 20) kJ·mol⁻¹, which is comparable with the enthalpy of adsorption for these systems.

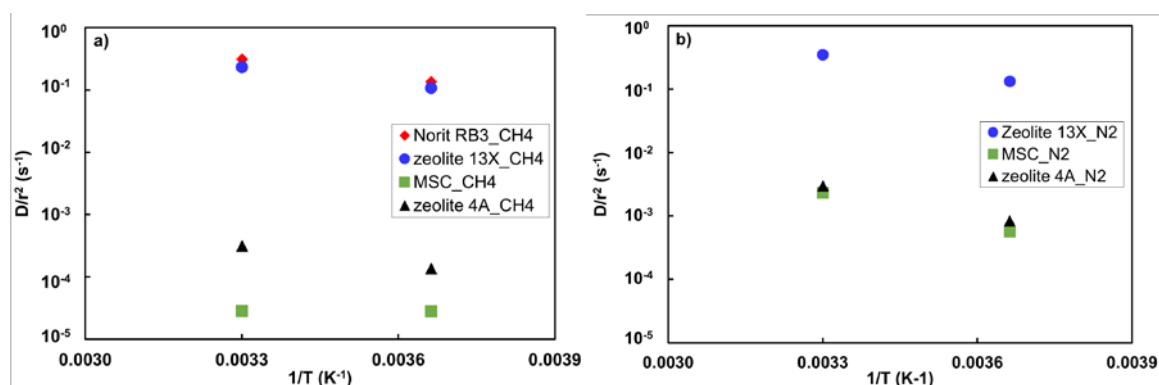


Figure 3.8 Temperature dependence of effective sorption rate

3.7 Conclusions

Equilibrium capacities and sorption kinetics for pure CH₄ and N₂ were measured for several widely-available adsorbents using a commercial volumetric system at pressures from (5 to 100) kPa and temperatures of (273 and 303) K. Literature values for the effective sorption rate, D/r^2 of both gases on these adsorbents varied in all cases by nearly an order of magnitude or more. Accurate measurements of the sorption rate in this work were found to require two key elements in the method and analysis of the dynamic uptake data. First, correction of the dynamic uptake data for the effects of gas expansion by calibrating the system response with helium was important to the accurate determination of the initial condition. Second, use of the non-isothermal Fickian diffusion model was found to be essential for reliable analysis of the ROA data, even for the small sample masses studied here. For adsorbents with small heat-to-mass transfer ratios (i.e. small values of α as defined in Eq (9)), such as activated carbon Norit RB3 and zeolite 13X, use of the isothermal linear driving force model results in apparent sorption rate values at least an order of magnitude too small. A small pressure dependence was observed only for the adsorbents MSC-3K 172 and zeolite 4A, with an increased (but still small) effective sorption rate observed at higher pressures. The sorption rates of both CH₄ and N₂ for all four adsorbents showed a clear temperature dependence with Arrhenius-type activation energies around (10 - 20) kJ·mol⁻¹.

For the adsorbents studied here, Norit RB3 and zeolite 13X have such fast and similar kinetics that any separation of N₂ and CH₄ would rely on their equilibrium selectivity for CH₄ over N₂. However, while

zeolite 4A and MSC-3K 172 are also methane selective at equilibrium, their uptake of N₂ is sufficiently faster than that of CH₄ that they are kinetically selective for N₂ over CH₄. In both cases the kinetic selectivity $\left(\beta_{N_2/CH_4} = \frac{1}{\alpha_{CH_4/N_2}} \sqrt{\frac{D_{N_2}}{D_{CH_4}}}\right)$ [234] is modest (1.4 to 2.2) at the conditions studied in this work, in comparison for example with those reported for Sr-UPRM-5 [235] (β_{N_2/CH_4} =25.42) and Sr-ETS-4 [90] (β_{N_2/CH_4} =21.62). However, both zeolite 4A and MSC-3K 172 are more readily available and lower in price than these specialised adsorbents, and might be engineered for N₂ removal from CH₄ rich gas streams using novel cycle designs such as dual reflux pressure swing adsorption [75].

3.8 Acknowledgements

The research was funded by Australian Research Council Industrial Transformation Training Centre for LNG Futures (Project IC150100019).

Chapter 4: Separation of Nitrogen from Methane Using A Transitional Metal Complex (TMC) Solution

4.1 Forward

In this chapter, in total 14 transition metal complexes (TMCs) have been rigorously screened based on the absorption performance of nitrogen, and the results have been summarized in Section 4.2. Among these 14 TMCs, the TMC named $K[Ru^{II}(EDTA)]$ in an aqueous solution gave the best performance. And thus, the main content (section 4.3 to 4.8) of this chapter will be based on this TMC and written in the format of a journal article which will be submitted after the submission of this thesis. Section 4.4 describes the motivations of developing alternative technologies to separate nitrogen from methane as introduced in Chapter 2, it can be skipped if Chapter 2 has been read.

4.2 Summary of the Screened TMC Solutions

All the 14 transitional metal complexes that have studied and the nitrogen absorption performance of their solutions are summarized in Figure 4.1 and Table 4.1 The measurement methods and the apparatus are the same as the ones used for $K[Ru^{II}(EDTA)]$ aqueous solution that are discussed in Section 4.5 and 4.6. The synthesis methods for TMC 1 to 4 and TMC 6 to 12 are essentially the same as the one for TMC 2 ($K[Ru^{II}(EDTA)]$) which is listed in Section A. 1.1. The synthesis method for TMC 14 is different and is summarised separately in Section A.2. TMC 4 and TMC 13 are used as received from the providers.

Based on the transitional metal center, these 14 TMC solutions can be classified into four groups: (1) Ru(II) based TMCs, (2) Fe(II) based TMCs, (3) V(II) and (III) based TMCs, and (4) Ag(I) based TMCs. The reasons for exploring Ru(II) based TMCs is that Ru^{II} is the first reported transitional metal center that can absorb nitrogen molecule and have been studied for the separation of nitrogen from methane.[29, 32, 236] Therefore, Ru-based TMCs are intensively studied in this work. Three types of ligands were chosen to support Ru, naming EDTA, HEDTA and NTA. EDTA (Ethylenediaminetetraacetic acid) is one of most common ligands which has been used in cosmetics[237], medicine[238, 239], and other industry[237, 240-242], and thus it is chosen as the first ligand to be studied. HEDTA has a very similar structure and properties as EDTA, but with one carboxylic group replaced by a hydroxyl group which leads to a slightly weaker affinity to cations and a higher solubility in aqueous solution. NTA (Nitrilotriacetic acid) is another type of commercially available ligands, which can support Ru or Fe to bind gas molecules, such as NO.[243]

The limitation of such Ru based TMC solution is that its annual global production of Ruthenium is only around 20 tonnes,[167] which is too small and confines the application of this solution from an industrial scale. Fe is located within the same chemical element group as Ru and has similar chemical properties to Ru. In addition, there are plenty of reported studies showing that Fe^{II} based TMCs can absorb N₂ molecules under various conditions. Therefore Fe-based TMCs have the potential to capture nitrogen from methane. However, most of the reported Fe-based TMCs are not soluble in aqueous solution,[105, 244-247] and only a few can dissolve in an aqueous solution which involves highly flammable phosphine ligands.[248] The Fe-based TMCs combined with low cost and safe ligands are desired and screened in this work. Except for EDTA, HEDTA and NTA, another two supporting ligands are studied as well: Lactate and Triethyl phosphate. In the molecule of Fe^{II}Lactate, the Fe^{II} is supported by two lactate anions and this structure has a potential to absorb σ donor and π acceptor. However, the solubility of this compound in aqueous solution is small. Akin to phosphine ligands, Triethyl phosphate tends to donate an electron to Fe^{II} as well. [249-251] More importantly, the easy availability and relatively less flammability of Triethyl phosphate drive us to study its combination with Fe^{II}.

The aqueous solutions of V^{II} or V^{III} based TMCs were reported having the ability to reduce nitrogen to ammonia[130, 252, 253] and thus are also selected in our study. Ag^I ion-exchanged zeolite can absorb nitrogen molecule after auto-reduction at elevated temperature,[254-256] and thus it is worthwhile to explore Ag^I centered TMC as well.

From Figure 4.1 it is clear that only three Ru-based TMCs can bind nitrogen under testing conditions of 30 °C and 0-3000 kPa. Ru^{II}[NTA] aqueous solution gives a slightly higher capacity of nitrogen than the pure solvent of water. Ru^{II}[HEDTA] aqueous solution gives around 5 times higher capacity of nitrogen. The TMC solution with the best performance is K[Ru^{II}(EDTA)] aqueous solution which gives 8 times higher capacity of nitrogen than the pure solvent does, and thus this TMC solution will be intensively studied in this work. The Fe, V and Ag based TMC solutions do not show enhancement of the nitrogen capacity, and thus will not be discussed in details in this work.

Table 4.1 Summary of the performance of the TMC solutions that have been studied in this project

Compound	Solvent	Concentration (mol/L)	T (°C)	P bar	Overall capacity	Baseline capacity	N ₂ absorption capacity	
					10 ⁻³ mol N ₂ / mol solution	10 ⁻³ mol N ₂ / mol solvent		
1	K[Ru ^{II} (EDTA)]	water	0.14	30	10	8.41E-04	9.75E-05	High (>8 times of baseline)
2	Ru ^{II} [HEDTA]	water	0.53	30	10	5.36E-04	1.13E-04	High (>5 times of baseline)
3	Ru ^{II} [NTA]	water	0.22	30	10	2.59E-04	1.23E-04	Moderate (2 times of baseline)
4	K[Fe ^{II} (EDTA)]	water	0.23	30	10	1.66E-04	1.03E-04	Low
5	Fe ^{II} [HEDTA]	water	0.39	30	10	2.18E-04	1.72E-04	Low
6	Fe ^{II} [NTA]	water	0.18	30	10	9.79E-05	9.22E-05	Low
7	Fe ^{II} Lactate	water	0.08	30	10	4.92E-05	1.09E-04	No
8	Fe(H) ₂ (P(OEt) ₃) ₄	TEG	0.45	30	10	9.70E-04	9.04E-04	No
9	VCl ₂	water	0.05	30	10	1.73E-05	1.03E-04	No
10	K[V ^{II} (EDTA)]	water	0.05	30	10	9.19E-05	9.22E-05	No
11	V ^{II} [HEDTA]	water	0.05	30	10	1.31E-04	1.24E-04	No
12	V ^{III} [EDTA]	water	0.12	30	17	1.18E-04	1.86E-04	No
13	V ^{III} [HEDTA]	water	0.15	30	10	1.03E-04	1.17E-04	No
14	Ag[EDTA]	water	0.10	30	5	4.39E-05	4.96E-05	No

EDTA: Ethylenediaminetetraacetic acid

HEDTA: N-(2-Hydroxyethyl)ethylenediamine-N,N',N'-triacetic acid

NTA: Nitritotriacetic acid

P(EtO)₃: Triethyl phosphate

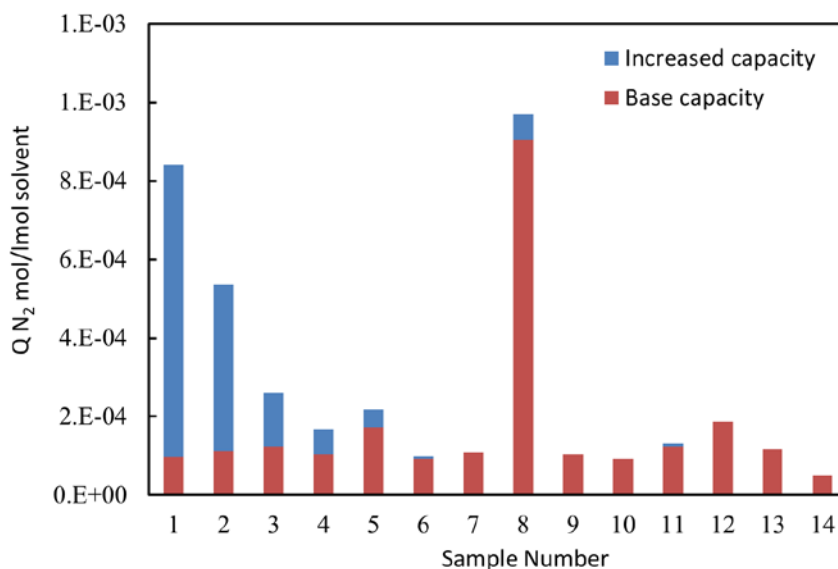


Figure 4.1 Summary of the performance of the TMC solutions studied in this project.

Red: the capacity of nitrogen in pure solvents (pure water or pure TEG); Blue: the increased capacities of nitrogen in TMC solutions

4.3 Abstract

Nitrogen is an inherent impurity in natural gas. Currently, the principle technology for the separation of nitrogen from natural gas is a cryogenic distillation, a highly energy-intensive process. A continuous recirculating absorption process operating at ambient temperature is a highly preferred alternative, which could be analogous to the stripping process for the removal of carbon dioxide (CO₂). The key step to developing such an absorption process for removal of nitrogen is to find a solution that can selectively and reversibly absorb nitrogen over methane under moderate conditions. Here, we report an aqueous solution consisting of a “task-specific” transition metal complex (TMC) which can meet such requirements. The TMC, K[Ru^{II}(EDTA)], was synthesized in this work and was characterized by elemental analysis and infrared spectroscopy (IR) to confirm its structure. The absorption equilibrium capacities of nitrogen in this aqueous TMC solution were measured using a custom-built volumetric apparatus at temperatures of 20 °C, 30 °C and 40 °C and at pressures ranging from (0 to 4000) kPa. The results showed that this Ru^{II} based TMC aqueous solution is able to selectively capture nitrogen

over methane with a specific capacity up to 0.5 mole nitrogen per mole of Ru^{II} – half of the stoichiometric amount. A desorption hysteresis was observed under the measured conditions, which suggests a combination of pressure swing and temperature swing process is required to recycle the TMC solution. The calculated absorption enthalpy of nitrogen (30-60 kJ/mol) was moderate compared to that of carbon dioxide (~90 kJ/mol) in aqueous monoethanolamine (MEA) solutions (30 wt %), indicating a viable regeneration energy requirement.

4.4 Introduction

Nitrogen is a ubiquitous impurity in natural gas that has no heating value but poses a safety concern in the transportation and storage of liquefied natural gas (LNG). While the product specification for LNG is no more than 1 mol % nitrogen [257], the inert nature and the similarity of its physical properties to methane (CH₄) make the separation of nitrogen from natural gas challenging[1]. Currently, cryogenic distillation is the most frequently used commercial technology for separating nitrogen from natural gas in LNG production[257]. This technology utilizes the difference in the boiling points of nitrogen and methane to separate the binary mixture at cryogenic temperatures, and has a track record of being economically viable (95-98 % methane recovery) but only for large-scale gas flow rates (>15 MMscfd) [1, 257]. However, the cryogenic process is energetically parasitic because a significant fraction of nitrogen gas needs to be cooled to cryogenic temperatures unnecessarily. Furthermore, the cryogenic Nitrogen Rejection Unit (NRU) is located at the end of the LNG production process. Consequently, the low-temperature gas processing facilities have to be designed to handle a greater volume of gas than if the nitrogen could have been removed at ambient temperature. Unfortunately, no other conventional technology that can effectively separate nitrogen under moderate temperature on a large scale exists.

Potential alternative technologies for nitrogen separation from natural gas include pressure swing adsorption (PSA), membranes, and absorption processes. PSA using molecular gate adsorbents has been demonstrated for nitrogen rejection in small scales. This process has been shown to be effective for nitrogen rejection (95 – 98% methane recovery) at low flow rates (2 - 15 MMscfd) [15]. However, the technology is still in its early stages of commercialization and struggles to accommodate high gas flow rates (>15 MMscfd). Also, PSA process typically employs multiple beds, requiring complicated switching controls between beds. Thus, the capital cost and operational cost remains high for large flow rate systems.[50]

Membrane technology has attracted much attention because of its ability to separate gas species without undergoing a phase change, its low energy input and labor intensity, and the relatively simple process with fewer pieces of moving parts [1, 50]. One successful implementation of this technology is the hydrogen (H_2) purification process using inorganic membranes. This success is mainly attributed to the significant difference in the physical properties of H_2 from that of other gas species, such as carbon monoxide (CO), carbon dioxide (CO_2) and nitrogen (N_2), which leads to a high H_2 selectivity.[258] However, the lack of nitrogen-selective membranes has hindered the applicability of membrane technology for nitrogen separation. Prior studies show that N_2/CH_4 selectivity of 15 is required to make this process economically viable.[50] Currently, the highest reported N_2/CH_4 selectivity is only around 8 from carbon molecular sieve membranes[12, 259] and 2-3 for polymer membranes.[50] Such N_2/CH_4 selectivity is too low to make this process economically feasible.

The absorption process for separation is based on the difference in the solubility of different gases in the circulating solvent. This process has been widely used in natural gas industry for carbon dioxide removal with various aqueous solutions of amine. If one could find a sufficiently robust and affordable nitrogen-selective solvent, it would be possible to deploy an absorption process for the nitrogen rejection from natural gas. However nitrogen is very stable and inert at room temperature and materials which are reactive with nitrogen are rare. Fortunately, certain transitional metal complexes (TMCs) have been reported to be able to bind nitrogen.[29-34, 128, 247, 260-262] Therein, the TMC functions in a similar way as the metal co-factor in the nitrogenase functions for nitrogen bio-fixation [24, 25, 109]. By dissolving the TMC in a solvent, the resulting solution will have the potential for nitrogen rejection. The binding of nitrogen with TMCs under various conditions has been previously studied, showing that nitrogen can bind to TMCs to a diverse extent depending on the type of the transition metal center and the type of its supporting ligands. [27, 34, 114, 128, 130, 131, 247, 262-264] However, most TMCs require an organic solvent, which has an inherently high solubility of methane, making the solution unsuitable for nitrogen-selective absorption. Therefore, a task-specific TMC that has the ability to reversibly bind nitrogen under moderate conditions ($T \sim 30^\circ C$, $P = 0-3000$ kPa) over methane in a proper solvent is desired. Here, a “proper solvent” should have (1) a high solubility for the TMCs achieve higher absorption capacity for nitrogen and low capacity for methane, (2) a low viscosity for better mass transfer properties, and (3) low volatility to avoid solvent loss. An absorption process based on such TMC solutions would be analogous to CO_2 capture with aqueous amine solutions, having the potential to remove high-concentration nitrogen from a large-scale natural gas flow rates (>30 MMscfd) with low capital and operational cost compared to the cryogenic process. Three groups of researchers have reported the possibility of utilizing this technology to

remove nitrogen from natural gas [27, 29-32, 139]. However, they did not provide either detailed solubility data with quantitative uncertainties or the absorption heat for nitrogen on corresponding TMC solutions, which are both essential for absorption process design.

In this work, a nitrogen-selective TMC has been synthesized and its aqueous solution has been prepared, in which water served as the solvent. The absorption equilibria of nitrogen in this TMC-water solution were measured using a custom-designed static solubility apparatus under different conditions to assess its potential application for the removal of nitrogen from natural gas. To validate this method, baseline experiments of nitrogen in the water were performed using the proposed solubility apparatus system, which would also serve as the loading baseline for possible nitrogen loading in TMC solutions. The absorption equilibria measurements of nitrogen in TMC solution was conducted over the temperature range of 20, 30 and 40 °C, and the pressure range of 100 kPa to 3000 kPa. From the overall nitrogen loading capacity, the specific absorption capacities of nitrogen were extracted and compared with the reported data. To estimate the regeneration cost, the enthalpy of absorption was extracted. A desorption study at 30 °C has also been conducted to characterize the reversibility of the binding of nitrogen in TMC. Moreover, we present a quantitative method to estimate the uncertainties of these absorption capacities.

4.5 Materials and Apparatus

4.5.1 Materials Preparation

Anhydrous toluene (99.9 wt%), magnesium metal (chips, 4-30 mesh, 99.98 wt%), ethylenediaminetetraacetic acid tri-potassium salt dihydrate ($K_3EDTA \cdot 2H_2O$, 98 wt%) and Ruthenium (III) Chloride Hydrate ($RuCl_3 \cdot xH_2O$) were purchased from Sigma-Aldrich (Australia) and used without further treatment. Hydrochloric acid aqueous solution (HCl, 37 vol%) and potassium hydroxide pellets (KOH, 85 wt%) were purchased from Sigma-Aldrich as well and dissolved in deionized (DI) water. The pH values of the solutions were measured by an Oakton pH 5+ Handheld Meter with a pH Probe (John Morris Scientific Pty Ltd). The nitrogen (N_2), methane (CH_4), and Argon (Ar) gases used in this work were purchased from Coregas with the following claimed purities: N_2 99.999 mol%, CH_4 99.995 mol%, and Ar 99.995 mol%.

The synthesis of $K[Ru^{III}(EDTA)(Cl)] \cdot 2H_2O$ was carried out according to a method reported in literature. [244, 265] A mass of 4.43 g (~ 0.01 mol) of $K_3EDTA \cdot 2H_2O$ was first placed in 20.00 mL of deionized water in a 100.00 mL glass beaker, and the resultant mixture was gently heated up on a hot plate until all solid dissolved to give a clear solution. A ruthenium (III) chloride water solution composed of 2.08 g

(~0.01 mol) $\text{RuCl}_3 \cdot x \text{H}_2\text{O}$ and 20.00 mL of DI water was added to the K_3EDTA solution while swirling the beaker. The pH value of this solution was adjusted and maintained in the range of 4-5 by adding 0.10 M KOH aqueous solution or 0.10 M HCl aqueous solution. The resulted mixture solution was gently boiled off at 140-145 °C until no more solid precipitated out. Then, another 40.00 mL DI water was added to the beaker to dissolve the solid precipitate fully. Following that, the water in the solution was evaporated again. This dissolving-precipitating process was carried out several times until the color of the solid precipitate became light yellow. The collected solid product was washed thoroughly with ice water until it was free of Ru^{III} ions (transparent residual solution without the brown color). Afterwards, the product was washed with ethanol twice, pre-dried using filter paper, and thoroughly dried in an oven at 80 °C for 10 hours. A mass of 3.52 g of dry $\text{K}[\text{Ru}^{\text{III}}(\text{EDTA})(\text{Cl})] \cdot 2\text{H}_2\text{O}$ was obtained with an overall yield of ~70% based on ruthenium mass balance calculation. A Spectrum One FT-IR Spectrometer (PerkinElmer) equipped with an attenuated total reflection (ATR) sampler and a deuterated triglycine sulfate (DTGS) detector was used to record the IR spectra of both the raw $\text{K}_3\text{EDTA} \cdot 2\text{H}_2\text{O}$ and the synthesized ruthenium complex. The synthesized $\text{K}[\text{Ru}^{\text{III}}(\text{EDTA})(\text{Cl})]$ gave IR peaks at 3410 (-OH), 1724 (free -COOH) and 1610 (coordinated $-\text{COO}^-$) cm^{-1} which were consistent with literature data [266-268]; while the raw $\text{K}_3\text{EDTA} \cdot 2\text{H}_2\text{O}$ gave IR peaks at 3410, 1634 and 1595 cm^{-1} . An Elementary Vario Macro was used to analyze the total carbon and nitrogen contents. The theoretical weight percentage (wt %) of carbon (C) and nitrogen (N) for $\text{K}[\text{Ru}^{\text{III}}(\text{EDTA})(\text{Cl})] \cdot 2\text{H}_2\text{O}$ were C 23.98 % and N 5.59 %; the measured values were C 24.90 %, N 5.82 %, which matched well with the theoretical values.

To prepare $\text{K}[\text{Ru}^{\text{II}}(\text{EDTA})]$ aqueous solution for N_2 absorption, 2.93 g dry $\text{K}[\text{Ru}^{\text{III}}(\text{EDTA})(\text{Cl})]$ was first dissolved in 58.86 g of degassed DI water; the pH of the solution was adjusted to 7 by adding 0.10 M KOH solution and 0.10 M HCl solution as requested with a total added mass of 0.95 g. This procedure was conducted in a glove box filled with argon. Next, 0.42 g of magnesium chips (an excess amount compared to that required for reducing Ru(III) due to the slow reaction of magnesium and the side reaction with water) was added to the resultant solution to reduce the Ru^{III} in $\text{K}[\text{Ru}^{\text{III}}(\text{EDTA})(\text{Cl})]$ to Ru^{II} [29] in the glovebox. The solution with the added magnesium was kept in the glove box for 10 hours before the nitrogen absorption measurements. The overall ruthenium element concentration in the solution was calculated to be 0.10 M by mass balance. The density of $\text{K}[\text{Ru}^{\text{II}}(\text{EDTA})]$ aqueous solution was obtained independently from volumetric methods using 5 mL and 10 mL volumetric flasks, which resulted in an averaged density of 1.02 g/mL.

To transfer the $\text{K}[\text{Ru}^{\text{II}}(\text{EDTA})]$ aqueous solution into an absorption cell (described in Section 4.4.2) for the nitrogen absorption measurements, 10-15 g of the solution was measured to a precision of 4

decimal places using a digital balance in the glove box. The absorption cell was then sealed with a stainless-steel lid on which a 1/8 inch VCR gland was sealed with PARAFILM (purchased from Sigma-Aldrich). The completely sealed absorption cell was transferred out from the glove box and quickly connected to the absorption apparatus through VCR fittings.

4.5.2 Apparatus

The sorption capacities of pure gasses in solutions were measured with a volumetric method using a custom-designed apparatus. A schematic diagram of the apparatus is shown in

Figure 4.2. Pure gases were first transferred to and stored in a syringe pump (ISCO 260 D) which has a maximum volume of 266.05 mL and is capable of delivering gas at constant pressure (up to 51,710 kPa) by volume displacement. Then, a required amount of gas was transferred from the syringe pump to the accumulation cell (AC). When the temperature and pressure of the gas in the accumulation cell became steady, the valve between the accumulation cell and solubility cell (SC) was opened to introduce the gas to the SC and start the sorption measurements. The AC, SC, and their associated pressure transmitters and platinum resistance thermometers were all located inside a well-insulated air bath with a temperature uniformity and stability of 0.1 °C. The tapered seal valves for controlling gas flow to or from the accumulation and solubility cell were also located inside the air bath, with their long shafts accessible from the outside of the air bath. The solubility cell is equipped with a mini magnetic stirrer to ensure excellent mixing of the solution and gas species after they were introduced into the cell. A vacuum pump is attached to the solubility measurement system to evacuate the system before introducing gas.

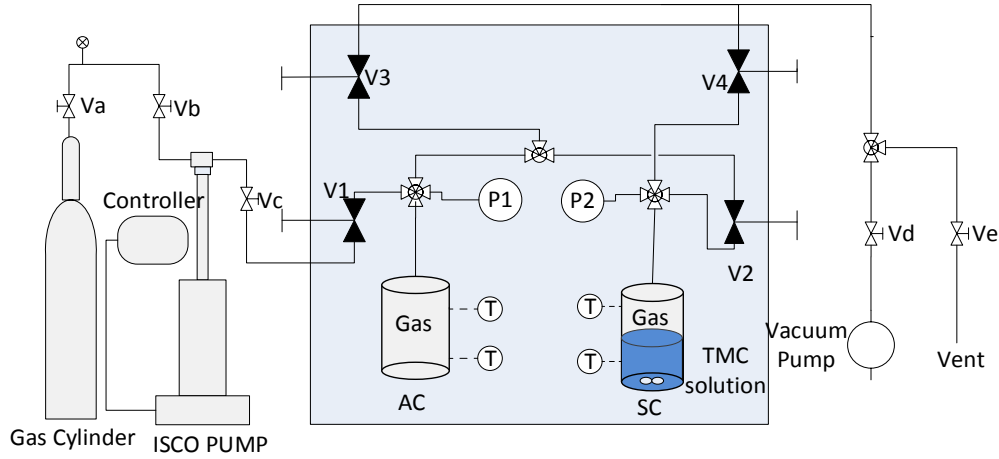


Figure 4.2 Schematic of the air-bath static gas solubility apparatus. V: valve; AC: Accumulation cell; SC: solubility cell. An ISCO pump is used to inject the gas component into the AC to a specific pressure. An air oven (shown as the blue rectangle) is used to control and maintain the experimental temperatures. Four high pressure needle valves are used to connect the two cells and the associated line, which are extended to outside of the oven. A valve (V_e) is used to depressurize the system and a vacuum pump is used to evacuate the system.

The Digiquartz® pressure transmitter for the accumulation cell has a full scale of 13,790 kPa and 0.01% uncertainty of reading over this range. The four 100 Ω platinum resistance thermometers on the accumulation cell and solubility cell were calibrated over the range of 0 °C to 70 °C with an uncertainty of 0.1 °C according to the International Temperature Scale of 1990 (ITS-90).

4.6 Analysis and Uncertainty

The volumetric method for measuring gas absorption is based on the transfer of a known amount of gas from the accumulation cell (AC) to the solubility cell (SC) that contains the TMC solution. Because the two cells and the associated lines constitute a closed system, the mass balance of the gas in the system can be expressed by Equation 4.1 below.

$$\begin{aligned}
 n_{\text{abs}} = & V_{\text{AC}}^{\text{G}} * \rho_{\text{AC}}^{\text{G}}(P_{i(\text{AC})}, T_{i(\text{AC})}) \\
 & + \left(V_{\text{SC}}^{\text{G}} - \frac{m^{\text{L}}}{\rho_{\text{SC}}^{\text{L}}(P_{i(\text{SC})}, T_{i(\text{SC})})} \right) \rho_{\text{SC}}^{\text{G}}(P_{i(\text{SC})}, T_{i(\text{SC})}) \\
 & - V_{\text{AC}}^{\text{G}} * \rho_{\text{AC}}^{\text{G}}(P_{f(\text{AC})}, T_{f(\text{AC})}) \\
 & - \left(V_{\text{SC}}^{\text{G}} - \frac{m^{\text{L}}}{\rho_{\text{SC}}^{\text{L}}(P_{f(\text{SC})}, T_{f(\text{SC})})} \right) \rho_{\text{SC}}^{\text{G}}(P_{f(\text{SC})}, T_{f(\text{SC})})
 \end{aligned}
 \tag{Equation 4.1}$$

Subscripts “abs”, “AC”, “SC”, “i” and “f” refer to absorbed gas, accumulation cell, solubility cell, initial value and final values, respectively; the superscripts “G” and “L” refer to gas phase and liquid phase, respectively; V is the measured volume; P is the measured pressure; T is the measured temperature; ρ^G is the molar gas density determined using an equation of state at the measured P and T ; ρ^L is the density of the solution, m^L is the mass of the solvent; and n_{abs} is the moles of gas absorbed in the solvent.

From Equation 4.1, it is evident that the accuracy of the measured absorption capacity relies on three factors: (1) the volumes of the accumulation section (V_{AC}) and the solubility section (V_{SC}), (2) the volume of the transition metal complex solution, and (3) the density of the gas phase at corresponding temperature and pressures. The V_{AC} and V_{SC} were measured via the displaced volume in the ISCO pump (Figure 4.2) at a constant pressure mode. Specifically, the ISCO pump and the associated line until V_1 was filled with nitrogen at 5000 kPa and operated in constant pressure mode at room temperature. A vacuum pump was used to evacuate the absorption apparatus, and then V_2 , V_3 and V_4 were closed to isolate AC from SC and the atmosphere. A certain amount of nitrogen was transferred from the ISCO pump into the AC by opening V_1 . After few minutes, the equilibrium of gas between the pump and the AC was reached and the decrease of volume in the ISCO pump was recorded as V_{AC} . Ten repeated measurements of the volume of AC were performed, and the averaged volume of V_{AC} was 33.10 ± 0.02 mL. The same method was used to measure V_{SC} , and the averaged volume was 32.59 ± 0.02 mL. The density of the TMC solution was measured twice using a 5 mL and a 10 mL volumetric measuring flasks at room temperature and pressure, and the obtained density was assumed to remain constant throughout the experiment conditions. The densities of the gas phase in the AC and SC at different pressures and temperatures were calculated by using equation of state (0.01% uncertainty at 0-77 °C and < 120 bar for the density of nitrogen; 0.03% uncertainty at < 77 °C and < 120 bar for density of methane) implemented in REFPROP software (version 9.1).[224, 269] The equilibrium temperatures were measured by the four 100 Ω platinum resistance thermometers, and the equilibrium pressures were measured by the two Digiquartz[®] pressure transmitters. By substituting these data into Equation 1, we can calculate the amount of gas absorbed by a particular TMC solution under a certain pressure and temperature.

The uncertainties for each component of the sorption measurements, $u(x)$, were calculated by taking the individual uncertainties associated with the static solubility apparatus into account, as listed in Table 4.2 below. We assumed that contributions of chemical and gas impurities to the estimated uncertainty were negligible.

Table 4.2 The uncertainties of the components associated with the static solubility apparatus

Component	Uncertainty, $u(x)$
Pressure transducer for AC	0.01% of reading
Pressure transducer for SC	0.01% of reading
Thermo-sensor for AC	0.1 °C
Thermo-sensor for SC	0.1 °C
Volume for AC	0.015 ml
Volume for SC	0.015 ml
Solution weight in a volumetric flask	0.0001 g
Solution volume in volumetric flask	0.1 ml
Solution weight in SC	0.0001 g
N ₂ gas phase density	0.01%[269]
CH ₄ gas phase density	0.03%[224]

The final uncertainties for capacities, $u(n_{abs})$, were propagated from these uncertainties according to the uncertainty propagation formula shown in Equation 4.2[230], where $u(x)$ denotes the standard uncertainty of a quantity x , under the assumption that the uncertainties for the parameters listed in Table 4.2 are independent of each other.

$$\begin{aligned}
 (u(n_{abs}))^2 = & \left[\left(\frac{\partial n_{abs}}{\partial V_{AC}^G} \right) u(V_{AC}^G) \right]^2 & \text{Equation 4.2} \\
 & + \left[\left(\frac{\partial n_{abs}}{\partial \rho_{AC}^G(P_{i(AC)}, T_{i(AC)})} \right) u(P \rho_{AC}^G(P_{i(AC)}, T_{i(AC)})) \right]^2 \\
 & + \left[\left(\frac{\partial n_{abs}}{\partial V_{SC}^G} \right) u(V_{SC}^G) \right]^2 + \left[\left(\frac{\partial n_{abs}}{\partial m^L} \right) u(m^L) \right]^2 \\
 & + \left[\left(\frac{\partial n_{abs}}{\partial \rho_{SC}^L(P_{i(SC)}, T_{i(SC)})} \right) u(\rho_{SC}^L(P_{i(SC)}, T_{i(SC)})) \right]^2 \\
 & + \left[\left(\frac{\partial n_{abs}}{\partial \rho_{SC}^G(P_{i(SC)}, T_{i(SC)})} \right) u(\rho_{SC}^G(P_{i(SC)}, T_{i(SC)})) \right]^2 \\
 & + \left[\left(\frac{\partial n_{abs}}{\partial \rho_{AC}^G(P_{f(AC)}, T_{f(AC)})} \right) u(\rho_{AC}^G(P_{f(AC)}, T_{f(AC)})) \right]^2 \\
 & + \left[\left(\frac{\partial n_{abs}}{\partial \rho_{SC}^L(P_{f(SC)}, T_{f(SC)})} \right) u(\rho_{SC}^L(P_{f(SC)}, T_{f(SC)})) \right]^2 + \\
 & \left[\left(\frac{\partial n_{abs}}{\partial \rho_{SC}^G(P_{f(SC)}, T_{f(SC)})} \right) u(\rho_{SC}^G(P_{f(SC)}, T_{f(SC)})) \right]^2
 \end{aligned}$$

The solution density, $u(\rho_{SC}^l(P_{i,f(SC)}, T_{i,f(SC)}))$, was derived from the solution volume and solution weight, which has taken into account the uncertainties of solution mass and solution volume as measured using the volumetric flask.

4.7 Results and Discussion

4.7.1 Validation Measurements

To validate the performance of the static gas solubility apparatus, control experiments of the absorption of nitrogen in water at 30 °C were conducted. Additionally, the amount of nitrogen absorbed in water serves as the baseline for experiments of nitrogen absorptions in aqueous TMC solutions. The experiment results of absorption of nitrogen in pure water were compared with the predicted results from MultiFlash (MF) as shown in Figure 4.3 and Table 4.3. The absolute deviations were below 1×10^{-3} mol/L within the measured pressure range from 0 to 3000 kPa, which was almost one order of magnitude smaller than the nitrogen absorption amount in water under the experimental conditions (30 °C, 500-3000 kPa). This indicates that the apparatus is reliable to provide accurate solubility data, even when the TMC solutions can only absorb nitrogen at a level of 1×10^{-3} mol/L.

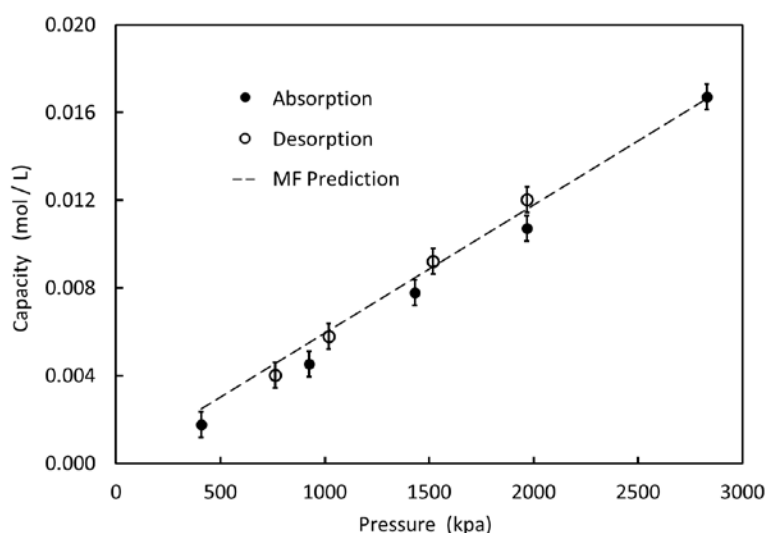


Figure 4.3 Isotherms of nitrogen loading in water at 30 °C. Absorption (●) and desorption (○) data were measured based on a cumulative method. The prediction data (dash line) were obtained from CPA-Infochem model implemented within MultiFlash (MF).[270]

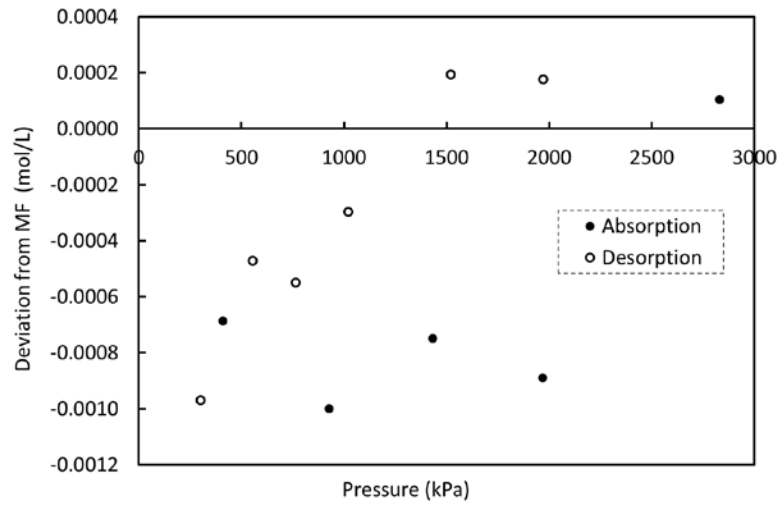


Figure 4.4 Deviations of absorption from CPA-Infochem model which is implemented within MultiFlash. The pressure range is from 0 kPa to 3000 kPa and the testing temperature is 30 °C.

Table 4.3 Loading capacities of nitrogen in water with the associated uncertainties and their deviations from MF. MF: multiflash.

	T	P	Capacity (MF)	Capacity	Uncertainty	Deviation from MF
			N ₂	N ₂		
	°C	kPa	10-Mar mol N ₂ / L water	10-Mar mol N ₂ / L solution	10-Mar mol N ₂ /L	10-Mar mol N ₂ /L
Absorption	30.6	407	2.44	1.75	0.58	-0.69
	30.6	925	5.53	4.53	1.36	-1.00
	30.5	1431	8.52	7.77	2.33	-0.75
	30.6	1967	11.60	10.71	3.5	-0.89
	30.6	2829	16.60	16.71	5.13	0.11
Desorption	30.6	1969	11.64	11.82	5.91	0.18
	30.5	1518	9.02	9.22	6.3	0.19
	30.6	1018	6.08	5.79	6.49	-0.30
	30.6	762	4.56	4.01	6.59	-0.55
	30.6	554	3.32	2.85	6.64	-0.47
	30.6	298	1.78	0.81	6.66	-0.97

4.7.2 Nitrogen Absorption in K[Ru^{II}(EDTA)] Aqueous Solution

4.7.2.1 Overall Absorption Isotherms

The binding of a nitrogen molecule to the vacant site of a TMC can be explained by a σ -donor/ π -acceptor coordination model. It involves a σ -donation of electrons from the nitrogen non-bonding electron pair to the metal vacant d_{z^2} or $d_{x^2-y^2}$ orbitals, and a back- π -donation of electrons from the filled metal d_{xz} , d_{yz} , or d_{xy} orbitals to the vacant π^* orbitals of nitrogen. However, the nitrogen molecule is both a poor σ -donor and a poor π -acceptor because of the stable nitrogen lone pair and the large highest occupied molecular orbital-lowest unoccupied molecular orbital (HOMO-LUMO) gap which reduce the overlap between the metal and nitrogen orbitals.[129, 131] Nevertheless, a large number of TMCs have been synthesized with the ability to bind nitrogen, although unfortunately most

of them require organic solvents.[128] Ruthenium is the first transition metal that has been shown to bind nitrogen in aqueous solutions,[236] which have been reported to bind nitrogen reversibly by tuning the nitrogen pressure.[29] A schematic of nitrogen binding to Ru(II) supported by the ligand of EDTA is shown in Figure 4.5 below.

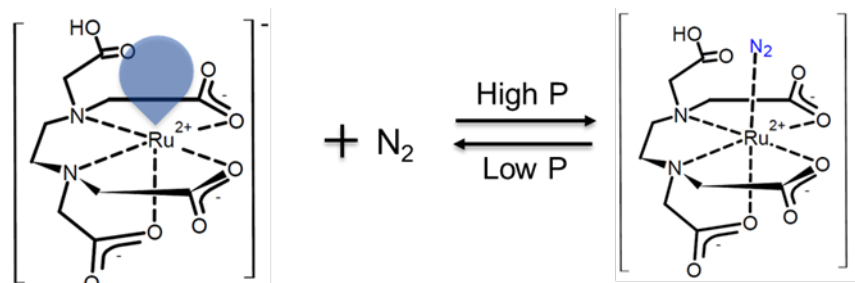


Figure 4.5 Schematic of nitrogen binding to $[\text{Ru}(\text{EDTA})]^-$. The shaded balloon stands for the vacant site of $[\text{Ru}(\text{EDTA})]^-$ which accepts nitrogen at high pressure; while at low pressure, nitrogen escapes from $[\text{Ru}(\text{EDTA})]^-$ and makes this nitrogen-binding process reversible.

In this work, the nitrogen loading capacities in ruthenium-based aqueous solution, $\text{K}[\text{Ru}^{\text{II}}(\text{EDTA})]$ water solution, were measured at 20 °C, 30 °C and 40 °C within the pressure range of 500 kPa to 4000 kPa. All experiments used the molar concentration of $\text{K}[\text{Ru}^{\text{II}}(\text{EDTA})]$ in the aqueous solution of 0.10 M. The absorption results under three temperatures are summarized in Figure 4.6, together with the baseline of nitrogen absorption capacities in pure water at corresponding temperatures. The uncertainty bars shown in the graph are calculated uncertainties using the error propagation method by taking into account every factor listed in Table 4.2 that might have affected the solubility measurement. Therefore, the final uncertainty is a conservative estimate. These results show that the $\text{K}[\text{Ru}^{\text{II}}(\text{EDTA})]$ water solutions have much higher absorption capacities than that of the solvent (water) at the same conditions, which confirms the reported N_2 -Ru chemisorption under elevated pressures [29, 32, 271, 272].

At 40 °C, the isotherm is almost linear and the nitrogen loading capacity reaches 0.04 mol N_2 /L solution at 3000 kPa. For the isotherm at 30 °C, a sharp uptake appears at around 1000 kPa, and the nitrogen loading capacity reaches 0.05 mol /L at 3000 kPa. At 20 °C, the isotherm gives a sharper uptake at even lower pressure (around 500 kPa) and eventually reaches 0.06 mol /L at 3000 kPa. Moreover, it is evident from Figure 4.6 that the nitrogen loading capacities increased with the decrease of solution temperature, indicating that the TMC- N_2 binding reaction is an exothermic reaction,[29] and that low temperatures are preferred to achieve high nitrogen loading capacities.

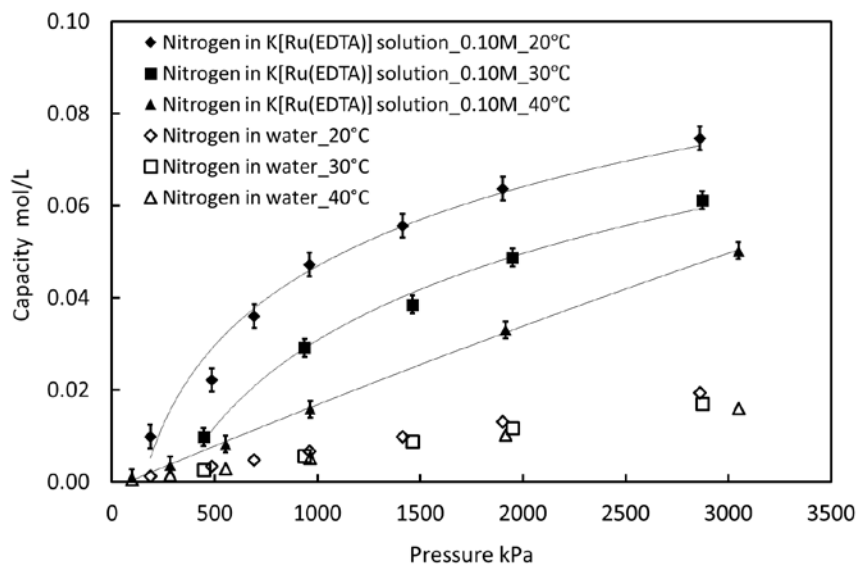


Figure 4.6 The loading capacities of nitrogen in pure water and $K[Ru^{II}(EDTA)]$ aqueous solutions at the pressure range of 0 to 3000 kPa and at the temperatures of 20, 30 and 40 °C. The capacities of nitrogen in pure water are shown with hollowed markers; the capacities of nitrogen in $K[Ru^{II}(EDTA)]$ aqueous solutions are shown with solid markers.

4.7.2.2 Specific Absorption Isotherms

The overall nitrogen loading capacity in the TMC solution depends on both the TMC concentration and the specific nitrogen absorption capacity. At a specific TMC concentration, increasing the specific nitrogen absorption capacity would lead to a higher overall nitrogen loading capacity. Stoichiometrically, each $K[Ru^{II}(EDTA)]$ molecule has one vacant site accepting incoming nitrogen and thus can only absorb one nitrogen molecule when saturated. The nitrogen specific absorption capacity measurements under different temperatures and pressures are critical to evaluate the overall nitrogen loading performance of a TMC solution. The nitrogen specific capacities per Ru^{II} with associated uncertainties at 20 °C, 30 °C and 40 °C are summarized in Figure 4.7 together with two sets of reported data at 21 °C and 41 °C [29]. It is apparent that the measured results are comparable to and aligned reasonably well with the literature results at 20 °C, but are slightly different at 40 °C [273]. The differences in nitrogen absorption capacity between our measurements and the literature data at 40°C are negligible in the low-pressure region and increase with pressure. This could be attributed to an experimental error in the estimated solution volume or density that could cause slope difference in the isotherms.

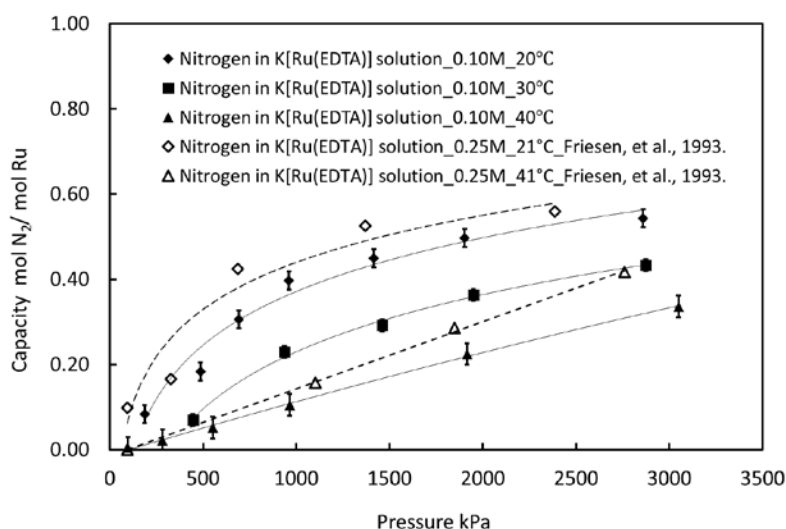


Figure 4.7 Comparison of the specific capacities of nitrogen on Ru^{II} solution in this work and in the literature for a pressure range from 0 kPa to 3000 kPa. Three temperatures (20, 30 and 40 °C) were studied in this work; while only two temperatures (20 and 40 °C) were reported by Friesen, et al., (1993). The results in this work are shown with the solid markers; the results reported in literatures were shown with hollow markers.

Although the prepared metal complex solutions in this work has lower concentrations (0.10M) than that stated in the literature (0.25M), it is clear that the specific nitrogen loading capacity per Ru^{II} was not affected. The measured data shows that the solution absorbs about 0.30 moles of nitrogen per mole of the Ru compound at 30 °C and 3000 kPa and about 0.45 moles of nitrogen per mole of the compound at 20 °C at a similar pressure. The N₂ specific capacity in this TMC solution at 20 °C is similar to that of CO₂ capture by monoethanolamine (MEA) solutions, in which CO₂ to MEA molar ratio in the CO₂-rich amine is about 0.3-0.5 [274-277]. Because the N₂ specific capacity in this TMC solution can reach a level comparable to the CO₂ specific capacity in MEA solution, which has been well-established on an industrial scale to separate CO₂ from natural gas, the N₂ specific capacity would not be a potential limiting factor of this K[Ru^{II}(EDTA)] aqueous solution to be scaled up for nitrogen removal from natural gas. However, the low overall capacity would require high TMC solution flowrate when using an absorption process to remove the same amount of nitrogen from natural gas. The low overall capacity is mainly due to the low concentration of this bulk TMC which lacks polar functional groups. The carboxyl groups of EDTA ligands are polar groups, but are still not able to provide K[Ru^{II}(EDTA)] with high enough solubility in the aqueous solution. This EDTA-based TMC concentration (0.1mol/L for our work, 0.25mol/L for the literature) is one order of magnitude smaller than the typical concentration of MEA aqueous solution that has been used in the natural gas sweetening plants

(ranging from 3-7mol/L[278]), which is a limitation of this TMC system for industrial absorption applications.

Until now, the only reported absorption process that selectively captures nitrogen from natural gas by a physical solvent uses liquid ammonia.[102] The Henry selectivity of nitrogen over CH₄ in liquid ammonia is around 0.25 and the nitrogen loading at 3400 kPa is around 0.1 mol/L.[101, 103, 104] In this study, the chemical solvent of K[Ru^{II}(EDTA)] aqueous solution gives a nitrogen over methane selectivity of around 2 at 3000 kPa with a nitrogen loading capacity of 0.06 mol/L, shown in Figure 4.8 and Table 4.4. Compared to the liquid ammonia, the K[Ru^{II}(EDTA)] aqueous solution gives a moderate nitrogen loading capacity but with much higher nitrogen over methane selectivity. In addition, the K[Ru^{II}(EDTA)] aqueous solution does not involve severe handling concerns which complicate the liquid ammonia process. The K[Ru^{II}(EDTA)] aqueous solution which chemically and selectively absorbs nitrogen, would seem to have a greater potential than the ammonia-based physical solvent to separate nitrogen from methane in terms selectivity and loading capacities of nitrogen up to 3000 kPa.

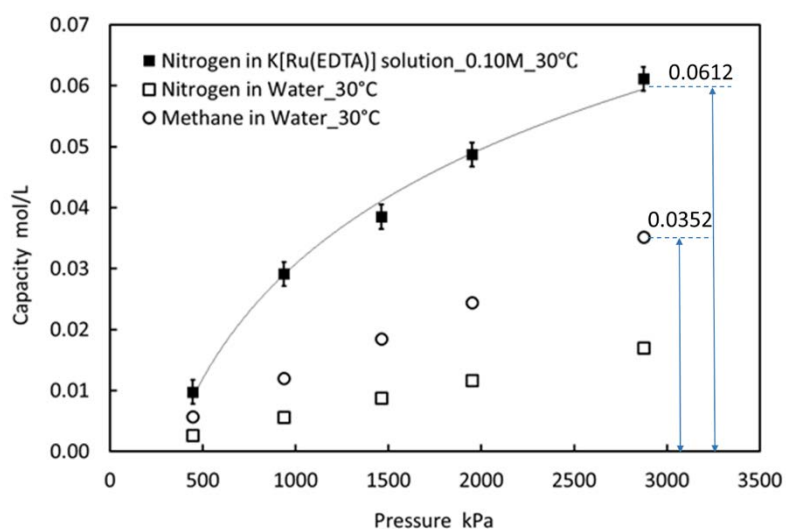


Figure 4.8 The comparison of the capacity of nitrogen in K[Ru^{II}(EDTA)] aqueous solution and the capacities of N₂ and CH₄ in pure water at the pressure range from 0 to 3000 kPa and at the temperature of 30 °C.

Table 4.4 The capacities and the specific capacities of nitrogen in K[Ru^{II}(EDTA)] aqueous solution and pure water at 20 °C, 30 °C and 40 °C.

T	P	Capacity	Capacity	Capacity	Uncertainty	Specific Capacity	Uncertainty
		(MF) CH ₄	(MF) N ₂	solution N ₂		solution N ₂	
°C	kPa	10 ⁻³ mol CH ₄ /	10 ⁻³ mol N ₂ /				
		L water	L water	L solution	L solution	mol Ru ^{II}	mol Ru ^{II}
20	187	2.83	1.28	9.83	0.89	83.77	7.53
20	486	7.41	3.38	22.13	2.57	183.87	21.27
20	692	10.50	4.81	35.98	4.63	305.48	39.15
20	961	14.58	6.69	47.22	7.10	397.14	59.55
20	1415	21.14	9.78	55.60	10.53	449.51	85.03
20	1902	28.02	13.08	63.69	15.06	497.12	117.40
20	2860	40.90	19.40	74.62	21.72	543.59	158.15
30	446	5.75	2.68	9.76	1.98	69.47	14.05
30	937	12.02	5.65	29.13	4.90	229.79	38.54
30	1461	18.52	8.78	38.52	8.88	291.41	67.12
30	1950	24.42	11.66	48.73	13.64	363.37	101.64
30	2873	35.15	17.02	61.15	20.13	433.26	142.56
40	98	0.96	0.46	0.95	0.58	4.86	3.00
40	283	3.08	1.46	3.71	1.83	22.14	10.94
40	552	6.13	2.93	8.18	4.00	51.77	25.32
40	964	10.71	5.14	15.82	7.51	105.04	49.81
40	1916	20.91	10.17	33.05	14.41	224.82	97.97
40	3049	32.41	16.03	50.21	25.07	336.09	167.70

4.7.2.3 Enthalpy of absorption

It is important to estimate the absorption enthalpy for gas separations, as this indicates the energy required to operate the process [279]. The enthalpy of the nitrogen absorption on Ru^{II} determined in

this work and also in the literature [29] are calculated using the following Gibbs-Helmholtz equation as shown in Equation 4.3, and the results are summarized in Figure 4.9.[229, 280]

$$\frac{\Delta_{abs}H}{R} = - \left(\frac{\partial \ln P}{\partial (1/T)} \right) \quad \text{Equation 4.3}$$

where R is the gas constant, R = 8.314 J /mol K

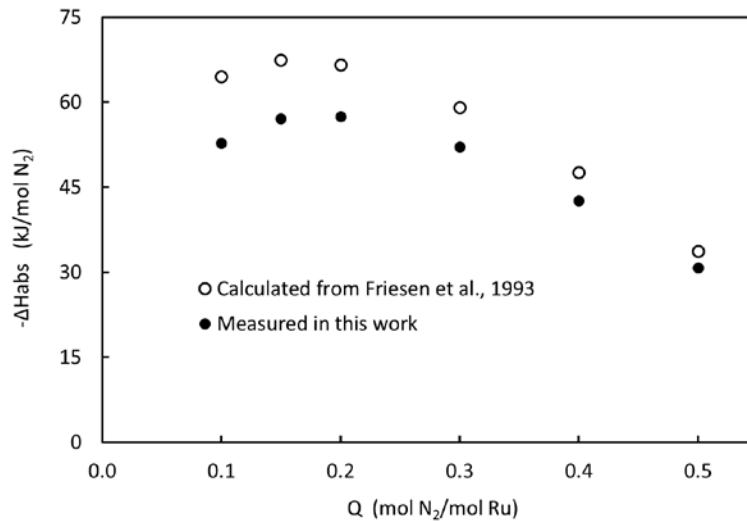


Figure 4.9 The absorption enthalpies of the nitrogen on Ru^{II} Calculated with Equation 4.3. The solid circle stands for the absorption enthalpy of nitrogen on Ru^{II} calculated from the absorption capacities measured in this work at three temperatures (20, 30 and 40 °C); the hollow circle stands for the absorption enthalpy of nitrogen on Ru^{II} calculated from the absorption capacities reported in literature at two temperatures (20 and 41 °C).[29, 32]

In the literature, the enthalpy of absorption was not reported directly; the results shown in this work were calculated from the N₂ specific capacity on Ru^{II} at 21 °C and 41 °C. The absorption enthalpy from this work and the calculated absorption enthalpy from literature matched with each other when the specific absorption capacity was higher than 0.3mol N₂/mol Ru^{II}. At lower absorption capacities in the region (< 0.3 mol N₂/mol Ru^{II}), the enthalpy calculated from the literature data was 7-15% higher than the one from this work. Both of the measured data in this work and the literature data show that the absorption enthalpy decreases with the increase of N₂ specific absorption capacity, which follows a similar trend of CO₂ absorption enthalpy in amine solutions [281]. However, at a specific N₂ absorption capacity of 0.2 mol N₂/mol Ru^{II}, a small peak appears with the highest absorption enthalpy of -67 kJ/mol N₂ for results calculated from the literature and -57 kJ/mol N₂ for this work. At a specific

capacity of 0.55 mol N₂/mol Ru^{II} (in this work, at 3000 kPa and 20 °C), the absorption enthalpy was estimated to be about -30 kJ/mol for both literature and this work. This absorption enthalpy is considered to be moderate when compared with the CO₂ scrubbing by aqueous MEA (30 wt %) solution (around -90kJ/mol) [275, 282]. Therefore, it would require less energy to regenerate the N₂ rich solution than that for CO₂ desorption.

Table 4.5 The absorption enthalpies of the nitrogen on Ru^{II}. [29, 32]

Specific capacity	ΔH kJ/mol	
	Measured in this work	Calculated from literature
0.10	52.78	64.56
0.15	57.12	67.41
0.20	57.45	66.55
0.30	52.16	59.12
0.40	42.66	47.58
0.50	30.82	33.73

4.7.2.4 Reversibility of the nitrogen sorption in K[Ru^{II}(EDTA)] aqueous solution

To evaluate the reversibility of nitrogen sorption in this K[Ru^{II}(EDTA)] aqueous solution, desorption tests were conducted at the moderate temperature of 30 °C over a pressure range of 0 to 3000 kPa. Figure 4.10 shows that the desorption capacities are higher than the absorption ones under the measured experimental conditions, giving a pronounced hysteresis loop which might indicate that the absorption of N₂ on Ru^{II} is not fully reversible. When the pressure decreased from 2075 kPa to 812 kPa, the specific capacity of nitrogen remains essentially the same, around 0.38 mol N₂/mol of Ru^{II}. Further decreasing the pressure to 112 kPa, the specific capacity of nitrogen reduces to 0.27 mol N₂/mol Ru^{II}, which indicates that the coordination bond between nitrogen and Ru^{II} is partially reversible under the experimental temperature. Similar hysteresis has been observed on other chemisorption systems as well, for example, the chemisorption of CO₂ on Li₈SiO₆ or amine-grafted zeolite 13 X, [283, 284], and the chemisorption of H₂ on carbon nanotubes. [285] The nitrogen specific

capacity reduces to 0.11 N₂/mol Ru^{II}, when the temperature increased from 30 °C to 60 °C, which suggests a combination of pressure swing and temperature swing is required to fully release nitrogen from Ru^{II}.

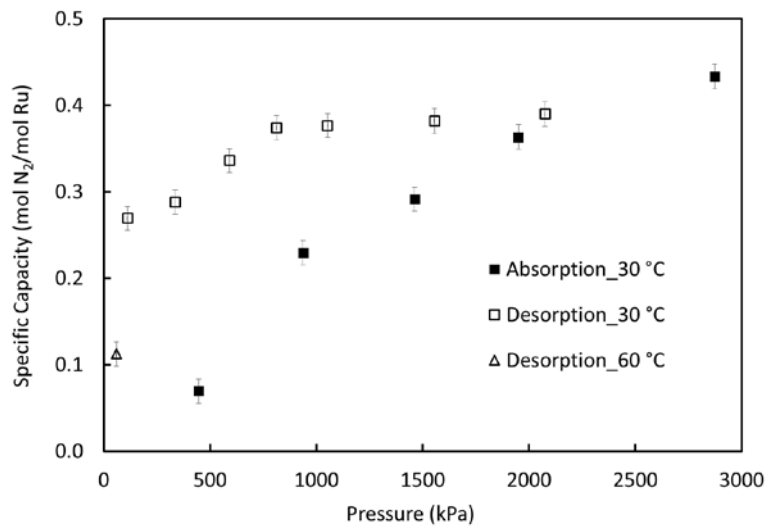


Figure 4.10 The absorption (■) and desorption (□_30 °C and Δ_60 °C) of nitrogen in K[Ru^{II}(EDTA)] aqueous solution at a pressure range from 0 to 3000 kPa and temperatures of 30 and 60 °C

Table 4.6 The absorption/desorption of nitrogen on Ru^{II} with an uncertainty of 0.01 mol N₂/mol Ru^{II}. At a pressure range from 0 to 3000 kPa and at temperatures of 30 °C and 60 °C.

	Temperature	Pressure	Specific Capacity of N ₂
	°C	kPa	mol N ₂ /mol Ru ^{II}
Absorption	29.5	446	0.07
	29.6	937	0.23
	29.6	1461	0.29
	29.6	1950	0.36
	29.5	2873	0.43
Desorption	29.5	2075	0.39
	29.5	1555	0.38
	29.4	1053	0.38
	29.4	812	0.37
	29.5	592	0.34
	30.1	336	0.29
	29.9	112	0.27
	59.0	143	0.11

4.8 Conclusion

A nitrogen-selective transition metal complex, K[Ru^{III}(EDTA)(Cl)] · 2H₂O, has been successfully synthesized in this work. The equilibrium capacities and their associated uncertainties of pure nitrogen absorption on this Ru^{II}-based TMC aqueous solution were measured experimentally at three different temperatures using a custom-built solubility apparatus. The apparatus has a capacity ranging from 1 x 10⁻³ to 1 mol/L and working conditions ranging from 20°C to 40°C and from 0 kPa to 5,000 kPa. The TMC aqueous solution showed the ability to selectively absorb nitrogen over methane, with an overall N₂ capacity of 6.11 x 10⁻² mol/L and a N₂/CH₄ selectivity of 2 at ~30°C and ~3000 kPa when the concentration of Ru^{II} is 0.1M. Our work shows that the specific equilibrium capacities of N₂ per Ru^{II} remain essentially constant at different TMC concentrations of 0.1 M and 0.25M, which means that both the overall N₂ capacity and N₂/CH₄ selectivity in this Ru^{II}-based TMC aqueous solution are proportional to the TMC concentration. The calculated absorption enthalpy (30-60 kJ/mol N₂) was relatively moderate compared to CO₂ absorption enthalpies in aqueous MEA (30 wt %) solution (around ~90 kJ/mol CO₂), meaning that this TMC aqueous solution would require less regeneration energy for N₂ scrubbing than what is required for the MEA aqueous solution used in CO₂ scrubbing.

An absorption/desorption hysteresis was observed which indicates that a combination of pressure and temperature swing process is required to generate the TMC solution. This work suggests that an absorption process which is analogous to the CO₂ removal by MEA aqueous solution could potentially be developed to reject nitrogen at moderate temperature and pressure. The continual development of better TMC solutions containing abundant transition metals that can reversibly bind and release nitrogen may meet the demand of the large-scale natural gas treatment in the future.

Chapter 5: Separation of Nitrogen from Natural Gas by Lithium Metal

5.1 Introduction

Lithium is the only metal and one of the few elements that can react with nitrogen directly, slowly at ambient temperatures and violently at elevated temperatures (>200 °C).[42, 46] Lithium reactions with different gas species, including nitrogen, have been studied for decades. The primary reason has been the safety hazards caused by lithium spill in fusion reactors where lithium functions as a tritium breeder blanket and as a coolant [174-177]. Recently, lithium has also been proposed as energy-carrier to store renewable energies.[178-180] In such a process, lithium reacts with carbon dioxide and nitrogen from the flue gas of power plants to generate electricity. The resulting Li_3N and Li_2CO_3 would go through a series of treatments to be converted to LiCl , and eventually to be electrolyzed back to lithium metal using seasonal renewable energy (solar energy or wind energy). In the 1990s, the application of lithium metal for gas separation was reported through a patent, where it was used to separate trace amounts of nitrogen and oxygen impurities from crude argon.[43] Due to the high reactivity of lithium with nitrogen at temperatures higher than its melting point (180.6 °C), it was claimed that the concentration of nitrogen in the Ar stream could be reduced to less than 1ppm.

Inspired by the Ar purification process, the use of lithium metal to separate nitrogen from natural gas is studied in this chapter. The separation process could be operated in a batch mode analogous to an adsorption process: lithium captures nitrogen from the natural gas stream to produce a pure methane stream; then, the resulted product of lithium nitride is regenerated back to lithium metal by various methods.[43, 46, 192, 286] Compared to conventional adsorbents that have been studied for the separation of nitrogen from natural gas, lithium metal shows significant advantages: (1) the theoretical uptake of for nitrogen on lithium is 24 mmol $\text{N}_2/\text{g Li}$ (calculated from the reaction equation shown in Equation 5.1), which is an order of magnitude higher than the best reported nitrogen-selective adsorbents.[1] This uptake is about twice of the update of H_2O on molecular sieves, which have been successfully employed in a liquefied natural gas (LNG) production plants.[287] This high separation performance suggests that a lithium-based process could be adapted to natural gas processing plants. (2) Moreover, lithium does not react with methane which implies that lithium could have a very large selectivity for nitrogen over methane allowing full methane recovery in principle. However, the reactions of lithium with nitrogen mentioned above are all at temperatures higher than the melting point of lithium metal (180.6 °C). Using melted lithium poses safety concerns in natural

gas processing plants, and it would be desirable to operate the reaction of lithium with nitrogen at a temperature below its melting point.



In the presence of moisture, lithium can react with nitrogen smoothly under ambient temperature [46, 181, 182]. However, the involvement of water could cause two potential concerns: (1) the reaction of lithium with water could become violent and uncontrollable when the water concentration in the stream is higher than a certain level (1 mol%)[186]; (2) lithium metal would be wasted if it reacts with water rather than with the target nitrogen.

When water is absent, the reaction of lithium with nitrogen is poorly understood. Some studies showed that in the absence of water moisture, lithium remains stable in dry nitrogen or even dry air for days at room temperature.[41, 184] Other studies have claimed that lithium can react with dry nitrogen under moderate temperatures.[42, 185, 186] Here, dry nitrogen usually means nitrogen that contains less than 10 ppm water content, but usually the nitrogen used contained <2 ppm water due to further dehydration by various methods.[182] It is interesting to note that reports of lithium metal not reacting with dry nitrogen under moderate temperatures have been the ones which were stored either in hydrocarbon solvents[41], or in Ar atmosphere (like the ones in this study). In contrast, when lithium metal that is freshly made in-situ, either by recrystallization from molten lithium,[42] vapor lithium,[185] or by electrodeposition,[186] it was reported to be able to react with dry nitrogen. The main difference between the freshly made lithium metal and the lithium that had been exposed to other compounds is that there are likely more active edge sites on the former rather than on the latter. Such active edge sites are expected to be rapidly consumed by materials surrounding them, and thus the lithium metal with an exposure/storage history has lost its activity toward dry nitrogen. Because the in-situ production of lithium involves high cost, it would be desirable to explore a simple and economical method to activate contaminated lithium metal so that it can react with dry nitrogen.

In this work, an activation method using moisture to activate the lithium metal was developed. Various techniques were used to investigate this method, and then a mechanism for the reaction of lithium with dry nitrogen was proposed. The uptakes of nitrogen and methane on different lithium samples were measured individually through pure fluid measurements and the reaction of enthalpies were extracted as well. A flow-based breakthrough study using a binary gas mixture of nitrogen and methane on lithium samples was conducted to assess the potential of lithium for separating of methane and nitrogen. Thermal regeneration of lithium metal from lithium nitride was considered

further by both thermodynamic calculation and experimental exploration. For the chemical loop process, as each step of it is already well-established, only an economic estimation was conducted.

Finally, to achieve a cyclic process, the lithium metal would need to be regenerated from lithium nitride if the whole process is to be cyclic. Various methods can potentially achieve the regeneration of lithium metal from lithium nitride: thermal decomposition of lithium nitride; chemical looping; direct electrolysis of lithium nitride. In principle, lithium can be recycled from the thermal decomposition of lithium nitride by increasing the temperature and by reducing the partial pressure of nitrogen. Several studies have shown that under certain conditions lithium metal can be regenerated from lithium nitride.[192, 288-290] The most recent study has experimentally produced lithium metal from lithium nitride at 382 °C with a partial pressure of nitrogen at 10^{-3} Pa. A rigorous study needs to be conducted to explore this approach to regenerate lithium metal. A chemical loop involving H₂O, CO₂ and HCl for recycling lithium from lithium nitride has been proposed.[46] However, there is no reported study estimating its economic feasibility in the application of separating nitrogen from natural gas. Electrolysis of lithium nitride to recycle lithium has been proposed due to the low electrical decomposition potential of lithium nitride.[43] However, no experimental exploration of this approach has been reported so far, and thus it was not included in this study.

5.2 Experimental Section

5.2.1 Materials and Preparation of Samples

5.2.1.1 Materials

In the experiments conducted with a scanning electron microscope & energy-dispersive X-ray spectroscopy (SEM-EDS), thermogravimetric analyzer (TGA) and the ASAP2020, the lithium metal was purchased from Sigma-Aldrich with a product number: 444456. The lithium was granular in shape with a size of 4-10 mesh. The purity of the lithium metal was 99 % trace metal basis. Each granule weighted 5-10 mg. The lithium samples which were used as received without any treatment were named as non-activated lithium samples; the lithium samples which were subsequently activated with water moisture were named as the pre-activated lithium samples.

In the experiments conducted with synchrotron X-ray diffraction (XRD) and binary gas mixture breakthrough, the lithium metal was also purchased from Sigma-Aldrich but with a different product number: 266000. The lithium was in a ribbon shape with a thickness of 1.5 mm. The purity of the lithium is 99.9 % trace metal basis. The reason to choose the lithium with a ribbon shape was that the

ribbon was easier to cut into the desired shapes needed for the apparatus compared to the lithium with granular shape. For example, in the mixture gas breakthrough experiment, the lithium samples needed to be cut into a shape with a thickness of 1.5 mm, a width of 2-3 mm and a length of 5 mm. In the synchrotron XRD experiments, the lithium metal needed to be scraped into tiny slices with a thickness less than 1mm, a width less than 1mm and a length of ~2mm. Except where specifically mentioned, all the operations that involved lithium metal were conducted in an Ar-filled glove box.

In the experiments conducted with the TGA, ASAP2020 and the binary gas mixture breakthrough apparatus, nitrogen, methane, helium and argon were purchased from Coregas Pty Ltd with a purity of 99.999 vol. %. The water moisture concentrations in these gases were all less than 2ppm. For the synchrotron XRD experiments, the nitrogen was purchased from BOC with a purity of 99.99% in which the water concentration was less than 10 ppm. The reason for choosing nitrogen with a higher water content was that the size of the lithium samples used in the study of synchrotron XRD was tiny, with a mass of only $1\text{e-}3$ mg. Thus it was not possible to activate the lithium samples with a separate pretreatment in water moisture. The nitrogen with a purity of 99.99% provided more moisture needed to activate the lithium samples in-situ.

5.2.1.2 Preparation of the Lithium Samples

The pre-activated lithium samples were prepared as shown in Figure 5.1. Two round bottom flasks, which were connected by a plastic tube (ID = 6.35 mm) with an isolation valve in between, were put into a glovebox which had been filled with Ar (Coregas, 99.999 vol. %). One of the flasks was filled with deionized water (DI) water, and the other was loaded with the non-activated lithium samples as received. When a black coating was observed on the surface of lithium metal, the lithium samples were ready for the nitridation reaction. The empirical time found necessary for the activation of lithium particles was around 8-12 hours.

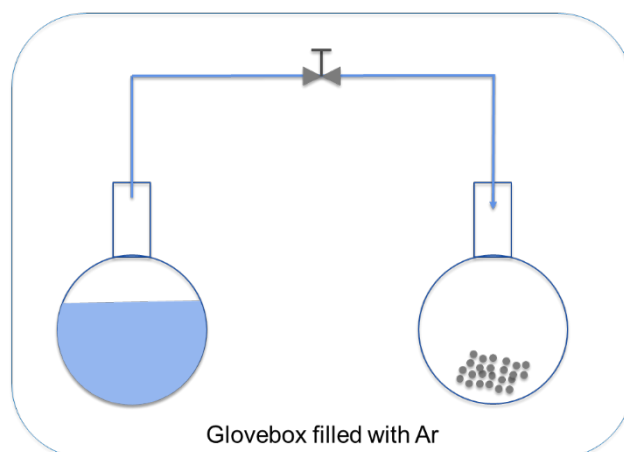


Figure 5.1 Schematic of the activation of lithium samples by water moisture. The two flasks were located in an Ar-filled glove box. An isolation valve was used to stop moisture flowing after the lithium samples were activated. The left flask was filled with DI water (light blue color); the right flask was filled with as received lithium samples (light grey color).

In the synchrotron XRD experiments, quartz capillaries with an outside diameter (OD) of 1mm were purchased from the Charlessupper Company. The lithium metal was first scraped into tiny slices and then these slices were loaded into quartz capillaries, which were sealed with wax. All the operations were conducted in a glove-box filled with Ar which contained less than 2 ppm of water moisture and less than 4 ppm of nitrogen. The capillaries were fixed to the beamline apparatus and connected to a nitrogen stream. In the flow-through cell experiments, the ends of the capillaries were cut off, so nitrogen could keep flowing through; in the static cell experiments, no further action was required.

5.2.2 Sample Characterisation

The surface morphology and surface chemical elemental compositions of the lithium metal and lithium nitride samples were studied with an SEM-EDS (FEI Verios XHR SEM). The in-situ identification of the transformation of crystalline phases from lithium to lithium nitride was measured by synchrotron powder X-ray diffraction (XRD) (powder diffraction beamline Australia Synchrotron). The surface area of the samples of lithium and lithium nitride were measured by ASAP2020, using a BET analysis at 77 K.

5.2.3 The Reaction of Lithium with Dry Nitrogen

The reactions of different lithium samples with dry nitrogen containing less than 2 ppm water were examined using a simultaneous thermogravimetric analyzer and differential scanning calorimeter (Model: SDT Q600). This Q600 can simultaneously measure the weight change and the true differential heat flow of the same sample with an operating temperature range from ambient to 1500 °C. The

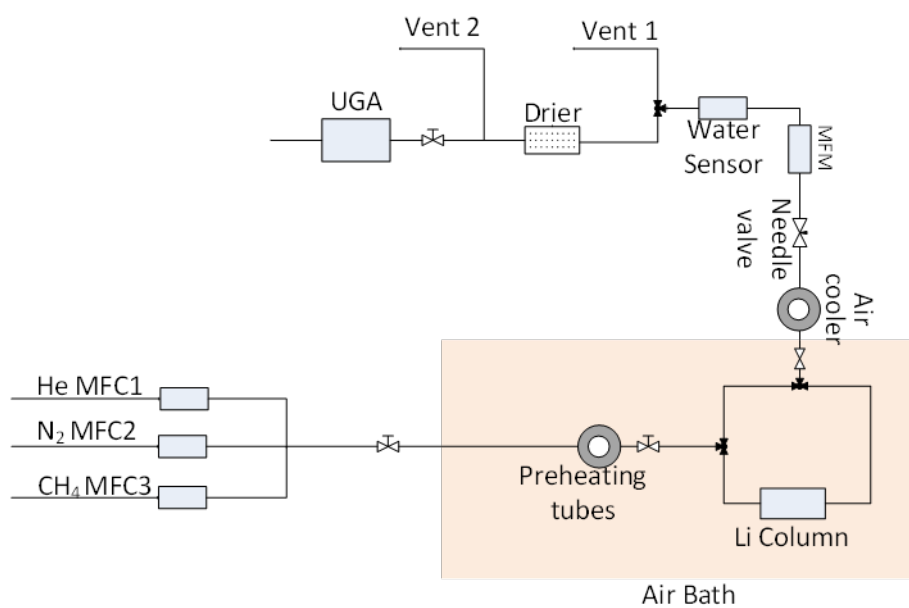
integrated mass flow controller with automatic gas switching enables the selection of two different streams with certain flow rates. In this study, the two gas streams were an Ar stream and a nitrogen or methane stream. Alumina sample crucibles with a capacity of 90 μL which is intended for operation from ambient to 1500°C were chosen for the experiments of nitrogen/methane uptake. The uptake of nitrogen and methane can be calculated from the weight change of the samples. The enthalpies of reaction can be directly extracted from the measured heat flow.

Equilibrium sorption isotherms of nitrogen and methane on lithium samples were measured using a volumetric method by a commercial Micromeritics ASAP 2020 as well to confirm the uptakes measured by the TGA. This ASAP2020 was also used to measure the surface areas of lithium samples and produced lithium nitride samples.

The regeneration of lithium from lithium nitride was examined with a thermogravimetric analyzer Q50 (TGA Q50). Alumina sample crucibles with a capacity of 90 μL , which is intended for operation at temperatures from ambient to 1500°C were chosen. A platinum crucible with a capacity of 100 μL which is intended for operation from ambient to 1000 °C was also used to conduct the lithium regeneration experiments.

5.2.4 Binary Gas Mixture Breakthrough

A custom-designed flow-through apparatus was built to measure lithium's ability to separate nitrogen from a binary gas mixture of nitrogen and methane, shown in Figure 5.2. The flow-through apparatus consists of a stainless steel column (130 mm long and 22.2 mm internal diameter) that can be packed with up to ~4 g of lithium samples. This column and its associated lines were located in an oven with a controllable temperature range from 30 to 400 °C. The feed gas was supplied through three mass flow controllers (MFCs) where a manual valve controls whether helium or a combination of methane and nitrogen flowed to the column. A pre-heating coil located before the lithium column inside the air oven was used to heat the gas mixture to the desired temperature. The effluent gas flow rate was measured by a mass flow meter (MFM), which was calibrated according to a method reported by Hofman et al.[291] The pressure of the system was adjusted by a needle valve located next to the MFC. The composition of effluent gas was measured by a universal gas analyzer (UGA) from Stanford Research Systems, which was calibrated in advance with a method described by Hofman et al.[291] A water sensor and a drier filled with silica gel were installed to prevent any high concentrations of water from being carried into the UGA.



(a)



(b)

Figure 5.2 Schematic (a) and picture (b) of the gas mixture breakthrough apparatus. The system was filled with helium before the binary gas mixture test and the helium flow rate was controlled by MFC-1. The binary gas mixture of nitrogen and methane was made by setting the flow rates with MFC-2 and MFC-3. The lithium-containing column and its associated lines were located in an air bath with a controllable temperature range from 30 to 400 °C. An air cooler was used to cool down the effluent gas stream to room temperature. An MFM was used to measure the effluent flow rate. The water sensor and the drier were used to avoid moisture entering the UGA. Two vents were installed to release the high pressure of the effluent before it was sent to UGA.

5.2.4.1 Experimental Procedure

The gas mixture breakthrough experiments were performed with similar method as described previously albeit using a differently sized column.[291, 292] In a typical run, the column was packed with samples of activated lithium metal inside an Ar-filled glovebox before being isolated under atmospheric pressure of Ar. After the column was connected back to the flow through apparatus, the flow of He was set to 30 sccm, allowing the system to be purged through the bypass line. After the air in the system was fully purged, the He flow was switched to the column to purge Ar out of the system. Then the binary mixture of nitrogen and methane with the desired composition was pre-mixed and sent to purge the system through the bypass line. At the same time the He flow was stopped by the manual valve. When the feed composition recorded by UGA became stable, the binary gas mixture was switched to go through the column. The UGA and the MFM were programmed to record the effluent compositions and the effluent flow rate respectively. When the effluent gas composition and the flow rate reached the original values of the feed gas, the reaction of lithium with nitrogen was considered to be finished.

5.2.4.2 The Determination of Uptake

The uptakes of nitrogen and methane on lithium metal were determined by an analysis of mass balance across the breakthrough column :

$$n_{i,accumulation} = n_{i,moles\ in} - n_{i,moles\ out} \quad \text{Equation 5.2}$$

$$n_{i,mole\ in} = \int_{t_0}^t F_0 y_{i,t_0} dt \quad \text{Equation 5.3}$$

$$n_{i,mole\ out} = \int_{t_0}^t F y_{i,t} dt \quad \text{Equation 5.4}$$

t_0 : the starting point of the experiment when the binary gas mixture was switched to the column

F_0 : the flowrate of the binary gas mixture (measured by MFM)

y_{i,t_0} : the composition of component i in feed gas (measured by UGA)

F : the total flowrate of effluent

$y_{i,t}$: the composition of component i at the time of t .

The accumulation of component i consists of two parts: the accumulation of component i in the gas phase in the system and the uptake of component i by lithium metal, as shown in Equation 5.5.

$$n_{i,accumulation} = \Delta n_i^{gas} + \Delta n_i^{uptake} \quad \text{Equation 5.5}$$

The uptake of component i on lithium metal can be calculated by combining Equation 5.2 to Equation 5.5, with the results shown in Equation 5.6.

$$\Delta n_i^{uptake} = \int_{t_0}^t F_0 y_{i,t_0} dt - \int_{t_0}^t F y_{i,t} dt - \Delta n_i^{gas} \quad \text{Equation 5.6}$$

The accumulation of component i in the gas phase in the system can be determined from the void volume of the system. As helium doesn't react with lithium, the displaced volume of helium equals the void volume of the system, as shown in Equation 5.7 and Equation 5.8.

$$\Delta n_{He} = \int_{t_0}^t F y_{He,t} dt \quad \text{Equation 5.7}$$

$$V_{void} = \frac{\Delta n_{He} R T_{initial}}{P_{initial}} \quad \text{Equation 5.8}$$

R : the gas constant

$y_{He,t}$: the He mole fraction in the effluent at time t

The needle valve used in the apparatus could not maintain the system pressure precisely, and consequently the initial pressure and the final pressure in the system would vary. Thus, the total moles

of the gas mixture and the accumulation of gas component i in the void space of the system at the final stage were calculated using Equation 5.9 and Equation 5.10, respectively.

$$n_{total,final}^{(gas)} = \frac{P_{final}V_{void}}{RT_{final}} = \Delta n_{He}^{(gas)} \frac{P_{final}}{P_{initial}} \frac{T_{initial}}{T_{final}} \quad \text{Equation 5.9}$$

$$\begin{aligned} n_{i,final}^{(gas)} &= n_{total,final}^{(gas)} y_{i,final} = \frac{P_{final}V_{void}}{RT_{final}} y_{i,final} \\ &= \Delta n_{He}^{(gas)} \frac{P_{final}}{P_{initial}} \frac{T_{initial}}{T_{final}} y_{i,final} \end{aligned} \quad \text{Equation 5.10}$$

Thus, the amount of component i that was loaded on the lithium sample can be calculated by Equation 5.11, as follows:

$$\Delta n_i^{uptake} = \int_{t_0}^t F_0 y_{i,0} dt - \int_{t_0}^t F y_i dt - \Delta n_{He}^{(gas)} \frac{P_{final}}{P_{initial}} \frac{T_{initial}}{T_{final}} y_i \quad \text{Equation 5.11}$$

The uptake of gas component i on lithium can then be calculated from Equation 5.12.

$$Q_i = \Delta n_i^{uptake} / m \quad \text{Equation 5.12}$$

5.3 The Results of the Reaction of Lithium with Nitrogen

5.3.1 Synchrotron XRD

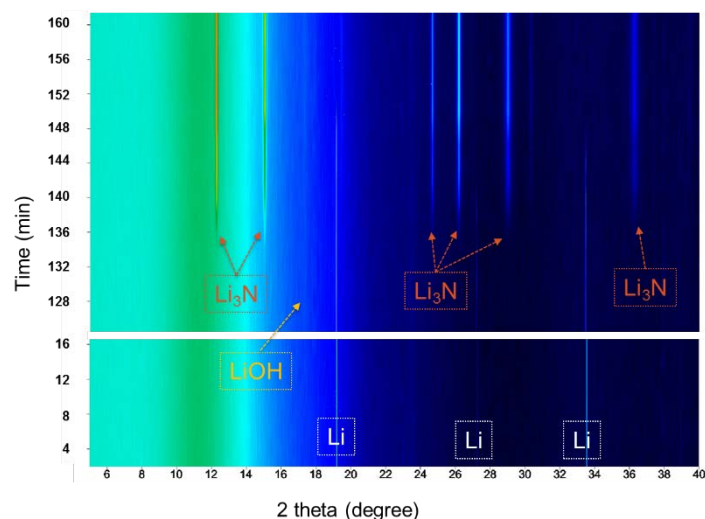
Measurements using the Synchrotron XRD apparatus have been conducted to obtain an in-situ characterization of the crystal switching from lithium metal to lithium nitride. A static cell and a flow-through were set up to control the lithium surface chemistry. In the static cell, there was only a trace amount of moisture (less than 10 ppm) in the nitrogen atmosphere, which meant that moisture would have less/slower effect to the surface of lithium metal. In the flow-through cell, as nitrogen gas was flowing through continuously, a larger amount of moisture passed across the surface of lithium metal, thus creating more active edge sites.

The results of the Synchrotron XRD measurements at 90 °C in atmospheric nitrogen from both the static and the flow through cell are shown in Figure 5.3 (a) and (b). For both cases, strong peaks of lithium at 19, 27.3, and 33.5 could be seen at the initial time of the experiment, which intensity faded over time as new peaks at 12.3, 15.1, 25.3, 26.1, 29.0, and 36.0, representing the presence of lithium

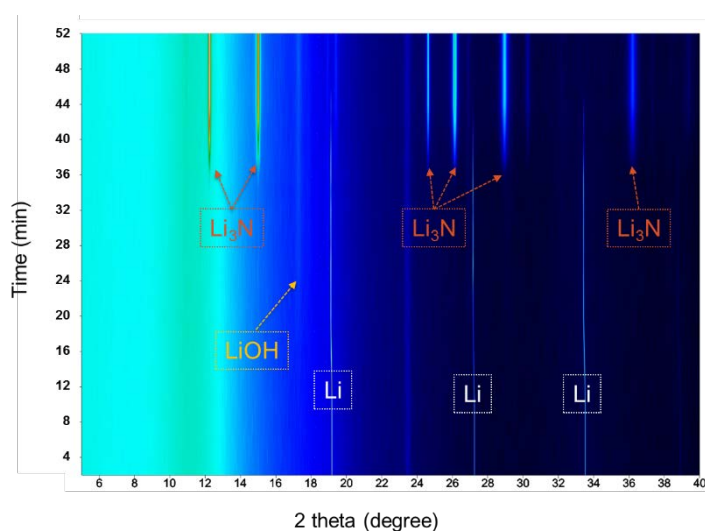
nitride, began forming. This observation proved that the phase transformation from lithium to lithium nitride did occur at 90°C and atmospheric nitrogen condition.

Additionally, the LiOH phase, with a peak at 17.3, was always detected before the formation of the lithium nitride phase in both cases. This might be due to the higher reactivity of water moisture to lithium and lithium nitride, which would result in the side product of LiOH. The side reaction of lithium and water moisture is beneficial, as it would result in creation and reveal of more active edge sites, which is crucial for the nitrogen and lithium reaction.

Lastly, although in both cells the phase transformation from lithium to lithium nitride was observed, the initiation times differed: 132 minutes for static cell and 32 minutes for the flowthrough cell. With more water moisture flowing across the surface of the lithium metal forming LiOH in the flow-through cell, more active edge sites could be created, which lead to a faster initiation time of the reaction between lithium and nitrogen.



(a) Static cell



(b) Flow through cell

Figure 5.3 In situ synchrotron XRD patterns of phase transformation from lithium to the lithium nitride in the atmosphere of nitrogen at 90 °C. (a) In situ synchrotron XRD patterns obtained from the static cell; (b) In situ synchrotron XRD patterns obtained from the flow-through cell with a nitrogen flowrate of 50 mL/min. The scanning angle (2 theta) is plotted as the x-axis; while the time of measurement is plotted as the y-axis. Characteristic peaks of lithium are located at 19, 27.3, and 33.5, while the characteristic peaks of lithium nitride are located at 12.3, 15.1, 25.3, 26.1, 29.0 and 36.0. Additionally, the main peak characteristic of LiOH is located at 17.3.

5.3.2 Thermogravimetric Measurements of Uptake

The uptakes of nitrogen and methane on different lithium samples were measured on the TGA (Model: SDT Q600). Both the non-activated and pre-activated lithium samples were heated at a temperature ramp rate of 10 °C/min and kept at 60 °C for 10 mins under an argon flow (100 ml/min) before the gas was switched to nitrogen or methane (100 ml/min). The uptakes were calculated from the weight change of the lithium samples and the reaction enthalpies were extracted from the measured heat flow directly.

The uptake of nitrogen and methane on non-activated and pre-activated lithium samples at 60 °C and 138 kPa are shown in Figure 5.4. There was no uptake of nitrogen observed on the non-activated lithium sample within the experimental time scale (200 mins). On the pre-activated lithium sample, significant uptake of nitrogen of 24 mmol/g was observed, which indicates a full conversion of lithium to lithium nitride. Similar to the results observed in the Synchrotron XRD measurements, an initial delay period was observed before the weight of the sample started to increase. Moreover, the initiation period was of around 45 minutes – which is within the same magnitude as the results from Synchrotron XRD studies. The uptakes of methane on both non-activated and pre-activated lithium samples were also measured. Negligible uptake of methane were observed, indicating a significantly large selectivity of nitrogen over methane on lithium metal.

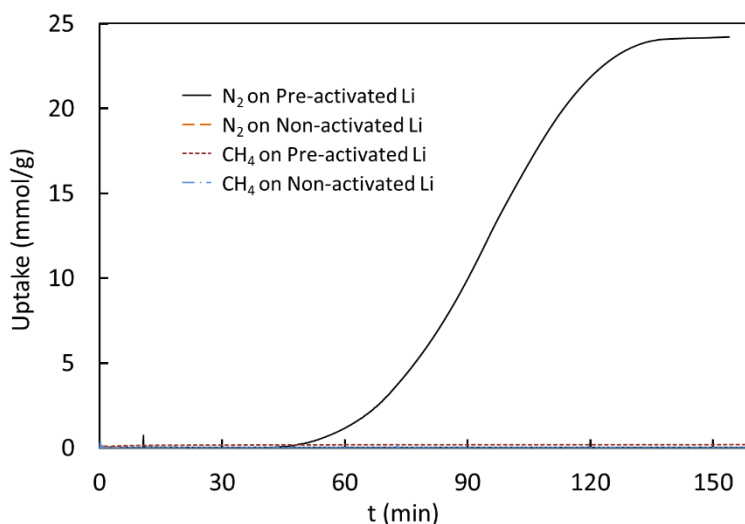


Figure 5.4 The uptakes of nitrogen and methane as a function of time on both non-activated and pre-activated lithium samples at 60°C and 138 kPa.

To obtain the enthalpy of the reaction, the heat flows of the reactions of both non-activated lithium and pre-activated lithium with nitrogen under at 60 °C are measured and shown in Figure 5.5. Negligible heat flow was observed for the non-activated lithium, while significant heat flow was

detected for the reaction of pre-activated lithium with nitrogen. From the heat flow curves, the enthalpy of reaction of the pre-activated lithium with nitrogen at 60 °C and 138 kPa was extracted. The resulting enthalpy from the heat flow curves was 55 kJ/mol (lithium), which is consistent with the theoretical value of 54 kJ/mol.[46]

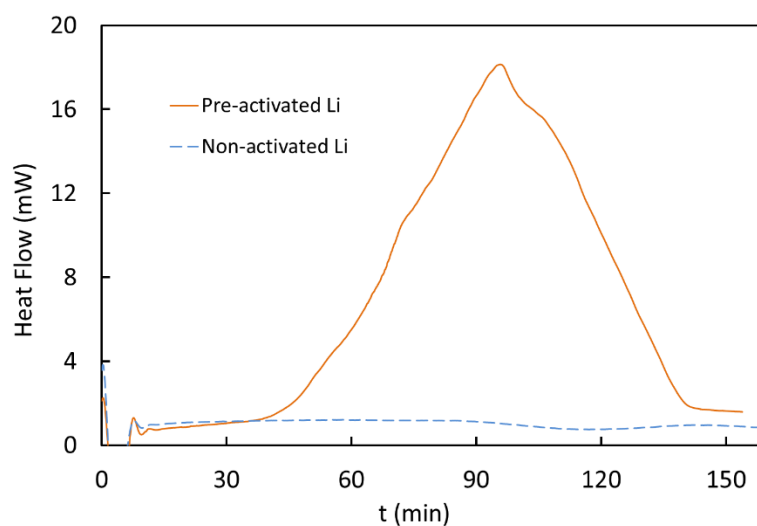


Figure 5.5 Heat flow of the reactions of different lithium samples with nitrogen at the experimental temperature of 60 °C and pressure of 138 kPa. The integrated enthalpy for the reaction of pre-activated lithium with nitrogen is 55 kJ/mol (Li); the integrated enthalpy of the reaction of non-activated lithium with nitrogen is 0 kJ/mol (Li).

5.3.3 ASAP2020 Measurements of Uptake

The uptakes of nitrogen and methane on the non-activated and pre-activated lithium samples at 60°C were also measured using the ASAP2020 apparatus via the static volumetric method, and the results are shown in Figure 5.6. The reaction of the pre-activated lithium sample with nitrogen started when the pressure reached 33 kPa at 60 °C, and continued until the uptake of nitrogen on the pre-activated lithium eventually reached 21.5 mmol/g. The color of the sample changed from metallic luster to dark purple, which indicates the formation of lithium nitride. Titration with an aqueous solution of the produced lithium nitride showed an alkaline level consistent with the amount of lithium reacted with nitrogen (1 pellet of lithium nitride fully dissociate in 160 ml cold water, giving pH of 11.8, equivalent to 0.006719 g lithium). There was no uptake of nitrogen on non-activated lithium across the experimental pressure up to 100 kPa. There were no observed uptakes of methane on either pre-

activated or non-activated lithium samples, which are consistent with the observation in the SDT Q600 measurements.

The BET analysis at 77 K for both the pre-activated lithium sample and the produced lithium nitride were conducted to measure the surface areas. The surface area of pre-activated lithium was too small to be detected; the surface area of the produced lithium nitride was estimated to be 1.37 m²/g.

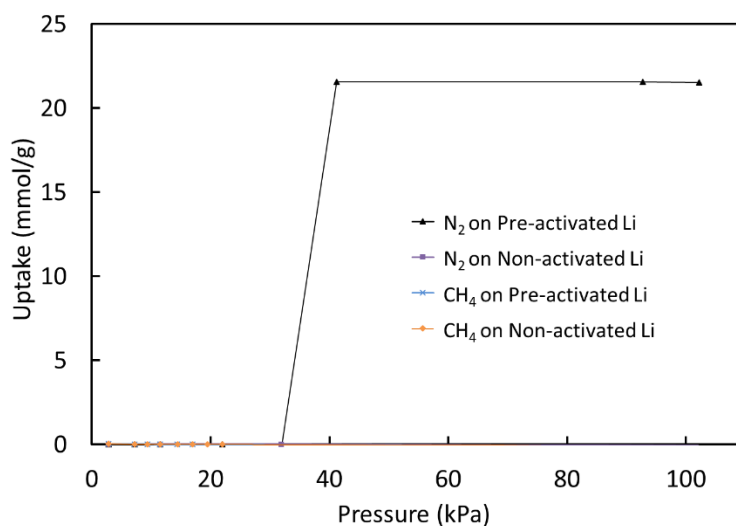


Figure 5.6 The uptakes of nitrogen and methane on non-activated and pre-activated lithium samples at 60°C and at a pressure range of 0 to 100 kPa

5.3.4 SEM-EDS Characterisation

The SEM images of the lithium sample as-received and after being exposed to air for 5 minutes are shown in Figure 5.7. The areas marked by the dotted circles in the two images confirmed that these two images were taken on the same location of the same lithium sample. Before exposed to air, the as-received lithium sample already contains some grains, as shown on the top and bottom parts of Figure 5.7 (a). The EDS results (covering the entire image area) gave an oxygen content of 85.9 wt %, which suggests that the main impurities on the surface of the as-received lithium sample were oxygen-contained impurities. Because the EDS detector was not able to detect the element of lithium, the content of elements reported excluded the evident presence of lithium. After being exposed to air for 5 minutes, more grains appeared on the sample surface, as shown prominently in the center area of Figure 5.7 (b). The oxygen content increased to 94.5 wt %, which suggests that the newly appeared grains mainly consisted of oxygen. No nitrogen element was detected by EDS, which indicate that no detectable lithium nitride had been formed. These observations are consistent with the reported

studies which stated that upon exposure to air, the resulting products formed on the surface of lithium metal would be LiOH, and not lithium nitride.[42, 44]

Another important observation is that the grains which have been previously existed remained in essentially the same morphology before and after being exposed to air for 5 minutes. It suggests that such areas are relatively inert to air, which explains the inert nature of as received lithium sample to dry nitrogen at moderate temperatures. In comparison, the surrounding area of the newly formed grains is expected to contain active edge sites which can initiate the reaction of activated lithium with dry nitrogen.

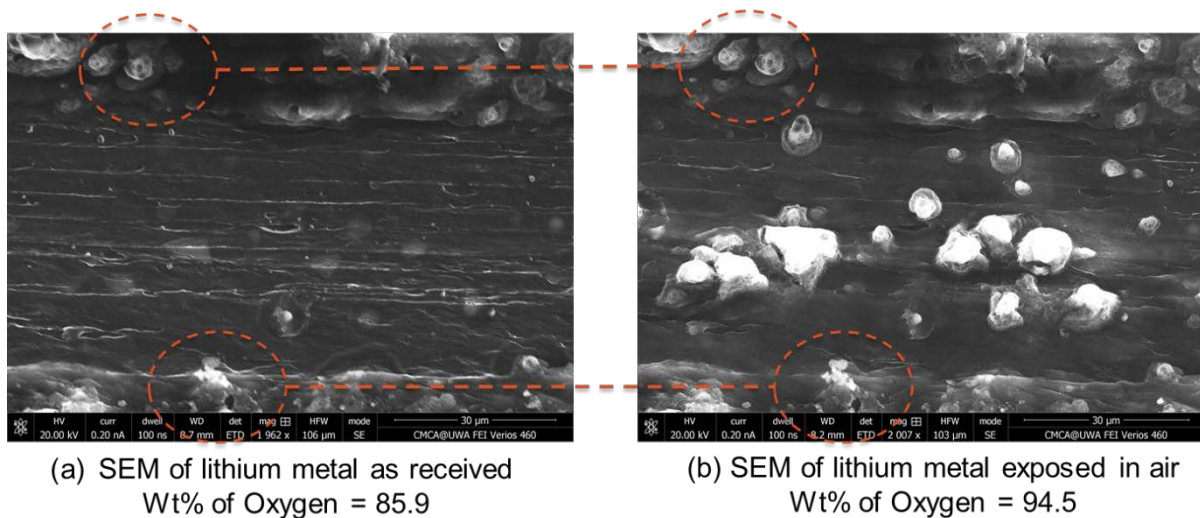
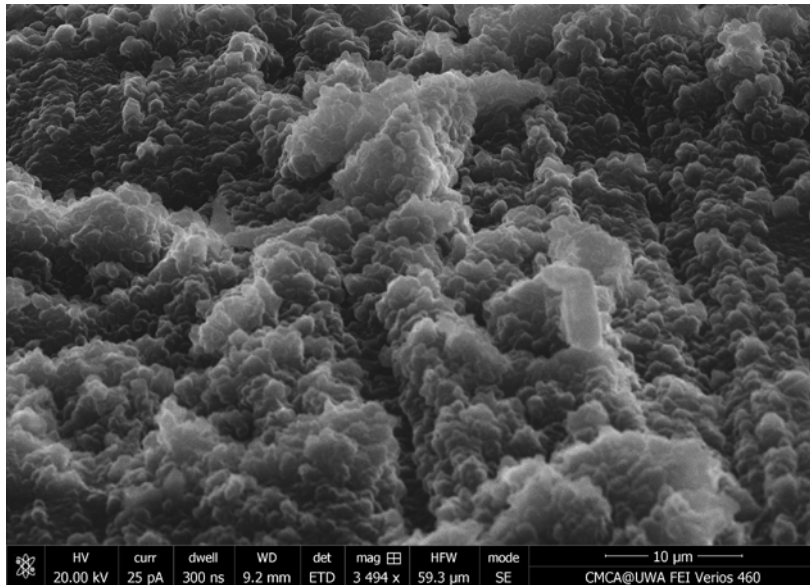


Figure 5.7 SEM and EDS of (a) as received lithium sample and (b) air-exposed lithium sample. The circled area confirms the SEM pictures are taken at the same position of the lithium metal. The oxygen content on the surface of lithium increased from 85.9 wt% to 94.5 wt% after exposure to air for 5 minutes.

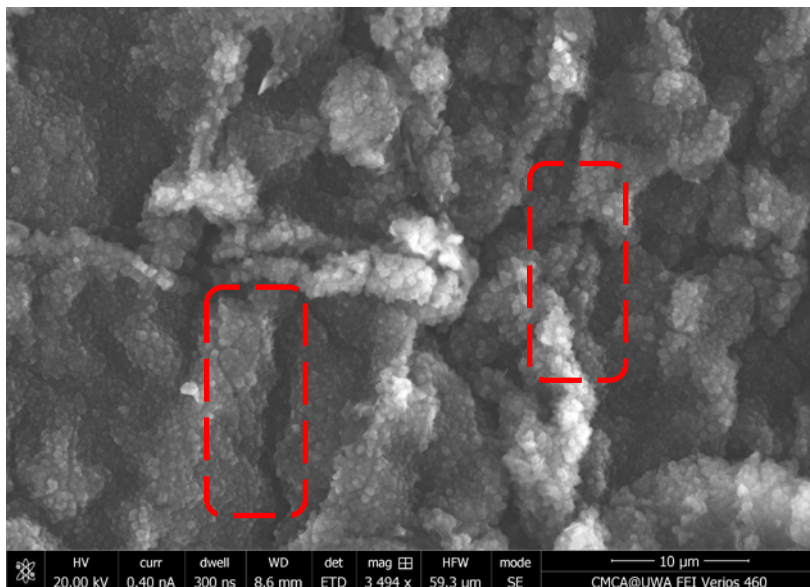
The surface morphologies of the pre-activated lithium sample and the produced lithium nitride are shown in Figure 5.8. Compared to the surface of pre-activated lithium, the surface of the produced lithium nitride has apparent cracks (marked with red squares). This is consistent with the results of surface area measurement using ASAP2020, which state that lithium nitride has higher surface area than lithium metal. Such cracks are believed to provide channels for the diffusion of nitrogen. The formation of such cracks is due to the low Pilling-Bedworth ratio (PB ratio) of lithium nitride over lithium (Pilling-Bedworth ratio = 0.64).[42] Here, the Pilling-Bedworth Ratio stands for the ratio of the volume of the elementary cell of lithium nitride to the volume of the elementary cell of lithium metal,

which indicates whether the coated lithium compound can form a passivation layer on the lithium metal:[41]

- PB ratio < 1: the coating layer is likely broken to form cracks and provides no protective effect;
- 1 < PB ratio < 2: the coating layer is a passivating layer and provides a protective effect;
- PB ratio > 2: the coating layer is likely to chip off and provides no protective effect.



(a) Air-exposed lithium



(b) Produced Li_3N from lithium and nitrogen

Figure 5.8 Surface morphologies of (a) pre-activated lithium and (b) produced lithium nitride. The circled area on the surface of lithium nitride are cracks on lithium nitride, which provide the channels for the diffusion of nitrogen molecules.

5.3.5 Discussion

The observed difference in the uptakes of nitrogen on non-activated and pre-activated lithium metal prompted us to consider the role of water moisture in the reaction. It has been reported that freshly made lithium with active edge sites can react with dry nitrogen under moderate temperatures.[42, 185, 186] However, freshly made metal is too expensive to produce in-situ and impractical to store. Additionally, the active edge sites on freshly made lithium is easily lost through reactions with various species during storage. As a result, it is not practical to use freshly made lithium for nitridation reaction in large-scale applications. When the moisture is present in the nitrogen stream or when lithium has been pre-activated in moisture, the lithium surface is covered by a layer of “black coating”. [41, 42] “The black coating” is the amorphous form of lithium metal covered by a thin and transparent coating of lithium hydroxide.[42] When exposed to dry nitrogen, the amorphous lithium metal regains the ability to react with the dry nitrogen at low temperatures. The role of water moisture is to create an amorphous layer on the surface of lithium metal, which produces active edge sites.[41] The presence of water moisture disrupts the normal body-centered cubic structure of lithium metal, and yields to additional active edge sites due to the reaction between lithium and water. Such active edge sites are similar to the ones on the freshly made lithium metal, and they are the key for the initiation of the reaction of lithium metal.

Continuous flow while exposing the lithium metal to an atmosphere of water moisture is also crucial to stimulate the initiation process. In the synchrotron study, the surface of the lithium in the flow through cell was exposed to more moisture compared to the one in the static cell, resulting in a higher number of active edge sites, which led to the faster initiation time. The role of active edge sites was also confirmed with the results from the other two characterization methods: TGA and ASAP2020. The results from TGA experiments confirmed the importance of active edge sites, as the non-activated lithium, which is lacking active edge sites, remained inert to dry nitrogen within the experimental time scale (~200 mins) at the set temperature of 60 °C, while the pre-activated lithium samples, having freshly revealed additional active sites, reacted with dry nitrogen readily and take in nitrogen gas to its theoretical uptake value. Similarly, the results from ASAP 2020 showed that while the pre-activated lithium sample uptook nitrogen, there was a negligible amount of nitrogen uptaken by the non-activated lithium sample.

A simplified proposed schematic of the initiation pathways for the reaction of lithium with dry nitrogen (containing less than 2 ppm water moisture) is shown in Figure 5.9.

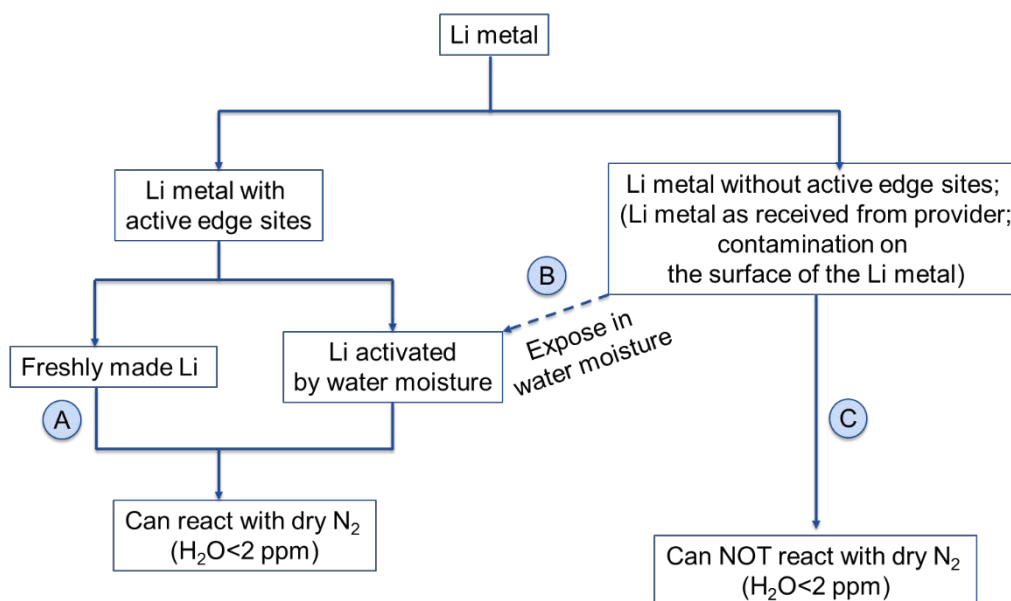


Figure 5.9 Simplified schematic of the reaction routes of lithium with dry nitrogen. Route A has been proposed in the literature; [185, 186] Routes B and C are based on the tests conducted with the TGA and ASAP2020 in this work

Once the reaction of lithium with dry nitrogen is initiated, the reaction becomes self-sustained and gives a sigmoid curve of weight growth with time. [42, 183, 185] The results from the experiments on the TGA shown in Figure 5.4 show that the rate of reaction ramped up rapidly upon the completion of the initiation phase, and then slowed down gradually, which agreed well with the reported results. [42, 183, 185] As the reaction proceeds, the crystals of lithium metal are constantly being disrupted and active edge sites were continuously generated on the surface of the lithium metal. Such active edge sites on the disrupted lithium crystal were similar to the ones on freshly made lithium and also those created by water moisture, which makes reaction self-sustained and thus the water moisture is not necessary beyond initiation.

At the same time, cracks are forming on the newly produced lithium nitride layer due to the Pilling-Bedworth ratio of lithium nitride of 0.64 (less than 1), [41, 42], which is confirmed by the observation in Figure 5.8. The geometrical diameters of the produced lithium nitride particle and the original lithium particle remain essentially the same, as shown in Table 5.1, which indicates the void fraction of the produced lithium nitride is around 36 %, as calculated by Equation 5.13. The cracks are large enough to provide channels for nitrogen to diffuse through. [42, 185, 186]

Table 5.1 The geometrical diameters and the density of the original lithium sample and the produced lithium nitride. (The geometrical diameters were measured by a caliper with an uncertainty of 0.01 mm)

	Lithium	Lithium Nitride
Length (mm)	3.75	3.74
Diameter (mm)	2.24	2.24
Density (g/cm ³)	0.534	1.27
Void Fraction	-	36%

$$\text{Void Fraction} = \frac{m_{Li}/\rho_{Li} - m_{Li_3N}/\rho_{Li_3N}}{m_{Li}/\rho_{Li}} \quad \text{Equation 5.13}$$

In summary, through an activation method, commercially available lithium metal can be activated to react with dry nitrogen (water content less than 2 ppm) at moderate temperatures. Once activated, the reaction of lithium with dry nitrogen becomes self-sustained, producing a substantial uptake of nitrogen.

5.4 Separation of Nitrogen from A Binary Gas Mixture of Nitrogen and Methane Lithium

Lithium performance for the separation of nitrogen from a binary gas mixture of nitrogen and methane was studied using a dynamic column breakthrough (DCB) apparatus. The tests were conducted under the following conditions: 10% nitrogen and 90% methane at 60 °C, the total pressure of 884 kPa, the total flow rate of 20 sccm ($f_{N_2} = 2$ sccm; $f_{CH_4} = 18$ sccm) and lithium sample mass of 0.80 g.

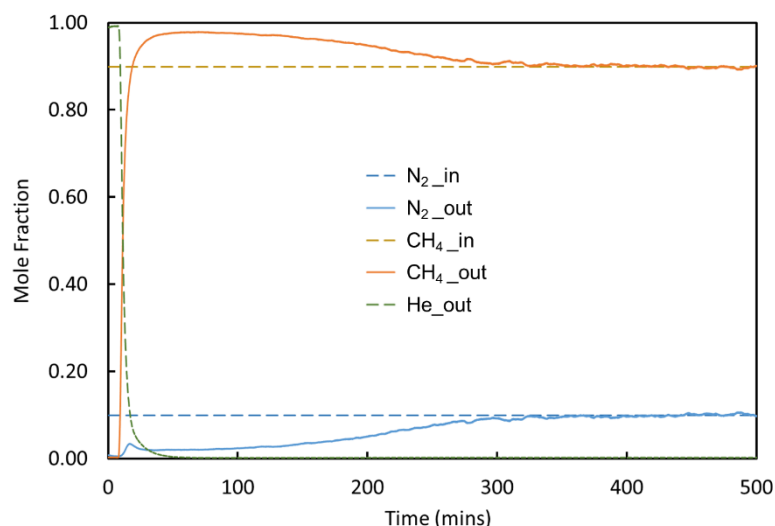


Figure 5.10 Breakthrough curve of nitrogen (10 mol %) and methane (90 mol %) feed mixture passing through a lithium loaded column with, the total flow rate of 20 sccm and lithium sample mass of 0.80 g

The breakthrough curves of nitrogen, methane and helium are shown in Figure 5.10. The nitrogen mole fraction in the effluent gas was significantly reduced from the loading composition of 10% to a low level of 2% for around 100 mins, and then slowly increased back to 10% after around 300 minutes. Meanwhile, methane broke through the lithium column immediately after the gas mixture was switched to feed the lithium column. The methane mole fraction reached 98% from the original 90% and was maintained at this high level for around 100 mins before decreasing slowly back to 90% at around 300 mins. The uptakes of nitrogen and methane are calculated by Equation 5.12: the uptake of nitrogen reached 19 mmol/g which is consistent with the uptake of nitrogen calculated by the weight change measured before and after the reaction; the uptake of methane was zero which was consistent with the results from the TGA and ASAP2020. In conclusion, this test of binary gas mixture breakthrough shows that lithium metal has substantial potential to separate nitrogen effectively from gas mixtures of nitrogen and methane.

5.5 Regeneration of Lithium from Lithium Nitride

5.5.1 Regeneration of Lithium by Thermal Decomposition of Lithium Nitride

5.5.1.1 Thermal Decomposition Calculation

In principle, lithium metal could be regenerated from lithium nitride by thermal decomposition through a combination of pressure and temperature swing process, although the conditions of the regeneration are expected to be harsher than those normally applied in industry. The chemical

equation for the decomposition of lithium nitride to lithium and nitrogen is shown in Equation 5.14. The conditions for such thermal decomposition were investigated by both a thermodynamic calculation and an experimental exploration described in this section.

The change of Gibbs free energy of a certain reaction is the thermodynamic indicator to evaluate this reaction's feasibility and spontaneity: when $\Delta G_r < 0$, the reaction is spontaneous; when $\Delta G_r > 0$, the reaction is non-spontaneous. By definition, the change in the Gibbs free energy of the system equals to the change in the enthalpy of the system minus the change in the product of the temperature times the entropy of the system, shown in Equation 5.19. The enthalpy change of the system is the sum of the formation enthalpy of the products minus those of reactants, shown in Equation 5.17. The entropy change of the system is the sum of the formation entropy of the products minus those of the reactants, shown in Equation 5.18. The formation enthalpy and formation entropy of the studied chemicals are functions of temperature, and the thermochemical data and the calculation equation are shown in Table 5.2, Equation 5.15 and Equation 5.16.

The predicted change of Gibbs energy of the thermal decomposition of lithium nitride as a function of temperature is plotted in Figure 5.11. It is clear from Figure 5.11 that only when the temperature is higher than 1250 °C, will the thermal decomposition of lithium nitride become spontaneous and produce 100 kPa nitrogen and lithium vapor. This extremely high temperature is not suitable to be employed in the natural gas processing plant.

Table 5.2 Thermochemistry data of studied materials[293, 294]

	N₂ (G)	LI (G)	LI₃N (S)
ΔH_f (kJ/mol)	0.00	159.30	-164.56
ΔS_f (J/K/MOL)	191.61	138.78	62.66
A	19.5058	23.3341	54.9246
B	19.8871	-2.7724	86.2155
C	-8.5985	0.7674	8.4280
D	1.3698	-0.0036	-8.1037
E	0.5276	-0.0352	-0.5213
F	-4.9352	151.5035	-186.5499
G	212.3900	166.1885	100.1871
H	0.0000	159.3004	-164.5571



$$\Delta H_f = \Delta H_{298.15}^0 + A * t + B * \frac{T^2}{2} + C * \frac{T^3}{3} + D * \frac{T^4}{4} - \frac{E}{t} + F - H \quad \text{Equation 5.15}$$

$$\Delta S_f = A * \ln(T) + B * T + C * \frac{T^2}{2} + D * \frac{T^3}{3} - \frac{E}{2 * T^2} + G \quad \text{Equation 5.16}$$

$$\Delta H_r = \sum H_f(\text{products}) - \sum H_f(\text{reactants}) \quad \text{Equation 5.17}$$

$$\Delta S_r = \sum S_f(\text{products}) - \sum S_f(\text{reactants}) \quad \text{Equation 5.18}$$

$$\Delta G_r = \Delta H_r - T * \Delta S_r \quad \text{Equation 5.19}$$

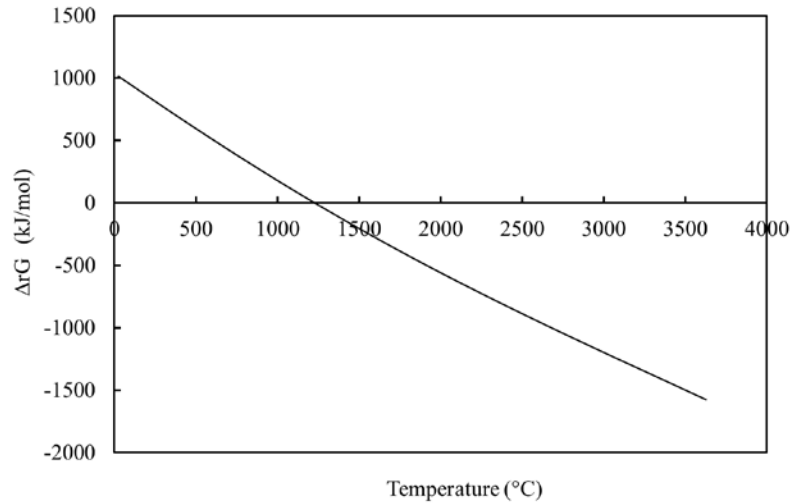


Figure 5.11 Predicted Gibbs energy for the thermal decomposition of lithium nitride as a function of temperature. The calculation suggests that only when the temperature is above 1250 °C, will the thermal decomposition of lithium nitride become spontaneous.

Regeneration conditions at low temperatures are preferred and could potentially be achieved by reducing the partial pressure of nitrogen and lithium vapor. To obtain the relationship between the change of Gibbs energy and the reaction equilibrium constant (K), the definition of Gibbs free energy change of reaction as shown in Equation 5.20 below is used.

$$\Delta G_r = \Delta G^0 + RT \ln(K) \quad \text{Equation 5.20}$$

When $\Delta G_r = 0$, the reaction is at its equilibrium state. The change of Gibbs energy at standard conditions is then a function of the reaction equilibrium constant, as shown in Equation 5.21 below.

$$G^0 = -RT \ln(K) \quad \text{Equation 5.21}$$

Assuming the activity coefficients for nitrogen and lithium are unity and lithium nitride stays in the solid state during the decomposition, the reaction equilibrium constant (K) is correlated to the partial pressure of nitrogen and lithium vapor, as shown in Equation 5.22

$$K = \frac{P_{N_2} * P_{Li}^6}{P_{Li_3N}^0} = P_{N_2} * P_{Li}^6 \quad \text{Equation 5.22}$$

Next, the partial equilibrium pressure of nitrogen and lithium vapor are assumed to follow the stoichiometric relation, as shown in Equation 5.23 below.

$$P_{Li} = 6P_{N_2} \quad \text{Equation 5.23}$$

Finally, by combining Equation 5.21, Equation 5.22 and Equation 5.23, the partial pressure of nitrogen can be expressed as a function of temperature, as shown in Equation 5.24,

$$P_{N_2} = (e^{-\frac{\Delta G^0}{RT}} / (6^6))^{\frac{1}{7}} \quad \text{Equation 5.24}$$

Therefore, the temperature for the spontaneous thermal decomposition of lithium nitride as a function of the partial pressure of nitrogen can be estimated, as shown in Figure 5.12. Also shown is another thermodynamic calculation reported by Lian et al., 2009 and two sets of experimental data reported by Hitoshi et al., (1980) and Yonco et al., (1975). [192, 288, 289], Lian et al., (2009) also validated their thermodynamic calculation with one set of experimental data at 382 °C and 10^{-3} Pa [192]. Yonco et al.'s data showed the biggest deviation from the calculation shown here, which might be due to their misuse of total pressure (which equals the sum of the partial pressure of nitrogen and partial pressure of lithium) as the partial pressure of nitrogen. The other two reported data sets from Hitoshi et al. and Lian et al. match the calculation reasonably well. The calculation shown in Figure 5.12 indicates that it is possible to decompose lithium nitride at relatively low temperatures by decreasing the partial pressure of nitrogen. For example, the temperature of the decomposition of lithium nitride can be potentially reduced to 600 °C if the partial pressure of nitrogen can be reduced to 1.2 Pa.

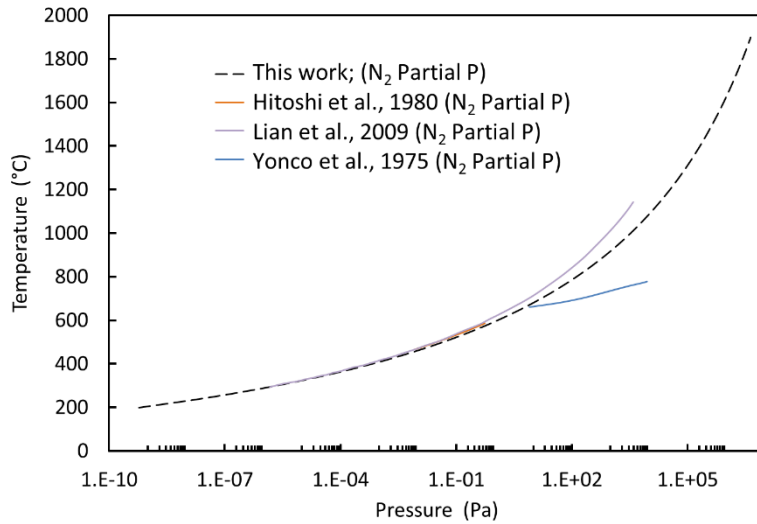


Figure 5.12 The thermal decomposition temperature of lithium nitride as a function of the partial pressure of nitrogen estimated by thermodynamic calculation, together with previously reported computed[192] and experimental data[288, 289]

Another parameter relevant to the feasibility of the thermal decomposition of lithium nitride is the vapor pressure of lithium metal. The comparison of the saturated vapor pressure of lithium and the partial pressure of lithium decomposed from lithium nitride as a function of temperature is shown in Figure 5.13. The partial pressure of lithium decomposed from lithium nitride aligns well with the saturated vapor pressure of lithium, which indicates that almost all the produced lithium would go to the gas phase and escape out with the carrier gas, making it even more challenging to recycle the lithium metal in situ.

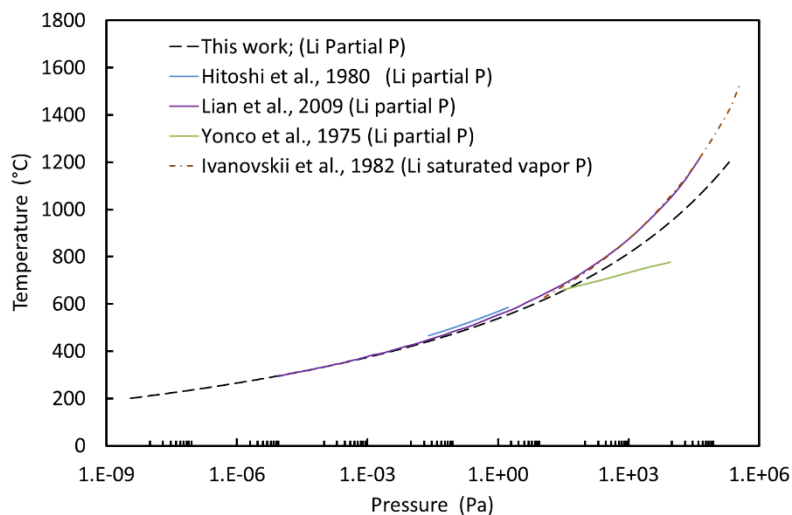
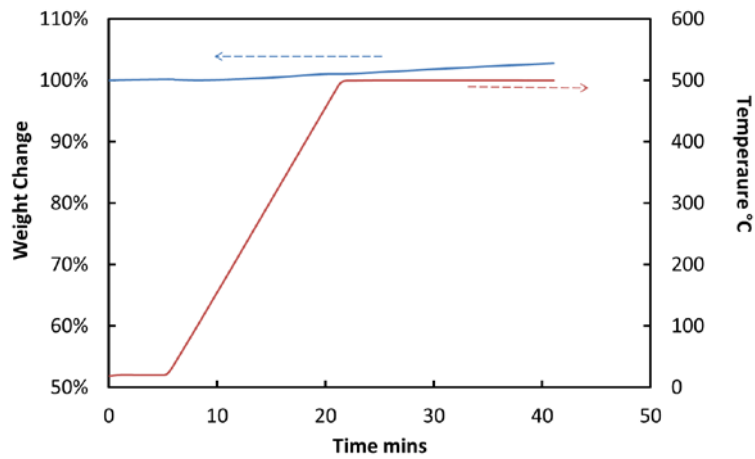


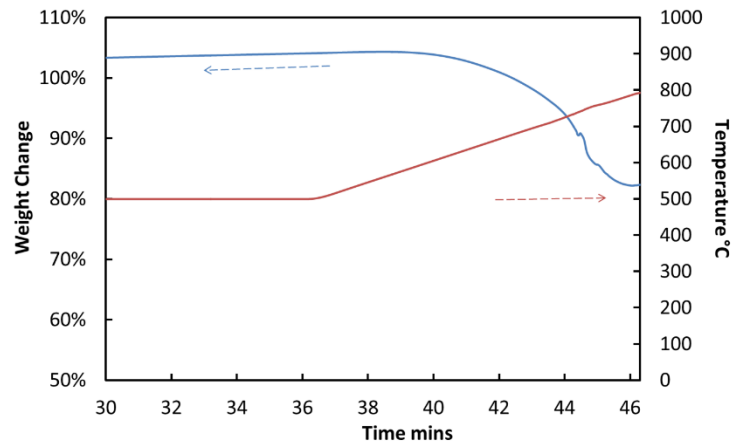
Figure 5.13 Comparison of the saturated vapor pressure of lithium and the lithium partial pressure of lithium decomposed from lithium nitride as a function of temperature

5.5.1.2 Thermal Decomposition Experiments

The feasibility of the regeneration of lithium metal from thermal decomposition of lithium nitride was experimentally investigated to confirm the prediction of the above calculation. Three sets of experiments were performed using the TGA Q50. In the first two sets of experiments, ceramic crucibles were chosen with a capacity of 90 μL , which is intended for the operation from ambient temperature to 1500 $^{\circ}\text{C}$. The results are shown in Figure 5.14 (a) and (b). The temperature of the lithium nitride sample was increased to 500 $^{\circ}\text{C}$ at a ramp rate of 30 $^{\circ}\text{C}/\text{min}$ and then maintained at this temperature for 20 minutes. Helium with a nominal concentration of 99.999 vol. % ($\text{N}_2 < 4$ ppm; $\text{H}_2\text{O} < 2$ ppm) was used as the purge gas and the flow rate was set at 100 mL/min. The total pressure of the helium purge gas was adjusted to 138 kPa, so the partial pressure of nitrogen was estimated to be 0.55 Pa. Theoretically, full decomposition of lithium nitride would lead to a decrease in the sample weight by 40 %, assuming that the released nitrogen was purged out and the produced lithium stayed in the crucible. However, within the duration of the experiment, the weight of lithium nitride sample essentially remained the same, indicating that no lithium nitride has decomposed. In a second experiment, as shown in Figure 5.14 (b), the furnace temperature was first increased to 500 $^{\circ}\text{C}$ and maintained at this temperature for 30 minutes, before being further increased with a target of 800 $^{\circ}\text{C}$ at a ramp rate of 30 $^{\circ}\text{C}/\text{min}$. The helium purge gas was set to the same conditions with the previous experiment. The sample showed a 20% weight loss between temperatures of 600 $^{\circ}\text{C}$ and 800 $^{\circ}\text{C}$, suggesting that the lithium nitride started to decompose at 600 $^{\circ}\text{C}$: the 20% weight loss was equivalent to the decomposition of 20% of the lithium nitride. The decomposition temperature (600 $^{\circ}\text{C}$) and the partial pressure of nitrogen (0.55 Pa) were consistent with the calculated relationship between decomposition temperature and pressure. However, cracking of the ceramic sample crucible in the following 20 mins forced the experiment to conclude prematurely.



(a) Ramp 30 °C/min; 500 °C; $P_{\text{nitrogen}} < 0.55 \text{ Pa}$



(b) Ramp 30 °C/min; 500 °C < T < 800 °C; $P_{\text{nitrogen}} < 0.55 \text{ Pa}$

Figure 5.14 Thermal decomposition tests of lithium nitride on the thermogravimetric analyzer (TGA) with the ceramic crucible. The blue line corresponds to the weight change of the lithium nitride sample, shown on the left vertical axis. The red line corresponds to the temperature profile, shown on the right vertical axis. (a) Experiment 1 with a temperature target of 500 °C at a ramp rate of temperature of 30 °C/min; the partial pressure of nitrogen is estimated to be smaller than 0.55 Pa. (b) Experiment 2 with an initial temperature target of 500 °C at a ramp rate of 30 °C/min, and a second temperature target of 800 °C at the same ramp rate; the partial pressure of nitrogen is estimated to be smaller than 0.55 Pa.

In a third experiment, a platinum crucible with a capacity of 100 μL , which is intended for operation from ambient temperature to 1000 °C, was used to try to overcome the cracking issue encountered with the ceramic crucible. In this test, the temperature of the lithium nitride sample was increased to 800 °C at a ramp rate of 5 °C/min and the helium purge gas was set to the same conditions with the

previous experiments. From the result shown in Figure 5.15, a 5% weight increase was observed, which might be due to side reactions of lithium nitride with impurities in the purge gas, such as moisture or carbon dioxide. When the temperature reached 800 °C, the weight of the sample dropped sharply and then increased again. The bottom of the platinum crucible was deformed and observed to be “melted”, as shown in Figure 5.16. This was most likely due to the formation of Li-Pt alloy at elevated temperatures.[295-298] While lithium metal might have been regenerated from lithium nitride at 800 °C, it is highly reactive at elevated temperature and would immediately react with any surrounding material, producing an alloy as a product of its reaction with the platinum crucible. Therefore, although lithium can be thermally regenerated from lithium nitride, a specially designed material is required to be able to handle the produced high-temperature lithium vapor.

In conclusion, considering the harsh conditions required and the high reactivity of lithium reactivity toward conventional materials at elevated temperatures, the thermal decomposition of lithium nitride to recycle lithium using the described approach is concluded to be not feasible.

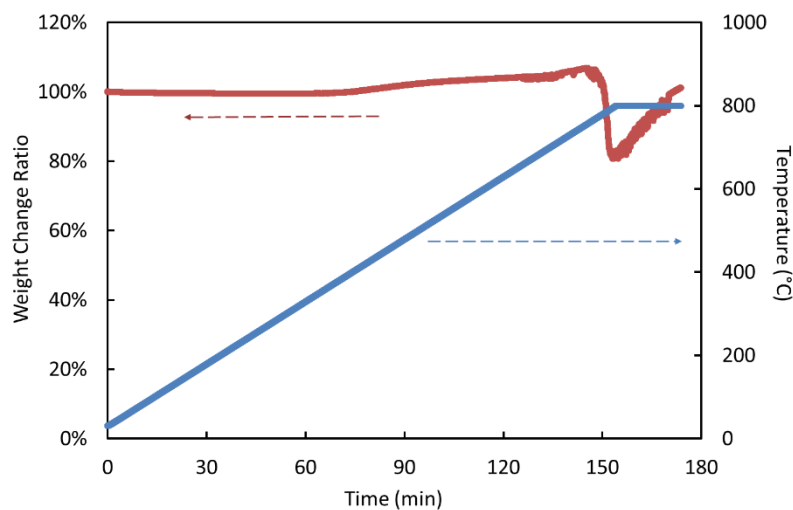


Figure 5.15 Thermal decomposition of lithium nitride on the thermogravimetric analyzer (TGA) with the platinum crucible. The green line corresponds to the weight change of the lithium nitride sample, shown on the left vertical axis. The blue line corresponds to the temperature profile, shown on the right vertical axis. The target temperature was 800 °C at a ramp rate of 5 °C/min; the partial pressure of nitrogen was estimated to be smaller than 0.55 Pa.



Figure 5.16 Platinum crucible after the thermal decomposition of lithium nitride experiment at 800 °C. The bottom of the platinum crucible was “melted” by the produced lithium vapor, which was due to the formation of Li-Pt alloy.

5.5.2 Regeneration of Lithium by A Chemical Loop

Lithium metal might alternatively be recycled from lithium nitride in a closed loop with a three-step regeneration process as shown in Figure 5.17. Step 1: The lithium nitride is first converted to LiOH by bringing it into contact with water. This step also produces ammonia, which is intrinsically a valuable material. Step 2: The resultant LiOH from Step 1 is converted to LiCl by adding hydrochloric acid. Step 3: The LiCl from Step 2 is converted to lithium metal by the mature commercial process of LiCl electrolysis[299-302], while the side product of chlorine gas can be recycled to form hydrochloric acid.

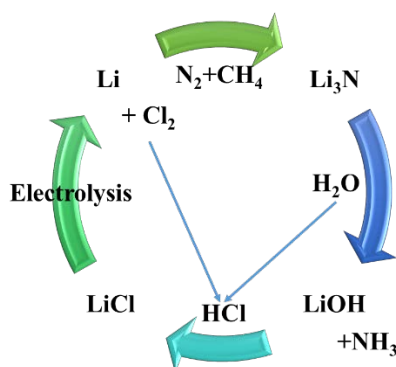


Figure 5.17 Lithium recycle loop for the capture of nitrogen and production of NH₃

A brief economic analysis of the regeneration loop is given for the following case study: assuming the requirement is to remove nitrogen from a gas mixture with composition of 10 mol% nitrogen + 90 mol% methane to meet the specification for LNG (1 mol. % N₂ + 99 mol. % CH₄), and this LNG train produces 5 million tonnes of LNG per annum.

Based on the above assumptions, the amount of nitrogen which needs to be removed from the feed to be able to meet the LNG specification is 99 tonnes/hr. Subsequently, the required amount of lithium is 149 tonnes/hr, given that the lithium reacts with nitrogen according to the lithium/nitrogen reaction stoichiometry. To ensure continuous processing of the feed gas, three adsorption towers containing

the lithium would need to be used, where each of these towers would be used for 3 hours for the feed processing step and 6 hours for the regeneration step. Hence, each tower in the adsorption process would require 446 tonnes of lithium, assuming that the reaction kinetics are sufficiently fast. Therefore, the required initial one-off purchase of lithium metal would be 1338 tonnes. As the unit price of lithium metal is USD \$110,000/tonne (Industrial grade), the total cost of the lithium required would be USD 147 million – assuming that the lithium could be fully recovered so that no further lithium metal purchase is required.

Step 1 involves the conversion of Li_3N to LiOH . This conversion requires an additional reactant of water and produces a side product ammonia, which has an economical value. The water required might be sourced by recycling the water produced in the natural gas production process, and therefore its cost could be considered as negligible. At the same time, the yearly production of 1.05 million tonnes of ammonia could be sold with a unit price of USD 400/tonne, producing an annual revenue of USD 421 million.

In Step 2, the LiOH is converted to LiCl by adding HCl acid. As the HCl could be formed from the reaction of water with the chlorine gas produced from the electrolysis of LiCl , its cost could be considered as negligible.

In Step 3, the LiCl produced in Step 2 will go through an electrolysis process to recycle the lithium metal. This electrolysis is a mature commercial process for extracting lithium metal from lithium compounds and energy consumption for the best performing process is about 8 kWh/kg. If the electricity is generated from a methane gas turbine, then the unit electricity price could be about USD 0.033/k Wh, which can be converted to USD 1.155/kg (\$1155/tonne) of lithium produced. The total amount of lithium that needs to be electrolyzed each year is about 1.3 million tonnes. Therefore, the total cost of regenerating the lithium nitride to lithium metal is USD 344 million. When this total cost is offset against the revenue generated by the ammonia production, the process of removing nitrogen could make a profit of USD 88 per tonne of nitrogen removed.

5.6 Conclusion

The reaction of lithium with dry nitrogen ($\text{H}_2\text{O} < 2$ ppm) under moderate temperatures has been studied by TGA, ASAP2020 and synchrotron XRD. The mechanism of this reaction under moderate temperatures can be summarized by the following two points: (1) The reaction of lithium metal with dry nitrogen (moisture < 2 ppm) is initiated by active edge sites on the lithium metal. Such active edge sites can be either found on freshly made lithium metal or on commercially available lithium metal that has been activated by water moisture; (2) Once the reaction is initiated, it becomes self-sustained.

Active edge sites on lithium metal are continuously created through the reaction with nitrogen. The diffusion of nitrogen to the interface of lithium and lithium nitride occurs through the cracks in the layer of produced lithium nitride. A viable feasible and effective activation method for lithium metal toward the reaction with dry nitrogen was developed and demonstrated in this work.

A case study of the separation of nitrogen from a binary gas mixture by lithium metal has been studied using the proposed activation method with a custom built apparatus. The lithium metal shows significant advantages compared to the normal adsorbents. First of all, the uptake of nitrogen on lithium metal consistently reached its theoretical value of 24 mmol/g, which is an order of magnitude higher than that of the best-reported nitrogen selective adsorbents. Moreover, as lithium metal remains inert to methane under the tested condition, it has a very large selectivity for nitrogen over methane, allowing for almost 100% methane recovery.

Two approaches to the regeneration of lithium metal from lithium nitride have been considered in this chapter. Firstly, it would be ideal to regenerate lithium in-situ by a temperature and pressure swing from lithium nitride, analogous to the conventional temperature/pressure swing adsorption process. However, both the thermodynamic calculation and experimental results show that this approach is not feasible due to the extremely harsh conditions required for the thermal decomposition of lithium nitride. Such harsh conditions include but are not limited to high operation temperature, low nitrogen partial pressure and the need for specially designed furnace/tower material for handling high-temperature lithium. The second approach toward regeneration was using a closed chemical loop, which appears to be both technically and economically feasible. Each step of this loop can be handled by an industrial process that has already been well-established. A high-level economic analysis indicates that this chemical loop could potentially both recycle lithium from lithium nitride and make a profit of USD 88 per tonne of nitrogen from the conversion of nitrogen to ammonia.

Chapter 6: Conclusion and Future Work

6.1 Conclusion

Natural gas is going to play a more important role in the worldwide energy market due to its relatively low emissions to the environment compared to oil and coal. It will serve as the bridging energy before the renewable energy technologies become mature and economically competitive. However, advanced separation technologies are required to upgrade raw natural gas to meet transportation and sale requirements. Nitrogen is one of the inherent impurities in raw natural gas and is considered to be the hardest impurity to remove efficiently and economically due to its similar physical properties to the main component of natural gas – methane. The current approach of removing nitrogen from natural gas is to liquefy nitrogen and methane together, and then separate the liquefied mixture by cryogenic distillation utilizing the difference in their volatility. Such nitrogen rejection units are energy-intensive to run because of the low boiling points of nitrogen (-195.8 °C) and methane (-161.5 °C). Technologies that can separate nitrogen from methane under moderate conditions are highly desired. A key contribution of this work has been to critically analyse the physical and chemical properties of nitrogen and methane, to review the conventional separation technologies that are mainly based on the difference in the physical properties of nitrogen and methane, and to assess emerging separation technologies that are mainly based on the difference in the chemical properties of nitrogen and methane.

The adsorption process is one of the most attractive conventional separation processes for removing nitrogen from methane. Adsorption equilibria and kinetics are the two most crucial sets of properties to simulate and design an adsorption-based gas separation process. However, the availability of consistent kinetic data for each gas on various adsorbents is limited in literature, which leads to large uncertainties when using such data in process design. Motivated by this, the adsorption equilibria and kinetics data of nitrogen and methane on four commercial adsorbents are studied experimentally in this work using a commercial volumetric system ($T = 273$ and 303 K; $P = 5$ to 120 kPa). Two key elements were addressed: first, the dynamic uptake data acquired were corrected for the effects of gas expansion, which was done by calibrating the system response with helium to determine the initial condition; Second, a non-isothermal Fickian Diffusion (FD) model was used to analyse the kinetic data, which was able to describe the dynamic data with a deviation of only 1% for all the studied cases, compared to the commonly used isothermal linear driving force model with a relative root mean square deviation of 10%.

On MSC-3K 172 and zeolite 4A, a weak pressure dependence was observed for the sorption rate. On Norit RB3 and zeolite 13X, no pressure dependence was observed for the sorption rate. A clear temperature dependence was observed for all four adsorbents studied, and the Arrhenius type activation energies were all around (10 to 20) $\text{kJ}\cdot\text{mol}^{-1}$. Both Norit RB 3 and Zeolite 13X showed fast but similar kinetics for nitrogen and methane, and thus any separation of this gas mixture using these two adsorbents could only utilize their equilibrium selectivity, which was too small to be industrially feasible. Zeolite 4A and MSC-3K 172 show sufficiently faster uptake of nitrogen than that of methane, although they are still methane-selective at equilibrium. The kinetic selectivity of nitrogen over methane on Zeolite 4A and MSC-3K 172 are still moderate (1.4 to 2.2) compared to the reported best adsorbents such as Sr-UPRM-5 (25.42) or Sr-ETS-4 (21.62). However, the inexpensive price and the ease of availability of these two adsorbents play a huge contribution in giving them the potential to be scaled up for industrial application, particularly, with novel process design, such as dual-reflux pressure swing adsorption.[303-305]

An absorption process operating at ambient temperature was proposed in this work as an alternative technology, which could be analogous to the process used to separate carbon dioxide from natural gas with an aqueous solution of amine. An aqueous solution of transition metal complexes (TMC) which can selectively absorb nitrogen is the key to differentiate this proposed absorption process from the conventional methane-selective absorption processes which use physical solvents. Mimicking nitrogenase enzymes in biological nitrogen fixation, TMCs have been studied intensively to fix nitrogen from the atmosphere and then to convert nitrogen to ammonia. The TMCs required to separate nitrogen from methane is relatively easier to study compared to those in the applications of fixation and conversion of nitrogen. The reason is that such TMCs only need to bond nitrogen molecules without cleaving the extremely strong triple bonds in nitrogen molecules which is the most challenging step in the conversion of nitrogen to ammonia.

In this work, fourteen TMC systems have been studied to absorb nitrogen. Three Ru-based TMC systems showed the abilities to absorb nitrogen, with the best one being the $\text{K}[\text{Ru}^{\text{II}}(\text{EDTA})]$ aqueous solution, which gave eight times the higher capacity of nitrogen than that of water. The preparation of this TMC was done according to previously reported methods of synthesis.[244, 265] The structure of this TMC was confirmed by elemental analysis and infrared spectroscopy (IR). The absorption equilibria and associated uncertainties of nitrogen in this TMC solution were measured on a custom designed solubility apparatus under various conditions. The apparatus can measure the adoption equilibria ranging from $1\text{E}-3$ to 1 mol/L , with a temperature ranging from $20\text{ }^{\circ}\text{C}$ to $40\text{ }^{\circ}\text{C}$ at pressures ranging from 0 kPa to $5,000\text{ kPa}$. When the molar concentration of this Ru-based TMC was 0.1M , this

TMC solution showed an overall capacity of nitrogen of 6.11×10^{-2} mol/L and selectivity of nitrogen over methane of 2 at ~ 30 °C and ~ 3000 kPa. The specific capacities of nitrogen per Ru^{II} were estimated to remain essentially the same at different TMC concentrations (0.1M and 0.25M). A desorption hysteresis was observed which is typical for chemisorption and a combination of pressure swing and temperature swing is required to generate the TMC solution. The enthalpy of absorption of nitrogen in this solution is estimated to be 30-60 kJ/mol N₂ which varied with the loading of nitrogen. These enthalpies of absorption of nitrogen are relatively low compared to the enthalpy of absorption of CO₂ in an aqueous solution of amine (around 100kJ/mol CO₂), which implies that only moderate amount of energy would be required to regenerate this solution of TMC. Overall, this work demonstrates the potential of using TMC solutions to absorb nitrogen from methane under moderate conditions. The high cost and the limited annual production of ruthenium impede the application of this Ru-based TMC solution on a large scale. However, this can be overcome by replacing ruthenium with more abundant transition metals, such as iron and vanadium. Several TMC candidates have been tested as well, but none of them can absorb nitrogen. Therefore, a fundamental understanding of the binding mechanism between nitrogen and TMCs and systematic screening of TMCs consisting of an abundant transition metal and low-cost ligands are highly desired.

Lastly, a novel process using lithium to separate nitrogen from methane was proposed and investigated. Lithium metal has been studied to remove nitrogen from crude argon, but has not been applied to the separation of nitrogen from natural gas. The main challenge of adapting the lithium metal-based separation process to a natural gas processing plant has been to make the reaction of lithium with dry nitrogen happen at moderate temperatures. However, the mechanism of this reaction under moderate conditions remained a mystery. In this study, the reaction of lithium with dry nitrogen (water content < 2 ppm) was intensively studied at moderate temperatures by various methods, including TGA, ASAP2020, synchrotron XRD and a custom-built flow-through apparatus. Furthermore, two approaches of regenerating of lithium from lithium nitride were proposed and critically analysed.

There are three contributions of this study to the separation of nitrogen from natural gas by lithium metal. First, a mechanism for the reaction of lithium with dry nitrogen was proposed and verified. Active edge sites on the lithium metal are mandatory to initiate the reaction. Such high free energy sites can be found either on freshly made lithium or on lithium metal that has been activated by water moisture. The reaction becomes self-sustained once initiated: the active edge sites are continuously created as the reaction proceeds; the cracks in the lithium nitride layer provides the channels for the diffusion of nitrogen molecules. Second of all, a simple and efficient method was discovered to activate contaminated lithium metal toward the reaction with nitrogen at moderate temperatures.

After exposure to water moisture, the contaminated lithium regains the ability to react with dry nitrogen. The results from TGA and ASAP2020 show that the uptake of nitrogen on activated lithium can be as high as the theoretical value of 24 mmol/g at temperatures from 30 to 90 °C and pressures from 30 to 100 kPa. Third, the performance of lithium metal to separate nitrogen from a binary gas mixture of nitrogen and methane was demonstrated on a flow-through apparatus. The results show that lithium metal can reduce the content of nitrogen from 10% to 2% in the binary gas mixture. Overall, lithium metal shows two significant advantages to capture nitrogen: (1) the uptake of nitrogen on lithium metal can reach the theoretical capacity of 24 mmol N₂/g, one order of magnitude higher than the best reported nitrogen-selective adsorbents; (2) the selectivity of nitrogen over methane can be infinitely large due to the inert nature of lithium to methane.

Two methods of recycling lithium from lithium nitride were discussed in this work as well: (1) regeneration of lithium by thermal decomposition of lithium nitride; (2) regeneration of lithium by a chemical loop. The thermal decomposition of lithium nitride was found to be unfeasible given that high operation temperatures, high purity purge gas, and specially designed furnace/tower material would be needed for handling high-temperature lithium. The chemical loop method is theoretically feasible, given that each step is already a part of mature industrial processes. Furthermore, the economic estimation showed that when taking the by-product of ammonia into account, a profit of USD 88 per tonne of nitrogen can be made through this process. Therefore, regeneration of lithium from lithium nitride by the chemical loop is both technically and economically feasible.

6.2 Recommendations and Future Work

Among the physical properties of nitrogen and methane, the difference in the kinetic diameter is the most promising one in which to develop new separation processes that can separate nitrogen from methane as an alternative to distillation. Such new and alternative separation processes include membrane and adsorption processes. Inorganic membranes, such as zeolite, MOF or carbon molecular sieve membranes, can distinguish this physical property difference effectively. However, the major challenge for them remains the scale-up ability. Most of the inorganic membranes suffer poor mechanical properties and engineering problems. For adsorption process, Zeolite 4A and MSC-3K 172 remains the best candidates when taking availability and cost into account. Effective separation performance can be achieved through novel process design, such as dual-reflux pressure swing process (DRPSA). More effects should be focused on the optimization of the light/heavy reflux rate, feed time and purge pressure.[303-305]

The most promising chemical property of nitrogen that can be utilized to separate nitrogen from methane is its role as a weak ligand coordinating to the TMC. For adsorption, recent research has shown that unsaturated Cr sites on MIL-100 and MIL-101 (MOFs)[140, 141] and unsaturated Ni or Cu sites on ion-exchanged MFI and ZSM (zeolites)[306] can selectively bind nitrogen. The overall equilibria favour nitrogen over methane at relatively low pressure due to the high affinity of nitrogen to the unsaturated transition metal sites, although it becomes methane selective when the pressure increases. One way to overcome this problem is to design a material that combines the molecular sieve effect (with pore size locating between 3.68 and 3.8 Å) and the nitrogen coordinating effect (with unsaturated transition metal sites for nitrogen bonding). There is no reported study focusing on this approach yet. For membrane process, one approach could be integrating nitrogen binding chemicals, either porous or non-porous TMCs, into the polymer matrix to make mixed matrix membrane, which has the advantage of being easy to scale up. Another approach is to make an inorganic membrane composed of the nitrogen binding porous zeolites or MOFs, but the processibility of such inorganic membranes could be challenging.

Lastly, the lithium-based process is a promising process for the separation of nitrogen from natural gas. The activated lithium metal shows considerably high uptake of nitrogen and gives a significant large selectivity of nitrogen over methane. The regeneration of lithium from the produced lithium nitride by a proposed chemical loop is technically and economically feasible, proved by critical analyses. Future efforts can be focused on the process simulation and more detailed analysis of the feasibility of this process. Furthermore, the in-situ regeneration of lithium can be potentially achieved by direct electrolysis of the produced lithium nitride. Lithium nitride has small electrolysis potential of 4.6 eV and it is a good electron conductor, all of which make it theoretically feasible to recycle lithium metal from the electrolysis of lithium nitride.[43] So far, there have only been limited data available on the electrolysis of lithium nitride, hence new efforts in this electrolytic approach to recycling lithium from lithium nitride could prove to be highly beneficial for the advancements in this field.

Appendix A. Uptake of N₂ on Zeolite 4A

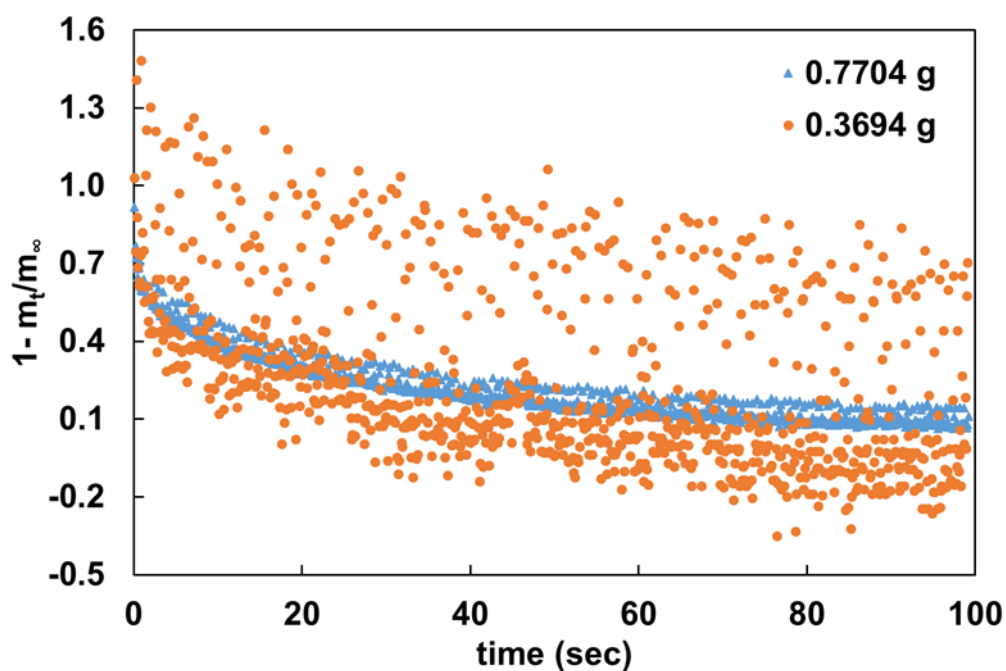


Figure A.1 Experimental uptake data for N₂ on zeolite 4A at 283 K with sample masses of 0.7704 g and 0.3694 g at 100 kPa

Appendix B. TMC Synthesis Method

Appendix B.1. K[Ru^{II}(EDTA)]

Synthesis Method

This SOP does not claim to address all the safety problems associated with its use. It is the responsibility of the user to determine and follow appropriate safety and health practices.

Materials

- Na₃EDTA=Ethylenedinitrilo)tetraacetic acid trisodium salt hydrate
- Ruthenium(III) chloride hydrate

Experiment Overview

Target Reactions[244, 307, 308]



Condition: T=25-100 °C, the temperature should be high enough that the solution is kept at a constant slow boiling off state; P= Atmospheric pressure



Condition: T= Room temperature ; P=Under Argon at atmospheric pressure

Side Reactions [309, 310]



Chemicals Amount

Table A.2 The amounts of raw reactants and products for the synthesis of X*[Ru^{II}(EDTA)]

	Raw Chemicals			Intermediate Product	Target Product
	RuCl ₃	Na ₃ EDTA	Mg	Ru ^{III} [EDTA]	X*[Ru ^{II} (EDTA)]
MW (g/mol)	207.43	358.19	24.31	390.31	
n (mol)	0.005	0.005	0.0025*	0.005	0.005
m (g)	1.0372	2.2127	0.0608	3.6371	

X= Mg²⁺ or Na⁺

*: Ensure that the Mg metal is in excess

WARNINGS

- Air sensitive material: Ru^{II} complex
- Pyrophoric material: N/A

- Strong reducing agent: Mg

REQUIREMENTS

- No partner needed

Standard Operation Procedure

Step 1 Prepare RuCl₃/water – solution (I)

1. Dissolve 1.0372 g (0.005 mol) RuCl₃ into 20mL DI water in a centrifuge tube and swirl the tube with hands to speed up the dissolving of RuCl₃ until no apparent solid particles could be seen.

Step 2 Prepare Na₃EDTA/water – solution (II)

- 1 Dissolve 2.2127 g (0.005 mol) Na₃[EDTA] into 10mL DI water in a 100 mL glass beaker
- 2 Gently warm up the solution on a hot plate to 140 °C until the solid dissolves to give a clear solution. In this process, no magnetic stirrer rod is needed, just use hands to swirl the glass beaker on the hot plate.

Step 3 Prepare Ru^{III}[EDTA]/water – solution (III)

1. After the Na₃EDTA/water solution turns transparent, turn up the heating control of the hot plate so that the solution maintains a simmering state.
2. Then, slowly add the RuCl₃/water solution (the 20mL RuCl₃ solution in 2 minutes) to the Na₃EDTA/water solution while swirling the beaker with Na₃EDTA/water solution. If there is a significant amount of RuCl₃ left in the centrifuge tube, another 20 mL of DI water can be added to the tube to rinse out the leftover RuCl₃ and add this RuCl₃ solution to the Na₃EDTA/water solution while swirling the beaker.

Step 4 Ru^{III}[EDTA] powder

1. Turn up/down the hot plate temperature to keep the resulting solution at simmering state until the solution turns to a slurry state, and turns off the heating on the hot plate and leave the beaker to cool down naturally on the hot plate.
2. After the product cools down, collect the precipitate and dry it with suction filtration.
3. Wash the product thoroughly with ice water until it is free of Ru^{III} ions.

4. Wash the product with ethanol twice and dry it with filter paper.
5. Weigh the product and calculate its yields based on Ru.

Step 5 Ru^{III}[EDTA]_water – solution (IV)

1. Dissolve X mol Ru^{III}[EDTA] into Y mol water
2. Adjust the PH value of the solution to 6-8 by adding Z g 0.1M NaOH solution.

Step 6 Ru^{II}[EDTA]^-_water – solution (V)

1. Transfer the solution (IV) to the glovebox. (in glovebox)
2. Add 2X mol Mg into solution(IV). (in the glovebox)
3. Wait for overnight and achieve solution (V). (in the glovebox)



Figure A.2 Synthesized Ru(III)[EDTA] powder. The synthesis method is described above. The product is kept in atmospheric condition.

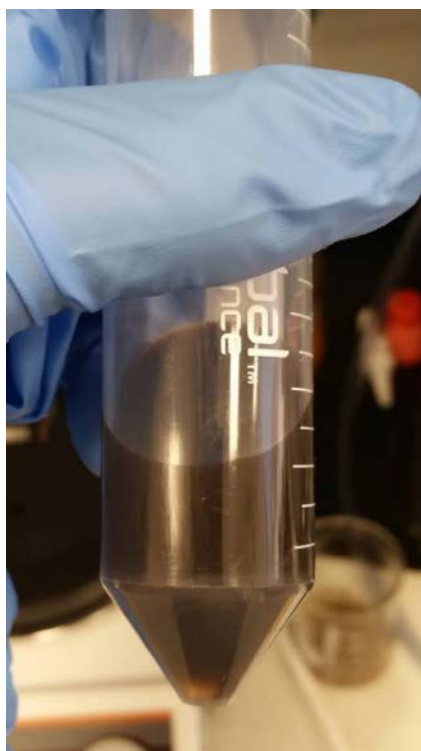


Figure A.3 Synthesized $\text{Ru}^{\text{II}}[\text{EDTA}]^-$ aqueous solution. The preparation method of this solution is described above and the solution is stored in glove-box.

Infrared Spectroscopy (IR)

$\text{K}[\text{Ru}(\text{EDTA})]$ was synthesized according to the method reported in the literature [267, 311, 312] and was characterized with an infrared spectrometer to confirm its structure. Spectrum One FT-IR Spectrometer (PerkinElmer) equipped with a universal attenuated total reflection (ATR) sampler and a deuterated triglycine sulfate (DTGS) detector was used to record the IR spectra of both pure $\text{K}_3[\text{EDTA}]$ and the synthesized ruthenium complex.

The IR results are shown in Figure A.4 The starting material, $\text{K}_3[\text{EDTA}]$, is plotted by the red line, showing two peaks at wavenumbers of 1630 and 1597 cm^{-1} . Two samples of $\text{K}[\text{Ru}^{\text{II}}(\text{EDTA})]$ synthesized from different batches are plotted by the solid green line and the orange line. On the IR spectra for the synthesized $\text{K}[\text{Ru}^{\text{II}}(\text{EDTA})]$, the two peaks at 1630 and 1597 cm^{-1} on IR spectrum for pure $\text{K}_3[\text{EDTA}]$ disappeared and two new peaks at 1724 (free $-\text{COOH}$) and 1610 cm^{-1} (coordinated $-\text{COO}^-$). The IR spectrum of synthesized $\text{K}[\text{Ru}^{\text{II}}(\text{EDTA})]$ is consistent with literature reported IR spectra of the same material, confirming the structure of the synthesized material [266-268].

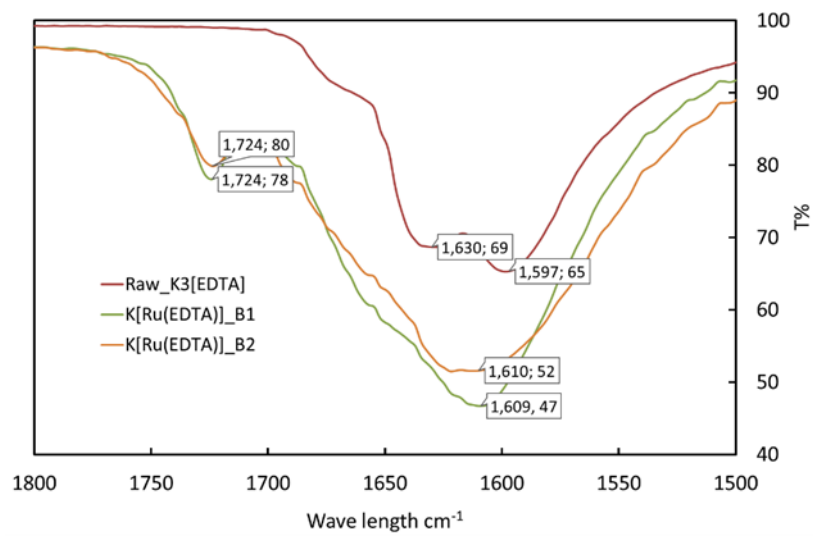


Figure A.4 FR-IR spectra for pure $K_3[EDTA]$ and $K[Ru^{II}(EDTA)]$, which could be classified into two regions: $1650\text{--}1350\text{ cm}^{-1}$ (coordinated -COO^-) and $1750\text{--}1700\text{ cm}^{-1}$ (free -COOH). T% stands for transmittance

Appendix B.2. $\text{Fe}(\text{H})_2(\text{P}(\text{OEt})_3)_4$

This SOP does not claim to address all the safety problems associated with its use. It is the responsibility of the user to determine and follow appropriate safety and health practices.

Equipment

Most of the nitrogen-binding TMCs are expected to be sensitive toward air and/or moisture. In addition, some elements of the TMC synthesis or preparation procedures involves air-sensitive reactants. Isolating these air/water-sensitive compounds from the atmosphere and handling them in a controlled inert environment is thus essential. However, while the Glovebox provides an argon atmosphere able to protect air-sensitive chemicals, it is not convenient for conducting chemical reactions which may involve reflux, heating, and vacuum operations. Therefore, we constructed a Schlenk line system which is widely used in organic metal chemistry. Figure A.5 shows a schematic of a typical Schlenk line system. Figure A.6 shows the Schlenk line system built in our lab (the vacuum pump is not shown in the picture).

The Schlenk line apparatus consists of a dual manifold with 3 ports. One end of the manifold is connected to an inert gas supply (which in our case is argon), while the other is connected to a cold trap and then to a vacuum pump. The argon line is vented through an oil bubbler to avoid air back flow. The cold trap avoids contamination of the vacuum pump from TMC solvents connected through valves B – D. This apparatus allows us to conduct chemical reactions at various conditions in an argon atmosphere and can help to remove the last traces of solvent from the sample.

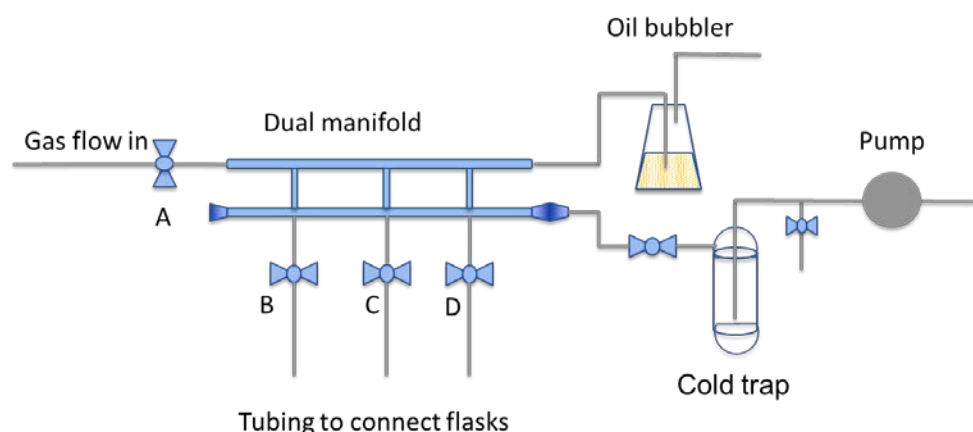


Figure A.5 Schematic of Schlenk line apparatus

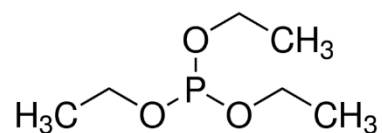


Figure A.6 Schlenk line system in our lab.

Synthesis Method^[313, 314]

Materials

P(OEt)₃= Triethyl phosphite

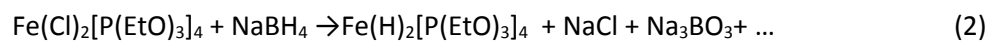


Experiment Overview

Target Reactions



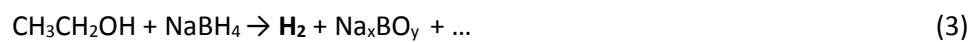
Condition: T=78°C; P=1bar Ar



Condition: T=0°C; P=1bar Ar

Exothermic Reaction

Side Reactions



Exothermic Reaction

Chemicals Amount

Table A.3 The amounts of raw reactants and products for the synthesis of $\text{Fe}(\text{H})_2[\text{P}(\text{EtO})_3]_4$

	Raw Chemicals			Intermediate Product	Target Product
	FeCl_2	$\text{P}(\text{EtO})_3$	NaBH_4	$\text{Fe}(\text{Cl})_2[\text{P}(\text{EtO})_3]_4$	$\text{Fe}(\text{H})_2[\text{P}(\text{EtO})_3]_4$
MW (g/mol)	126.75	166.16	37.83	791.39	722.39
n (mol)	0.0050	0.0150	0.0025	0.0050	0.0050
m (g)	0.6338	2.4924	0.0946	3.9570	3.6120

WARNINGS

- Air sensitive material: FeCl_2
- Pyrophoric material: $\text{P}(\text{EtO})_3$
- Strong reducing agent: NaBH_4
- Step 2 and Step 3 would involve exothermic reactions and produce explosive gas- H_2

REQUIREMENTS

- Must have lab partner for Step 2 and Step 3

Standard Operation Procedure

Step 1 $\text{Fe}(\text{Cl})_2[\text{P}(\text{OEt})_3]_4$ _ethanol – solution (I)

- 1) Add 0.005mol $\text{Fe}(\text{Cl})_2$ into 15-20ml absolute ethanol and keep stirring for 30 mins (in glovebox)
- 2) Add 0.02mol $\text{P}(\text{OEt})_3$ into above solution. Heat up the mixture to reflux under a flow of Ar and keep stirring for 5 hours (Schlenk Line)

Step 2 NaBH_4 _ethanol – solution (II)

- 1) Add 0.0025mol NaBH_4 into a round-bottom flask (in glovebox)
- 2) Transfer the round-bottom flask to fume hood and set an ice bath (in fume hood)
- 3) Put the flask into the ice bath and dropwise add 15ml ethanol into the round-bottom flask with stirring (in fume hood)

- 4) Keep stirring until NaBH_4 completely dissolved (fume hood)

Step 3 $\text{Fe}(\text{H})_2(\text{P}(\text{OEt})_3)_4$ _ethanol – solution (III)

- 1) Connect solution (I) flask to Schlenk Line with Ar flowing through and then put it into an ice bath (Schlenk Line)
- 2) Dropwise add solution (II) into solution (I) – a lot of H_2 is supposed to be produced. (Schlenk Line)
- 3) Keep stirring for 24 hours (Schlenk Line)

Step 4 $\text{Fe}(\text{H})_2(\text{P}(\text{OEt})_3)_4$ powder

- 1) Connect a vacuum pump to solution (III) flask (Schlenk Line)
- 2) Set up a water bath with $T=40^\circ\text{C}$
- 3) Evaporate all the ethanol from solution (III) and then back fill the flask with Ar (Schlenk Line)
- 4) Collect the powder (in glovebox)

Step 5 $\text{Fe}(\text{H})_2(\text{P}(\text{OEt})_3)_4$ _TEG – solution (IV)

- 1) Calculate $\text{Fe}(\text{H})_2(\text{P}(\text{OEt})_3)_4$ yield on the base of Fe
- 2) Add 3 g $\text{Fe}(\text{H})_2(\text{P}(\text{OEt})_3)_4$ into 10 g TEG and keep the solution stirring for 24 hours (in glovebox)
- 3) Filtrate any left sedimentation if there would be any and collect the filtrated solution. (in glovebox)
- 4) Transfer a certain amount of this TEG solution into solubility cell which is ready for N_2/CH_4 solubility tests. (in glovebox)

Reference

- [1] T. E. Rufford, S. Smart, G. C. Y. Watson, B. F. Graham, J. Boxall, J. C. Diniz da Costa, *et al.*, "The removal of CO₂ and N₂ from natural gas: a review of conventional and emerging process technologies," *Journal of Petroleum Science and Engineering*, vol. 94-95, pp. 123-154, 2012.
- [2] PwC, "The World in 2050: How will the global economic order change?," 2017.
- [3] U. S. E. I. Administration, "International energy outlook 2017," 2017.
- [4] BP, "BP energy outlook," 2017.
- [5] U. S. E. I. Administration, "Annual energy outlook 2017 with projections to 2050," 2017.
- [6] I. E. Agency, "World energy outlook 2017," 2017.
- [7] A. J. Kidnay, W. R. Parrish, and D. G. McCartney, *Fundamentals of Natural Gas Processing* vol. 218: CRC Press, 2011.
- [8] OECD, "OECD environmental outlook to 2050," 2017.
- [9] I. a. S. Australian Government Department of Industry, "Australian energy statistics," 2016.
- [10] Bloomberg, "Australia is challenging Qatar's LNG crown," 2017.
- [11] C. C. Tannehill, M. Raven, and K. Brown, *Nitrogen removal requirements from natural gas: topical report*: Gas Research Institute, 1999.
- [12] X. Ning and W. J. Koros, "Carbon molecular sieve membranes derived from Matrimid® polyimide for nitrogen/methane separation," *Carbon*, vol. 66, pp. 511-522, 2014.
- [13] Jariwala A and L. KA., "Nitrogen-rejecting membranes to increase gas heating value and recover pipeline natural gas: A simple wellhead process approach," 12th Annual International Petroleum Environmental Conference. Houston, TX2005.2005.
- [14] C. M. Ott, M. J. Roberts, S. R. Trautmann, and G. Krishnamurthy, "State-of-the-art nitrogen removal for natural gas liquefaction: New solutions to meet market needs," presented at the Gas Tech Conference 2014.
- [15] Tagliabue, M., Farrusseng, D., Valencia, S., Aguado, S., Ravon, U., Rizzo, C., Corma, A. and Mirodatos, C., "Natural gas treating by selective adsorption: Material science and chemical engineering interplay," *Chemical Engineering Journal*, vol. 155, pp. 553-566, 2009.
- [16] Rufford, T.E., Smart, S., Watson, G.C., Graham, B.F., Boxall, J., Da Costa, J.D. and May, E.F., "The removal of CO₂ and N₂ from natural gas: A review of conventional and emerging process technologies," *Journal of Petroleum Science and Engineering*, vol. 94-95, pp. 123-154, 2012.
- [17] Z. Zakaria and S. K. Kamarudin, "Direct conversion technologies of methane to methanol: an overview," *Renewable and Sustainable Energy Reviews*, vol. 65, pp. 250-261, 2016.
- [18] M. Ravi, M. Ranocchiari, and J. A. van Bokhoven, "A critical assessment of the direct catalytic oxidation of methane to methanol," *Angewandte Chemie International Edition*, 2017.
- [19] B. L. Farrell, V. O. Igenegbai, and S. Linic, "A viewpoint on direct methane conversion to ethane and ethylene using oxidative coupling on solid catalysts," *ACS Catalysis*, vol. 6, pp. 4340-4346, 2016.
- [20] A. Galadima and O. Muraza, "Revisiting the oxidative coupling of methane to ethylene in the golden period of shale gas: A review," *Journal of Industrial and Engineering Chemistry*, vol. 37, pp. 1-13, 2016.

- [21] S. D. Angeli, G. Monteleone, A. Giaconia, and A. A. Lemonidou, "State-of-the-art catalysts for CH₄ steam reforming at low temperature," *International Journal of Hydrogen Energy*, vol. 39, pp. 1979-1997, 2014.
- [22] A. Iulianelli, S. Liguori, J. Wilcox, and A. Basile, "Advances on methane steam reforming to produce hydrogen through membrane reactors technology: A review," *Catalysis Reviews*, vol. 58, pp. 1-35, 2016.
- [23] D. C. Rees and J. B. Howard, "Nitrogenase: standing at the crossroads. ," *Current Opinion in Chemical Biology*, vol. 4, pp. 559-566, 2000.
- [24] S. S. Kumar and K. B. Rao, "Biological nitrogen fixation: A Review," *International Journal of Advanced Life Sciences*, vol. 1, pp. 1-9, 2012.
- [25] B. M. Hoffman, D. Lukoyanov, D. R. Dean, and L. C. Seefeldt, "Nitrogenase: a draft mechanism," *Accounts of Chemical Research*, vol. 46, pp. 587-595, 2013.
- [26] M. L. McKee, "A new nitrogenase mechanism using a CFe₈S₉ model: does H₂ elimination activate the complex to N₂ addition to the central carbon atom," *The Journal of Physical Chemistry A*, vol. 120, pp. 754-764, 2016.
- [27] Gilbertson, J.D., Szymczak, N.K., Crossland, J.L., Miller, W.K., Lyon, D.K., Foxman, B.M., Davis, J. and Tyler, D.R., "Coordination chemistry of H₂ and N₂ in aqueous solution. reactivity and mechanistic studies using trans-FeII(P₂)₂X₂-type complexes (P₂ = a chelating, water-solubilizing phosphine)," *Inorganic Chemistry*, vol. 46, pp. 1205-1214, 2007.
- [28] J. L. Crossland, D. M. Young, L. N. Zakharov, and D. R. Tyler, "Precursors to dinitrogen reduction: structures and reactivity of trans-[Fe(DMeOPrPE)₂(N₂-H₂)H]⁺ and trans-[Fe(DMeOPrPE)₂(N₂)H]⁺," *Dalton Transactions*, pp. 9253-9259, 2009.
- [29] D. T. Friesen, Babcock, W.C., Edlund, D.J., Miller, W.K., "Nitrogen sorption", U.S. Patent 5,516,745, 1993.
- [30] D. B. Alvarado, Asaro, M., Bomben, J.L., Damle, A.S., Bhowan, A.S., "Nitrogen removal from low quality gas," SRI International, US Department of Energy, 1996.
- [31] D. C. Bomberger, Bomben, J.L., Amirbahman, A., Asaro, M., "Nitrogen removal from natural gas: phase 2. ," SRI International, US Department of Energy, 1999.
- [32] D. T. Friesen, Babcock, W.C., Edlund, D.J., Lyon D.K., Miller, W.K., "Liquid absorbent solutions for separating nitrogen from natural gas. ," *U.S. Patent 6,136,222*, 2000.
- [33] H.-P. Jia and E. A. Quadrelli, "Mechanistic aspects of dinitrogen cleavage and hydrogenation to produce ammonia in catalysis and organometallic chemistry: relevance of metal hydride bonds and dihydrogen," *Chemical Society Reviews*, vol. 43, pp. 547-564, 2014.
- [34] Y. Nishibayashi, "Recent progress in transition-metal-catalyzed reduction of molecular dinitrogen under ambient reaction conditions," *Inorganic Chemistry*, vol. 54, pp. 9234-9247, 2015.
- [35] S. Kozuch and S. Shaik, "Kinetic-quantum chemical model for catalytic cycles: the Haber-Bosch process and the effect of reagent concentration," *The Journal of Physical Chemistry A*, vol. 112, pp. 6032-6041, 2008.
- [36] J. R. Jennings, *Catalytic ammonia synthesis: fundamentals and practice*, Springer Science & Business Media, 2013.

- [37] S. Giddey, S. P. S. Badwal, and A. Kulkarni, "Review of electrochemical ammonia production technologies and materials," *International Journal of Hydrogen Energy*, vol. 38, pp. 14576-14594, 2013.
- [38] R. Lan, J. T. Irvine, and S. Tao, "Synthesis of ammonia directly from air and water at ambient temperature and pressure," *Scientific Reports*, vol. 3, pp.1145, 2013.
- [39] A. Q. Fenwick, J. M. Gregoire, and O. R. Luca, "Electrocatalytic reduction of nitrogen and carbon dioxide to chemical fuels: challenges and opportunities for a solar fuel device," *Journal of Photochemistry and Photobiology B: Biology*, vol. 152, Part A, pp. 47-57, 2015.
- [40] Ali, M., Zhou, F., Chen, K., Kotzur, C., Xiao, C., Bourgeois, L., Zhang, X. and MacFarlane, D.R., "Nanostructured photoelectrochemical solar cell for nitrogen reduction using plasmon-enhanced black silicon," *Nature Communications*, vol. 7, pp.11335, 2016.
- [41] M. M. Markowitz and D. A. Boryta, "Lithium metal-gas reactions," *Journal of Chemical & Engineering Data*, vol. 7, pp. 586-591, 1962.
- [42] E. McFarlane and F. Tompkins, "Nitridation of lithium," *Transactions of the Faraday Society*, vol. 58, pp. 997-1007, 1962.
- [43] A. V. Joshi, "Inert gas purification," US Patent 5,399,246, 1995.
- [44] T. I. N.Futamura, N. Imanishi, Y. Takeda, and O. Yamamoto, "Lithium nitride formation on lithium metal," presented at the Honolulu PRiME 2012.
- [45] U. Wietelmann, C. Hartnig, U. Emmel, and V. NICKEL, "Stabilised lithium metal formations coated with a shell containing nitrogen, and a method for the production of same," U.S. Patent 14/785,237, 2016.
- [46] M. Schiemann, J. Bergthorson, P. Fischer, V. Scherer, D. Taroata, and G. Schmid, "A review on lithium combustion," *Applied Energy*, vol. 162, pp. 948-965, 2016.
- [47] M. J. R. Christopher M. Ott, Scott R. Trautmann, Gowri Krishnamurthy, "State-Of-The-Art nitrogen removal for natural gas liquefaction: new solutions to meet market needs," presented at the Gas Tech Conference Hamburg, Germany, 2015.
- [48] H. C. B. M. Lang, "Versatile cryogenic nitrogen rejection," presented at the 18th International Conference & Exhibition on Liquefied Natural Gas, Perth, Australia, 2016.
- [49] R. W. Baker, "Membrane technology," in *Encyclopedia of polymer science and technology*, ed: John Wiley & Sons, Inc., 2002.
- [50] K. A. Lokhandwala, M. Ringer, H. Wijmans, and R. W. Baker, "Nitrogen removal from natural gas using membranes," in *Proceedings of the Natural Gas Conference, Federal Energy Technology Center (FETC), Houston, Texas, March, 1999*.
- [51] Zong, Z., Feng, X., Huang, Y., Song, Z., Zhou, R., Zhou, S.J., Carreon, M.A., Yu, M. and Li, S., "Highly permeable N₂/CH₄ separation SAPO-34 membranes synthesized by diluted gels and increased crystallization temperature," *Microporous and Mesoporous Materials*, vol. 224, pp. 36-42, 2016.
- [52] R. W. Baker and K. Lokhandwala, "Natural gas processing with membranes: an overview," *Industrial & Engineering Chemistry Research*, vol. 47, pp. 2109-2121, 2008.
- [53] K. A. Lokhandwala, I. Pinnau, Z. He, K. D. Amo, A. R. DaCosta, J. G. Wijmans, *et al.*, "Membrane separation of nitrogen from natural gas: a case study from membrane synthesis to commercial deployment," *Journal of Membrane Science*, vol. 346, pp. 270-279, 2010.

- [54] K. Tanaka, H. Kita, M. Okano, and K.-i. Okamoto, "Permeability and permselectivity of gases in fluorinated and non-fluorinated polyimides," *Polymer*, vol. 33, pp. 585-592, 1992.
- [55] I. P. Blume, Ingo, "Composite membrane, method of preparation and use," US Patent 4963165, 1990.
- [56] R. W. Baker, K. A. Lokhandwala, I. Pinnau, and S. Segelke, "Methane/nitrogen separation process," Patent 5,669,958, 1997.
- [57] R. W. Baker, K. A. Lokhandwala, J. G. Wijmans, and A. R. Da Costa, "Nitrogen removal from natural gas using two types of membranes," U.S. Patent 6,630,011, 2003.
- [58] Jariwala A and L. KA., "Nitrogen-rejecting membranes to increase gas heating value and recover pipeline natural gas: A simple wellhead process approach," presented at the 12th Annual International Petroleum Environmental Conference. Houston, TX2005.
- [59] K. Lokhandwala, "Field demonstration of a membrane process to separate nitrogen from natural gas – Final technical report," Membrane Technology and Research, Inc.(US)2007.
- [60] T. Kim, W. Koros, G. Husk, and K. O'brien, "'Reverse permselectivity' of N₂ over CH₄ in aromatic polyimides," *Journal of Applied Polymer Science*, vol. 34, pp. 1767-1771, 1987.
- [61] L. M. Robeson, "Correlation of separation factor versus permeability for polymeric membranes," *Journal of Membrane Science*, vol. 62, pp. 165-185, 1991.
- [62] L. M. Robeson, "The upper bound revisited," *Journal of Membrane Science*, vol. 320, pp. 390-400, 2008.
- [63] A. Singh and W. J. Koros, "Significance of entropic selectivity for advanced gas separation membranes," *Industrial & Engineering Chemistry Research*, vol. 35, pp. 1231-1234, 1996.
- [64] X. Ning, "Carbon molecular sieve membranes for nitrogen/methane separation," Ph.D, School of Chemical & Biomolecular Engineering, Georgia Institute of Technology, US, 2014.
- [65] W. J. Koros and C. Zhang, "Materials for next-generation molecularly selective synthetic membranes," *Nature Materials*, vol. 16, pp. 289-297, 2017.
- [66] M. A. Carreon, "Molecular sieve membranes for N₂/CH₄ separation," *Journal of Materials Research*, vol. 33, pp. 32-43, 2018.
- [67] S. Sircar, "Air fractionation by adsorption," *Separation Science and Technology*, vol. 23, pp. 2379-2396, 1988.
- [68] D.-K. Moon, Y.-H. Kim, H. Ahn, and C.-H. Lee, "Pressure swing adsorption process for recovering H₂ from the effluent gas of a melting incinerator," *Industrial & Engineering Chemistry Research*, vol. 53, pp. 15447-15455, 2014.
- [69] K. B. Lee, M. G. Beaver, H. S. Caram, and S. Sircar, "Novel thermal-swing sorption-enhanced reaction process concept for hydrogen production by low-temperature steam methane reforming," *Industrial & Engineering Chemistry Research*, vol. 46, pp. 5003-5014, 2007.
- [70] J. Yang, C.-H. Lee, and J.-W. Chang, "Separation of hydrogen mixtures by a two-bed pressure swing adsorption process using zeolite 5A," *Industrial & Engineering Chemistry Research*, vol. 36, pp. 2789-2798, 1997.
- [71] G. Xiao, R. Singh, A. Chaffee, and P. Webley, "Advanced adsorbents based on MgO and K₂CO₃ for capture of CO₂ at elevated temperatures," *International Journal of Greenhouse Gas Control*, vol. 5, pp. 634-639, 2011.

- [72] G. Xiao, P. Xiao, S. Lee, and P. A. Webley, "CO₂ capture at elevated temperatures by cyclic adsorption processes," *RSC Advances*, vol. 2, pp. 5291-5297, 2012.
- [73] N. Hedin, L. Andersson, L. Bergström, and J. Yan, "Adsorbents for the post-combustion capture of CO₂ using rapid temperature swing or vacuum swing adsorption," *Applied Energy*, vol. 104, pp. 418-433, 2013.
- [74] A. Samanta, A. Zhao, G. K. H. Shimizu, P. Sarkar, and R. Gupta, "Post-combustion CO₂ capture using solid sorbents: A review," *Industrial & Engineering Chemistry Research*, vol. 51, pp. 1438-1463, 2011.
- [75] Saleman, T.L., Li, G.K., Rufford, T.E., Stanwix, P.L., Chan, K.I., Huang, S.H. and May, E.F., "Capture of low grade methane from nitrogen gas using dual-reflux pressure swing adsorption," *Chemical Engineering Journal*, vol. 281, pp. 739-748, 2015.
- [76] J. A. Ritter and A. D. Ebner, "State - of - the - art adsorption and membrane separation processes for hydrogen production in the chemical and petrochemical industries," *Separation Science and Technology*, vol. 42, pp. 1123-1193, 2007.
- [77] D. Saha, Z. Bao, F. Jia, and S. Deng, "Adsorption of CO₂, CH₄, N₂O, and N₂ on MOF-5, MOF-177, and zeolite 5A," *Environmental Science & Technology*, vol. 44, pp. 1820-1826, 2010.
- [78] D. M. Ruthven, "Molecular sieve separations," *Chemie Ingenieur Technik*, vol. 83, pp. 44-52, 2011.
- [79] J. A. Delgado, M. A. Uguina, J. M. Gomez, and L. Ortega, "Adsorption equilibrium of carbon dioxide, methane and nitrogen onto Na- and H-mordenite at high pressures," *Separation and Purification Technology*, vol. 48, pp. 223-228, 2006.
- [80] N. Heymans, B. Alban, S. Moreau, and G. De Weireld, "Experimental and theoretical study of the adsorption of pure molecules and binary systems containing methane, carbon monoxide, carbon dioxide and nitrogen. Application to the syngas generation," *Chemical Engineering Science*, vol. 66, pp. 3850-3858, 2011.
- [81] P. J. E. Harlick and F. H. Tezel, "Adsorption of carbon dioxide, methane and nitrogen: pure and binary mixture adsorption for ZSM-5 with SiO₂/Al₂O₃ ratio of 280," *Separation and Purification Technology*, vol. 33, pp. 199-210, 2003.
- [82] X. Xu, X. Zhao, L. Sun, and X. Liu, "Adsorption separation of carbon dioxide, methane and nitrogen on monoethanol amine modified β -zeolite," *Journal of Natural Gas Chemistry*, vol. 18, pp. 167-172, 2009.
- [83] P. Li and F. Handan Tezel, "Adsorption separation of N₂, O₂, CO₂ and CH₄ gases by β -zeolite," *Microporous and Mesoporous Materials*, vol. 98, pp. 94-101, 2007.
- [84] T. J. Grey, K. P. Travis, J. D. Gale, and D. Nicholson, "A comparative simulation study of the adsorption of nitrogen and methane in siliceous heulandite and chabazite," *Microporous and Mesoporous Materials*, vol. 48, pp. 203-209, 2001.
- [85] J. A. Delgado, M. A. Uguina, J. L. Sotelo, and B. Ruíz, "Modelling of the fixed-bed adsorption of methane/nitrogen mixtures on silicalite pellets," *Separation and Purification Technology*, vol. 50, pp. 192-203, 2006.
- [86] J. A. Delgado, M. A. Uguina, J. L. Sotelo, V. I. Águeda, and P. Gómez, "Numerical simulation of a three-bed PSA cycle for the methane/nitrogen separation with silicalite," *Separation and Purification Technology*, vol. 77, pp. 7-17, 2011.

- [87] S. Cavenati, C. A. Grande, and A. E. Rodrigues, "Separation of CH₄/CO₂/N₂ mixtures by layered pressure swing adsorption for upgrade of natural gas," *Chemical Engineering Science*, vol. 61, pp. 3893-3906, 2006.
- [88] S. Sircar and A. L. Myers, "Gas separation by zeolites," in *Handbook of Zeolite Science and Technology*, S. M. Auerbach, K. A. Carrado, and P. K. Dutta, Eds., CRC Press, 2003.
- [89] Kouvelos, E., K. Kesore, T. Steriotis, H. Grigoropoulou, D. Bouloubasi, N. Theophilou, S. Tzintzos, and N. Kanelopoulos, "High pressure N₂/CH₄ adsorption measurements in clinoptilolites," *Microporous and Mesoporous Materials*, vol. 99, pp. 106-111, 2007.
- [90] A. Jayaraman, A. J. Hernandez-Maldonado, R. T. Yang, D. Chinn, C. L. Munson, and D. H. Mohr, "Clinoptilolites for nitrogen/methane separation," *Chemical Engineering Science*, vol. 59, pp. 2407-2417, 2004.
- [91] R. S. Pillai, S. A. Peter, and R. V. Jasra, "Adsorption of carbon dioxide, methane, nitrogen, oxygen and argon in NaETS-4," *Microporous and Mesoporous Materials*, vol. 113, pp. 268-276, 2008.
- [92] T. L. H. Saleman, "Adsorption-based separations of gaseous nitrogen and methane mixtures," Ph.D, Chemical Engineering, The University of Western Australia, 2016.
- [93] R. T. Yang, *Adsorbents: Fundamentals and Applications*. John Wiley & Sons, Inc., 2003.
- [94] M. A. Sheikh, M. M. Hassan, and K. F. Loughlin, "Adsorption equilibria and rate parameters for nitrogen and methane on Maxsorb activated carbon," *Gas Separation & Purification*, vol. 10, pp. 161-168, 1996.
- [95] S. Jain, A. S. Moharir, P. Li, and G. Wozny, "Heuristic design of pressure swing adsorption: a preliminary study," *Separation and Purification Technology*, vol. 33, pp. 25-43, 2003.
- [96] S. Cavenati, C. A. Grande, and A. E. Rodrigues, "Separation of methane and nitrogen by adsorption on carbon molecular sieve," *Separation Science and Technology*, vol. 40, pp. 2721-2743, 2005.
- [97] A. I. Fatehi, K. F. Loughlin, and M. M. Hassan, "Separation of methane—nitrogen mixtures by pressure swing adsorption using a carbon molecular sieve," *Gas Separation & Purification*, vol. 9, pp. 199-204, 1995.
- [98] P. Kowalczyk, P. A. Gauden, A. P. Terzyk, and S. Furmaniak, "Microscopic model of carbonaceous nanoporous molecular sieves-anomalous transport in molecularly confined spaces," *Physical Chemistry Chemical Physics*, vol. 12, pp. 11351-11361, 2010.
- [99] M. Mitariten, "Nitrogen removal from natural gas with the Molecular Gate™ adsorption process," in *88th Annual Convention of The Gas Processors Association*, San Antonio, Texas, 2009, pp. 544-555.
- [100] TGPE. (2009). *Nitrogen Rejection Units 11-11-2010*. Available: www.tuckergas.com
- [101] R. Wiebe and V. Gaddy, "The solubility in liquid ammonia of hydrogen at 0 °C and of nitrogen at 0, 50, 75, 90 and 100 °C at pressures to 1000 atmospheres critical phenomena of ammonia-nitrogen mixtures," *Journal of the American Chemical Society*, vol. 59, pp. 1984-1987, 1937.
- [102] J. J. W. Latchum, "Absorption of nitrogen by liquid ammonia," US Patent 2521233A, 1950.
- [103] H. Reamer and B. Sage, "Phase behavior in the nitrogen-ammonia system," *Journal of Chemical and Engineering Data*, vol. 4, pp. 303-305, 1959.
- [104] I. R. E. Krichevskii, G. D., "Phase and volume correlations in liquid-gas systems at high pressures V the ammonia - methane system," *Zh. Fiz. Khim.*, vol. 27, pp. 1682-1685, 1953.

- [105] N. Hazari, "Homogeneous iron complexes for the conversion of dinitrogen into ammonia and hydrazine," *Chemical Society Reviews*, vol. 39, pp. 4044-4056, 2010.
- [106] I. Coric, B. Q. Mercado, E. Bill, D. J. Vinyard, and P. L. Holland, "Binding of dinitrogen to an iron-sulfur-carbon site," *Nature*, vol. 526, pp. 96-99, 2015.
- [107] J. M. Berg, *Biochemistry*, 6th ed. New York, N.Y.: W. H. Freeman, 2007.
- [108] J. R. Knowles, "Enzyme-catalyzed phosphoryl transfer reactions," *Annual Review of Biochemistry*, vol. 49, pp. 877-919, 1980.
- [109] B. M. Hoffman, D. Lukoyanov, Z.-Y. Yang, D. R. Dean, and L. C. Seefeldt, "Mechanism of nitrogen fixation by nitrogenase: the next stage," *Chemical Reviews*, vol. 114, pp. 4041-4062, 2014.
- [110] R. N. Thorneley and D. J. Lowe, "Kinetics and mechanism of the nitrogenase enzyme system," *Molybdenum Enzymes*, vol. 7, pp. 89-116, 1985.
- [111] B. Zhao and Y. Su, "Process effect of microalgal-carbon dioxide fixation and biomass production: A review," *Renewable and Sustainable Energy Reviews*, vol. 31, pp. 121-132, 2014.
- [112] D. Moreira and J. C. M. Pires, "Atmospheric CO₂ capture by algae: negative carbon dioxide emission path," *Bioresource Technology*, vol. 215, pp. 371-379, 2016.
- [113] M. D. Fryzuk and S. A. Johnson, "The continuing story of dinitrogen activation," *Coordination Chemistry Reviews*, vol. 200-202, pp. 379-409, 2000.
- [114] G. J. Leigh, "So that's how it's done--Maybe," *Science*, vol. 301, pp. 55-56, 2003.
- [115] J. Sgrignani, D. Franco, and A. Magistrato, "Theoretical studies of homogeneous catalysts mimicking nitrogenase," *Molecules*, vol. 16, pp. 442-465, 2011.
- [116] H. Q. Huang, M. Kofford, F. B. Simpson, and G. D. Watt, "Purification, composition, charge, and molecular weight of the FeMo cofactor from *Azotobacter vinelandii* nitrogenase," *Journal of Inorganic Biochemistry*, vol. 52, pp. 59-75, 1993.
- [117] K. C. MacLeod and P. L. Holland, "Recent developments in the homogeneous reduction of dinitrogen by molybdenum and iron," *Nature chemistry*, vol. 5, pp. 559-565, 2013.
- [118] D. Kleiner and C. H. Chen, "Physical and chemical properties of the nitrogenase proteins from *Azotobacter vinelandii*," *Archives of Microbiology*, vol. 98, pp. 93-100, 1974.
- [119] R. Dixon and D. Kahn, "Genetic regulation of biological nitrogen fixation," *Nat Rev Micro*, vol. 2, pp. 621-631, 2004.
- [120] R. Asatryan, J. W. Bozzelli, and E. Ruckenstein, "Dihydrogen catalysis: a degradation mechanism for N₂-fixation intermediates," *The Journal of Physical Chemistry A*, vol. 116, pp. 11618-11642, 2012.
- [121] Ciais, P., Sabine, C., Bala, G., Bopp, L., Brovkin, V., Canadell, J., Chhabra, A., DeFries, R., Galloway, J., Heimann, M. and Jones, C., "Carbon and other biogeochemical cycles," in *Climate change 2013: the physical science basis. Contribution of Working Group I to the Fifth Assessment Report of the Intergovernmental Panel on Climate Change*, Cambridge University Press, pp. 465-570, 2014.
- [122] D. Herridge, M. Peoples, and R. Boddey, "Global inputs of biological nitrogen fixation in agricultural systems," *Plant and Soil*, vol. 311, pp. 1-18, 2008.

- [123] P. M. Vitousek, D. N. Menge, S. C. Reed, and C. C. Cleveland, "Biological nitrogen fixation: rates, patterns and ecological controls in terrestrial ecosystems," *Philosophical Transactions of the Royal Society B: Biological Sciences*, vol. 368, 2013.
- [124] B. Bergman, G. Sandh, S. Lin, J. Larsson, and E. J. Carpenter, "Trichodesmium—a widespread marine cyanobacterium with unusual nitrogen fixation properties," *FEMS Microbiology Reviews*, vol. 37, pp. 286-302, 2013.
- [125] BP, "BP statistical review of world energy," 2017.
- [126] D. Herridge, M. Peoples, and R. Boddey, "Global inputs of biological nitrogen fixation in agricultural systems," *Plant and Soil*, vol. 311, pp. 1-18, 2008.
- [127] J. R. Postgate, *The fundamentals of nitrogen fixation*: CUP Archive, 1982.
- [128] P. L. Holland, "Metal–dioxygen and metal–dinitrogen complexes: where are the electrons?," *Dalton Transactions*, vol. 39, pp. 5415-5425, 2010.
- [129] M. P. Shaver and M. D. Fryzuk, "Activation of molecular nitrogen: coordination, cleavage and functionalization of N₂ mediated by metal complexes," *Advanced Synthesis & Catalysis*, vol. 345, pp. 1061-1076, 2003.
- [130] T. A. Bazhenova and A. E. Shilov, "Nitrogen fixation in solution," *Coordination Chemistry Reviews*, vol. 144, pp. 69-145, 1995.
- [131] B. A. MacKay and M. D. Fryzuk, "Dinitrogen coordination chemistry: on the biomimetic borderlands," *Chemical Reviews*, vol. 104, pp. 385-402, 2004.
- [132] S. Gambarotta and J. Scott, "Multimetallc cooperative activation of N₂," *Angewandte Chemie International Edition*, vol. 43, pp. 5298-5308, 2004.
- [133] P. L. Holland, "Electronic structure and reactivity of three-coordinate iron complexes," *Accounts of Chemical Research*, vol. 41, pp. 905-914, 2008.
- [134] J. R. Hagadorn and J. Arnold, "Titanium (II), (III), and (IV) complexes supported by benzamidinate ligands," *Organometallics*, vol. 17, pp. 1355-1368, 1998.
- [135] D. Pun, E. Lobkovsky, and P. J. Chirik, "Indenyl zirconium dinitrogen chemistry: N₂ coordination to an isolated zirconium sandwich and synthesis of side-on, end-on dinitrogen compounds," *Journal of the American Chemical Society*, vol. 130, pp. 6047-6054, 2008.
- [136] Smith, J.M., Sadique, A.R., Cundari, T.R., Rodgers, K.R., Lukat-Rodgers, G., Lachicotte, R.J., Flaschenriem, C.J., Vela, J. and Holland, P.L., "Studies of low-coordinate iron dinitrogen complexes," *Journal of the American Chemical Society*, vol. 128, pp. 756-769, 2006.
- [137] W. A. Chomitz and J. Arnold, "Transition metal dinitrogen complexes supported by a versatile monoanionic [N₂P₂] ligand", *Chemical Communications*, vol. 45, pp. 4797-4799, 2007.
- [138] Ding, K., Pierpont, A.W., Brennessel, W.W., Lukat-Rodgers, G., Rodgers, K.R., Cundari, T.R., Bill, E. and Holland, P.L., "Cobalt–dinitrogen complexes with weakened N–N bonds," *Journal of the American Chemical Society*, vol. 131, pp. 9471-9472, 2009.
- [139] Miller, W.K., Gilbertson, J.D., Leiva-Paredes, C., Bernatis, P.R., Weakley, T.J., Lyon, D.K. and Tyler, D.R., "Precursors to water-soluble dinitrogen carriers. synthesis of water-soluble complexes of iron(II) containing water-soluble chelating phosphine ligands of the type 1,2-bis(bis(hydroxyalkyl)phosphino)ethane," *Inorganic Chemistry*, vol. 41, pp. 5453-5465, 2002.
- [140] Pillai, R.S., Yoon, J.W., Lee, S.J., Hwang, Y.K., Bae, Y.S., Chang, J.S. and Maurin, G., "N₂ capture performances of the hybrid porous MIL-101 (Cr): from prediction towards experimental validation," *The Journal of Physical Chemistry C*, vol. 121(40), pp. 22130-22138, 2017.

- [141] Yoon, J.W., Chang, H., Lee, S.J., Hwang, Y.K., Hong, D.Y., Lee, S.K., Lee, J.S., Jang, S., Yoon, T.U., Kwac, K. and Jung, Y., "Selective nitrogen capture by porous hybrid materials containing accessible transition metal ion sites," *Nature Materials*, vol. 16, pp. 526-531, 2017.
- [142] H. Jeazet, T. Koschine, C. Staudt, K. Raetzke, and C. Janiak, "Correlation of gas permeability in a Metal-Organic Framework MIL-101(Cr)-Polysulfone mixed-matrix membrane with free volume measurements by positron annihilation lifetime spectroscopy (PALS)," *Membranes*, vol. 3, pp. 331, 2013.
- [143] T. C. Golden, D. E. Guro, W. C. Kratz, J. M. Occhialini, and T. E. Sabram, "Fundamentals of adsorption," Elsevier Amsterdam, The Netherlands, 1998.
- [144] J. Yokoe, M. Takeuchi, and T. Tsuji, "Adsorbent for separation-recovery of CO, preparing method thereof and process for separation-recovery of high purity CO, using the adsorbent," U.S. Patent 4,713,090, 1987.
- [145] Y. Xie, J. Zhang, J. Qiu, X. Tong, J. Fu, G. Yang, *et al.*, "Zeolites modified by CuCl for separating CO from gas mixtures containing CO₂," *Adsorption*, vol. 3, pp. 27-32, 1997.
- [146] R. T. Yang and E. S. Kikkinides, "New sorbents for olefin/paraffin separations by adsorption via π -complexation," *AIChE Journal*, vol. 41, pp. 509-517, 1995.
- [147] Z. Wu, S.-S. Han, S.-H. Cho, J.-N. Kim, K.-T. Chue, and R. T. Yang, "Modification of resin-type adsorbents for ethane/ethylene separation," *Industrial & Engineering Chemistry Research*, vol. 36, pp. 2749-2756, 1997.
- [148] L. S. Cheng and R. T. Yang, "Monolayer cuprous chloride dispersed on pillared clays for olefin-paraffin separations by π -complexation," *Adsorption*, vol. 1, pp. 61-75, 1995.
- [149] S. U. Rege, J. Padin, and R. T. Yang, "Olefin/paraffin separations by adsorption: π - Complexation vs. kinetic separation," *AIChE Journal*, vol. 44, pp. 799-809, 1998.
- [150] J. Padin and R. T. Yang, "New sorbents for olefin/paraffin separations by adsorption via π -complexation: synthesis and effects of substrates," *Chemical Engineering Science*, vol. 55, pp. 2607-2616, 2000.
- [151] A. Takahashi, F. H. Yang, and R. T. Yang, "Aromatics/aliphatics separation by adsorption: New sorbents for selective aromatics adsorption by π -complexation," *Industrial & Engineering Chemistry Research*, vol. 39, pp. 3856-3867, 2000.
- [152] A. Takahashi, F. H. Yang, and R. T. Yang, "New sorbents for desulfurization by π -complexation: thiophene/benzene adsorption," *Industrial & Engineering Chemistry Research*, vol. 41, pp. 2487-2496, 2002.
- [153] A. Takahashi and R. T. Yang, "New adsorbents for purification: Selective removal of aromatics," *AIChE journal*, vol. 48, pp. 1457-1468, 2002.
- [154] J. Padin, C. L. Munson, and R. T. Yang, "Method for selective adsorption of dienes," U.S. Patent 6,215,037, 2001.
- [155] A. Takahashi, R. T. Yang, C. L. Munson, and D. Chinn, "Cu (I)- Y-zeolite as a superior adsorbent for diene/olefin separation," *Langmuir*, vol. 17, pp. 8405-8413, 2001.
- [156] Y. Kuroda, S.-I. Konno, K. Morimoto, and Y. Yoshikawa, "Strong adsorption of dinitrogen on copper-ion-exchanged mordenite at room temperature," *Journal of the Chemical Society, Chemical Communications*, pp. 18-20, 1993.

- [157] Kuroda, Y., Yoshikawa, Y., Konno, S.I., Hamano, H., Maeda, H., Kumashiro, R. and Nagao, M., "Specific feature of copper ion-exchanged mordenite for dinitrogen adsorption at room temperature," *The Journal of Physical Chemistry*, vol. 99, pp. 10621-10628, 1995.
- [158] A. Itadani, H. Sugiyama, M. Tanaka, T. Mori, M. Nagao, and Y. Kuroda, "New information related to the adsorption model of N₂ on CuMFI at room temperature," *The Journal of Physical Chemistry C*, vol. 111, pp. 16701-16705, 2007.
- [159] A. Itadani, M. Tanaka, T. Mori, M. Nagao, H. Kobayashi, and Y. Kuroda, "A new strategy for the improvement of the N₂ adsorption properties of copper-ion-exchanged MFI-type zeolites at room temperature," *The Journal of Physical Chemistry C*, vol. 111, pp. 12011-12023, 2007.
- [160] A. Itadani, M. Tanaka, T. Mori, H. Torigoe, H. Kobayashi, and Y. Kuroda, "Potential for fixation of N₂ at room temperature utilizing a copper-ion-exchanged MFI-Type zeolite as an adsorbent: evaluation of the bond dissociation energy of adsorbed N-N and the bond strength of the Cu⁺-N-N species," *The Journal of Physical Chemistry Letters*, vol. 1, pp. 2385-2390, 2010.
- [161] Y. Kuroda, Y. Yoshikawa, S. Emura, R. Kumashiro, and M. Nagao, "Characterization of specific N₂-adsorption site existing on CuZSM-5 type zeolite: effect of ion-exchange level on adsorption properties," *The Journal of Physical Chemistry B*, vol. 103, pp. 2155-2164, 1999.
- [162] S. Recchia, C. Dossi, R. Psaro, A. Fusi, R. Ugo, and G. Moretti, "Dinitrogen irreversible adsorption on overexchanged Cu-ZSM-5," *The Journal of Physical Chemistry B*, vol. 106, pp. 13326-13332, 2002.
- [163] Lee, K., Isley III, W.C., Dzubak, A.L., Verma, P., Stoneburner, S.J., Lin, L.C., Howe, J.D., Bloch, E.D., Reed, D.A., Hudson, M.R. and Brown, C.M., "Design of a Metal-Organic Framework with enhanced back bonding for separation of N₂ and CH₄," *Journal of the American Chemical Society*, vol. 136, pp. 698-704, 2014.
- [164] Chang, J.S., Hwang, Y.K., Yoon, J.W., Do-Young, H.O.N.G., Lee, S., Cho, K.H., Hwang, D.W., Bae, Y.S. and Lee, S.J., "Inorganic-organic hybrid nanoporous material with nitrogen selective adsorptivity and method for separating nitrogen-containing gas mixture using the same," U.S. Patent 9,687,772., 2017.
- [165] D. B. Alvarado, Asaro, M., Bomben, J.L., Damle, A.S., Bhowan, A.S., "Nitrogen Removal from Low Quality Gas.", (No. DOE/MC/32265--97/C0875; CONF-970367--), SRI International, Menlo Park, CA (United States), 1997.
- [166] D. C. Bomberger, Bomben, J.L., Amirbahman, A., Asaro, M., "Nitrogen Removal from Natural Gas: Phase 2. ," (No. DE--AC21-95MC32265-01), Federal Energy Technology Center, Morgantown, WV (US); Federal Energy Technology Center, Pittsburgh, PA (US).1999.
- [167] J. Emsley, *Nature's building blocks: an AZ guide to the elements*: Oxford University Press, 2011.
- [168] Kitano, M., Inoue, Y., Yamazaki, Y., Hayashi, F., Kanbara, S., Matsuishi, S., Yokoyama, T., Kim, S.W., Hara, M. and Hosono, H., "Ammonia synthesis using a stable electricle as an electron donor and reversible hydrogen store," *Nature Chemistry*, vol. 4, pp. 934-940, 2012.
- [169] T. Lipman and N. Shah, "Ammonia as an alternative energy storage medium for hydrogen fuel cells: scientific and technical review for near-term stationary power demonstration projects: final report," *UC Berkeley Transportation Sustainability Research Center*, 2007.
- [170] G. Xu and R. Liu, "Sm_{1.5}Sr_{0.5}MO₄ (M=Ni, Co, Fe) cathode catalysts for ammonia synthesis at atmospheric pressure and low temperature," *Chinese Journal of Chemistry*, vol. 27, pp. 677-680, 2009.

- [171] V. Kordali, G. Kyriacou, and C. Lambrou, "Electrochemical synthesis of ammonia at atmospheric pressure and low temperature in a solid polymer electrolyte cell," *Chemical Communications*, vol.17, pp. 1673-1674, 2000.
- [172] G. Xu, R. Liu, and J. Wang, "Electrochemical synthesis of ammonia using a cell with a Nafion membrane and $\text{SmFe}_{0.7}\text{Cu}_{0.3-x}\text{Ni}_x\text{O}_3$ ($x = 0-0.3$) cathode at atmospheric pressure and lower temperature," *Science in China Series B: Chemistry*, vol. 52, pp. 1171-1175, 2009.
- [173] R. Liu and G. Xu, "Comparison of electrochemical synthesis of ammonia by using sulfonated polysulfone and nafion membrane with $\text{Sm}_{1.5}\text{Sr}_{0.5}\text{NiO}_4$," *Chinese Journal of Chemistry*, vol. 28, pp. 139-142, 2010.
- [174] Maroni, V.A., Beatty, R.A., Brown, H.L., Coleman, L.F., Foose, R.M., McPheeters, C.C., Slawewski, M., Smith, D.L., Van Deventer, E.H. and Weston, J.R., "Analysis of the October 5, 1979 lithium spill and fire in the lithium processing test loop," Argonne National Lab., IL (USA)1981.
- [175] R. A. Rhein and C. M. Carlton, "Extinction of lithium fires: Thermodynamic computations and experimental data from literature," *Fire Technology*, vol. 29, pp. 100-130, 1993.
- [176] F. A. Anderson, "Primer for the safe use of liquid alkali metals," Oak Ridge National Lab., Tenn.1967.
- [177] D. Barnett, T. Gil, and M. Kazimi, "Lithium-mixed gas reactions," *Fusion Technol.:(United States)*, vol. 15, pp.967-972, 1989.
- [178] Y. Yavor, S. Goroshin, J. M. Bergthorson, D. L. Frost, R. Stowe, and S. Ringuette, "Enhanced hydrogen generation from aluminum–water reactions," *International Journal of Hydrogen Energy*, vol. 38, pp. 14992-15002, 2013.
- [179] Brockhinke, A., Koppmann, J., Brockhinke, R., Kellermann, R., Eckert, H., Taroata, D. and Schmid, G., "Spectroscopic characterization of lithium combustion," in *MRS Proceedings*, pp. 1644., 2014
- [180] Kellermann, R., Taroata, D., Schiemann, M., Eckert, H., Fischer, P., Scherer, V., Hock, R. and Schmid, G., "Reaction products in the combustion of the high energy density storage material lithium with carbon dioxide and nitrogen," in *MRS Proceedings*, pp. 1644, 2014.
- [181] J. Besson and W. Muller, "The reaction of nitrogen on lithium at ordinary temperatures and the role of water vapor in this reaction," *Compt. Rend.*, vol. 247, pp. 2370-2372, 1958.
- [182] R. A. Rhein, "Lithium combustion: a review," DTIC Document, 1990.
- [183] W. R. Irvine, "The reactions of lithium with nitrogen and water vapour," Master Thesis, University of British Columbia, 1961.
- [184] a. W. M. J. Besson, "The reaction of nitrogen on lithium at ordinary temperatures and the role of water vapor in this reaction," *Compt. Rend.*, vol. 247, pp. 2370-2372, 1958.
- [185] W. Frankenburger and L. Rh, "Über die chemische bindung des stickstoffs an lithium und den mechanismus dieser reaktion," *Berichte der Bunsengesellschaft für physikalische Chemie*, vol. 32, pp. 481-491, 1926.
- [186] Y. Li, Y. Li, Y. Sun, B. Butz, K. Yan, A. L. Koh, *et al.*, "Revealing nanoscale passivation and corrosion mechanisms of reactive battery materials in gas environments," *Nano Letters*, vol. 17, pp. 5171-5178, 2017.
- [187] D. L. Esmay, "Preparation of lithium nitride," US Patent 2910347A, 1959.
- [188] J. Wahl and A. Breitschwerdt, "Lithium nitride of increased conductivity, method for its preparation, and its use," US Patent 06095714, 1982.

- [189] A. Rabenau, U. Von Alpen, E. Schonherr, and G. Muller, "Stable crystalline lithium nitride and process for its preparation," US Patent 4234554A, 1980.
- [190] A. V. Joshi, "Inert gas purification," U.S. Patent 5,399,246, 1995.
- [191] Hirai, C., Uekado, K., Yuasa, A., Nozue, A., Okumura, H., Ishihara, K. and Yamasue, E., "Gas-absorbing substance, gas-absorbing alloy and gas-absorbing material.", U.S. Patent 8,211,202, Kyoto University and Panasonic Corp, 2012.
- [192] Duan, L., Liu, Q., Li, Y., Gao, Y., Zhang, G., Zhang, D., Wang, L. and Qiu, Y., "Thermally decomposable lithium nitride as an electron injection material for highly efficient and stable OLEDs," *The Journal of Physical Chemistry C*, vol. 113, pp. 13386-13390, 2009.
- [193] V. P. Mulgundmath, F. H. Tezel, F. Hou, and T. C. Golden, "Binary adsorption behaviour of methane and nitrogen gases," *Journal of Porous Materials*, vol. 19, pp. 455-464, 2012.
- [194] G. Spoorthi, R. S. Thakur, N. Kaistha, and D. P. Rao, "Process intensification in PSA processes for upgrading synthetic landfill and lean natural gases," *Adsorption*, vol. 17, pp. 121-133, 2011.
- [195] A. Olajosy, "Effective recovery of methane from coal mine methane gas by vacuum pressure swing adsorption: a pilot scale case study," *Chemical Engineering and Science*, vol. 1, pp. 46-54, 2013.
- [196] J.-S. Bae, S. Su, and X. X. Yu, "Enrichment of ventilation air methane (VAM) with carbon fiber composites," *Environmental Science & Technology*, vol. 48, pp. 6043-6049, 2014.
- [197] D. Do, "Analysis of adsorption kinetics in a single homogeneous particle," in *Adsorption Analysis: Equilibria and Kinetics*, Imperial College Press, pp. 519-602, 2011.
- [198] R. M. Rynders, M. B. Rao, and S. Sircar, "Isotope exchange technique for measurement of gas adsorption equilibria and kinetics," *AIChE Journal*, vol. 43, pp. 2456-2470, 1997.
- [199] Y. Yang, A. M. Ribeiro, P. Li, J.-G. Yu, and A. E. Rodrigues, "Adsorption equilibrium and kinetics of methane and nitrogen on carbon molecular sieve," *Industrial & Engineering Chemistry Research*, vol. 53, pp. 16840-16850, 2014.
- [200] Y. Ju, Y. Park, D. Park, J.-J. Kim, and C.-H. Lee, "Adsorption kinetics of CO₂, CO, N₂ and CH₄ on zeolite LiX pellet and activated carbon granule," *Adsorption*, vol. 21, pp. 419-432, 2015.
- [201] T. J. Giesy, Y. Wang, and M. D. LeVan, "Measurement of mass transfer rates in adsorbents: new combined-technique frequency response apparatus and application to CO₂ in 13X zeolite," *Industrial & Engineering Chemistry Research*, vol. 51, pp. 11509-11517, 2012.
- [202] M. I. Hossain, "Volumetric swing frequency response method for determining mass transfer mechanisms in microporous adsorbents (Doctoral dissertation)" University of South Carolina, College of Engineering and Computing, University of South Carolina, 2014.
- [203] T. E. Rufford, G. C. Y. Watson, T. L. Saleman, P. S. Hofman, N. K. Jensen, and E. F. May, "Adsorption equilibria and kinetics of methane + nitrogen mixtures on the activated carbon Norit RB3," *Industrial & Engineering Chemistry Research*, vol. 52, pp. 14270-14281, 2013.
- [204] J. A. C. Silva, K. Schumann, and A. E. Rodrigues, "Sorption and kinetics of CO₂ and CH₄ in binderless beads of 13X zeolite," *Microporous and Mesoporous Materials*, vol. 158, pp. 219-228, 2012.
- [205] D. Friedrich, E. Mangano, and S. Brandani, "Automatic estimation of kinetic and isotherm parameters from ZLC experiments," *Chemical Engineering Science*, vol. 126, pp. 616-624, 2015.
- [206] A. Malek and S. Farooq, "Kinetics of hydrocarbon adsorption on activated carbon and silica gel," *AIChE Journal*, vol. 43, pp. 761-776, 1997.

- [207] Y. Park, Y. Ju, D. Park, and C.-H. Lee, "Adsorption equilibria and kinetics of six pure gases on pelletized zeolite 13X up to 1.0 MPa: CO₂, CO, N₂, CH₄, Ar and H₂," *Chemical Engineering Journal*, vol. 292, pp. 348-365, 2016.
- [208] Dantas, T.L., Luna, F.T., Silva Jr, I.J., Torres, A.E., De Azevedo, D.C.S., Rodrigues, A.E. and Moreira, R.F.P.M., "Modelling of the fixed-bed adsorption of carbon dioxide and a carbon dioxide-nitrogen mixture on zeolite 13X," *Brazilian Journal of Chemical Engineering*, vol. 28, pp. 533-544, 2011.
- [209] J. A. Delgado, V. I. Águeda, M. A. Uguina, J. L. Sotelo, P. Brea, and C. A. Grande, "Adsorption and diffusion of H₂, CO, CH₄, and CO₂ in BPL activated carbon and 13X zeolite: Evaluation of performance in pressure swing adsorption hydrogen purification by simulation," *Industrial & Engineering Chemistry Research*, vol. 53, pp. 15414-15426, 2014.
- [210] Y. S. Bae and C. H. Lee, "Sorption kinetics of eight gases on a carbon molecular sieve at elevated pressure," *Carbon*, vol. 43, pp. 95-107, 2005.
- [211] H. Ahn, H.-K. Yoo, Y. Shul, S. Hyun, and C.-H. Lee, "Diffusion mechanism of N₂ and CH₄ in pelletized zeolite 4A, 5A and CaX," *Journal of Chemical Engineering of Japan*, vol. 35, pp. 334-345, 2002.
- [212] R. J. Mohr, D. Vorkapic, M. B. Rao, and S. Sircar, "Pure and binary gas adsorption equilibria and kinetics of methane and nitrogen on 4A zeolite by isotope exchange technique," *Adsorption*, vol. 5, pp. 145-158, 1999.
- [213] N. Haq and D. M. Ruthven, "Chromatographic study of sorption and diffusion in 4A zeolite," *Journal of Colloid and Interface Science*, vol. 112, pp. 154-163, 1986.
- [214] D. M. Ruthven, L.-K. Lee, and H. Yucel, "Kinetics of non-isothermal sorption in molecular sieve crystals," *AIChE Journal*, vol. 26, pp. 16-23, 1980.
- [215] C. Guan, C. Yang, and K. Wang, "Adsorption kinetics of methane on a template-synthesized carbon powder and its pellet," *Asia-Pacific Journal of Chemical Engineering*, vol. 6, pp. 294-300, 2011.
- [216] Z. Zhang, W. Zhang, X. Chen, Q. Xia, and Z. Li, "Adsorption of CO₂ on zeolite 13X and activated carbon with higher surface area," *Separation Science and Technology*, vol. 45, pp. 710-719, 2010.
- [217] X. Hu, E. Mangano, D. Friedrich, H. Ahn, and S. Brandani, "Diffusion mechanism of CO₂ in 13X zeolite beads," *Adsorption*, vol. 20, pp. 121-135, 2014.
- [218] M. Kocirik, P. Struve, and M. Bulow, "Analytical solution of simultaneous mass and heat transfer in zeolite crystals under constant-volume/variable-pressure conditions," *Journal of the Chemical Society, Faraday Transactions 1: Physical Chemistry in Condensed Phases*, vol. 80, pp. 2167-2174, 1984.
- [219] M. I. Hossain, "Volume swing frequency response method for determining mass transfer mechanisms in microporous adsorbents", Doctoral dissertation, University of South Carolina, 2014.
- [220] N. K. Jensen, T. E. Rufford, G. Watson, D. K. Zhang, K. I. Chan, and E. F. May, "Screening zeolites for gas separation applications involving methane, nitrogen, and carbon dioxide," *Journal of Chemical & Engineering Data*, vol. 57, pp. 106-113, 2011.
- [221] J.-G. Jee, M.-B. Kim, and C.-H. Lee, "Pressure swing adsorption processes to purify oxygen using a carbon molecular sieve," *Chemical Engineering Science*, vol. 60, pp. 869-882, 2005.

- [222] L.-K. Lee and D. M. Ruthven, "Analysis of thermal effects in adsorption rate measurements," *Journal of the Chemical Society, Faraday Transactions 1: Physical Chemistry in Condensed Phases*, vol. 75, pp. 2406-2422, 1979.
- [223] R. Span, E. W. Lemmon, R. T. Jacobsen, and W. Wagner, "A reference quality equation of state for Nitrogen," *International Journal of Thermophysics*, vol. 19, pp. 1121-1132, 1998.
- [224] U. Setzmann and W. Wagner, "A new equation of state and tables of thermodynamic properties for methane covering the range from the melting line to 625 K at pressures up to 100 MPa," *Journal of Physical and Chemical Reference Data*, vol. 20, pp. 1061-1155, 1991.
- [225] T. H. Saleman, G. Y. Watson, T. Rufford, P. Hofman, K. I. Chan, and E. May, "Capacity and kinetic measurements of methane and nitrogen adsorption on H⁺-mordenite at 243–303 K and pressures to 900 kPa using a dynamic column breakthrough apparatus," *Adsorption*, vol. 19, pp. 1165-1180, 2013.
- [226] S. Sircar and J. R. Hufton, "Why does the linear driving force model for adsorption kinetics work?," *Adsorption*, vol. 6, pp. 137-147, 2000.
- [227] M. S. Shafeeyan, W. M. A. Wan Daud, and A. Shamiri, "A review of mathematical modeling of fixed-bed columns for carbon dioxide adsorption," *Chemical Engineering Research and Design*, vol. 92, pp. 961-988, 2014.
- [228] E. Glueckauf and J. I. Coates, "241. Theory of chromatography. Part IV. The influence of incomplete equilibrium on the front boundary of chromatograms and on the effectiveness of separation," *Journal of the Chemical Society (Resumed)*, pp. 1315-1321, 1947.
- [229] D. M. Ruthven, *Principles of adsorption and adsorption processes.*, John Wiley & Sons, 1984.
- [230] B. N. Taylor and C. E. Kuyatt, "Guidelines for evaluating and expressing the uncertainty of NIST measurement results," National Institute of Standards and Technology, 1994.
- [231] T. L. Saleman, G. Xiao, and E. F. May, "Key adsorbent properties for N₂/CH₄ separations measured with a specialised breakthrough column apparatus, to be submitted to Adsorption," 2016.
- [232] T. L. Saleman, "Adsorption-based separations of gaseous nitrogen and methane mixtures," Doctor of Philosophy, School of mechanical and chemical engineering, The University of Western Australia, Perth, Western Australia, 2016.
- [233] M. Bulow. (2016, Aug 1st, 2016). Comments on the publication " Adsorption kinetics of CO₂ , CO, N₂ and CH₄ on zeolite LiX pellet and activated carbon granule " by Youngsan Ju, Yongha Park, Dooyoung Park, Jae-Jeon Kim and Chang-Ha Lee, *Adsorption*, vol. 21, pp. 419-432, 2015.
- [234] D. M. Ruthven, S. Farooq, and K. S. Knaebel, *Pressure swing adsorption*. New York: VCH Publishers, Inc., 1994.
- [235] M. Yu, J. N. Primera-Pedrozo, M. E. Marcano-González, and A. J. Hernández-Maldonado, "Selective adsorption of N₂ over CH₄ in flexible Sr²⁺ and Ba²⁺UPRM-5 (TEA) titanium silicates: effect of activation temperature," *Chemical Engineering Journal*, vol. 252, pp. 311-319, 2014.
- [236] A. Allen and C. Senoff, "Nitrogenopentammineruthenium (II) complexes," *Chem. Commun.(London)*, vol. 24, pp. 621-622, 1965.
- [237] R. Lanigan and T. Yamarik, "Final report on the safety assessment of EDTA, calcium disodium EDTA, diammonium EDTA, dipotassium EDTA, disodium EDTA, TEA-EDTA, tetrasodium EDTA, tripotassium EDTA, trisodium EDTA, HEDTA, and trisodium HEDTA," *International Journal of Toxicology*, vol. 21, pp. 95-142, 2002.

- [238] D. Shirley, S. Walter, and F. Noormohamed, "Natriuretic effect of caffeine: assessment of segmental sodium reabsorption in humans," *Clinical Science*, vol. 103, pp. 461-466, 2002.
- [239] A. A. Kadry, S. I. Fouda, A. M. Shibl, and A. A. Abu El-Asrar, "Impact of slime dispersants and anti-adhesives on in vitro biofilm formation of staphylococcus epidermidis on intraocular lenses and on antibiotic activities," *Journal of Antimicrobial Chemotherapy*, vol. 63, pp. 480-484, 2009.
- [240] T. E. Furia, "EDTA in foods-technical review," *Food Technology*, vol. 18, pp. 1874-&, 1964.
- [241] W. Norvell and W. Lindsay, "Reactions of EDTA complexes of Fe, Zn, Mn, and Cu with soils," *Soil Science Society of America Journal*, vol. 33, pp. 86-91, 1969.
- [242] J. R. Hart, "Ethylenediaminetetraacetic acid and related chelating agents," *Ullmann's Encyclopedia of Industrial Chemistry*, 2000.
- [243] Schnepfensieper, T., Finkler, S., Czap, A., Van Eldik, R., Heus, M., Nieuwenhuizen, P., Wreesmann, C. and Abma, W., "Tuning the reversible binding of NO to Iron(II) aminocarboxylate and related complexes in aqueous solution," *European Journal of Inorganic Chemistry*, vol. 2001, pp. 491-501, 2001.
- [244] Bambagioni, V., Bani, D., Bencini, A., Biver, T., Cantore, M., Chelli, R., Cinci, L., Failli, P., Ghezzi, L., Giorgi, C. and Nappini, S., "Polyamine- polycarboxylate metal complexes with different biological effectiveness as nitric oxide scavengers. Clues for drug design," *Journal of Medicinal Chemistry*, vol. 51, pp. 3250-3260, 2008.
- [245] M. M. Rodriguez, E. Bill, W. W. Brennessel, and P. L. Holland, "N₂ reduction and hydrogenation to ammonia by a molecular iron-potassium complex," *Science*, vol. 334, pp. 780-783, 2011.
- [246] M. Yuki, H. Tanaka, K. Sasaki, Y. Miyake, K. Yoshizawa, and Y. Nishibayashi, "Iron-catalysed transformation of molecular dinitrogen into silylamine under ambient conditions," *Nature Communications*, vol. 3, p. 1254, 2012.
- [247] J. L. Crossland and D. R. Tyler, "Iron-dinitrogen coordination chemistry: dinitrogen activation and reactivity," *Coordination Chemistry Reviews*, vol. 254, pp. 1883-1894, 2010.
- [248] O. Franke, B. E. Wiesler, N. Lehnert, G. Peters, P. Burger, and F. Tuczek, "The iron hydrido complex [FeH(dppe)₂]⁺: solution and solid-state reactivity with dinitrogen," *Zeitschrift für Anorganische und Allgemeine Chemie*, vol. 632, pp. 1247-1256, 2006.
- [249] T. Harris, J. Rathke, and E. Muetterties, "Chemistry of zero- and low-valent metal phosphine and phosphite complexes. 4. The iron system," *Journal of the American Chemical Society*, vol. 100, pp. 6966-6977, 1978.
- [250] Y. Inada, H. Hayashi, K.-i. Sugimoto, and S. Funahashi, "Solvation structures of manganese (II), iron (II), cobalt (II), nickel (II), copper (II), zinc (II), and gallium (III) ions in methanol, ethanol, dimethyl sulfoxide, and trimethyl phosphate as studied by EXAFS and electronic spectroscopies," *The Journal of Physical Chemistry A*, vol. 103, pp. 1401-1406, 1999.
- [251] R. B. Bedford, M. Betham, D. W. Bruce, A. A. Danopoulos, R. M. Frost, and M. Hird, "Iron-Phosphine,- Phosphite,- Arsine, and- Carbene Catalysts for the Coupling of Primary and Secondary Alkyl Halides with Aryl Grignard Reagents," *The Journal of Organic Chemistry*, vol. 71, pp. 1104-1110, 2006.
- [252] A. F. Shestakov and A. E. Shilov, "On the nuclearity of the Vanadium(II)-Pyrocatechol complex active in the reaction of molecular nitrogen reduction," *Kinetics and Catalysis*, vol. 42, pp. 653-656, 2001.

- [253] A. E. Shilov, "Catalytic reduction of molecular nitrogen in solutions," *Russian Chemical Bulletin*, vol. 52, pp. 2555-2562, 2003.
- [254] J. Sebastian and R. V. Jasra, "Anomalous adsorption of nitrogen and argon in silver exchanged zeolite A," *Chemical Communications*, pp. 268-269, 2003.
- [255] Ansón, A., Kuznicki, S.M., Kuznicki, T., Haastrup, T., Wang, Y., Lin, C.C., Sawada, J.A., Eyring, E.M. and Hunter, D., "Adsorption of argon, oxygen, and nitrogen on silver exchanged ETS-10 molecular sieve," *Microporous and Mesoporous Materials*, vol. 109, pp. 577-580, 2008.
- [256] M. Fischer and R. G. Bell, "A DFT-D study of the interaction of methane, carbon monoxide, and nitrogen with cation-exchanged SAPO-34," *Zeitschrift für Kristallographie-Crystalline Materials*, vol. 230, pp. 311-323, 2015.
- [257] A. J. Kidnay, W. R. Parrish, and D. G. McCartney, *Fundamentals of Natural Gas Processing*, 2nd ed. Bosa Roca: CRC Press, 2011.
- [258] Lu, G.Q., Da Costa, J.D., Duke, M., Giessler, S., Socolow, R., Williams, R.H. and Kreutz, T., "Inorganic membranes for hydrogen production and purification: a critical review and perspective," *Journal of Colloid and Interface Science*, vol. 314, pp. 589-603, 2007.
- [259] S. Fu, E. S. Sanders, S. S. Kulkarni, and W. J. Koros, "Carbon molecular sieve membrane structure–property relationships for four novel 6FDA based polyimide precursors," *Journal of Membrane Science*, vol. 487, pp. 60-73, 2015.
- [260] C. Sivasankar, S. Baskaran, M. Tamizmani, and K. Ramakrishna, "Lessons learned and lessons to be learned for developing homogeneous transition metal complexes catalyzed reduction of N₂ to ammonia," *Journal of Organometallic Chemistry*, vol. 752, pp. 44-58, 2014.
- [261] N. Cherkasov, A. O. Ibhaddon, and P. Fitzpatrick, "A review of the existing and alternative methods for greener nitrogen fixation," *Chemical Engineering and Processing: Process Intensification*, vol. 90, pp. 24-33, 2015.
- [262] N. Khoenkhoen, B. de Bruin, J. N. H. Reek, and W. I. Dzik, "Reactivity of dinitrogen bound to mid- and late-transition-metal centers," *European Journal of Inorganic Chemistry*, vol. 2015, pp. 567-598, 2015.
- [263] J. Chatt, J. R. Dilworth, and R. L. Richards, "Recent advances in the chemistry of nitrogen fixation," *Chemical Reviews*, vol. 78, pp. 589-625, 1978.
- [264] A. Poveda, I. C. Perilla, and C. R. Pérez, "Review: Some considerations about coordination compounds with end-on dinitrogen," *Journal of Coordination Chemistry*, vol. 54, pp. 427-440, 2001.
- [265] R. Meier and F. W. Heinemann, "Structures of the spontaneously resolved six-coordinate potassium chloro-(ethylenediaminetriacetato acetic acid) iron (III) monohydrate and the seven-coordinate potassium (ethylenediaminetetracetato) iron (III) sesquihydrate," *Inorganica Chimica Acta*, vol. 337, pp. 317-327, 2002.
- [266] A. A. Diamantis and J. V. Dubrawski, "Preparation and structure of ethylenediaminetetraacetate complexes of ruthenium(II) with dinitrogen, carbon monoxide, and other π -acceptor ligands," *Inorganic Chemistry*, vol. 20, pp. 1142-1150, 1981.
- [267] B. R. Cameron, M. C. Darkes, H. Yee, M. Olsen, S. P. Fricker, and R. T. Skerlj, "Ruthenium(III) polyaminocarboxylate complexes: efficient and effective nitric oxide scavengers," *Inorganic Chemistry*, vol. 42, pp. 1868-1876, 2003.

- [268] D. Chatterjee, E. Ember, U. Pal, S. Ghosh, and R. van Eldik, "Remarkably high catalytic activity of the Ru^{III}(edta)/H₂O₂ system towards degradation of the azo-dye orange II," *Dalton Transactions*, vol. 40, pp. 10473-10480, 2011.
- [269] R. Span, E. W. Lemmon, R. T. Jacobsen, W. Wagner, and A. Yokozeki, "A reference equation of state for the thermodynamic properties of nitrogen for temperatures from 63.151 to 1000 K and pressures to 2200 MPa," *Journal of Physical and Chemical Reference Data*, vol. 29, pp. 1361-1433, 2000.
- [270] "MultiFlash", InfoChem/KBC Advanced Technologies PLC, 2014.
- [271] M. J. Camenzind, B. R. James, D. Dolphin, J. W. Sparapany, and J. A. Ibers, "Molecular dinitrogen complexes of ruthenium (II) porphyrins," *Inorganic Chemistry*, vol. 27, pp. 3054-3057, 1988.
- [272] J. P. Collman, J. I. Brauman, J. P. Fitzgerald, J. W. Sparapany, and J. A. Ibers, "Reversible binding of dinitrogen and dioxygen by a ruthenium picnic-basket porphyrin," *Journal of the American Chemical Society*, vol. 110, pp. 3486-3495, 1988.
- [273] D. T. Friesen, W. C. Babcock, D. J. Edlund, and W. K. Miller, "Nitrogen sorption," US Patent US005516745A, 1996.
- [274] S. H. Park, K. B. Lee, J. C. Hyun, and S. H. Kim, "Correlation and prediction of the solubility of carbon dioxide in aqueous alkanolamine and mixed alkanolamine solutions," *Industrial & Engineering Chemistry Research*, vol. 41, pp. 1658-1665, 2002.
- [275] Y. E. Kim, J. A. Lim, S. K. Jeong, Y. I. Yoon, S. T. Bae, and S. C. Nam, "Comparison of carbon dioxide absorption in aqueous MEA, DEA, TEA, and AMP solutions," *Bull. Korean Chem. Soc.*, vol. 34, pp. 783-787, 2013.
- [276] Thee, H., Suryaputradinata, Y.A., Mumford, K.A., Smith, K.H., da Silva, G., Kentish, S.E. and Stevens, G.W., "A kinetic and process modeling study of CO₂ capture with MEA-promoted potassium carbonate solutions," *Chemical Engineering Journal*, vol. 210, pp. 271-279, 2012.
- [277] P. D. Vaidya and E. Y. Kenig, "CO₂ - Alkanolamine reaction kinetics: a review of recent studies," *ChemInform*, vol. 39, pp. 1467-1474, 2008.
- [278] I. J. Uyanga and R. O. Idem, "Studies of SO₂- and O₂-induced degradation of aqueous MEA during CO₂ capture from power plant flue gas streams," *Industrial & Engineering Chemistry Research*, vol. 46, pp. 2558-2566, 2007.
- [279] H. Kim, H. J. Cho, S. Narayanan, S. Yang, H. Furukawa, S. Schiffres, *et al.*, "Characterization of adsorption enthalpy of novel water-stable zeolites and metal-organic frameworks," *Scientific Reports*, vol. 6, 2016.
- [280] S.-W. Rho, K.-P. Yoo, J. S. Lee, S. C. Nam, J. E. Son, and B.-M. Min, "Solubility of CO₂ in aqueous methyldiethanolamine solutions," *Journal of Chemical & Engineering Data*, vol. 42, pp. 1161-1164, 1997.
- [281] X. Chen, "Carbon dioxide thermodynamics, kinetics, and mass transfer in aqueous piperazine derivatives and other amines.," University of Texas at Austin, 2011.
- [282] G. T. Rochelle, "Amine scrubbing for CO₂ capture," *Science*, vol. 325, pp. 1652-1654, 2009.
- [283] Bezerra, D.P., da Silva, F.W., de Moura, P.A., Sousa, A.G., Vieira, R.S., Rodriguez-Castellon, E. and Azevedo, D.C., "CO₂ adsorption in amine-grafted zeolite 13X," *Applied Surface Science*, vol. 314, pp. 314-321, 2014.

- [284] P. R. Díaz-Herrera, M. J. Ramírez-Moreno, and H. Pfeiffer, "The effects of high-pressure on the chemisorption process of CO₂ on lithium oxosilicate (Li₈SiO₆)," *Chemical Engineering Journal*, vol. 264, pp. 10-15, 2015.
- [285] S. H. Barghi, T. T. Tsotsis, and M. Sahimi, "Chemisorption, physisorption and hysteresis during hydrogen storage in carbon nanotubes," *International Journal of Hydrogen Energy*, vol. 39, pp. 1390-1397, 2014.
- [286] Yamaguchi, S., Ichikawa, T., Wang, Y., Nakagawa, Y., Isobe, S., Kojima, Y. and Miyaoka, H., "Nitrogen dissociation via reaction with lithium alloys," *ACS Omega*, vol. 2, pp. 1081-1088, 2017.
- [287] K. F. Loughlin, "Water isotherm models for 4A (NaA) zeolite," *Adsorption*, vol. 15, pp. 337-353, 2009.
- [288] R. M. Yonco, E. Veleckis, and V. A. Maroni, "Solubility of nitrogen in liquid lithium and thermal decomposition of solid Li₃N," *Journal of Nuclear Materials*, vol. 57, pp. 317-324, 1975.
- [289] H. Kimura, M. Asano, and K. Kubo, "Vaporization of solid lithium nitride," *Journal of Nuclear Materials*, vol. 91, pp. 200-204, 1980.
- [290] J. Sangster and A. D. Pelton, "The Li-N (lithium-nitrogen) system," *Journal of Phase Equilibria*, vol. 13, pp. 291-296, 1992.
- [291] P. S. Hofman, T. E. Rufford, K. I. Chan, and E. F. May, "A dynamic column breakthrough apparatus for adsorption capacity measurements with quantitative uncertainties," *Adsorption*, vol. 18, pp. 251-263, 2012.
- [292] T. L. Saleman, G. C. Watson, T. E. Rufford, P. S. Hofman, K. I. Chan, and E. F. May, "Capacity and kinetic measurements of methane and nitrogen adsorption on H⁺-mordenite at 243–303 K and pressures to 900 kPa using a dynamic column breakthrough apparatus," *Adsorption*, vol. 19, pp. 1165-1180, 2013.
- [293] J. D. Cox, D. D. Wagman, and V. A. Medvedev, *CODATA key values for thermodynamics: Chem/Mats-Sci/E*, 1989.
- [294] M. W. Chase, "NIST-JANAF thermochemical tables," *J. Phys. Chem. Ref. Data. Monograph*, 1998.
- [295] O. Loebich and C. J. Raub, "Reactions between some alkali and platinum group metals," *Platinum Metals Review*, vol. 25, pp. 113-120, 1981.
- [296] N. Yao, L. Heredy, and R. Saunders, "Emf measurements of electrochemically prepared lithium - aluminum alloy," *Journal of The Electrochemical Society*, vol. 118, pp. 1039-1042, 1971.
- [297] S. A. Mahi P, Fray DJ, Charles JA., "Lithium—metal of the future," *Journal of the Minerals, Metals and Materials Society*, vol. 38, pp. 20-26, 1986.
- [298] R. A. Huggins, "Lithium alloy negative electrodes," *Journal of Power Sources*, vol. 81-82, pp. 13-19, 1999.
- [299] W. A. Averill and D. L. Olson, "A review of extractive processes for lithium from ores and brines," *Energy*, vol. 3, pp. 305-313, 1978.
- [300] V. De Nora, P. M. Spaziante, and A. Nidola, "Molten salt electrolysis," US Patent 4,187,155, 1980.
- [301] K. Sintim-Damoa, S. S. Reddy, and E. S. McCormick, "Electrolytic production of lithium metal," US Patent 4,455,202, 1984.

- [302] D. R. Sadoway, "Toward new technologies for the production of lithium," *Journal of the Minerals, Metals and Materials Society*, vol. 50, pp. 24-26, 1998.
- [303] Saleman, T.L., Li, G.K., Rufford, T.E., Stanwix, P.L., Chan, K.I., Huang, S.H. and May, E.F., "Capture of low grade methane from nitrogen gas using dual-reflux pressure swing adsorption," *Chemical Engineering Journal*, vol. 281, pp. 739-748, 2015.
- [304] Y. Zhang, T. L. H. Saleman, G. K. Li, G. Xiao, B. R. Young, and E. F. May, "Non-isothermal numerical simulations of dual reflux pressure swing adsorption cycles for separating $N_2 + CH_4$," *Chemical Engineering Journal*, vol. 292, pp. 366-381, 2016.
- [305] E. F. May, Y. Zhang, T. L. H. Saleman, G. Xiao, G. K. Li, and B. R. Young, "Demonstration and optimisation of the four dual-Reflux pressure swing adsorption configurations," *Separation and Purification Technology*, vol. 177, pp. 161-175, 2017.
- [306] S. Morpurgo, G. Moretti, and M. Bossa, "A computational study on N_2 adsorption in Cu-ZSM-5," *Physical Chemistry Chemical Physics*, vol. 9, pp. 417-424, 2007.
- [307] K. Shimizu, "Reaction of Ru (II)-EDTA in sodium formate-formic acid solutions," *Bulletin of the Chemical Society of Japan*, vol. 50, pp. 2921-2926, 1977.
- [308] D. Chatterjee, A. Mitra, and G. De, "Ruthenium polyaminocarboxylate complexes," *Platinum Metals Review*, vol. 50, pp. 2-12, 2006.
- [309] J. Prywer, M. Olszynski, A. Torzewska, and E. Mielniczek-Brzóska, "Comparative in vitro studies on disodium EDTA effect with and without *Proteus mirabilis* on the crystallization of carbonate apatite and struvite," *Journal of Crystal Growth*, vol. 395, pp. 123-131, 2014.
- [310] P. J. V. d. Schaar, R. T. B. Pahlplatz, and E. Blaurock-Busch, "The effects of Magnesium-EDTA chelation therapy on arterial stiffness," *Health*, vol. Vol.06No.21, p. 6, 2014.
- [311] A. A. Diamantis and J. V. Dubrawski, "Preparation and structure of ethylenediaminetetraacetate complexes of ruthenium(II) with dinitrogen, carbon monoxide, and other π -acceptor ligands," *Inorganic Chemistry*, vol. 20, pp. 1142-1150, 1981.
- [312] N. A. Davies, Wilson, M.T., Slade, E., Fricker, S.P., Murrer, B.A., Powell, N.A. and Henderson, G.R., 1997. Kinetics of nitric oxide scavenging by ruthenium (III) polyaminocarboxylates: novel therapeutic agents for septic shock., "Kinetics of nitric oxide scavenging by ruthenium(iii) polyaminocarboxylates: novel therapeutic agents for septic shock," *Chemical Communications*, pp. 47-48, 1997.
- [313] D. Titus, A. A. Orio, H. B. Gray, G. W. Parshall, and J. J. Mrowca, "Low-valent metal complexes of diethylphenylphosphonite," in *Inorganic Syntheses*, John Wiley & Sons, Inc., pp. 117-121, 2007
- [314] Y. G. Borod'ko, M. O. Broitman, L. M. Kachapina, A. K. Shilova, and A. E. Shilov, "Infrared spectra of complexes of molecular nitrogen with iron(II) compounds," *Journal of Structural Chemistry*, vol. 12, pp. 498-499, 1971.